

**Laminar and turbulent liquid-liquid dispersions:
a lattice Boltzmann study**

by
Alexandra E. Komrakova

A thesis submitted in partial fulfillment of the requirements for the degree of

**Doctor of Philosophy
in
Chemical Engineering**

Department of Chemical and Materials Engineering
University of Alberta

©Alexandra E. Komrakova, 2014

Abstract

A numerical approach based on a diffuse-interface free energy lattice Boltzmann equation method is developed to gain fundamental insight in liquid-liquid dispersions. The approach relies on detailed resolution of the interaction of the dispersed and continuous phases at the microscopic level, including drop breakup and coalescence. Several studies have been performed. A study of the gravity-driven motion of a single *n*-butanol drop in water demonstrates that the method handles complex drop deformations, including shape-oscillating motion of drops. Simulations of a single liquid drop in simple shear flow were used to assess the impact of numerical parameters on drop deformation levels. At higher capillary numbers the simulations capture end-pinching and capillary wave breakup mechanisms. The method handles a range of shearing conditions from near-creeping flow, to drop Reynolds of 50, also a viscosity ratio range (dispersed phase over continuous phase viscosity) of 0.1 – 3.0. The feasibility of direct numerical simulations of turbulently agitated liquid-liquid dispersions is demonstrated. Three-dimensional simulations are carried out in fully-periodic cubic domains with grids of size 500^3 and 1000^3 and the resolution of the Kolmogorov length scale in the range 1 – 10 lattice units. The process of dispersion formation is visualized, revealing the details of breakup and coalescence. However, several numerical issues are encountered: appearance of spurious currents over liquid-liquid interface, dissolution of small drops, and easy coalescence of drops. The effects of each drawback on the results are discussed.

Preface

Chapter 2 of this thesis has been published as A.E. Komrakova, D. Eskin, J.J. Derksen, Lattice Boltzmann simulations of a single n-butanol drop rising in water, *Phys. Fluids*, 25, 042102 (2013). D. Eskin and J.J. Derksen were the supervisory authors and were involved in discussions of the results and manuscript composition.

Chapter 3 of this thesis has been published as A.E. Komrakova, Orest Shardt, D. Eskin and J.J. Derksen, Lattice Boltzmann simulations of drop deformation and breakup in shear flow, *IJMF*, 59, 24-43 (2014). Part of the simulations in this study have been performed by me using the computer code provided by Orest Shardt. I was responsible for data analysis and the manuscript composition. Orest Shardt assisted with the code usage and modifications and contributed to manuscript edits. D. Eskin and J.J. Derksen were the supervisory authors and were involved in discussions of the results and manuscript composition.

Chapter 4 of this thesis is submitted to a journal as A.E. Komrakova, Orest Shardt, D. Eskin and J.J. Derksen, Effects of dispersed phase viscosity on drop deformation and breakup in inertial shear flow, *Phys. Fluids*. It was my responsibility to perform simulations using the computer code provided by Orest Shardt who also assisted with manuscript composition. I carrying out data analysis and worked on the manuscript composition. D. Eskin and J.J. Derksen were the supervisory authors and were involved in discussions of the results and manuscript composition.

To My Family

Acknowledgements

I would like to thank my supervisor Dr. Jos Derksen for his professionalism and boundless enthusiasm in research that motivated and inspired me throughout this project. I am particularly grateful for his patient assistance and strong support of my research and writing efforts. I would also like to thank my co-supervisor Dr. Dmitry Eskin for his invaluable guidance and contribution from industrial perspective. He could always bring a light into discussion with new engineering ideas.

My thanks and appreciation to Dr. Suzanne Kresta who opened up new to me the field of mixing research.

My special thanks to friends and colleagues: Monika Wasylkiewicz, Alexandr Kuzmin, Orest Shardt, Nitesh Goyal, Radompon Sungkorn for their help and support. I will never forget the days we have spent in NREF discussing lattice Boltzmann concepts and capabilities.

I gratefully acknowledge the financial support from Schlumberger. I also acknowledge Compute Canada for the opportunity to use WestGrid clusters. This work could not have been accomplished without this computational facility. I am particularly grateful to Masao Fujinaga, Doug Phillips and Kamil Marcinkowski for the computational support.

A sincere thank to my husband Aleksey Baldygin and my little daughter Olivia for their love, support and endless patience.

Finally, I would like to thank my parents and sister whose love and tremendous support has allowed me to pursuit my research studies.

Contents

1	Introduction	1
1.1	Motivation	1
1.2	Literature review	3
1.3	Research project objectives	8
1.4	Outline of the thesis	10
2	Lattice Boltzmann simulations of a single <i>n</i>-butanol drop rising in water	18
2.1	Introduction	18
2.2	Problem statement	23
2.3	Numerical method	25
2.3.1	Governing equations	25
2.3.2	LBE method implementation	28
2.3.3	Scaling procedure	33
2.3.4	Moving reference frame	38
2.4	Numerical technique verification	39
2.4.1	Domain size influence	42
2.4.2	Mesh resolution	43
2.4.3	Moving reference frame implementation	45
2.5	Analyses of <i>n</i> -butanol drop motion in water	46
2.6	Conclusion	56
3	Lattice Boltzmann simulations of drop deformation and breakup in shear flow	65

3.1	Introduction	65
3.2	Problem statement	69
3.3	Numerical method	70
3.4	Simulations of a single drop under simple shear flow	75
3.4.1	Choice of numerical parameters	76
3.4.2	Stokes flow simulations	85
3.4.3	Influence of inertia	86
3.4.4	Joint influence of viscosity ratio and inertia	91
3.5	Conclusions	98
4	Effects of dispersed phase viscosity on drop deformation and breakup in inertial shear flow	107
4.1	Introduction	107
4.2	Numerical method and its implementation	109
4.3	Stratified flow benchmark	113
4.4	Results	116
4.5	Conclusions	132
5	Numerical study of turbulent liquid-liquid dispersions	138
5.1	Introduction	138
5.2	Mathematical formulation	142
5.3	Simulation parameters	146
5.4	Single-phase turbulence	149
5.5	Two-phase flow	151
5.5.1	Effect of Kolmogorov scale resolution	151
5.5.2	Effect of dispersed phase volume fraction	160
5.5.3	Effect of dispersed phase volume fraction and resolution of Kolmogorov scales	165
5.5.4	Energy spectra in one- and two-phase turbulent flow	165
5.6	Conclusions	170

6	Conclusions and outlook	179
6.1	Conclusions	179
6.2	Outlook	185
	Appendix	189
A-1	The D3Q19 model parameters	189
A-2	Benchmark cases	192
A-3	Comparison of CPU and GPU codes	200

List of Tables

2.1	Physical parameters of the <i>n</i> -butanol/water binary system (Bertakis et al., 2010)	24
2.2	Drop diameter <i>d</i> and corresponding Eötvös number <i>Eo</i> considered in the present simulations	36
3.1	Wall proximity influence (<i>H</i> is a distance between the moving plates). Elongation <i>L/a</i> and orientation angle θ of a drop with undeformed radius <i>a</i> = 20 [lu] at <i>Ca</i> = 0.27, <i>Re</i> = 1, λ = 1, <i>Pe</i> = 1 and <i>Ch</i> = 0.057.	78
3.2	Deformation parameter for different <i>Re</i> numbers, <i>Ca</i> = 0.3, λ = 1.0	91
4.1	Capillary number <i>Ca</i> as a function of viscosity ratio λ at <i>Re</i> = 10	116
4.2	Effect of mesh resolution	126
5.1	Simulation parameters: <i>L_d</i> is the cubic simulation domain edge length; <i>u*</i> is the characteristic velocity; ν_c is the kinematic viscosity of continuous phase; η_K is the Kolmogorov length scale	148

List of Figures

2.1	Simulation domain with boundary conditions: $x = 0$ is the outflow boundary; $x = L_d$ is the inflow boundary; all the rest side boundaries are the free-slip walls. The drop is kept in the middle of the simulation domain and has a spherical shape at $t = 0$	28
2.2	Simulation domain slice ($z = 0$). Inertial (stationary) reference frame (x - y); non-inertial (moving) reference frame (\hat{x} - \hat{y})	37
2.3	The evolution of 2 mm drop rise velocity in time and terminal drop shape for different cases. — case 1 (TRT); --- case 2 (BGK)	40
2.4	Domain size influence. The evolution of 2.0 mm drop rise velocity in time for different simulation domain widths. The length of the domain is $14\tilde{d}$; - · - · - $W = 2\tilde{d}$; — $W = 3\tilde{d}$; - - - $W = 4\tilde{d}$	43
2.5	Mesh resolution. Terminal drop velocity as a function of drop diameter \tilde{d} in lattice units for 1.0 and 2.0 mm drops obtained	44
2.6	Time evolution of terminal rise velocity of 2.0 mm drop calculated in two test cases: — stationary reference frame; --- moving reference frame.	46
2.7	Streamlines with x -component of velocity for 2.0 mm drop in two cases: moving reference frame and stationary reference frame. The white curve represents the interface	47
2.8	Simulated drop terminal velocities (*) of n -butanol drops in water as a function of drop diameter compared to semi-empirical correlation proposed by Henschke (solid line), experiments (\circ) and simulations (\triangleright) by Bertakis et al. (2010), simulations (\square) by Bäumlner et al. (2011)	49

2.9	Simulated aspect ratio E (*) as a function of Eötvös number Eo in comparison with Bäumlner et al. (2011) (the results of numerical simulation due to (Bäumlner et al., 2011) are denoted as \square ; the solid curve stands for the data fitting curve described by equation (2.44))	49
2.10	Drop rise velocity as a function of time for different drop diameters; a - 1.0 mm drop in spherical regime and 1.5, 2.48 mm drops in deformed regime; b - 2.6 and 2.8 mm drops refer to transition between deformed and oscillating droplets; c - 3.0 mm drop; d - 3.48 mm drop; e - 3.8 mm drop; f - 4.0 mm drop is the largest simulated drop in the present study	52
2.11	Streamlines and drop shape for $d = 3.48$ mm (upper row) and $d = 3.8$ mm (bottom row) drops at different moments	53
2.12	The n -butanol drop deformation of 4.0 mm diameter at different time steps	54
2.13	Comparison of simulated Reynolds numbers Re as a function of Eötvös number Eo for Morton number $Mo = 1.23 \cdot 10^{-6}$ to the graphical correlation by (Clift et al., 1978)	55
2.14	Simulated Reynolds number Re versus Weber number We plotted with drop shapes in steady-state. (Gravitational acceleration is directed from right to left)	56
2.15	Capillary number Ca versus Eötvös number Eo ; (*) present simulations; (\square) the Ca number value plotted using the terminal velocity obtained with semi-empirical correlation proposed by (Bäumlner et al., 2011)	57
3.1	Single drop under simple shear flow	69
3.2	Simulation domain with boundary conditions: $x = 0$ and $x = L$ are periodic boundaries; $y = 0$ and $y = H$ are no-slip walls moving with constant velocity u_w ; $z = 0$ and $z = W$ are the symmetry planes. At $t = 0$ the drop has a spherical shape. Due to the symmetry of the problem only half of the drop has been simulated	75

3.3	Drop elongation L , deformation $D = (L - B)/(L + B)$ and orientation angle θ measurements	77
3.4	Drop deformation results at $Re = 1$, $Ca = 0.27$, $\lambda = 1$ and different Pe and Ch numbers. The L/a ratio (a) and the orientation angle θ (b) as a function of drop radius	79
3.5	Drop shape and streamlines at steady-state for drop with radius $a = 30$ [lu] at $Re = 10$, $Ca = 0.15$, $\lambda = 1$ and different Pe and Ch numbers	82
3.6	Drop shape (φ field) at steady state. The drop radius is $a = 30$ [lu] and $Pe = 3$. (a) $\xi = 1.14$ [lu], $\Gamma = 4.3$; (b) $\xi = 2$ [lu], $\Gamma = 13.3$	83
3.7	Deformation (a) and orientation (b) of a drop in simple shear flow under near Stokes conditions. Present simulation results (at $Re = 0.0625$) with free energy LBE *; Previous results: \diamond VOF computations of Li et al. (2000); \square boundary integral method of Rallison (1981); \times boundary integral method of Kwak and Pozrikidis (1998); \triangle boundary integral method of Kennedy et al. (1994); \circ experimental results by Rumscheidt and Mason (1961)	86
3.8	Steady state drop shape (black curve stands for the interface), streamlines and velocity fields ($x - y$ plane at $z = 0$). Stokes flow ($Re = 0.0625$), $\lambda = 1$	87
3.9	Evolution of the drop shape at $Re = 0.0625$, $Ca = 0.42$, $\lambda = 1.0$ and initial drop radius $a = 30$ [lu] ($\bar{t} = t\dot{\gamma}$). The images only show a portion of the full domain	88
3.10	Evolution of the drop shape at $Re = 0.0625$, $Ca = 0.42$, $\lambda = 1.0$ and initial drop radius $a = 64$ [lu] ($\bar{t} = t\dot{\gamma}$)	89
3.11	Steady-state velocity field and drop shape for $Ca = 0.3$, $\lambda = 1$ and different Re numbers	90
3.12	Capillary number Ca as a function of viscosity ratio λ . Present simulations with free energy LBE: * Ca for which drop attains steady shape; \triangle Ca for which drop breaks up; \circ critical capillary numbers Ca_c obtained by VOF method (Khismatullin et al., 2003)	92

3.13	Drop shape and velocity field inside the drop for different Reynolds numbers Re and near critical capillary number Ca for each Re ($\lambda = 1$); $Ch = 0.0568$; (a) $Pe = 0.41$; (b) $Pe = 1.45$; (c) $Pe = 1$; (d) $Pe = 4.15$	93
3.14	Drop shape and internal circulations at $Re = 1$ and near critical capillary number for each λ ; $Ch = 0.0568$; (a) $Pe = 1.45$; (b) $Pe = 1.5$; (c) $Pe = 1.65$	94
3.15	Drop shape and velocity field change in time for $Re = 1$, $Ca = 0.3$, $\lambda = 2$ ($\bar{t} = t\dot{\gamma}$). Initial drop radius $a = 20$ [lu]; the Cahn number $Ch = 0.0568$, the Peclet number $Pe = 1.55$	95
3.16	Drop shape and velocity field change in time for $Re = 50$, $Ca = 0.09$, $\lambda = 2$ ($\bar{t} = t\dot{\gamma}$). Initial drop radius $a = 20$ [lu]; the Cahn number $Ch = 0.0568$, the Peclet number $Pe = 3.93$	96
3.17	Drop shape and velocity field change in time for $Re = 50$, $Ca = 0.085$, $\lambda = 2$ ($\bar{t} = t\dot{\gamma}$). Initial drop radius $a = 30$ [lu]; the Cahn number $Ch = 0.0379$, the Peclet number $Pe = 3.71$	97
4.1	Simulation domain with the following boundary conditions: $x = 0$ and $x = L_d$ are periodic boundaries; $y = 0$ has a rotational symmetry boundary condition; $y = H$ is a no-slip wall moving with constant velocity u_w ; $z = 0$ and $z = -W$ are symmetry planes. At $t = 0$ the drop has a spherical shape with initial radius a . Due to the symmetry of the problem only one quarter of the domain needed to be simulated	112
4.2	A slice of the simulation domain at $z = 0$ for validation simulations of stratified shear flow; $h = 64$ [lu], $H = 4h$, $\lambda = \mu_d/\mu_c = 0.1 - 2$	113
4.3	The x -velocity component as a function of position between the domain center and the sheared plate for different λ in stratified flow; $y/H = 0.25$ is the location of the interface	115

4.4	Relative deviation of x -velocity component in the fluid between numerical and analytical solutions as a function of position between the domain center and the sheared plate for different λ in stratified flow; $y/H = 0.25$ is the location of the interface	115
4.5	Capillary number Ca as a function of viscosity ratio λ for the Reynolds number $Re = 10$. Present simulations with free energy LBE: \square Ca for which drop attains steady shape; \circ Ca for which drop breaks; * critical capillary numbers Ca_c obtained by VOF method (Khismatullin and Renardy, 2003)	117
4.6	Drop elongation L and orientation angle θ measurements	117
4.7	Drop deformation results at $Re = 10$. The L/a ratio (a) and the orientation angle θ (b) as a function of viscosity ratio λ at the highest subcritical Ca (the square symbols in Fig. 4.5)	118
4.8	Drop shape and internal circulations at $Re = 10$ and the highest subcritical capillary number for each viscosity ratio λ . The colour of the streamlines shows the speed based on x - and y -velocity components in the $(x - y)$ section (see Fig. 4.1) and varies from minimum (dark blue) to maximum (dark red) values	119
4.9	Drop shape and velocity field over time at the lowest supercritical capillary number $Ca = 0.149$, $Re = 10$, $\lambda = 2$ ($\bar{t} = t\dot{\gamma}$). The images show $\sim 40\%$ of the full domain height. Colour indicates velocity magnitude from lowest (dark blue) to highest (dark red)	121
4.10	Enlarged image of satellite drop shape and velocity field at $Ca = 0.149$, $Re = 10$, $\lambda = 2$ and $\bar{t} = 135.1$ showing a tendency to form two sub-satellite drops due to formation of bridges at the locations indicated by the arrows	122
4.11	Drop shape and velocity field over time at the lowest supercritical capillary number $Ca = 0.193$, $Re = 10$, $\lambda = 0.1$. The images show $\sim 40\%$ of the full domain height. Colour indicates velocity magnitude from lowest (dark blue) to highest (dark red) values	123

4.12	The L/a ratio at the moment of breakage as a function of viscosity ratio λ at the lowest supercritical capillary number	124
4.13	The L/a ratio as a function of time for different viscosity ratios at the corresponding lowest supercritical capillary numbers. The time series are stopped at the time instant just before the breakup event	124
4.14	Drop shape and velocity field for different viscosity ratios at $Ca \sim Ca_c$ (the lowest supercritical value) just before breakup. Colour indicates velocity magnitude from lowest (dark blue) to highest (dark red) values	125
4.15	Drop breakup process at $Ca = 1.2Ca_c$: (a) $\lambda = 2$; $Ca = 0.178$ (b) $\lambda = 0.1$; $Ca = 0.231$	127
4.16	Drop breakup process at $Ca = 1.5Ca_c$: (a) $\lambda = 2$; $Ca = 0.223$ (b) $\lambda = 0.1$; $Ca = 0.289$	129
4.17	Drop breakup process at $Ca = 2Ca_c = 0.385$ and $\lambda = 0.1$	130
4.18	Drop breakup process at $Ca = 2Ca_c = 0.297$ and $\lambda = 2$	131
4.19	Capillary wave breakup at $Ca = 2Ca_c$ and $\lambda = 2$ (The images show a portion of the full domain)	132
5.1	Volume-averaged root-mean-square fluid velocity u_{rms} as a function of time in one-phase systems for varying resolution of Kolmogorov scales (η_K is the Kolmogorov length scale). The simulation domain size is 500^3 . The parameters are related to the corresponding Kolmogorov scales	149
5.2	Velocity magnitude fields of fully-developed turbulent flows in the cross-sections of 500×500 [lu] for different resolution of Kolmogorov scales. (a) $\eta_K = 1$ [lu]; (b) $\eta_K = 2.5$ [lu]; (c) $\eta_K = 5$ [lu]; (d) $\eta_K = 10$ [lu]	150
5.3	Velocity fields of fully-developed single-phase turbulent flow in the cross-sections of a 1000^3 domain for different resolution of Kolmogorov length scale η_K	151

5.4	Longitudinal (a) and lateral (b) velocity correlation functions for the case with Kolmogorov length scale resolution $\eta_K = 5$ [lu] at the time instant $t = 199.2\tau_K$. Symbols refer to the value of the functions at a given distance between two points; curves represent the data fit .	152
5.5	Iso-surfaces of order parameter $\varphi = 0$ at different time instants relative to the Kolmogorov time scale τ_K for the case with $\eta_K = 1$ [lu] and viscosity ratio $\lambda = 1$. The dispersed phase volume fraction is $\phi = 0.005$. The moment of drop injection refers to $t = 0$	153
5.6	Number of drops (a) and dispersed volume V in the system relative to the initial value V_{init} (b) as functions of time for the case with Kolmogorov length scale resolution $\eta_K = 1$ [lu] and viscosity ratio $\lambda = 1$. The dispersed phase volume fraction is $\phi = 0.005$	155
5.7	Dimensionless maximum d_{max} and Sauter mean d_{32} diameters as a function of time for the case with Kolmogorov length scale resolution $\eta_K = 1$ [lu] and viscosity ratio $\lambda = 1$. The dispersed phase volume fraction is $\phi = 0.005$	155
5.8	Drop size distribution (a) and cumulative log-normal probability plot (b) for the case with the Kolmogorov length scale resolution $\eta_K = 1$ [lu], viscosity ratio $\lambda = 1$, dispersed phase volume fraction $\phi = 0.005$ at the time instant $t = 59.7\tau_K$	156
5.9	Number of drops (a) and dispersed volume V in the system relative to the initial value V_{init} (b) as functions of time for the cases with Kolmogorov length scale resolution $\eta_K = 2.5$ [lu] and viscosity ratio $\lambda = 1$ and $1/3$. The dispersed phase volume fraction is $\phi = 0.005$	157
5.10	Iso-surfaces of order parameter $\varphi = 0$ at different time instants relative to the Kolmogorov time scale τ_K for the case with $\eta_K = 2.5$ [lu]; (a)-(c) viscosity ratio is $\lambda = 1$; (d)-f) viscosity ratio is $\lambda = 0.3$. The dispersed phase volume fraction is $\phi = 0.005$. Drop injection time refers to $t = 0$	158

5.11	Dimensionless maximum d_{\max} (a) and Sauter mean d_{32} (b) diameters as functions of time for the cases with Kolmogorov length scale resolution $\eta_K = 2.5$ [lu] and viscosity ratios $\lambda = 1$ and 0.3. The dispersed phase volume fraction is $\phi = 0.005$	159
5.12	Iso-surfaces of order parameter $\varphi = 0$ at different time instants relative to the Kolmogorov time scale τ_K for the case with $\eta_K = 2.5$ [lu] and viscosity ratio $\lambda = 1$. The dispersed phase volume fraction is $\phi = 0.001$. Drop injection time refers to $t = 0$	159
5.13	Dispersed phase at $t = 14.7\tau_K$ for the case with $\eta_K = 10$ [lu] and viscosity ratio $\lambda = 1$. The dispersed phase volume fraction is $\phi = 0.005$. The moment of drop injection refers to $t = 0$	160
5.14	Number of drops (a) and dispersed volume V in the system relative to the initial value V_{init} (b) as functions of time for the cases with Kolmogorov length scale resolution $\eta_K = 2.5$ [lu] and viscosity ratio $\lambda = 1$. The dispersed phase volume fraction is $\phi = 0.05$ and 0.2	161
5.15	Iso-surfaces of order parameter $\varphi = 0$ at different time instants relative to the Kolmogorov time scale τ_K for the case with $\eta_K = 2.5$ [lu]; (a)-(c) dispersed phase volume fraction is $\phi = 0.05$; (d)-(f) dispersed phase volume fraction is $\phi = 0.2$. Viscosity ratio is $\lambda = 1$. The moment of drop injection refers to $t = 0$	162
5.16	Dimensionless maximum d_{\max} (a) and Sauter mean d_{32} (b) diameters as functions of time for the case with Kolmogorov length scale resolution $\eta_K = 2.5$ [lu] and viscosity ratio $\lambda = 1$. The dispersed phase volume fraction is $\phi = 0.05$ and 0.2	163
5.17	Simultaneous breakage and coalescence events happening in the system with $\eta_K = 2.5$ [lu] and the dispersed phase volume fraction $\phi = 0.2$. Viscosity ratio is $\lambda = 1$	163
5.18	Drop size distribution (a) and probability plots (b) at different time instants for system with $\eta_K = 2.5$ [lu]. The viscosity ratio $\lambda = 1$, the dispersed phase volume fraction $\phi = 0.2$	164

5.19	Iso-surfaces of order parameter $\varphi = 0$ at different time instants relative to the Kolmogorov time scale τ_K for the case with $\eta_K = 2.5$ [lu] in a 1000^3 simulation domain; dispersed phase volume fraction is $\phi = 0.14$. Viscosity ratio is $\lambda = 1$. The moment of drop injection refers to $t = 0$	166
5.20	Number of drops (a) and dispersed volume V in the system relative to the initial value V_{init} (b) as functions of time for the cases with Kolmogorov length scale resolution $\eta_K = 2.5$ [lu] and viscosity ratio $\lambda = 1$. The dispersed phase volume fraction is $\phi = 0.14$, the simulation domain edge $L_d = 1000$ [lu]	167
5.21	Iso-surfaces of order parameter $\varphi = 0$ at different time instants relative to the Kolmogorov time scale τ_K for the case with $\eta_K = 5$ [lu] and viscosity ratio $\lambda = 1$. The dispersed phase volume fraction is $\phi = 0.14$. Drop injection time refers to $t = 0$	167
5.22	Iso-surfaces of order parameter $\varphi = 0$ at different time instants relative to the Kolmogorov time scale τ_K for the case with $\eta_K = 5$ [lu] and viscosity ratio $\lambda = 1$. The dispersed phase volume fraction is $\phi = 0.14$. The drop temporary coalescence, followed by breakup is shown in the left bottom corner of the domain	168
5.23	Number of drops (a) and dispersed volume V in the system relative to the initial value V_{init} (b) as functions of time for the case with Kolmogorov length scale resolution $\eta_K = 5$ [lu] and viscosity ratio $\lambda = 1$. The dispersed phase volume fraction is $\phi = 0.14$	168
5.24	Dimensionless maximum d_{max} (a) and Sauter mean d_{32} (b) diameters as functions of time for the case with Kolmogorov length scale resolution $\eta_K = 5$ [lu] and viscosity ratio $\lambda = 1$. The dispersed phase volume fraction is $\phi = 0.14$	169

5.25	Kinetic energy spectrum in one- (black curves) and two-phase (red curves) systems for different resolution of Kolmogorov scales. Energy is scaled with $E_K = \varepsilon^{2/3} \eta_K^{5/3}$; wave number is scaled with $k_K = 2\pi/\eta_K$. Marker * stands for the wavenumber corresponding to the Kolmogorov length scale η_K	170
5.26	Deformed drop and velocity magnitude field (a); velocity magnitude along the black vertical line shown on the left (b). The figure demonstrates the appearance of small velocity spikes over the liquid/liquid interface	171
A-1	Drop deformation results at $Re = 1$, $Ca = 0.27$, $\lambda = 1$ and different Pe and Ch numbers. The L/a ratio (a) and the orientation angle θ (b) as a function of drop radius (Benchmark 1)	192
A-2	Drop deformation D (a) and orientation angle of a drop θ (b) for different drop radius a at $Re = 0.0625$, $Ca = 0.1$ and $\lambda = 1$; <i>I</i> first principle of mesh refinement at $Ch = 0.1136 = const$; <i>II</i> second principle of mesh refinement with $\xi = 1.14 = const$. Reference VOF computations of Li et al. (2000) are $D = 0.119$ and $(45 - \theta) = 8.48^\circ$ (Benchmark 2)	193
A-3	Elongation of a drop L related to initial drop radius a for different drop radii. $Re = 10$, $Ca = 0.15$, $\lambda = 1$. Cases denoted by \bullet , \blacksquare refer to the first principle of mesh refinement; cases denoted by \circ , \square refer to the second principle of mesh refinement (Benchmark 3)	195
A-4	Orientation angle of a drop θ for different drop radii. $Re = 10$, $Ca = 0.15$, $\lambda = 1$. Cases denoted by \bullet , \blacksquare refer to the first principle of mesh refinement; cases denoted by \circ , \square refer to the second principle of mesh refinement	196
A-5	Drop shape (φ field) and streamlines at steady-state at $Re = 10$, $Ca = 0.15$, $\lambda = 1$, $Pe = 1$ and different Ch numbers: (a)-(c) the first principle of mesh refinement; (a), (d), (e) the second principle of mesh refinement (Benchmark 3)	197

A-6	Drop shape (ϕ field) and streamlines at steady-state at $Re = 10$, $Ca = 0.15$, $\lambda = 1$, $Pe = 4$ and different Ch numbers: (a)-(c) the first principle of mesh refinement; (a), (d), (e) the second principle of mesh refinement (Benchmark 3)	198
A-7	Drop elongation L/a change in time obtained using CPU and GPU codes	200
A-8	The horizontal velocity component u obtained using CPU and GPU codes as a function of vertical coordinate y starting from the drop centre and up to the wall (a) and the difference between these two values (b)	201

Nomenclature

A	Free energy model parameter
a	Drop radius
A_f	Parameter related to a linear forcing for turbulence generation
a_F	Moving reference frame acceleration
a_V	Surface area per unit volume
B	Half-breadth of the elongated drop
B_f	Free energy model parameter
c	Lattice speed
c_s	Speed of sound
$c_{q\alpha}$	Discrete velocity set
d	Drop diameter
d_{32}	Sauter mean drop diameter
d_{\max}	Maximum stable drop diameter
$E(k)$	Turbulent kinetic energy
F_q	Forcing term in lattice space
\mathcal{F}	Free energy functional

f_q, g_q	Particle distribution functions
f_q^a, g_q^a	Anti-symmetric parts of the particle distribution functions
f_q^s, g_q^s	Symmetric parts of the particle distribution functions
$f_q^{\text{aeq}}, g_q^{\text{aeq}}$	Anti-symmetric parts of the equilibrium distribution functions
$f_q^{\text{seq}}, g_q^{\text{seq}}$	Symmetric parts of the equilibrium distribution functions
$f_q^{\text{eq}}, g_q^{\text{eq}}$	Equilibrium distribution functions
$F_{i\alpha}$	Macroscopic force
H	Domain height
k	Wavenumber
L	Half-length of the elongated drop
L_d	Domain length
L_{\perp}	Size of the drop perpendicular to the flow direction
L_{\parallel}	Size of the drop parallel to the flow direction
M	Mobility
$P_{\alpha\beta}$	Pressure tensor
$P_{\alpha\beta}^{\text{chem}}$	‘Chemical’ pressure tensor
$P_{\alpha\beta}^{\text{th}}$	‘Thermodynamic’ pressure tensor
p_{id}	Ideal gas pressure
\mathbf{r}	Position vector
T	Temperature
t	Time

Δt	Time step
u	Velocity
u^*	Characteristic velocity in turbulent flow
u_K	Kolmogorov velocity scale
u_{rms}	Root-mean-square velocity
u_w	Velocity of the wall
V	Volume
V_{init}	Initial volume of dispersed phase
\mathcal{V}	Symmetric double well potential
v_F	Velocity of moving reference frame
v_F^o	Velocity of moving reference frame at the previous time step
Δv_F	Correction for the velocity
W	Domain width
w_q	Weight coefficients
Δx	Mesh step
\hat{x}_d	Centre of mass of the drop relative to the moving reference frame

Greek Letters

$\Delta\rho$	Density difference
$\dot{\gamma}$	Shear rate
ε	Energy dissipation rate
η_K	Kolmogorov length scale

Γ	Mobility coefficient
κ	Free energy model parameters
$\lambda^{af}, \lambda^{ag}$	Anti-symmetric collision rates
$\lambda^{sf}, \lambda^{sg}$	Symmetric collision rates
λ_f, λ_o	Under-relaxation factors
$\Lambda_{af}, \Lambda_{ag}$	Anti-symmetric eigenvalue functions
$\Lambda_{sf}, \Lambda_{sg}$	Symmetric eigenvalue functions
$\Lambda_{eo}^f, \Lambda_{eo}^g$	'Magic' parameters
μ	Dynamic viscosity
$\mu(\varphi)$	Chemical potential
ν	Kinematic viscosity
ϕ	Dispersed phase volume fraction
ρ	Density
σ	Interfacial tension
τ_f, τ_g	Relaxation parameters
τ_K	Kolmogorov time scale
θ	Drop orientation angle
φ	Order parameter
φ_0	Value of order parameter in the bulk phase
ξ	Interface thickness

Subscript

α, β Cartesian directions, x , y and z

c Continuous phase

d Dispersed phase

q Number of the discrete velocity directions

Dimensionless numbers

$\lambda = \mu_d/\mu_c$ Viscosity ratio

$\lambda_\rho = \rho_d/\rho_c$ Density ratio

$Ca = a\dot{\gamma}\mu_c/\sigma$ Sheared drop capillary number

$Ca = u\mu_c/\sigma$ Capillary number based on drop terminal velocity

$Eo = g\Delta\rho d^2/\sigma$ Eötvös number

$Fr = u^2/(gd)$ Froude number

$Mo = g\Delta\rho v_c^4 \rho_c^2/\sigma^3$ Morton number

$Re = \dot{\gamma}a^2/\nu$ Sheared drop Reynolds number

$Re = ud\rho_c/\mu_c$ Reynolds number based on drop terminal velocity

$We = \rho_c u^2 d/\sigma$ Weber number

$Ch = \xi/a$ Cahn number

$D = (L - B)/(L + B)$ Taylor deformation parameter

$E = L_{\parallel}/(2L_{\perp})$ Aspect ratio

$Pe = \dot{\gamma}a\xi/(MA)$ Peclet number

Abbreviations

BGK Bhatnagar-Gross-Krook

CFD Computational fluid dynamics

DNS Direct numerical simulation

DSD Drop size distribution

LBE Lattice Boltzmann equation

MRT Multiple-relaxation-time

PBE Population balance equation

TRT Two-relaxation-time

Chapter 1

Introduction

1.1 Motivation

Numerous chemical, petroleum, food, and pharmaceutical engineering processes involve liquid-liquid dispersions. The dispersion properties, such as apparent viscosity, stability, and interfacial area available for heat and mass transfer, are determined by the size of the drops in the system. Therefore, knowledge and control of the drop size distribution (DSD) allow to obtain dispersion products with distinct functional properties, can help to optimize the performance of industrial equipment, and improve the economy and safety of unit operations. For instance, during suspension polymerization the final size distribution of the polymer beads is generally the result of the initial drop size distribution of the monomer-water dispersion (Kiparissides, 1996). Control of mean drop size and DSD is vital to emulsification applications (Paul et al., 2004). To efficiently accomplish the mass transfer process during liquid-liquid extraction, large interfacial area is needed (Treybal, 1951). In the oil recovery industry, formation damage caused by oil-based emulsions containing brine droplets can reduce well productivity (Fjelde, 2007). If a monodisperse emulsion is formed, then damage might occur even at low dispersed phase volume fractions. Therefore, it is necessary to know the conditions when primarily equal size drops form.

Significant amounts of experimental research have been performed over decades to study the different aspects of liquid-liquid dispersions that impact the drop sizes. Liquid properties, interfacial tension, dispersed phase holdup, the geometry of the

flow domain and the flow regime, all influence the resultant DSD. Usually the experiments are focused on determination of the mean drop diameters (e.g. the Sauter mean diameter) and the maximum stable drop diameter, neglecting the details of the breakup and coalescence events. However, dispersion formation is a complex process that occurs on multiple length and time scales: topological changes of the interface due to breakup and coalescence during milliseconds and long-term evolution of the entire system on the scale of industrial equipment, e.g. an extraction column. In order to better predict and control the DSD it is necessary to understand the dispersion formation on the microscopic level. For instance, capillary wave breakup produces drops of equal size. Knowledge of the conditions when this breakup mechanism occurs may improve the efficiency of monodisperse emulsion production. Interface dynamics can be captured experimentally for systems with low dispersed phase concentrations ($\leq 1\%$ of dispersed phase) where a variety of measuring techniques exist (Mavros, 2001). Nevertheless, sizing of drops even in dilute liquid-liquid dispersion is not an easy task (Maaß et al., 2011). Experimental investigation of highly concentrated turbulently flowing dispersion (usually 10% of dispersed phase and up) is even more challenging due to reduced optical accessibility and small time scales (Derksen and Van den Akker, 2007). In addition, special care should be given to the cleanliness of the experimental system (the fluids and the equipment). Even small amount of impurities can affect the interfacial tension, altering the drop coalescence and, consequently, the DSD.

In order to interpret changes of dispersed system morphology in complex flows, the experimental data is compared to fundamental analyses of drop behavior in simple and idealized flow geometry, such as extensional and simple shear. The fundamental studies provide more general insight in the dispersion formation process. Studies using idealized systems allow to isolate different phenomena, and examine them independent of other effects. For instance, investigation of single drop behavior in simple shear flow allows to define shearing conditions needed to break a drop. Study of two colliding drops provides details on coalescence conditions that can be used in phase separation processes. Even though both breakup and coalescence have been extensively studied, there are still some gaps to fill. Most of the funda-

mental studies on drop breakup and coalescence consider creeping flows. However inertial effects change drop deformation and breakup mechanism as well as coalescence conditions. Especially there is a lack of data on low viscosity dispersed phase in highly viscous continuous phase in inertial shear flows.

With the rapid development of computational facilities, numerical simulations become a valuable addition and in some cases an alternative to experimental studies. The main goal of the present research is to develop such a numerical approach that utilizes the details of fundamental investigations and has the possibility to produce data relevant to industrial applications. Numerical simulations are advantageous over experiments in several ways: in simulations one can control the external parameters (e.g. parameters that control operating conditions) in a way that is difficult or impossible to implement in a laboratory. It is possible to compute quantities that are difficult to measure in the laboratory (e.g. ‘in-line’ measurement of each drop diameter in dense dispersion). The entire liquid-liquid mixing can be visualized revealing drop breakup and coalescence as well as interactions of dispersed and continuous phases. However, it is necessary to verify and validate the numerical method, examine accuracy, study stability. Additionally, computational demands increase significantly as resolution of the flow increases, and in some cases calculations can become unaffordable.

1.2 Literature review

In chemical process equipment, dealing with liquid-liquid dispersion, such as stirred tanks, static mixers, extruders, and extraction columns, a vast amount of flow phenomena occur on different length (and time) scales: drop deformation, breakup, coalescence, suspension against gravity, dispersed phase interactions with carrying phase, phase inversion that might lead to significant increase in apparent viscosity of the dispersion and affect the performance of the device. It is computationally unfeasible to completely resolve the wide spectrum of scales, starting from the micro (interface-related) level and up to the macro level where the important integral parameters of the system can be estimated. Therefore, assumptions and simplification

should be made, and only physics that is relevant for the problem in question should be considered. A wide variety of numerical approaches to simulate multiphase flow problems with moving and deforming interfaces has been developed over the last decades. Depending on what phenomenon and what scale is being investigated, appropriate numerical methods should be chosen.

If the liquid-liquid interface itself is of interest, the problem can be considered on the atomistic scale which is the most fundamental level of phase description. Molecular dynamics (Alder and Wainwright, 1957) is the atomistic scale method that treats fluids as composed of atoms or molecules. The dynamics of these particles that obey statistical mechanics is explicitly calculated. The flow velocity and density field are calculated as averages over the trajectories of the particles. These methods are computationally demanding, and the computational effort increases linearly with the number of particles and the physical time scale simulated (Kadav et al., 2010). An example of molecular dynamics simulations of liquid-liquid interface can be found in (Rivera et al., 2003).

When it is necessary to obtain a representative characteristic of the dispersion, such as apparent viscosity, based on accurate resolution of microscopic events (interface dynamics and dispersed/continuous phases interaction), the meso-scale approach can be used. An example of a meso-scale method is the lattice Boltzmann equation (LBE). LBE allows to perform Direct Numerical Simulations (DNS) of fluid flow. For turbulent flow simulations DNS means that no turbulence modeling of small scale dynamics is employed, even the smallest (Kolmogorov) scales of turbulence are resolved. Sufficiently large simulation domains are required to capture the integral scale. In recent years, the rapidly developing LBE method has challenged the traditional methods of computational fluid dynamics (Chen and Doolen, 1998). LBE simulates fluid flow based on microscopic models and mesoscopic kinetic equations for velocity distribution functions in discrete physical and velocity space. Hypothetical (fictitious) particles move and collide on lattice sites according to the discretized Boltzmann equation. The macroscopic quantities (density, velocity, temperature, etc.) are evaluated through moment integration of the distribution function. Most of numerical operations are performed locally on each site. This

gives the important advantages of LBE which are simplicity of programming and parallelization of the algorithm allowing for very detailed simulations. A disadvantage of LBE methods is that in order to set the macroscopic quantities (for example, in boundary conditions), the underlying microscopic parameters (the distribution functions) should be adjusted. In addition, in its basic implementation, the method is constructed for uniform meshes only, thus, no local refinement near the interface can be performed.

Within the LBE framework, several models for immiscible fluid flow have been developed. The multiphase LBE model based on the lattice gas model was proposed by Gunstensen et al. (1991). Two kinds of particle distribution functions (red and blue) are utilized to mimic two phases. The algorithm attempts phase separation and maintenance of interfaces during a ‘recoloring’ step when two sets of populations are redistributed according to their color. This model was modified by Grunau et al. (1993) to allow variations of density and viscosity. Another multiphase model developed by Shan and Chen (1993) uses the concept of intermolecular potential between particles to simulate phase separation and surface tension. Swift et al. (1995, 1996) developed the LBE model that utilizes a free energy approach which relies on a second set of populations describing the fluid fraction by an order parameter. An isothermal model based on kinetic theory was proposed by He et al. (1999). A lattice-Boltzmann model for interacting amphiphilic fluids was developed by Nekovee et al. (2000). Each model has its own peculiarities (several of them are addressed below). The main advantage of LBE models for multiphase flows is that no interfaces tracking is required, changes in interface topology are handled automatically.

The next level of multi-phase flow simulations is macroscopic level which is covered by continuum methods based on macroscopic conservation laws of mass, momentum and energy. Generally a solver for Navier-Stokes equation is coupled with a model for the phase evolution description. Continuum methods are usually classified based on the way the interface is treated on sharp interface methods (the interface thickness is zero) and diffuse interface methods (the interface has finite thickness). In sharp interface methods, the physical properties, such as density and

viscosity, are discontinuous at the interface. In one group of sharp interface methods, the interface is resolved by a moving mesh (Quan et al., 2009). Local mesh adaptations, such as mesh refinement and coarsening, can be performed to achieve mesh resolution, capture the changing curvature, and improve computational efficiency (Worner, 2012). However, handling topological transitions of fluid particles such as coalescence, breakup or pinch-off requires rather complex somewhat arbitrary ‘cut-and-connect’ algorithms (Quan et al., 2009).

In the second group of sharp interface methods the momentum equation is solved on a structured grid and an interface representation and advection algorithm are used to define its evolution across the computational domain. The methods are classified as front-capturing and front-tracking. In front-capturing methods, the interface is represented implicitly using a scalar function determined on an Eulerian mesh. Among these methods are the interface reconstruction volume-of-fluid (Benson, 2002; Hirt and Nichols, 1981), level set (Osher and Sethian, 1988; Sussman et al., 1994) methods, or a combination of them (Lv et al., 2010). In front-tracking methods, the interface is explicitly represented by Lagrangian particles and its dynamics is tracked by the motion of these particles. For example, in the Marker in Cell method of Harlow and Welch (1965) a fixed number of discrete Lagrangian particles are advected by the local flow, while the front-tracking method of Unverdi and Tryggvason (1992) uses surface markers. Even though sharp interface methods can give a more precise evolution of a deforming interface, they are complex in implementation and computationally expensive since interface reconstruction and tracking is required. In addition, in front-tracking methods, the arbitrary ‘cut-and-connect’ algorithms are also used to carry out topological transitions of the interface during drop breakage and coalescence events.

In diffuse interface methods (Badalassi et al., 2003; Magaletti et al., 2013; Yue et al., 2004), the interface is a transition region of a finite thickness where physical quantities vary continuously. The numerical interface thickness in these methods is much larger than the actual physical thickness. However, the fact that the interface has a finite thickness and the physical properties are smoothed over it, gives computational advantages of these methods over sharp interface methods: there is no

need of any explicit interface treatments, as reconstruction or dynamic remeshing.

Even though the continuum methods with full resolution of the interface are widely used to investigate systems with a small number of drops (see e.g. (Cristini and Renardy, 2006; Cristini et al., 2003; Khismatullin et al., 2003; Watanabe and Ebihara, 2003; Wegener et al., 2009)), combination of these models with DNS of turbulent flow that involves direct solution of the Navier-Stokes equations are computationally very demanding especially for systems with hundreds of drops due to interface handling costs.

To obtain information on the global patterns of the flow at the scale of industrial equipment, the capturing of interfaces can be neglected. The Eulerian-Eulerian approach is commonly used for two-phase flow simulations for industrial applications. It gained popularity in implementation due to the fact that while giving the adequate flow details needed for engineering estimations, the computational power requirements are reduced by averaging the conservation equations (mass, momentum, and energy) (Al Taweel et al., 2006; Portela and Oliemans, 2006). The approach does not reveal the complex phenomena on the scale of drops; the liquid-liquid interface is not resolved. The main difficulty of this method is a closure problem: interphase forces (drag, virtual mass, lift, and turbulent dispersion forces per unit volume) need to be specified to obtain a closed set of momentum equations. Furthermore, drop size is an input parameter, not a result of simulations. Thus, two uncertainties arise in this approach: the lack of generally accepted closure relations, and the lack of generally accepted models to describe drop breakup and coalescence kernels (Al Taweel et al., 2006). The following examples of Computational Fluid Dynamics (CFD) implementation using Eulerian-Eulerian approach can be given. The investigation of two-phase turbulent flow of a dilute liquid-liquid systems (dispersion of organics in water) in a stirred tank was performed by Laurenzi et al. (2009). The authors aimed to assess the capability of a CFD approach to resolve the patterns of dispersed flow based on the solution of Reynolds averaged Navier-Stokes (RANS) equations with Eulerian-Eulerian description of the two phases. Feng et al. (2013) performed numerical simulations of turbulent immiscible liquid-liquid mixing processes in cylindrical stirred tanks based on an Eulerian-Eulerian

approach. For flow field simulations, an isotropic standard $k - \varepsilon$ turbulence model and an anisotropic two-phase explicit algebraic stress model (EASM) were utilized. The authors demonstrated that the key features of the complex liquid-liquid mixing on the macro scale in stirred tanks were successfully predicted by the EASM.

Finally, drop breakage and coalescence processes in turbulently flowing liquid-liquid dispersions can be modeled by population balance equations (PBEs). The PBE model has been widely used to predict the evolution of the particle size distribution for dispersed phase operations (Chen et al., 1998; Raikar et al., 2009, 2010; Singh et al., 2009; Venneker et al., 2002). The main challenge of the PBE models is determination and formulation of unknown drop breakage and coalescence kernels. Coualoglou and Tavlarides (1977) generalized droplet coalescence and breakage death and birth terms as functions of the basic hydrodynamics and physical properties of the system. However, as it is noted by Paul et al. (2004), the breakage and coalescence kernels are specific to the equipment used to acquire the data: it is highly scale dependent and all quantities are inclined to be flow dependent. To take these dependencies into account, the constants embedded in the population balance equations can be adjusted to specific flow conditions and equipment as demonstrated, for instance, by Amokrane et al. (2013). Therefore, the ultimate success of PBEs relies on its ability to yield realistic and accurate description of the overall drop breakage and coalescence processes (Azizi and Al Taweel, 2011). Additionally, accurate modeling of the flow field is required since the breakage and coalescence kernels depend on flow details.

In the present research project, the free energy lattice Boltzmann method is adopted to perform multi-phase simulations. The reasons of this choice and objectives of the project are presented in the next section.

1.3 Research project objectives

A major goal of the present research project is to develop a numerical approach able to perform direct numerical simulations of liquid-liquid binary systems. Theoretically, the predictive numerical approach should cover micro-, meso-, and macro-

scales of flow description. However practically, such simulations are computationally unfeasible at the present time, especially for multiphase systems. For that reason, the present numerical approach is limited to micro- and meso-scales. Among the variety of numerical methods discussed above, the lattice Boltzmann equation method is the most appropriate for this task since it allows meso-scale simulation with the resolution of underlying microscopic physics.

The developed numerical approach is applied to carry out fundamental studies of drops behavior in idealized flow geometries, such as shear flow, and the DNS of dense turbulently agitated liquid-liquid dispersion with accurate resolution of microscopic phenomena (evolution of the interface, interaction of dispersed and continuous phases). Pure liquids are considered, there are no surfactants or contaminations in the system.

A free energy lattice Boltzmann equation method (Swift et al., 1996) is used for two-phase flow modeling. The method refers to a class of diffuse interface methods. An advantageous characteristic of the method is that no interface treatments or reconstructions are required. The interface evolves naturally due to the thermodynamics mechanism employed. This issue allows to simulate binary liquid systems with hundreds of drops during a reasonable time and affordable computational efforts. However, diffuse interface methods require specification of interface-related numerical parameters. One of the objectives of the study is to outline these parameters, and present a guideline on how to specify their values. Additionally, the diffuse interface methods face the following drawbacks. First, unphysical currents (spurious velocities) appear close to curved interfaces (Pooley and Furtado, 2008). Second, the methods suffer from dissolution of small drops (Van der Sman and Van der Graaf, 2008). Third, the methods exhibit unphysical easy coalescence when drops are in close proximity (Jia et al., 2008). Every issue is taken into account and its impact on the results is critically assessed.

If the peculiarities of the method are addressed, the results of such a powerful approach as DNS would provide very detailed information about the flow since in DNS the Navier-Stokes equations are solved without any modeling on a fine mesh to resolve the smallest spatial and temporal scales present in the flow. When disper-

sion formation in turbulent flow is concerned, high resolution of the Kolmogorov microscales will result in capturing the liquid interface dynamics and drop interactions with microscopic eddies. Accurate resolution of the microscopic events, as drop breakup and coalescence, is of great importance since they are closely related to the DSD of the system. Therefore, detailed resolution of microscopic events would improve the understanding of the macroscopic system characteristics, help to reveal the complex flow patterns, and examine the influence of turbulence on two-phase system behavior. Moreover, DNS can provide useful information on breakup and coalescence kernels for PBEs and closure correlations for CFD methods.

The proposed research aims to answer major practical and fundamental questions arising during investigations of the dispersed systems: what is the DSD of the system for a given set of properties, shearing conditions, or energy input? What is a drop breakup mechanism in inertial sheared flows? How to resolve coalescence? What is the influence of turbulence on the DSD? How does the turbulent energy spectrum change when the second phase is introduced? What is the mechanism of dispersion formation at high dispersed phase volume fractions? Also it is necessary to show how a free energy LBE performs, and the ways to resolve the drawbacks of the method should be demonstrated.

1.4 Outline of the thesis

The developed numerical approach based on the free energy LBE method is applied to investigate several binary liquid systems. The four studies are the next four chapters of the thesis.

The first study (Chapter 2) is aimed to test the capabilities of the free energy LBE method to perform multiphase simulations. A single *n*-butanol drop rising in water under the influence of gravity is considered. This problem has reference experimental data and numerical results using other methods that allows validation of the LBE results, including interface dynamics, terminal drop velocity and flow patterns. To verify the developed computer code, simulation parameters such as computational domain size, mesh resolution, and LBE numerical parameters are

tested. The influence of the collision operator choice on stability and accuracy is investigated. The ability of the method to accurately resolve interface deformation is assessed. Additionally, the LBE method operates in lattice space, and all system parameters are presented in lattice units. A way to match the parameters of the physical system (in physical units) with the numerical system in lattice units is outlined. It is shown that the numerical technique can be adopted to perform multiphase simulations with moving and deforming interfaces.

Capturing of the interface disintegration is tested using numerical simulations of single liquid drops suspended in another liquid and subjected to simple shear flow. This study is presented in Chapter 3. Three-dimensional simulations of this binary systems are performed in order to determine the drop deformation and breakup conditions. It is demonstrated that the diffuse interface method requires specification of two numerical parameters: an interface-related Peclet number Pe , and the ratio of interface thickness and drop size (the Cahn number Ch). The influence of Pe , Ch and mesh resolution on accuracy and stability of the simulations is investigated. A guideline on how to choose Pe and Ch in order to reveal physically realistic behavior of the drop at given shearing conditions and physical properties of the liquids is presented. The numerical approach is verified and validated in a wide range of physical conditions: from near-creeping flow at drop Reynolds number $Re = 0.0625$ up to shearing with inertia at $Re = 50$, viscosity ratio $\lambda = 1, 2, 3$ (dispersed phase viscosity over continuous phase viscosity) and a capillary number range over which drops deform and break. Additionally, it is shown that even moderately resolved drops can be used to investigate the physics of drop deformation and breakup. This issue is important for simulation of turbulent liquid-liquid system which involves a wide range of drop sizes.

Furthermore, the effect of dispersed phase viscosity on the behavior of a sheared drop at a drop Reynolds number $Re = 10$ is investigated over the range of viscosity ratios $\lambda = 0.1 - 2$ with a focus on $\lambda < 1$ (Chapter 4). Even though dispersion of low viscosity liquid in highly viscous liquid is frequently encountered in industrial processes, there is a gap in fundamental results for such systems when they are exposed to inertial shearing conditions. It is of interest to see how the drops deform

under these conditions and what the breakup mechanism is. The guidelines outlined in Chapter 3 are used to choose the numerical parameters. A validation simulation of stratified shear flow is conducted to show that the numerical method can handle viscosity ratios $\lambda = 0.1 - 2$. It is demonstrated that high-resolution simulations capture drop breakup by end-pinching and capillary wave breakup mechanisms.

In Chapter 5, the numerical approach is applied to study liquid-liquid mixing in turbulent flow. The simulations are performed in three-dimensional, fully-periodic domain. Since simulations are carried out on the meso-scale, an assumption on turbulence characterization on the macro-scale is made: well-controlled homogeneous isotropic turbulence (away from walls) is generated by means of linear forcing (Lundgren, 2003) throughout the domain. With the adopted turbulence generation method the energy input into the system is known a priori. Therefore, it is possible to determine if the specified energy is sufficient to obtain a desired dispersion.

The dispersed phase volume fraction varies in the range $0.001 - 0.2$. The numerical parameters of the method are specified according to the guidelines and results presented in Chapters 3 and 4. The drop dissolution effect is addressed here. A way to mitigate the dissolution by increasing the resolution of Kolmogorov scales is tested. It is also shown that the increase of dispersed phase concentration slows down the dissolution. Thus, for the adopted numerical method dense systems are more preferable than dilute dispersion. The resolved Kolmogorov scales range from $\eta_K = 1$ to 10 lattice units. Two sizes of the domain edge L_d are considered 500 and 1000 lattice units. The scale separation in the turbulent flow is thus in a range $L_d/\eta_K = 50 - 400$. Between these scales there is the inertial sub-range of turbulence. The reproduction of this sub-range in turbulent energy spectrum improves as the ratio L_d/η_K increases. The viscous sub-range is always reproduced. To the author's knowledge there are no published results on two-phase flow simulations with this range of scale separation. However, this resolution is not enough to capture physical coalescence process, and drops merge if collision occurs.

Finally, Chapter 6 contains conclusions and outlook for the future work.

References

- A.M. Al Taweel, S. Madhavan, K. Podila, M. Koksai, A. Troshko, and Y.P. Gupta. CFD simulation of multiphase flow: closure recommendations for fluid-fluid systems. In *12th European Conference on Mixing*, 2006.
- B. J. Alder and T. E. Wainwright. Phase transition for a hard sphere system. *J. Chem. Phys.*, 27:1208–1209, 1957.
- A. Amokrane, S. Charton, N. Sheibat-Othman, J. Becker, J. P. Klein, and F. Puel. Development of a CFD-PBE coupled model for the simulation of the drops behaviour in a pulsed column. *Can. J. Chem. Eng.*, 9999:1–14, 2013.
- F. Azizi and A.M. Al Taweel. Turbulently flowing liquidliquid dispersions. Part I: Drop breakage and coalescence. *Chem. Eng. J.*, 166:715–725, 2011.
- V.E. Badalassi, H.D. Cenicerros, and S. Banerjee. Computation of multiphase systems with phase field models. *J. Comp. Phys.*, 190:371–397, 2003.
- D.J. Benson. Volume of fluid interface reconstruction methods for multi-material problems. *Appl. Mech. Rev.*, 55:151–165, 2002.
- S. Chen and G. D. Doolen. Lattice Boltzmann method for fluid flows. *Annu. Rev. Fluid Mech.*, 30:32964, 1998.
- Z. Chen, J. Pruss, and H.-J. Warnecke. A population balance model for disperse systems: Drop size distribution in emulsion. *Chem. Eng. Sci.*, 53:1059–1066, 1998.
- C.A. Coulaloglou and L.L. Tavlarides. Description of interaction processes in agitated liquid-liquid dispersions. *Chem. Eng. Sci.*, 32:1289–1297, 1977.

- V. Cristini and Y. Renardy. Scalings for droplet sizes in shear-driven breakup: non-microfluidic ways to monodisperse emulsions. *FDMP*, 2:77–93, 2006.
- V. Cristini, S. Guido, A. Alfani, J. Bławdziewicz, and M. Loewenberg. Drop breakup and fragment size distribution in shear flow. *J. Rheol.*, 45:1283–1298, 2003.
- J.J. Derksen and H.E.A. Van den Akker. Multi-scale simulations of stirred liquid-liquid dispersions. *ICChemE*, 85:697–702, 2007.
- X. Feng, X. Le, J. Cheng, C. Yang, and Z.-S. Mao. Numerical simulation of liquid-liquid turbulent flow in a stirred tank with an explicit algebraic stress model. *Chem. Eng. Res. Des.*, 91:2114–2121, 2013.
- I. Fjelde. Formation damages caused by emulsions during drilling with emulsified drilling fluids. *SPE*, 105858:1–8, 2007.
- D. Grunau, S. Chen, and K. Eggert. A lattice Boltzmann model for multiphase fluid flows. *Phys. Fluids A*, 5:2557–2562, 1993.
- A.K. Gunstensen, D.H. Rothman, S. Zaleski, and G. Zanetti. Lattice Boltzmann model for immiscible fluids. *Phys. Rev. A*, 43:4320–4327, 1991.
- F.H. Harlow and J.E. Welch. Numerical calculation of time-dependent viscous incompressible flow of fluid with free surface. *Phys. Fluids*, 8:1958–1988, 1965.
- X. He, S. Chen, and R. Zhang. A Lattice Boltzmann Scheme for Incompressible Multiphase Flow and Its Application in Simulation of Rayleigh-Taylor Instability. *J. Com. Phys.*, 152:642–663, 1999.
- C.W. Hirt and B.D. Nichols. Volume of fluid (VOF) method for the dynamics of free boundaries. *J. Comp. Phys.*, 39:201–225, 1981.
- X. Jia, J.B. McLaughlin, and K. Kontomaris. Lattice boltzmann simulations of flows with fluidfluid interfaces. *Asia-Pac. J. Chem. Eng.*, 3:124–143, 2008.

- K. Kadau, J. L. Barber, T.C. Germann, B.L. Holian, and B.J. Alder. Atomistic methods in fluid simulation. *Phil. Trans. R. Soc. A*, 368:1547–1560, 2010.
- D. B. Khismatullin, Y. Renardy, and V. Cristini. Inertia-induced breakup of highly viscous drops subjected to simple shear. *Phys. Fluids*, 15:1351–1354, 2003.
- C. Kiparissides. Polymerization reactor modeling: A review of recent developments and future directions. *Chem. Eng. Sci.*, 51:1637–1659, 1996.
- F. Laurenzi, M. Coroneo, G. Montante, A. Paglianti, and F. Magelli. Experimental and computational analysis of immiscible liquidliquid dispersions in stirred vessels. *Chem. Eng. Res. Des.*, 87:507–514, 2009.
- T.S. Lundgren. Linearly forced isotropic turbulence. *Annual Research Briefs*, 461–473, 2003.
- X. Lv, Q. Zou, Y. Zhao, and D. Reeve. A novel coupled level set and volume of fluid method for sharp interface capturing on 3D tetrahedral grids. *J. Comp. Phys.*, 229:2573–2604, 2010.
- S. Maaß, S. Wollny, A. Voigt, and M. Kraume. Experimental comparison of measurement techniques for drop size distributions in liquid/liquid dispersions. *Exp Fluids*, 50:259–269, 2011.
- F. Magaletti, F. Picano, M. Chinappi, L. Marino, and C.M. Casciola. The sharp-interface limit of the Cahn-Hilliard/Navier-Stokes model for binary fluids. *J. Fluid Mech.*, 714:95–126, 2013.
- P. Mavros. Flow visualization in stirred vessels. A review of experimental techniques. *Trans IChemE*, 79:113–127, 2001.
- M. Nekovee, P.V. Coveney, H. Chen, and B.M. Boghosian. Lattice-Boltzmann model for interacting amphiphilic fluids. *Phys. Rev. E*, 62:8282–8294, 2000.
- S. Osher and J.A. Sethian. Fronts propagating with curvature dependent speed: algorithms based on Hamilton-Jacobi formulations. *J. Comp. Phys.*, 79:12–49, 1988.

- E.L. Paul, V.A. Atiemo-Obeng, and S.M. Kresta, editors. *Handbook of Industrial Mixing: Science and Practice*. John Wiley & Sons, Inc., 2004.
- C.M. Pooley and K. Furtado. Eliminating spurious velocities in the free-energy lattice Boltzmann method. *Phys. Rev. E*, 77:046702–1–9, 2008.
- L.M. Portela and R.V.A. Oliemans. Possibilities and limitations of computer simulations of industrial turbulent dispersed multiphase flows. *Flow Turbulence Combust*, 77:381–403, 2006.
- S. Quan, J. Lou, and D.P. Schmidt. Modeling merging and breakup in the moving mesh interface tracking method for multiphase flow simulations. *J. Comp. Phys.*, 228:2660–2675, 2009.
- N.B. Raikar, S.R. Bhatia, M.F. Malone, and M.A. Henson. Experimental studies and population balance equation models for breakage prediction of emulsion drop size distributions. *Chem. Eng. Sci.*, 64:2433–2447, 2009.
- N.B. Raikar, S.R. Bhatia, M.F. Malone, D.J. McClements, C. Almeida-Rivera, P. Bongers, and M.A. Henson. Prediction of emulsion drop size distributions with population balance equation models of multiple drop breakage. *Colloids Surf., A: Physicochem. Eng. Aspects*, 361:96–108, 2010.
- J. L. Rivera, C. McCabe, and P.T. Cummings. Molecular simulations of liquid-liquid interfacial properties: Water-alkane and water-methanol-alkane systems. *Phys. Rev. E*, 67:011603, 2003.
- X. Shan and H. Chen. Lattice Boltzmann model for simulating flows with multiple phases and components. *Phys. Rev. E*, 47:1815–1819, 1993.
- K. K. Singh, S. M. Mahajani, K. T. Shenoy, and S. K. Ghosh. Population balance modeling of liquid-liquid dispersions in homogeneous continuous-flow stirred tank. *Ind. Eng. Chem. Res.*, 48:8121–8133, 2009.

- R.G.M. van der Sman and S. van der Graaf. Emulsion droplet deformation and breakup with Lattice Boltzmann model. *Comp. Phys. Commun.*, 178:492–504, 2008.
- M. Sussman, P. Smereka, and S. Osher. A level set approach for computing solutions to incompressible two-phase flow. *J. Comp. Phys.*, 114:146–159, 1994.
- M.R. Swift, W.R. Osborn, and J.M. Yeomans. Lattice Boltzmann simulation of nonideal fluids. *Phys. Rev. Lett.*, 75:830–834, 1995.
- M.R. Swift, E. Orlandini, W.R. Osborn, and J.M. Yeomans. Lattice Boltzmann simulations of liquid-gas and binary fluid systems. *Phys. Rev. E*, 54:5041–5052, 1996.
- R.E. Treybal. *Liquid extraction*. McGraw-Hill book company, inc., 1951.
- S.O. Unverdi and G. Tryggvason. A front-tracking method for viscous, incompressible, multi-fluid flows. *J. Comp. Phys.*, 100:25–37, 1992.
- B.C.H. Venneker, J.J. Derksen, and H.E.A. Van der Akker. Population balance modeling of aerated stirred vessels based on CFD. *AIChE Journal*, 48:673–685, 2002.
- T. Watanabe and K. Ebihara. Numerical simulation of coalescence and breakup of rising droplets. *Comput. Fluids*, 32:823–834, 2003.
- M. Wegener, T. Eppinger, K. Baumler, M. Kraume, and E. Paschedag, A.R. Bansch. Transient rise velocity and mass transfer of a single drop with interfacial instabilities – Numerical investigations. *Chem. Eng. Sci.*, 64:4835–4845, 2009.
- M. Worner. Numerical modeling of multiphase flows in microfluidics and micro process engineering: a review of methods and applications. *Microfluid Nanofluid*, 12:841–886, 2012.
- P. Yue, J.J. Feng, C. Liu, and J. Shen. A diffuse-interface method for simulating two-phase flows of complex fluids. *J. Fluid Mech.*, 515:293–317, 2004.

Chapter 2

Lattice Boltzmann simulations of a single *n*-butanol drop rising in water¹

2.1 Introduction

Liquid-liquid extraction is a method for separating the components of a solution based on mass transfer (Treybal, 1951). The dispersion of one liquid in the form of small drops in another liquid creates large interfacial surface; thus, enhancing the mass transfer between the liquids. Even though the motion of swarms of liquid drops under the influence of net gravity through continuous liquid is frequently encountered in extraction processes (Treybal, 1951), a comprehensive study of single droplet behavior is the essential starting point for analysis of the process. The obtained information can be used to develop engineering models for the full extraction process (Henschke and Pfennig, 1999). The mass transfer rate, drop terminal velocity, and related drag coefficient are the crucial parameters that need to be determined (Henschke and Pfennig, 1999; Wegener et al., 2010).

Experiments and numerical simulations have been utilized to understand the complex behavior of a buoyancy-driven drop moving through the ambient liquid. Accurate measurements require considerable effort (Bertakis et al., 2010). As discussed by Wegener et al. (2010), the comparison of experimental results might be difficult because different research groups can obtain dramatically different results while seemingly investigating the same system. The authors attribute the differ-

¹A version of this chapter has been published. A.E. Komrakova, D. Eskin, J.J. Derksen. Phys. Fluids. 25, 042102 (2013)

ences mainly to the impurities in the systems. In case of numerical studies, one can fully control the purity of the system: a mathematical description of the problem can be constructed for pure or contaminated systems. However, the capability of the numerical method to capture the correct physics of the problem must be carefully checked. Only numerical results verified with reliable experimental data can be used to analyze engineering systems. In this study numerical simulations have been applied to investigate liquid drop behaviour. A systematic comparison of the results with experiments has been performed.

Early experimental studies on the motion of single liquid drops falling/rising through a stationary liquid have been reported (Hu and Kintner, 1955; Johnson and Hamielec, 1960; Klee and Treybal, 1956; Krishna et al., 1959a,b; Thorsen et al., 1968). The influence of walls for the settling of single organic drops through an aqueous phase was examined by Strom and Kintner (1958). The effect of surfactant on the terminal velocity of drops at small Reynolds numbers was considered by Griffith (1962). Recent experiments were performed by Dehkordi et al. (2007), who studied the sedimentation of *n*-butanol droplets under mass transfer conditions with and without surfactants. Transient velocity measurements of toluene droplets rising in water were carried out by Wegener et al. (2010).

Bertakis et al. (2010) investigated the *n*-butanol/water system via experiments and numerical simulations. A three-dimensional finite element technique was used. The interface was captured with the level-set approach. The drop diameters covered the range relevant to extraction processes. The authors showed spherical, deformed, and oscillating drops. Five drops with diameters spanning all mentioned flow regimes were simulated. Both experimental and numerical results were in excellent agreement with each other and with semi-empirical correlations.

Bäumler et al. (2011) performed experiments and numerical simulations of three binary systems: toluene/water, *n*-butyl acetate/water and *n*-butanol/water. A numerical approach based on the finite element method was applied. A sharp interface representation and a mesh moving method were adopted. The simulated drop terminal velocities agreed well with their experimental findings and those reported by Bertakis et al. (2010) and Wegener et al. (2010): the mean deviation was below 5%.

A drawback of the applied moving-mesh method was its difficulty to capture the strong drop deformations in the oscillatory regime and the inability to handle drop breakup and coalescence.

Petera and Weatherley (2001) presented a two-dimensional axisymmetric method to determine the mass transfer from a deformable droplet moving in a continuous phase. A modified Lagrange-Galerkin finite element method with automatic remeshing to track the droplet shape was used. The calculated values of drop velocity and mass transfer rate were compared with experimental data determined for single drops of ethanol/water mixtures extracting into a continuous phase of *n*-decanol. It was shown that the method was capable of predicting the terminal velocity and the deformed droplet shape.

Watanabe and Ebihara (2003) performed numerical simulations of a rising droplet using the two-component two-phase lattice Boltzmann method. The authors outlined for the single droplet that the rise velocities were in good agreement with the empirical correlation proposed by Grace et al. (1976) which is valid for contaminated systems only, while the applied numerical technique was not constructed to take contaminations into account.

The commercial CFD software STAR-CD was used by Wegener et al. (2009) to simulate the mass transfer across the interface of moving drops with simultaneous Marangoni convection in a fully three-dimensional problem statement. Simulations of pure toluene/water systems were performed. The terminal drop rise velocity was in good agreement with experimental data only up to 3.0 mm droplets. The applied numerical method was not able to capture deformations of larger drops.

Ohta et al. (2010) presented a sensitivity study of the density and viscosity ratio on a drop moving through viscous fluid. A two-dimensional axisymmetric formulation of the coupled level-set/volume-of-fluid method with sharp interface treatment was implemented. The authors demonstrated good correlation of results using their method with several experimental cases; however, as was noted by the authors, the axisymmetric assumption might not be applicable for all physical conditions considered in the work. The essence of complex drop motion was captured, but fully three-dimensional simulations could reveal additional unstable drop behavior not

observed in their work especially for oscillatory regimes.

Thus, a broad range of numerical methods has been applied to simulate single drop motion under gravity. Nevertheless, to our knowledge there are no published results where the adopted numerical approach could simulate a wide range of drop diameters handling the regions of spherical, deformed, and oscillating drops with significant topological deformations, along with the ability to model mass transfer, surfactant influence, or swarms of droplets. One of the main issues in numerical simulations of multiphase flow that might limit the method to specific problems is the description of the interface between the fluids. The interface approximation methods can be divided in two groups: interface ‘capturing’ and ‘tracking’ methods. The level-set (Osher and Sethian, 1988; Sussman et al., 1994), volume of fluid (VOF) (Hirt and Nichols, 1981; Renardy et al., 2002), phase-field (Badalassi et al., 2003; Jacqmin, 1999) and lattice Boltzmann equation (LBE) (Gunstensen et al., 1991; He et al., 1999; Shan and Chen, 1993; Spencer et al., 2011; Swift et al., 1996) models are examples of interface capturing methods. In these methods the interface is implicitly captured by volume functions that use the data from the same fixed grid on which the flow is calculated. The front tracking models (Tome and McKee, 1994; Tryggvason et al., 2001; Unverdi and Tryggvason, 1992) track the interface explicitly using a Lagrangian mesh, while the flow field is solved on a fixed Eulerian grid. Interface capturing methods are easier to implement: only one mesh is needed for the calculations. In contrast, the interface tracking models require an additional interface mesh that needs to be dynamically remeshed and mapped onto the Eulerian mesh. The drawback of the interface capturing models is that they exhibit unphysical coalescence when drops are in close proximity if no additional preventing treatments are performed, while front tracking models need a sub-grid model to allow droplets to merge or break (Dijkhuizen et al., 2010).

With special handling, as high mesh resolution, higher order schemes for discretization, and suppressed artificial coalescence most methods can give accurate results, but only for a small number of droplets in the system. When the number of droplets is increased, multiple drop interactions as coalescence and breakup should be taken into account. This requires significant computational efforts for the inter-

face reconstruction in interface capturing methods or a proper sub-grid model in interface tracking methods.

In contrast to all multiphase methods discussed above, a diffuse interface method does not require any explicit interface treatments, as reconstruction or dynamic remeshing. The interface evolves naturally based on the thermodynamics of the model. It is assumed that the interface between two immiscible fluids has a small but finite width. Exactly this issue gives the advantage of the diffuse interface methods over the sharp interface methods because calculations are much easier for three-dimensional flows in which significant topological changes of the interface take place (Pooley and Furtado, 2008). However, the results obtained using the diffuse interface method might not be as accurate as they could be with a sharp interface description. In the diffuse interface methods the width of the interface is deliberately enlarged to allow easier computations while in real physical systems the interface is extremely thin. Thus, to properly and accurately model relevant physical phenomena, the interface thickness must be taken as small as possible which is not always an easy task in terms of numerical stability. On the positive side, diffuse interface methods provide the possibility to run simulations of large-scale three-dimensional systems with multiple interacting droplets.

In this study the motion of an organic *n*-butanol drop in water under the influence of gravity is simulated using a diffuse interface free energy LBE technique originally proposed by Swift et al. (1996) (see (Chen and Doolen, 1998) for a general LBE description). This method is not widely used for complex flow modeling yet; thus, one of the major goals of the present work is to investigate its capabilities of liquid-liquid flow simulations. The LBE models operate in so-called lattice space, where all physical parameters are expressed in lattice units. It is shown in the current paper that all essential physical parameters of the investigated system can be matched with the corresponding parameters in the lattice space. The numerical results obtained in this study are compared in great detail to the experimental and numerical results reported by Bertakis et al. (2010) and Bäumlner et al. (2011). A wide range of drop diameters is considered to show the ability of the method to capture the drop shape deformation especially in the oscillating regime. Thus, the

application of a trustworthy simulation approach, able to reveal the required flow details with reasonable computational cost is the aim of the present study.

The rest of the paper is organized as follows: the next section outlines the exact problem statement. The governing equations, the numerical method to solve these equations, the moving frame implementation and the scaling procedure are shown in Section 2.3. Section 2.4 contains the verification of the applied numerical method. The main results and comparison with experimental data are presented in Section 2.5. Finally, the main findings of this work are summarized in Section 2.6.

2.2 Problem statement

Numerical simulation of a single *n*-butanol drop moving through water under the influence of gravity is the focus of the present study. The computational setup mimics the experimental conditions described by Bertakis et al. (2010). A sedimentation apparatus was used in the experiments: the droplets were generated through a nozzle into a cylindrical cell that contained the continuous phase. The dimensions of the cell (height 500 mm and diameter 40 mm) were significantly larger compared to the drop diameters (4.0 mm and less) to minimize wall confinement effects. After generation, the droplets were given about 12 cm of acceleration distance to reach terminal velocity. Drops positions were monitored using a camera recording 30 frames per second. The droplet travel time for the given distance was calculated as the number of frames recorded from the time the drop enters the measuring region to the time of exit. The drop terminal rise velocity was calculated from these data. As outlined by Bertakis et al. (2010), the organic and aqueous phases were mutually saturated to avoid mass transfer. A precise cleaning procedure of experimental equipment was accomplished; deionized and distilled water and only chemicals of high purity were used. The computational approach applied in the present numerical study is constructed for binary liquid systems only; there are no surfactants or contaminations. The purity of the experimental system allows comparison of experimental results to those obtained using our proposed numerical procedure. The mass transfer between the two liquids was avoided in the experiments; thus, it is

not modeled in the present investigation. The physical parameters of the system are shown in Table 2.1.

The motion of drops in ambient liquid has two effects that distinguish it from solid particle motion: the mobility of the interface and the ability of a drop to change its shape. When the drop is driven by gravity the following parameters define the physics of the flow:

$$u = f(d, \rho_c, \rho_d, \mu_c, \mu_d, \sigma, g) \quad (2.1)$$

here the subscripts d and c stand for the dispersed and continuous phase, respectively; $d = (6V/\pi)^{1/3}$ is the volume-equivalent diameter of the drop, V is the drop volume; ρ_c and ρ_d are the densities and $\Delta\rho = \rho_c - \rho_d$ is the density difference; μ_c and μ_d are the dynamic viscosities; σ is the surface tension; g is the gravitational acceleration.

The system of these parameters gives five independent dimensionless numbers that fully determine the problem: the Reynolds number $Re = ud\rho_c/\mu_c$ (where u is the drop terminal velocity); the Weber number $We = \rho_c u^2 d/\sigma$; the Froude number $Fr = u^2/(gd)$; the density ratio $\lambda_\rho = \rho_d/\rho_c$ and the dynamic viscosity ratio $\lambda = \mu_d/\mu_c$.

Clift et al. (1978) organized the shapes and terminal velocities of the drops and bubbles based on the Reynolds, Eötvös (Eo) and Morton (Mo) numbers. The two latter ones are defined as:

$$Eo = \frac{g\Delta\rho d^2}{\sigma} = \frac{We|1 - \lambda_\rho|}{Fr} \quad (2.2)$$

$$Mo = \frac{g\Delta\rho v_c^4 \rho_c^2}{\sigma^3} = \frac{We^2 Eo}{Re^4} \quad (2.3)$$

The Eötvös number is the ratio of the buoyancy over interfacial tension. The Morton number characterizes the physical properties of the liquids and is constant for the

Table 2.1: Physical parameters of the *n*-butanol/water binary system (Bertakis et al., 2010)

Liquids	Density, [kg/m ³]	Dynamic viscosity, [mPa·s]	Surface tension, [mN/m]
<i>n</i> -butanol	$\rho_d=845.1$	$\mu_d=3.28$	$\sigma=1.63$
Water	$\rho_c=986.5$	$\mu_c=1.39$	

given binary system. The effect of three dimensionless numbers $Re - Eo - Mo$ on the shape of a drop/bubble moving through the liquid due to gravity is represented by a plot of Reynolds number against Eötvös number for different Morton numbers. This diagram of Clift et al. (1978) is considered a standard reference for predicting the shape and velocity of fluid particles.

2.3 Numerical method

2.3.1 Governing equations

In diffuse interface (or phase field) models (Ding et al., 2007; Jacqmin, 1999; Yue et al., 2004) the sharp interface between the fluids is represented by a thin transition region with finite thickness where fluids may mix. The main idea of the phase field model is that the state of the system at any given time can be described by the order parameter of the phase field φ which is a function of the position vector \mathbf{r} and time t (Penrose and Fife, 1990). Being mostly uniform in the bulk phases, the φ parameter varies continuously over the thin interfacial regions (Badalassi et al., 2003). If the phase field is used to describe the binary mixture behavior, the order parameter has a physical meaning: for an isothermal binary fluid (as in this study) φ is the relative concentration of the two components (Badalassi et al., 2003; Cahn and Hilliard, 1958). To simulate the fluid dynamics of the binary mixture of two fluids, the continuity and momentum equations are used in conjunction with Cahn Hilliard convection-diffusion equation for the order parameter (Bray, 1994).

To describe quantitatively the binary system even when it is not in equilibrium state, a Helmholtz free energy written as a functional of φ can be used (Penrose and Fife, 1990). The following form of the free energy functional is adopted in the present numerical model (Bray, 1994) (the Einstein summation convention has been used):

$$\mathcal{F}(\varphi) = \int \left[\mathcal{V}(\varphi) + \frac{\kappa}{2} (\partial_\alpha \varphi)^2 \right] d\mathbf{r} \quad (2.4)$$

Here, $\mathcal{V}(\varphi)$ is the bulk energy density which has a double-well structure with two minima corresponding to the two stable phases of the fluid. The term $\frac{\kappa}{2} (\partial_\alpha \varphi)^2$ accounts for the surface energy, with κ a positive constant.

The variation in \mathcal{F} for a small local variation in composition is described by the chemical potential μ :

$$\mu(\varphi) \equiv \frac{\delta \mathcal{F}(\varphi)}{\delta \varphi} = \frac{d\mathcal{V}}{d\varphi} - \kappa \partial_{\alpha\alpha}^2 \varphi \quad (2.5)$$

For a system with fixed volume and temperature, the equilibrium state refers to the minima of the functional $\mathcal{F}(\varphi)$ with respect to variations of the φ function (Jacqmin, 1999), i.e. $\mu(\varphi) = 0$. The evolution equation of φ is a non-linear convection-diffusion equation of the following form (Bray, 1994):

$$\partial_t \varphi + \partial_\alpha (\varphi u_\alpha) = M \partial_{\beta\beta}^2 \mu \quad (2.6)$$

where u_α is the velocity field and M is an order parameter mobility that controls the strength of the diffusion. The order parameter diffuses due to the composition gradients and is advected by the fluid flow (Kendon et al., 2001).

To simulate the two-phase flow, equation (2.6) has to be coupled with the Navier-Stokes equation. The non-uniformity of the composition causes a thermodynamic force density $-\varphi \partial_\alpha \mu$ that acts at each point in the fluid (Kendon et al., 2001) (the chemical potential gradient pulls the two species in opposite directions). If $\varphi = 0$ the net force vanishes. As an alternative way this thermodynamic force density can be introduced as the divergence of a ‘chemical’ pressure tensor:

$$\varphi \partial_\alpha \mu = \partial_\alpha P_{\alpha\beta}^{chem} \quad (2.7)$$

where the ‘chemical’ pressure tensor (Kendon et al., 2001) is given by

$$P_{\alpha\beta}^{chem} = \delta_{\alpha\beta} \left[\varphi \frac{\delta \mathcal{V}}{\delta \varphi} - \mathcal{V} - \kappa \left\{ \varphi \partial_{\gamma\gamma}^2 \varphi + \frac{1}{2} |\partial_\alpha \varphi|^2 \right\} \right] + \kappa (\partial_\alpha \varphi) (\partial_\beta \varphi) \quad (2.8)$$

Thus, the order parameter influence can be incorporated into the Navier-Stokes equation in two ways: either by introduction of the term $-\partial_\alpha P_{\alpha\beta}^{chem}$ or by a body force density $-\varphi \partial_\alpha \mu$. In the present study, the order parameter was taken into account using the first approach.

Complex morphological and topological flow transitions such as coalescence and interface breakup are captured naturally in the free energy based multiphase models. Moreover, different phenomena can be accounted for in the model by

a suitable modification of the free energy functional. The main drawback is that to properly model relevant physics, the interface layers have to be thin (Badalassi et al., 2003). This issue causes large gradients of the phase field in the interface region which must be resolved computationally.

Finally, the mathematical description of the binary mixture at constant temperature can be formulated. The evolution of density, velocity and concentration fields is governed by the continuity, momentum and convection-diffusion equations (De Groot and Mazur, 1984; Kendon et al., 2001; Swift et al., 1996), respectively:

$$\partial_t \rho + \partial_\alpha (\rho u_\alpha) = 0 \quad (2.9a)$$

$$\partial_t (\rho u_\alpha) + \partial_\beta (\rho u_\alpha u_\beta) = -\partial_\beta P_{\alpha\beta}^{th} + \partial_\beta \nu (\rho \partial_\alpha u_\beta + \rho \partial_\beta u_\alpha) + g_\alpha \Delta \rho - \rho a_{F\alpha} \quad (2.9b)$$

$$\partial_t \varphi + \partial_\alpha (\varphi u_\alpha) = M \partial_{\beta\beta}^2 \mu \quad (2.9c)$$

where ρ is the density of the mixture; and ν is the shear viscosity. Here $P_{\alpha\beta}^{th}$ is the ‘thermodynamic’ pressure tensor. It contains two parts (Kendon et al., 2001): an isotropic contribution $P \delta_{\alpha\beta}$ that represents the ideal gas pressure and the ‘chemical’ pressure tensor $P_{\alpha\beta}^{chem}$ defined by (2.8). The isotropic contribution to the pressure tensor as well as the explicit form of \mathcal{V} are discussed in Section 2.3.2.

This model can be used only for density-matched fluids. Since the relative density difference of the considered liquids is 14%, the Boussinesq approximation has been adopted for determining the net gravity forces. The buoyancy force on the dispersed drop is taken into account by introduction of the net force acting on the drop: the term $g_\alpha \Delta \rho$ in momentum equation (2.9b).

With the intent to limit the computational resources while studying the long-term evolution of the drops, the moving frame technique has been adopted (see Section 2.3.4 for details). In addition, all drops considered in the present simulations rise vertically; therefore, due to the symmetry of the flow, only a quarter of the drop is considered. The simulation domain is depicted in Fig. 2.1. Initially a spherical droplet is placed in the center of the domain. For an external observer, the drop is at rest while the non-inertial coordinate system is accelerated opposite to the inlet flow. The acceleration of the reference frame $a_{F\alpha}$ has been accounted

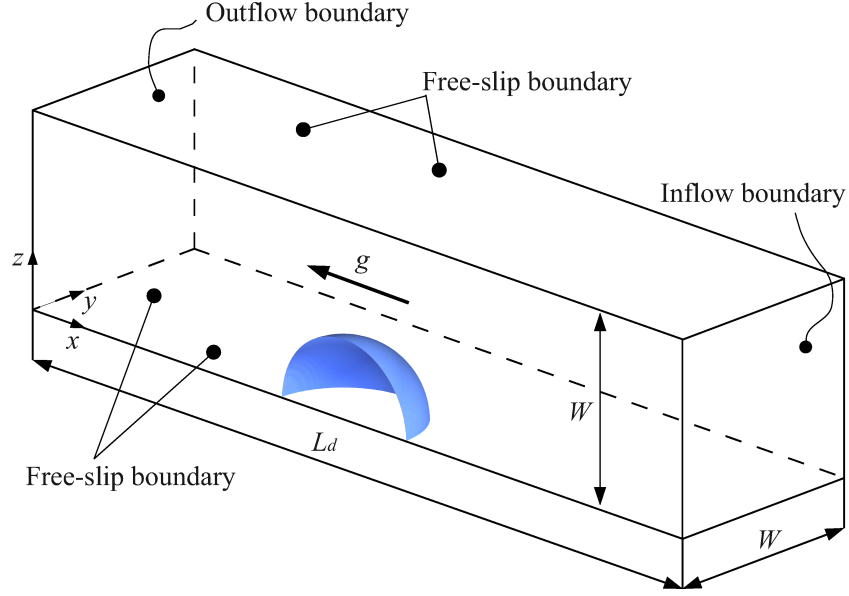


Figure 2.1: Simulation domain with boundary conditions: $x = 0$ is the outflow boundary; $x = L_d$ is the inflow boundary; all the rest side boundaries are the free-slip walls. The drop is kept in the middle of the simulation domain and has a spherical shape at $t = 0$

for in the momentum equation (2.9b) by the term $\rho a_{F\alpha}$.

2.3.2 LBE method implementation

The system of equations (2.9) that governs the binary system behavior can be solved using different numerical techniques. Swift et al. (1996) developed a lattice Boltzmann approach, known as free energy model, to solve the system. This method is adopted in the present study. Two particle distribution functions are utilized: one function $f(\mathbf{r}, t)$ is used to solve the continuity (2.9a) and the Navier-Stokes (2.9b) equations and the second one $g(\mathbf{r}, t)$ is used for the convection-diffusion equation (2.9c). The distribution functions evolve with discrete time steps Δt . Analysis of preliminary results showed that with the set of numerical parameters representing the given physical system, a two-relaxation-time (TRT) collision operator (Ginzburg et al., 2008) should be used to increase accuracy and improve stability.

The fully discretized lattice Boltzmann equations have the following form:

$$\begin{aligned}
f_q(r_\alpha + c_{\alpha q}\Delta t, t + \Delta t) &= f_q(r_\alpha, t) + \lambda^{\text{sf}} \left(f_q^{\text{s}}(r_\alpha, t) - f_q^{\text{seq}}(r_\alpha, t) \right) \\
&\quad + \lambda^{\text{af}} \left(f_q^{\text{a}}(r_\alpha, t) - f_q^{\text{aeq}}(r_\alpha, t) \right) + F_q \\
g_q(r_\alpha + c_{\alpha q}\Delta t, t + \Delta t) &= g_q(r_\alpha, t) + \lambda^{\text{sg}} \left(g_q^{\text{s}}(r_\alpha, t) - g_q^{\text{seq}}(r_\alpha, t) \right) \\
&\quad + \lambda^{\text{ag}} \left(g_q^{\text{a}}(r_\alpha, t) - g_q^{\text{aeq}}(r_\alpha, t) \right)
\end{aligned} \tag{2.10}$$

where the index q stands for the number of the velocity direction (each velocity vector has an opposite one); bold symbols stand for vectors; $c_{\alpha q}$ denotes the discrete velocity set, with the magnitude defined as $c = \Delta x / \Delta t$ (Δx is the mesh step); $f_q(r_\alpha + c_{\alpha q}\Delta t, t + \Delta t)$ and $g_q(r_\alpha + c_{\alpha q}\Delta t, t + \Delta t)$ represent the post-collision particle distribution function at (r_α, t) streamed to the neighboring nodes located at $(r_\alpha + c_{\alpha q}\Delta t)$ and at time $t + \Delta t$ along direction q ; $f_q(r_\alpha, t)$ and $g_q(r_\alpha, t)$ are the pre-collision particle distribution function; f_q^{s} , g_q^{s} and f_q^{seq} , g_q^{seq} are the symmetric parts of the particle distribution function and equilibrium distribution function, respectively; f_q^{a} , g_q^{a} and f_q^{aeq} , g_q^{aeq} are the anti-symmetric parts of the particle distribution function and equilibrium distribution function, respectively; λ^{sf} , λ^{sg} and λ^{af} , λ^{ag} are the symmetric and anti-symmetric collision rates for f and g populations, respectively; F_q is the forcing term.

In the TRT collision operator, particle distribution functions are relaxed to the equilibrium state by relaxing their symmetric and anti-symmetric parts separately, which are given by

$$\begin{aligned}
f_q^{\text{s}} &= \frac{f_q + \overline{f}_q}{2} & f_q^{\text{a}} &= \frac{f_q - \overline{f}_q}{2} \\
f_q^{\text{seq}} &= \frac{f_q^{\text{eq}} + \overline{f}_q^{\text{eq}}}{2} & f_q^{\text{aeq}} &= \frac{f_q^{\text{eq}} - \overline{f}_q^{\text{eq}}}{2}
\end{aligned} \tag{2.11}$$

where f_q^{eq} is Maxwellian-Boltzmann distributions (or equilibrium distributions); \overline{f}_q and $\overline{f}_q^{\text{eq}}$ are the particle distribution functions and equilibrium distribution function in the direction opposite of q . The same set of equations can be written for the particle distribution function g .

The D3Q19 lattice (see Appendix A – 1) is adopted here. In this lattice arrangement, each site communicates with six nearest and twelve diagonal neighbors. Only

a uniform cubic lattice can be used; the mesh step Δx is taken as unity, as is the time step Δt .

The particle distribution functions are defined such that the following summations over all directions q , at a single lattice point give the local density of the fluid, local fluid momentum and local order parameter, respectively:

$$\sum_q f_q = \rho \quad \sum_q c_{\alpha q} f_q = \rho u_\alpha + \frac{\Delta t}{2} F_{t\alpha} \quad \sum_q g_q = \varphi \quad (2.12)$$

The forcing term is incorporated as follows:

$$F_q = w_q (c_{\alpha q} F_{t\alpha}) \quad (2.13)$$

where $F_{t\alpha}$ is the macroscopic force and w_q are the weight coefficients presented in Appendix A – 1.

The full pressure tensor $P_{\alpha\beta}$ is given by

$$P_{\alpha\beta} = \sum_q f_q c_{q\alpha} c_{q\beta} \quad (2.14)$$

The equilibrium distributions can be derived from conditions (2.12) along with the condition that the order parameter is advected by the fluid

$$\sum_q g_q^{\text{eq}} c_{q\alpha} = \varphi u_\alpha, \quad (2.15)$$

and that the pressure tensor and chemical potential at equilibrium obey

$$\begin{aligned} \sum_q f_q^{\text{eq}} c_{q\alpha} c_{q\beta} &= P_{\alpha\beta}^{\text{th}} + \rho u_\alpha u_\beta, \\ \sum_q g_q^{\text{eq}} c_{q\alpha} c_{q\beta} &= \Gamma \mu \delta_{\alpha\beta} + \varphi u_\alpha u_\beta \end{aligned} \quad (2.16)$$

The equilibrium distributions (Kusumaatmaja, 2008) are presented in Appendix A – 1.

The two liquids have different kinematic viscosities. To take this into account, the kinematic viscosity of the mixture ν is set to be a linear function of the order parameter φ :

$$\nu(\varphi) = \nu_c \frac{1 - \varphi}{2} + \nu_d \frac{1 + \varphi}{2} \quad (2.17)$$

where ν_c and ν_d are the kinematic viscosities of continuous and dispersed phases, respectively.

Then the relaxation parameter for f is defined using the kinematic viscosity of the mixture:

$$\tau_f = \frac{\nu}{c_s^2 \Delta t} + \frac{1}{2} \quad (2.18)$$

$c_s^2 = 1/3$ is the speed of sound in lattice space.

The mobility M , the coefficient of mobility Γ and the relaxation parameter τ_g are connected by the following relation (Swift et al., 1996):

$$M = \Delta t \Gamma \left(\tau_g - \frac{1}{2} \right) \quad (2.19)$$

The symmetric collision rate for the f distribution function λ^{sf} is fixed by the kinematic viscosity of the fluid using the relation $\lambda^{\text{sf}} = -1/\tau_f$. The symmetric eigenvalue function is calculated as follows:

$$\Lambda^{\text{sf}} = - \left(\frac{1}{2} + \frac{1}{\lambda^{\text{sf}}} \right) \quad (2.20)$$

The symmetric and anti-symmetric functions (Ginzburg et al., 2008) are related by the ‘magic’ parameter Λ_{eo}^f :

$$\Lambda_{eo}^f = \Lambda^{\text{sf}} \Lambda^{\text{af}} \quad (2.21)$$

If the ‘magic’ parameter is fixed then the anti-symmetric eigenvalue function can be calculated as $\Lambda^{\text{af}} = \Lambda_{eo}^f / \Lambda^{\text{sf}}$. The anti-symmetric collision rate is then defined as:

$$\lambda^{\text{af}} = - \frac{1}{\Lambda^{\text{af}} + \frac{1}{2}} \quad (2.22)$$

The parameters for the g distribution function are determined in a similar way. The symmetric collision rate λ^{sg} is defined using the relaxation time τ_g as follows $\lambda^{\text{sg}} = -1/\tau_g$. All steps for determining λ^{sg} remain the same provided the ‘magic’ parameter for the g distribution function Λ_{eo}^g is given.

In this study, the following form of the free energy functional is used (Kendon et al., 2001; Lee, 2002):

$$\mathcal{F}[\varphi, \rho] = \int \left[c_s^2 \rho \ln \rho + \mathcal{V} + \frac{\kappa}{2} (\partial_\alpha \varphi)^2 \right] d\mathbf{r} \quad (2.23)$$

The ideal gas pressure $p_{id} = \rho T$ is incorporated via the first term in expression (2.23), and it does not affect the phase behavior. A symmetrical double well potential is utilized to describe the phase separation:

$$\mathcal{V} = \frac{A}{2}\varphi^2 + \frac{B_f}{4}\varphi^4 \quad (2.24)$$

where $A < 0$ and B_f determine the properties of the bulk phases.

The chemical potential thus reads

$$\mu(\varphi) = A\varphi + B_f\varphi^3 - \kappa\partial_{\alpha\alpha}^2\varphi \quad (2.25)$$

The analytical solution for the planar interface (Van der Sman and Van der Graaf, 2008) is:

$$\varphi(x) = \varphi_0 \tanh(x/\xi). \quad (2.26)$$

Here, $\varphi = \pm\varphi_0$ is the value of order parameter in the bulk phase at either side of the interface, and follows from equation (2.25)

$$\varphi_0 = \left(-\frac{A}{B_f}\right)^{1/2}. \quad (2.27)$$

It is assumed that $A = -B_f$ which means $\varphi_0 = 1$.

The thickness of the diffuse interface ξ is equal to

$$\xi = \left(-\frac{2\kappa}{A}\right)^{1/2}. \quad (2.28)$$

The surface tension σ follows from:

$$\sigma = \frac{4}{3}\kappa\frac{\varphi_0^2}{\xi}. \quad (2.29)$$

An important addition to (2.23) is the term dependent on density ρ , here chosen as an ‘ideal gas’ type contribution. This gives a diagonal term in the thermodynamic pressure tensor, which becomes:

$$P_{\alpha\beta}^{th} = \left[c_s^2\rho + \frac{A}{2}\varphi^2 + \frac{3B_f}{4}\varphi^4 - \kappa\varphi\partial_{\alpha\alpha}^2\varphi - \frac{1}{2}|\partial_{\alpha}\varphi|^2 \right] \delta_{\alpha\beta} + \kappa(\partial_{\alpha}\varphi)(\partial_{\beta}\varphi) \quad (2.30)$$

so that the thermodynamic stress obeys $P_{\alpha\beta}^{th} = c_s^2\rho\delta_{\alpha\beta} + P_{\alpha\beta}^{chem}$.

To determine the pressure tensor, the spatial gradients of φ have to be calculated. The stencils for gradients and Laplacian calculations adopted in this study are given in Appendix A – 1.

The discretized equations (2.10) are solved in two steps:

$$\begin{aligned} \text{Collision step: } f'_q(r_\alpha, t) &= f_q(r_\alpha, t) + \lambda^{\text{sf}}(f_q^s - f_q^{\text{seq}}) + \lambda^{\text{af}}(f_q^s - f_q^{\text{aeq}}) + F_q \\ g'_q(r_\alpha, t) &= g_q(r_\alpha, t) + \lambda^{\text{sg}}(g_q^s - g_q^{\text{seq}}) + \lambda^{\text{ag}}(g_q^s - g_q^{\text{aeq}}) \end{aligned} \quad (2.31)$$

$$\begin{aligned} \text{Streaming step: } f_q(r_\alpha + c_{\alpha q}\Delta t, t + \Delta t) &= f'_q(r_\alpha, t) \\ g_q(r_\alpha + c_{\alpha q}\Delta t, t + \Delta t) &= g'_q(r_\alpha, t) \end{aligned} \quad (2.32)$$

To complete the mathematical problem statement, boundary conditions have to be specified. Since the LBE method deals with particle distribution functions instead of general hydrodynamic variables, one should apply boundary conditions for the distribution functions such that boundary conditions for the hydrodynamic variables are met.

The solution of the problem in the moving reference frame requires inflow and outflow boundary conditions. At the inlet $x = L_d$ (Fig. 2.1), a uniform velocity is imposed. At the outlet $x = 0$, a constant pressure boundary condition corresponding to $\rho = 1$ is used. These boundary conditions for velocity u_α and pressure p can be set using the procedures proposed by Mussa et al. (2009). For the second distribution function g the periodic boundary condition is imposed on the inflow/outflow faces. On all side walls the free-slip condition for both distribution functions is applied. This type of boundary treatment can be handled by specular reflection of f and g (Ahmed and Hecht, 2009).

2.3.3 Scaling procedure

The lattice Boltzmann method operates in so-called lattice space, and all system parameters are presented in lattice units [lu]. Thus, it is very important to correctly match the parameters of the physical system (in physical units) with the numerical system in lattice units. The physical system translation into lattice space is performed using scaling factors. The scaling factor is the ratio of any parameter value in physical units to the corresponding parameter in lattice units. To obtain the

values of these scaling factors it is necessary to equate the essential dimensionless parameters defined in physical and lattice space. Further in this section, the symbols with a tilde stand for parameters in lattice units.

By definition, the scaling factor for surface tension reads $C_\sigma = \sigma/\tilde{\sigma}$. Two numerical parameters related to the free energy model and particularly to surface tension, κ and A , have to be determined. The expression for κ is derived from equation (2.29) and reads:

$$\kappa = \frac{3\xi}{4\varphi_0^2} \frac{\sigma}{C_\sigma} \quad (2.33)$$

In this study the interface width ξ was fixed to 1.14 [lu] for all cases (based on the results reported by Kendon et al. (2001)). Once κ is determined the value of A is calculated using equation (2.28).

For the adopted LBE model, the value of the density in the incompressible limit should be equal to unity. Thus, the continuous phase density in lattice space is set to $\tilde{\rho}_c = 1$. The dispersed phase density is defined by the density ratio $\tilde{\rho}_d = \lambda\rho\tilde{\rho}_c$.

The Boussinesq approximation states that if the density difference is small compared to the actual density of the liquids, density variations are only important in the forcing term $\Delta\rho g$ for the present problem. The proper scaling of forcing should be performed. Using the definition of the Eötvös number the forcing term reads:

$$\widetilde{\Delta\rho g} = \frac{\tilde{\sigma}}{\tilde{d}^2} \text{Eo} \quad (2.34)$$

where \tilde{d} is the drop diameter in lattice units.

Utilizing the definition of the Morton number and given the viscosity ratio λ , the dynamic viscosities of continuous $\tilde{\mu}_c$ and dispersed $\tilde{\mu}_d$ phases are calculated:

$$\tilde{\mu}_c = \left(\tilde{\rho}_c^2 \tilde{\sigma}^2 \tilde{d}^2 \frac{\text{Mo}}{\text{Eo}} \right)^{1/4} \quad \tilde{\mu}_d = \lambda \tilde{\mu}_c \quad (2.35)$$

The kinematic viscosities of the phases are $\tilde{\nu}_c = \tilde{\mu}_c/\tilde{\rho}_c$, $\tilde{\nu}_d = \tilde{\mu}_d/\tilde{\rho}_d$.

The relaxation parameters corresponding to both phases are given by:

$$\tau_c = \frac{\tilde{\nu}_c}{c_s^2 \Delta t} + \frac{1}{2} \quad \tau_d = \frac{\tilde{\nu}_d}{c_s^2 \Delta t} + \frac{1}{2} \quad (2.36)$$

Therefore, the following scale factors are introduced:

$$\begin{aligned}
&\text{Surface tension scale, N/m: } C_\sigma = \sigma / \tilde{\sigma} \\
&\text{Density scale, kg/m}^3: C_\rho = \rho / \tilde{\rho} \\
&\text{Kinematic viscosity scale, m}^2/\text{s: } C_\nu = \nu_c / \tilde{\nu}_c \\
&\text{Forcing scale, N/m}^3: C_{\text{force}} = \Delta\rho g / \widetilde{\Delta\rho g}
\end{aligned} \tag{2.37}$$

Using the definitions of Froude, Reynolds and Weber numbers and utilizing the scaling factors (2.37) the values of velocity, length, and time scaling factors, are defined as follows:

$$\begin{aligned}
&\text{Length scale, m: } C_d = C_\nu^2 C_\rho / C_\sigma \\
&\text{Velocity scale, m/s: } C_u = C_\sigma / (C_\nu C_\rho) \\
&\text{Time scale, s: } C_t = C_\nu^3 C_\rho^2 / C_\sigma^2
\end{aligned} \tag{2.38}$$

With the use of scaling factors (2.37) and (2.38) all parameters of the system in physical space are translated to the lattice space.

The dimensionless numbers that define the problem can be divided in two groups: the input dimensionless numbers that are based on input parameters and do not contain the resulting terminal drop velocity (Eo , Mo , λ_ρ , λ), and output dimensionless numbers (Re , We , Fr) that can be calculated only when the drop velocity is known. Thus, in the present study for the given binary liquid system (*n*-butanol/water) with density ratio $\lambda_\rho = 0.86$, dynamic viscosity ratio $\lambda = 2.36$ and the Morton number $Mo = 1.23 \cdot 10^{-6}$ the range of Eo numbers that corresponds to different drop diameters being considered is listed in Table 2.2.

To perform simulations that capture the physics of the problem, the input dimensionless numbers defined in physical and lattice spaces should be matched. With the proposed scaling procedure, the forcing term (2.34) and phase viscosities (2.35) depend on the drop diameter \tilde{d} . This means that the input parameters in lattice space are not unique. The simulation results obtained using different sets of input parameters all having the same Eo , Mo , λ_ρ , λ will not be precisely the same. There are three main factors that determine the choice of numerical parameters and, consequently, influence the results: accuracy, stability, and compressibility effects. The results of several test problems helped to define the proper set of input parameters in

Table 2.2: Drop diameter d and corresponding Eötvös number Eo considered in the present simulations

d , [mm]	Eo	d , [mm]	Eo
1.0	0.85	2.26	4.34
1.2	1.22	2.48	5.22
1.4	1.66	2.6	5.74
1.5	1.91	2.8	6.66
1.56	2.07	3.0	7.64
1.79	2.72	3.2	8.69
1.8	2.75	3.48	10.28
1.9	3.06	3.6	11.00
2.0	3.39	3.8	12.26
2.12	3.82	4.0	13.58

lattice space. First of all, the simulation results have to satisfy the incompressibility limit, i.e. the terminal drop velocity in lattice units should be not more than $0.1c_s$. If the resulting velocity of the drop does not fulfill this inequality, then the chosen set of parameters cannot be used. This criterion was used as the first filter to ‘sort’ the proper numerical parameters.

The choice of the drop diameter in lattice units \tilde{d} defines the spatial resolution and, thus, has a significant effect on the accuracy of the results and the computational effort. A proper balance between resolution and simulation time should be found. A drop diameter of 30 – 40 [lu] to represent the smallest drop of 1.0 mm gives small values of the phase viscosities in lattice space. This leads to relaxation parameters τ_c and τ_d close to 0.5. Such small values of the relaxation times for the flow field cause numerical instability. Moreover, together with a low surface tension value, they limit the range of τ_g values for which the simulation remains stable. To improve the stability and gain the accuracy the TRT collision operator has been adopted.

In order to make the proper choice of $\tilde{\sigma}$, a benchmark problem is needed to validate the numerical results. This validation gives strong evidence that the numerical model produces physically correct results.

In the present study, the drop diameter in lattice units \tilde{d} that represents a 1.0 mm drop is fixed to 30 [lu]. Also it was found during test simulations that the

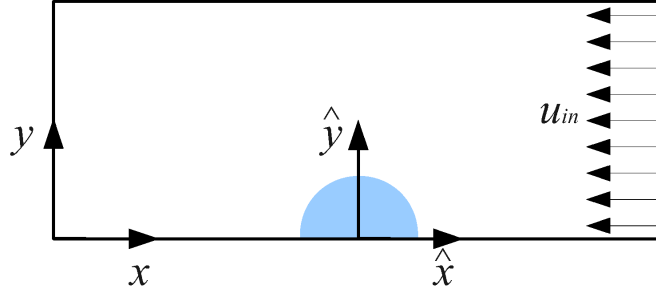


Figure 2.2: Simulation domain slice ($z = 0$). Inertial (stationary) reference frame (x - y); non-inertial (moving) reference frame (\hat{x} - \hat{y})

value of the surface tension scaling factor should be $C_\sigma = 1.0$ N/m. This choice of parameters gives a continuous phase kinematic viscosity of $\tilde{\nu}_c = 7.67 \cdot 10^{-3}$, the linear dimension scale factor, or the mesh step, $C_d = 3.33 \cdot 10^{-5}$ m and time scale factor, or the time step, $C_t = 6.04 \cdot 10^{-6}$ s. This set of parameters is our base set. The accuracy of the results obtained using this base set is discussed in Section 2.4.2. The diameters \tilde{d} of the larger drops are determined in a such way as to keep the kinematic viscosity of the continuous phase constant and equal to $7.67 \cdot 10^{-3}$.

To check the mesh convergence or possibility to coarsen the mesh, it is necessary to rescale the parameters. The idea of mesh refinement is to increase the drop diameter \tilde{d} f_m times ($\tilde{d}_2 = f_m \tilde{d}_1$, $f_m > 1.0$) while keeping all dimensionless numbers and liquid viscosities the same $\tilde{\mu}_{c2} = \tilde{\mu}_{c1}$, $\tilde{\mu}_{d2} = \tilde{\mu}_{d1}$. The same idea applies to mesh coarsening, but the drop diameter is reduced in $0 < f_m < 1$ times. The interface thickness remains the same ($\xi_2 = \xi_1$). To rescale the simulation parameters it is necessary to equate the Eötvös and Morton numbers for the fine and coarse drops. The following relations are obtained:

$$\frac{\tilde{\sigma}_2}{\tilde{\sigma}_1} = \frac{1}{f_m} \quad \frac{(\tilde{\Delta\rho g})_2}{(\tilde{\Delta\rho g})_1} = \frac{1}{f_m^3} \quad \frac{\kappa_2}{\kappa_1} = \frac{1}{f_m} \quad \frac{A_2}{A_1} = \frac{1}{f_m} \quad (2.39)$$

The results of the mesh convergence study are discussed in Section 2.4.2.

2.3.4 Moving reference frame

The larger the droplet diameter the longer distance it should travel to reach steady-state. Long computational domains can be avoided if the problem is solved in a moving reference frame. The idea is to move the computational domain along with the drop and keep the drop centered within the domain by adjusting the velocity of the frame. The implementation of the moving frame has been done in the same manner as presented by Rusche (2002).

The drop moves with respect to the stationary (inertial) reference frame $(x-y)$, but remains centered within the moving (non-inertial) reference frame $(\hat{x}-\hat{y})$ (see Fig. 2.2). Every time step the velocity of the moving reference frame v_F is corrected as follows

$$v_F = v_F^o + \Delta v_F \quad (2.40)$$

where v_F^o is the velocity of the reference frame at the previous (old) time step. The negative value of the moving frame velocity is imposed as the inlet boundary condition $u_{in} = -v_F$.

The correction for the velocity Δv_F is calculated using the following expression (Rusche, 2002):

$$\Delta v_F = \lambda_f \frac{\hat{x}_d^f - \hat{x}_d}{\Delta t} - \lambda_o \frac{\hat{x}_d - \hat{x}_d^o}{\Delta t} \quad (2.41)$$

where Δt is the time step and \hat{x}_d is the center of mass of the drop relative to the moving reference frame; the superscripts f and o denote values at the first ($t = 0$) and the previous time step. The λ_f and λ_o are under-relaxation factors. The center of mass of the drop relative to the moving frame is calculated as follows:

$$\hat{x}_d = \frac{\sum \varphi \hat{x}}{\sum \varphi} \quad (2.42)$$

where the summation is performed over all positive φ ; it is assumed that the drop is represented only by positive order parameter value ($\varphi = 0$ represents the interface).

As discussed by Rusche (2002), the first term in equation (2.41) is the velocity sufficient to translate the drop back to its original position in the moving frame of reference within a single time step. The second term represents the drop velocity relative to the moving reference frame. The purpose of the second term is to avoid

overshoots that appear as a result of the first term's corrections: these corrections accumulate until the drop reaches its original position. To damp both terms, under-relaxation factors λ_f and λ_o are used. It was outlined by Rusche (2002) that $\lambda_f = \lambda_o = 0.1$ yields good results. In the present study the same values have been used.

To account for the time-dependent motion of the domain an extra acceleration term is added to the momentum equation (2.9b). To obtain the value of moving reference frame acceleration, the time derivative of the frame velocity has to be determined as follows:

$$a_F = -\frac{\Delta v_F}{\Delta t} \quad (2.43)$$

The velocity of the drop in a stationary reference frame u is calculated as the sum of the volume-averaged drop velocity in the moving reference frame and the velocity of the moving frame v_F .

2.4 Numerical technique verification

A computer code for three-dimensional simulations has been developed using Fortran 90 in both serial and parallel versions. The parallel code uses domain decomposition and the MPI (Message Passing Interface) platform. The simulation domain was decomposed into slabs in the flow direction (x -axis), one for each CPU. The number of CPUs varied based on the drop diameter starting from 14 for $\tilde{d} = 30$ [lu] and up to 20 for $\tilde{d} = 60$. Depending on the drop diameter the duration of simulations ranged from several hours for the smallest drops to four days for the largest drops.

The details on the choice of the collision operator and related numerical parameters are discussed first. Only two collision operators were considered in the present study: a BGK (Bhatnagar et al., 1954) or single-relaxation-time (SRT) and a two-relaxation-time (TRT) (Ginzburg et al., 2008). The relaxation times (or symmetric contributions if TRT is used) for the f particle distribution function τ_c and τ_d are fixed by the kinematic viscosity of the liquids (2.36) and will not be changed. The relaxation time for the g distribution function can be tuned to obtain stable, accurate results. Based on test simulations τ_g equal to $1/(3 - \sqrt{3})$ was utilized (Van der

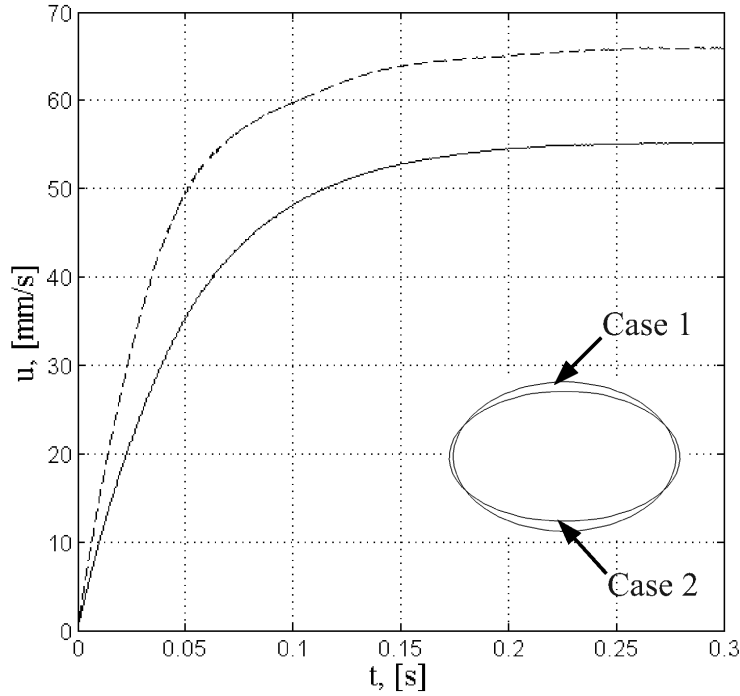


Figure 2.3: The evolution of 2 mm drop rise velocity in time and terminal drop shape for different cases. — case 1 (TRT); - - - case 2 (BGK)

Sman and Van der Graaf, 2008; Van der Sman, 2006). This value of τ is called the optimum value. Two simulations of a 2.0 mm diameter drop were carried out to outline the impact of the collision operator. Case 1 utilized TRT for both f and g with ‘magic’ numbers $\Lambda_{eo}^f = \Lambda_{eo}^g = 1/12$ and the optimum value of τ_g^s . Case 2 stands for BGK for both f and g and optimum τ_g . It can be noted that when $\tau_g^s = 1/(3 - \sqrt{3})$ and $\Lambda_{eo}^g = 1/12$ the anti-symmetric relaxation time τ_g^a is also equal to $1/(3 - \sqrt{3})$ and TRT for g reduces to BGK. Thus, with this choice of parameters the influence of the collision operator for f is demonstrated.

The evolution of the drop rise velocity for both cases together with terminal drop shape is shown in Fig. 2.3. The reference value of 2.0 mm drop terminal velocity (Bäumler et al., 2011) is 56.92 mm/s. The deviation between this reference velocity and velocities obtained in Cases 1 and 2 is 3% and 15.8%, respectively. In addition, slight drop shape oscillations are observed in Case 2. It can be seen from the drop rise velocity graph that drop acceleration undergoes non-monotonic variations in time. No shape oscillations for a 2.0 mm drop take place during neither

experiments nor Case 1. Moreover, the terminal drop shape is different in Cases 1 and 2. The reference aspect ratio (see definition below) is $E = 0.66$ while the values obtained in Cases 1 and 2 are 0.65 and 0.55, respectively. Based on this comparison we will be using a TRT scheme in the remainder of this paper.

The influence of ‘magic’ numbers Λ_{eo} was also examined. If $\Lambda_{eo} = 1/4$ or $1/6$ are specified for both f and g the simulations are unstable. If $\Lambda_{eo}^f = 1/12$ is kept and $\Lambda_{eo}^g = 1/4$ or $1/6$ the simulations are also unstable. Thus, for the *n*-butanol/water system the simulations are accurate and stable for a wide range of drop diameters only when $\Lambda_{eo}^f = \Lambda_{eo}^g = 1/12$ and $\tau_g^s = 1/(3 - \sqrt{3})$. The analyses of stability and high-order truncated corrections of physically simpler system performed by Ginzburg (2012) showed that $\Lambda_{eo} = 1/12$ with the BGK collision operator removes the third-order advection error. Additional investigation of the numerical scheme for the present complex physical system is required to further justify the choice of ‘magic’ numbers. This is beyond the scope of the present paper.

Hence, for the rest of the simulations the following parameters were used: TRT collision operator with $\Lambda_{eo}^f = \Lambda_{eo}^g = 1/12$, $\tau_g^s = 1/(3 - \sqrt{3})$, the mobility coefficient $\Gamma = 8$ and the mobility $M = 2.31$. For this base set of parameters the surface tension related values were $A = -4.3 \cdot 10^{-3}$, $\kappa = 2.8 \cdot 10^{-3}$.

The diffuse interface method adopted here is prone to spurious currents over the interface due to discretization of the velocity space. However, the velocities related to spurious currents are several orders of magnitude smaller than the physical velocities. The equilibration of a single stationary drop was simulated with the same stencils and relaxation times as mentioned before. Spurious velocities over the interface were $10^{-4} - 10^{-5}$ in lattice units, while the order of the velocity field in the rising drop simulation is of 10^{-2} in lattice units.

To verify the newly developed computer code and numerical technique, sensitivity analyses have been carried out on simulation domain size and mesh resolution. In addition, the correctness of the moving reference frame implementation has been checked. The results are presented below.

2.4.1 Domain size influence

The proper simulation domain size should have such width and length that wall confinement effects are negligibly small and there is no impact from the outflow boundary. On the other hand, the size of the domain should be reasonable to avoid extensive computations. The simulations of 2.0 mm drops were carried out in domains with the width W (see Fig. 2.1) equal to 2, 3 and 4 drop diameters. All computations were performed in a moving reference frame with drop diameter $\tilde{d} = 30$ [lu] and length of the domain $L_d = 14\tilde{d}$.

The terminal rise velocity was used to assess the wall effects for various domain sizes. The resulting drop terminal velocities for $W = 2\tilde{d}$, $3\tilde{d}$ and $4\tilde{d}$ are 53.81, 55.21 and 55.58 mm/s, respectively. In Fig. 2.4 the velocity evolution in time is shown. The terminal velocity of the drop obtained in the narrowest domain is within 5% of the one corresponding to the widest domain. The relative deviation of the steady-state velocity obtained for $W = 3\tilde{d}$ and $W = 4\tilde{d}$ is less than 1%. Thus, the simulation domain width was chosen to be $W = 3\tilde{d}$ to limit computational cost. In addition, the width of the domain caused only minor changes of the drop shape in the steady-state regime.

The influence of the simulation domain length was checked again using 2.0 mm drop simulations. The moving reference frame implementation requires the outflow boundary condition. The entire flow is influenced by the outlet boundary location: it is necessary to make sure that the wake behind the drop becomes fully-developed and does hardly interfere with the outlet. Several simulation domain lengths L_d were considered equal to 8, 10, 12, 14 and 16 drop diameters. The terminal drop velocity for the case with $L_d = 8\tilde{d}$ is 55.04 mm/s, and for the case $L_d = 16\tilde{d}$ the velocity is 55.22 mm/s. Thus, the influence of simulation domain length on terminal drop rise velocity is negligibly small. If not specified otherwise, the simulation domain length was set to $14\tilde{d}$.

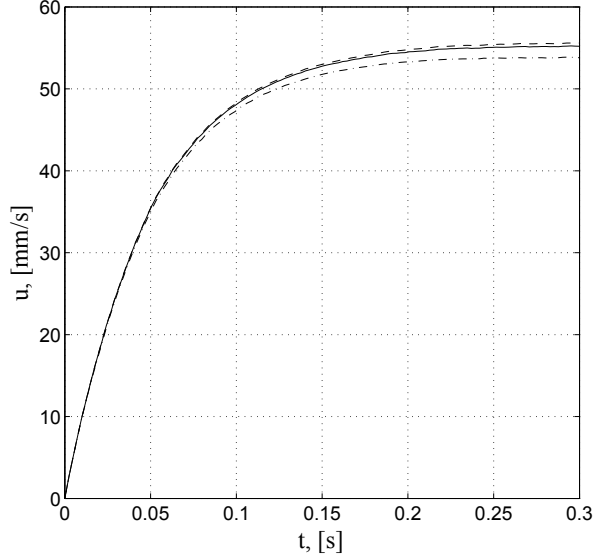


Figure 2.4: Domain size influence. The evolution of 2.0 mm drop rise velocity in time for different simulation domain widths. The length of the domain is $14\tilde{d}$; $-\cdot-\cdot-$ $W = 2\tilde{d}$; $—$ $W = 3\tilde{d}$; $---$ $W = 4\tilde{d}$

2.4.2 Mesh resolution

The accuracy of the results obtained using the basic set of parameters (discussed in Section 2.3.3) was examined. Two sensitivity analyses on mesh resolution were performed: mesh refinement ($f_m > 1.0$) and mesh coarsening ($0.0 < f_m < 1.0$). In both procedures the absolute value of the interface thickness was kept constant ($\xi = 1.14$).

Mesh refinement was performed for simulations of 1.0 mm drops with domain size $12\tilde{d} \times 3\tilde{d} \times 3\tilde{d}$. Six drop diameters in lattice units were considered with corresponding length scaling factors, or mesh steps, in the range $C_d = 1.7 \cdot 10^{-5} - 2.9 \cdot 10^{-5}$ m. The resulting terminal drop velocities are plotted in Fig. 2.5. The terminal drop velocity of the 1.0 mm drop obtained using the basic set of parameters with $\tilde{d} = 30$ [lu] is depicted by the red square. The relative deviation of the velocity between the basic mesh and the finest mesh is 6.2%. The basic set of parameters is adopted further for the simulations, since it is a good balance between accuracy and simulation time.

Mesh coarsening has also been checked for the 1.0 mm drop. Two cases were simulated with drop diameters 25 and 20 [lu], the corresponding length scaling

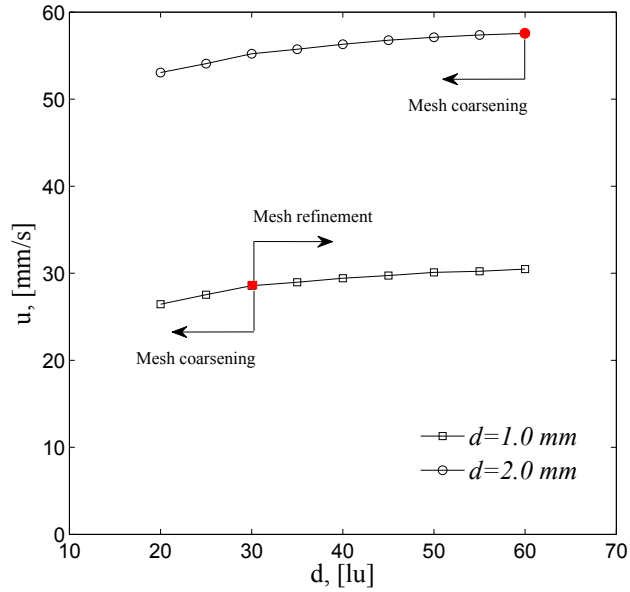


Figure 2.5: Mesh resolution. Terminal drop velocity as a function of drop diameter \tilde{d} in lattice units for 1.0 and 2.0 mm drops obtained

factors are $4.0 \cdot 10^{-5}$ and $5.0 \cdot 10^{-5}$ m. The results are shown in Fig. 2.5: the relative deviation of terminal velocity between 20 and 30 [lu] drops is 7.5%, while the deviation between 20 and 60 [lu] drops is 13.2%.

A mesh coarsening procedure has been applied for a 2.0 mm drop. With the basic set of parameters the drop is represented by a 60 [lu] drop diameters in lattice space (red circle in Fig. 2.5). Eight smaller drop diameters in lattice space were considered with the mesh step in the range $C_d = 3.33 \cdot 10^{-5} - 10.0 \cdot 10^{-5}$ m. The domain size was equal to $14\tilde{d} \times 3\tilde{d} \times 3\tilde{d}$. The terminal drop velocities for all cases are shown in Fig. 2.5. The relative deviation between the terminal velocity obtained with the basic set of parameters ($\tilde{d} = 60$ [lu] for 2.0 mm drop) and the rescaled parameters for coarser drops with $\tilde{d} = 30$ [lu] ($f_c = 0.5$) is 4%. This value of the coarsening factor is used for all drops larger than 2.0 mm, since it reduces the domain size and, subsequently, the simulation time while giving result that are in good agreement with those obtained using a finer mesh.

2.4.3 Moving reference frame implementation

In the present study the numerical simulations of a *n*-butanol drop moving in water were performed in a moving reference frame. Since the moving frame implementation involves modification of the governing equations it is important to verify the results by confronting them to those obtained on a stationary reference frame.

A 2.0 mm drop was simulated both in stationary and moving reference frames. The diameter of the drop in lattice space was $\tilde{d} = 30$. The size of the stationary domain was $24\tilde{d} \times 3\tilde{d} \times 3\tilde{d}$. Bounce-back (walls) boundary conditions were imposed on boundaries of the domain with $x = 0$ and $x = L_d$, specular reflection conditions were applied on all side walls since only a quarter of the domain was considered (see Fig. 2.1). The initial position of the drop in case of the stationary domain was at a distance $7.5\tilde{d}$ from the boundary $x = 0$.

In the moving reference frame implementation when a velocity inflow boundary condition is used together with outflow boundary condition, at the beginning of the simulation a pressure wave appears: it moves back and forth over the domain and eventually dissipates (Mussa et al., 2009). The cause of the wave is the inconsistency of the initialization: the density (pressure) field does not match the velocity values set at the inflow boundary (Mei et al., 2006). Since the simulated drop is initially at rest and smoothly accelerates by the external gravity force, the imposed velocity at the inlet boundary u_{in} is zero at the first time step and increases slowly over the time. Thus, the impact of the pressure wave on the flow development during the initial time steps is small as will be shown below.

The development of the drop rise velocity in time for both test cases carried out using stationary and moving reference frames is presented in Fig. 2.6. The results are in excellent agreement. The drop terminal velocity obtained using the moving reference frame is 55.21 mm/s and 55.35 mm/s using the stationary frame of reference. The streamlines corresponding to both frames have also been compared. To enable this comparison between the moving and stationary frames, the velocity of the moving frame was subtracted from the velocity field computed on stationary frame. The streamlines together with the x -component of the velocity field for the

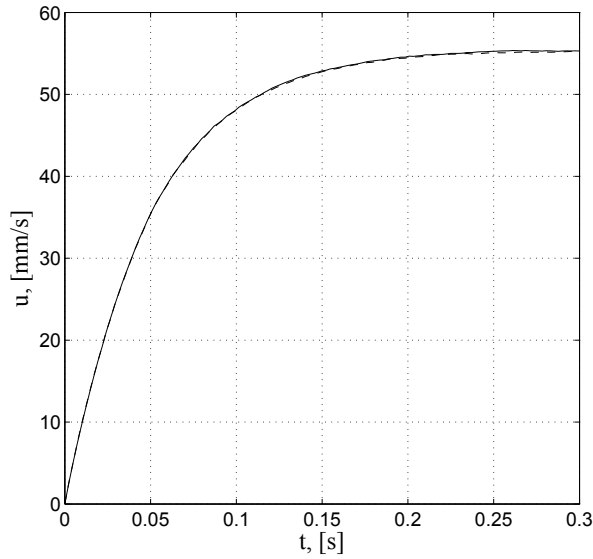


Figure 2.6: Time evolution of terminal rise velocity of 2.0 mm drop calculated in two test cases: — stationary reference frame; - - - moving reference frame.

test simulations at time instants 0.05, 0.15 and 0.3 s are shown in Fig. 2.7. The last moment is during steady-state. The white curve represents the interface. The external flow is from the right to left, the front of the drop is facing the positive x -direction. As one can see, the results agree well. The streamlines at time step 0.05 s are identical, which means there is no impact of the inflow/outflow boundary conditions or inconsistency of the initialization in the moving frame implementation. The slight difference of streamline behaviour in the wake of the drop is attributed to the sensitivity of streamlines plotting: there is a significant influence of the exact value of the subtracted velocity of the moving frame on the streamline pattern. Since the magnitude of the velocities in that region is small compared to the velocity of the drop, even slight differences of velocity cause notable changes in streamlines behaviour. Since the deviation of terminal velocities in both cases is negligible, the moving reference frame approach was adopted for the rest of the simulations.

2.5 Analyses of n -butanol drop motion in water

The numerical simulations of n -butanol droplets motion in water have been performed for drops within the diameter range 1.0 – 4.0 mm with the aim to observe

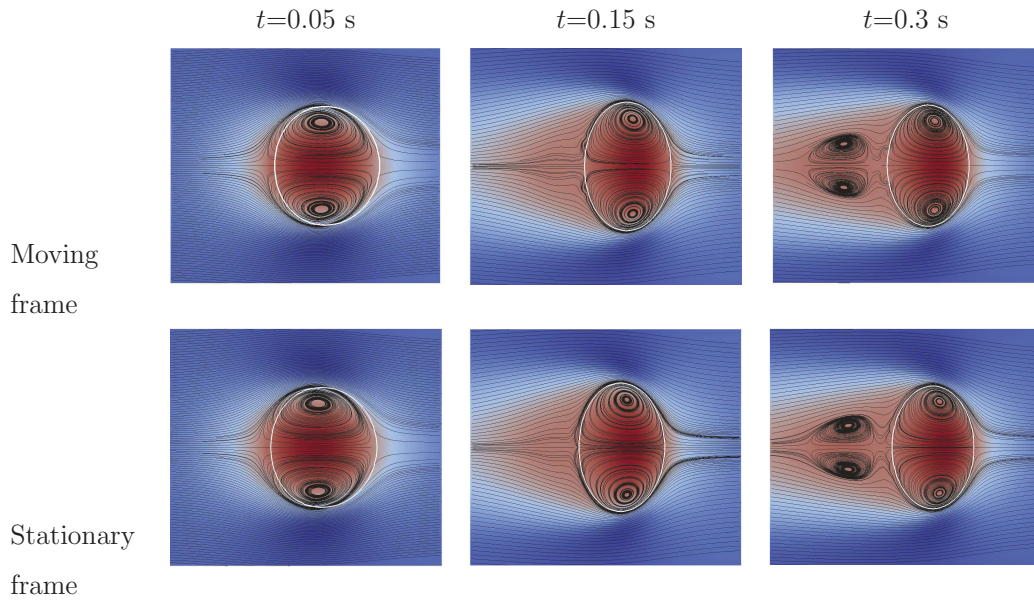


Figure 2.7: Streamlines with x -component of velocity for 2.0 mm drop in two cases: moving reference frame and stationary reference frame. The white curve represents the interface

three flow regimes relevant to extraction processes: spherical, deformed, and oscillating drops. For each drop the terminal rise velocity and drop deformation were analyzed. The terminal velocity of non-oscillating droplets was determined when steady-state had been reached after an acceleration period. The mean terminal velocity for shape oscillating drops was evaluated by averaging the rise velocity over the time spent on several shape oscillations. Each simulation was run until the steady-state was reached for non-oscillating drops or when the velocity of oscillating drops reached the steady oscillations. The terminal velocity values obtained in this study were compared to experimental and numerical results reported by Bertakis et al. (2010), a semi-empirical correlation proposed by Bertakis et al. (2010) and numerical results obtained by Bäumlner et al. (2011). The maximum diameter of the drop considered by Bäumlner et al. (2011) was 3.1 mm, Bertakis et al. (2010) considered the maximum drop diameter of 3.48 mm in experiments and 4.0 mm in simulations.

The terminal velocities as a function of drop diameter are plotted in Fig. 2.8. The results are in good agreement for drops up to 3.0 mm in diameter. The relative

deviation of velocity for the 3.0 mm drop compared to simulation results of Bertakis et al. (2010) is 8% and compared to Bäumlner et al. (2011) is 2%. The relative deviation in the terminal velocity for the 4.0 mm drop calculated here with the result presented by Bertakis et al. (2010) is 20% which is the largest deviation between the results of the present study and the existing data. However, several facts should be taken into account when comparing the results. As is shown later, Bertakis et al. (2010) performed simulations over a time window that is not long enough for the drop rise velocity to reach steady-state, and the values of the velocity might be larger than outlined. In addition, the authors mentioned that the larger the velocity of the drop, the bigger the relative error of the terminal velocity measurements (up to 2.1% for the fastest one). Bäumlner et al. (2011) obtained the maximum velocity of the drop at maximum considered drop diameter. A more detailed discussion of the results is presented below.

In the experimental data by Bertakis et al. (2010) the maximum velocity is reached at $d = 2.48$ mm, according to the data fit (Henschke model) the maximum velocity is found at 2.5 mm, whereas the simulations of Bertakis et al. (2010) have the maximum at 3.0 mm; just slightly below the simulations of Bäumlner et al. (2011), with 3.1 mm. In present simulation the maximum velocity is reached for the droplet of 3.8 mm diameter. However, it is difficult to clearly distinguish this maximum velocity since the drops with diameter $d \geq 3.5$ mm have close terminal drop velocity values (see Fig. 2.8).

To describe the shape deformation quantitatively, the aspect ratio E is used, which is defined as the ratio of the two principal axes of the drop (Michaelides, 2006). Referring to the simulation domain depicted in Fig. 2.1, the aspect ratio can be calculated as $E = L_{\parallel}/(2L_{\perp})$, where L_{\parallel} is the size of the drop parallel to the flow direction and L_{\perp} is the size of the drop perpendicular to the flow direction. $E = 1$ means that the droplet has spherical shape (Michaelides, 2006). If $E < 1$ the shape of the drop is called ‘oblate’ and if $E > 1$, then it is a ‘prolate’ shape. In all simulations presented here only spherical and oblate drop shapes were observed at steady-state drop motion. The value of E was compared to the results of Bäumlner

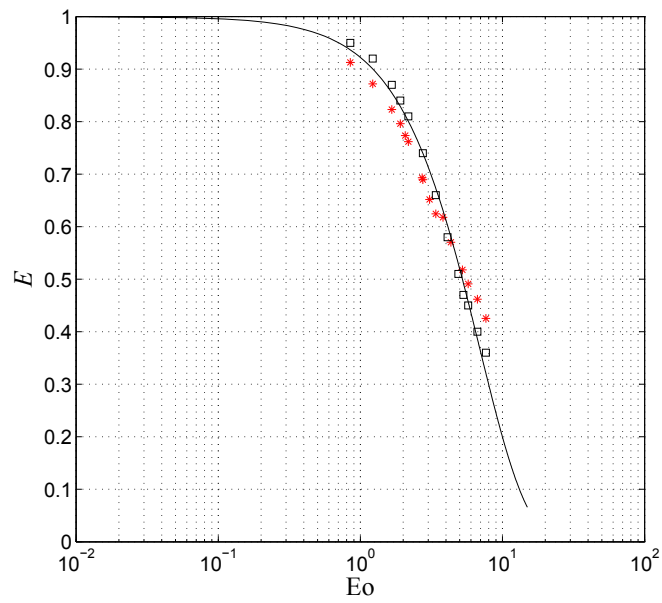
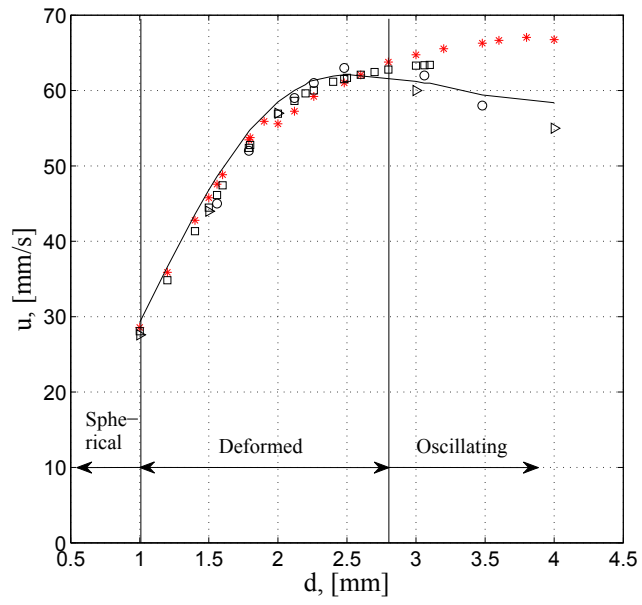


Figure 2.9: Simulated aspect ratio E (*) as a function of Eötvös number E_o in comparison with Bäumlér et al. (2011) (the results of numerical simulation due to (Bäumlér et al., 2011) are denoted as □; the solid curve stands for the data fitting curve described by equation (2.44))

et al. (2011) who fitted their simulated data with the following equation:

$$E = e^{-a} \text{Eo}^b \quad (2.44)$$

where $a = 0.081$ and $b = 1.299$. The simulated aspect ratio as a function of Eötvös number Eo is plotted in Fig. 2.9 together with the results obtained by Bäumlér et al. (2011). Good agreement is observed.

According to Michaelides (2006) if $E \geq 0.95$ the drop can be regarded as spherical. Among the drop diameters considered in the present simulations only the 1.0 mm drop has a spherical shape at steady-state. Drops with larger diameters are either deformed or shape-oscillating. Small drops accelerate monotonously over the time and, finally attain a steady-state terminal velocity. In Fig. 2.10a one can see the evolution of the drop rise velocity in time for 1.0, 1.5 and 2.48 mm drops. The acceleration period for 1.0 mm drop is less than 0.2 s which is in good correlation with results of Bertakis et al. (2010) and Bäumlér et al. (2011). For all drops with diameter $d > 2.0$ mm vortices appear in the wake.

When drop diameters exceed 2.6 mm a different behavior of the drop is noticed: slight oscillations appear over the acceleration period. The possible reason behind this is the low interfacial tension of the *n*-butanol/water system compared for example to a toluene/water system. In Fig. 2.10b time series of the rise velocity for drops with diameter 2.6 and 2.8 mm are depicted. The amplitude of oscillations of 2.6 mm drop is so small that they are damped during the acceleration period, and the drop reaches a steady terminal velocity. The acceleration of the 2.8 mm drop goes along with more developed oscillations that do not vanish over time. This denotes the onset of shape oscillations of drops with diameter $d \geq 2.8$ mm. The terminal velocity of the drop oscillates around the mean value at the steady-state regime. According to Bertakis et al. (2010) the onset of oscillations is at approximately 2.86 mm which agrees well with the present results.

The rise velocity of 3.0 mm drop is presented in Fig. 2.10c. The behavior is in excellent agreement with Bäumlér et al. (2011) (see their Fig.12). The following terminal velocities of the drop are obtained in present simulation, numerical simulation by Bertakis et al. (2010) and Bäumlér et al. (2011), respectively: 64.75, 60.0

and 63.30 mm/s. Even though all results are in good agreement, the lower value obtained by Bertakis et al. (2010) could be explained by the fact that simulations were carried out only until 0.4 s after startup, while the velocity of the drop keeps increasing until $t = 0.8$ s.

The larger the drop diameter, the longer the acceleration period. The amplitude of the velocity oscillations also becomes larger, both in accelerating and steady regimes. A representative result of the rise velocity evolution in time in the oscillating drop regime is shown in Fig. 2.10d that relates to a 3.48 mm drop. A further increase in drop diameter leads to significant drop deformations at initial times, that changes the value and oscillations behavior of drop rise velocity. The results of the 3.8 mm drop terminal velocity calculations are shown in Fig. 2.10e. For all previous oscillating drops (Fig. 2.10c and d), the second peak during the acceleration period was higher than the first one. In contrast, for the 3.8 mm drop, the value of the second peak is below the value of the first one. The evolution of rise velocity for later times has the same trends as discussed earlier. To see the difference in drop deformations at initial times, the flow streamlines together with the drop shape are presented in Fig. 2.11 for the 3.48 and 3.8 mm drops. At $t = 0.1$ s the shape of the drops and flow streamlines are similar in both cases. However, at $t = 0.2$ s the 3.8 mm drop deforms in a way (possibly because of the low surface tension and high velocity compared to the velocity of the 3.48 mm drop at this time instant) that at later time $t = 0.4$ s the droplet gets a concave shape. In addition, the size and shape of the wake behind the drops is different. The concave shaped drop has a wider and shorter wake compared to the ellipsoidal drop.

Notable differences in the drop rise velocity evolution are observed for the 4.0 mm drop (Fig. 2.10f). After significant velocity oscillations and shape deformations at initial time steps, the velocity rapidly increases and, finally, the droplet attains a steady regime with oscillations around a mean value. The 4.0 mm drop deformation at different times are presented in Fig. 2.12. After significant deformation up to $t = 0.6$ s the droplet gets a concave shape and with slight oscillations accelerates while changing its shape to ellipsoidal with a flattened surface on top. Finally, the drop oscillates around the mean terminal velocity and ellipsoidal drop

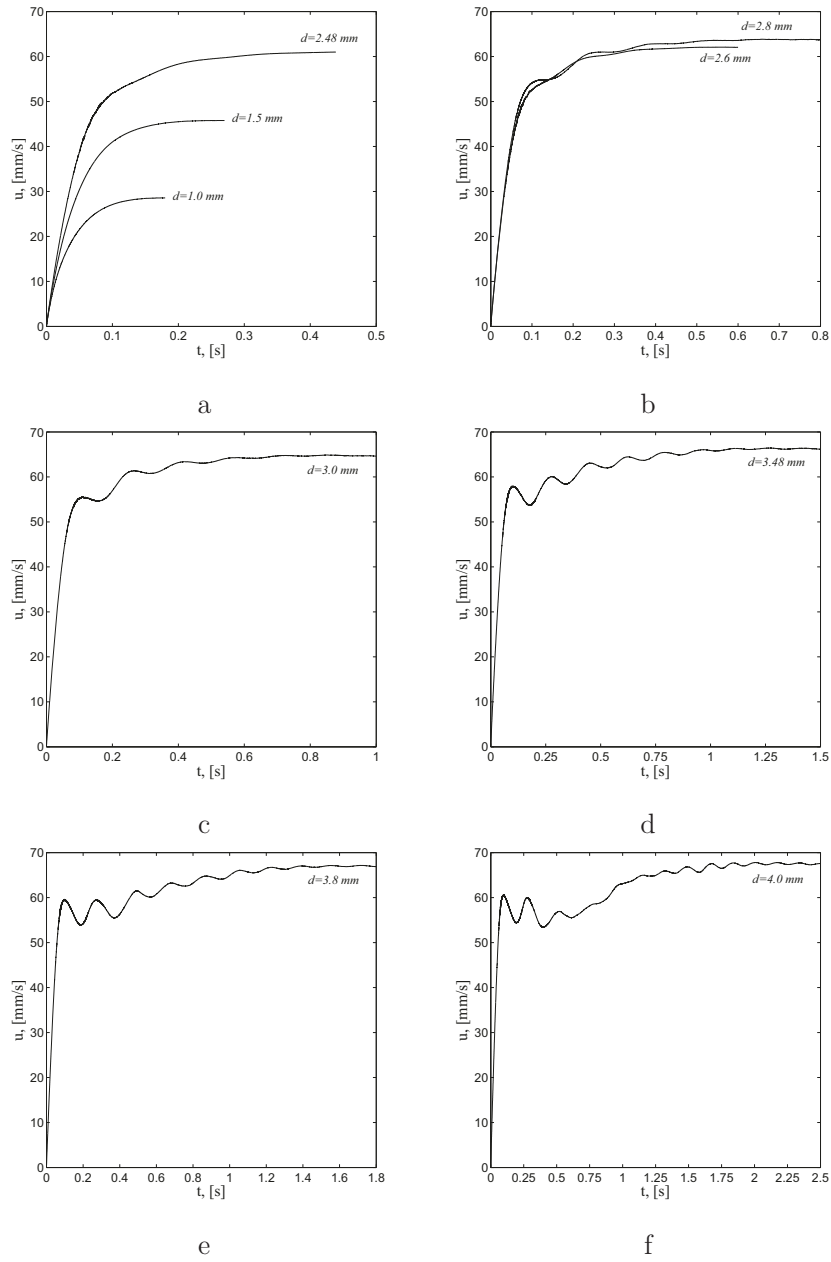


Figure 2.10: Drop rise velocity as a function of time for different drop diameters; a - 1.0 mm drop in spherical regime and 1.5, 2.48 mm drops in deformed regime; b - 2.6 and 2.8 mm drops refer to transition between deformed and oscillating droplets; c - 3.0 mm drop; d - 3.48 mm drop; e - 3.8 mm drop; f - 4.0 mm drop is the largest simulated drop in the present study

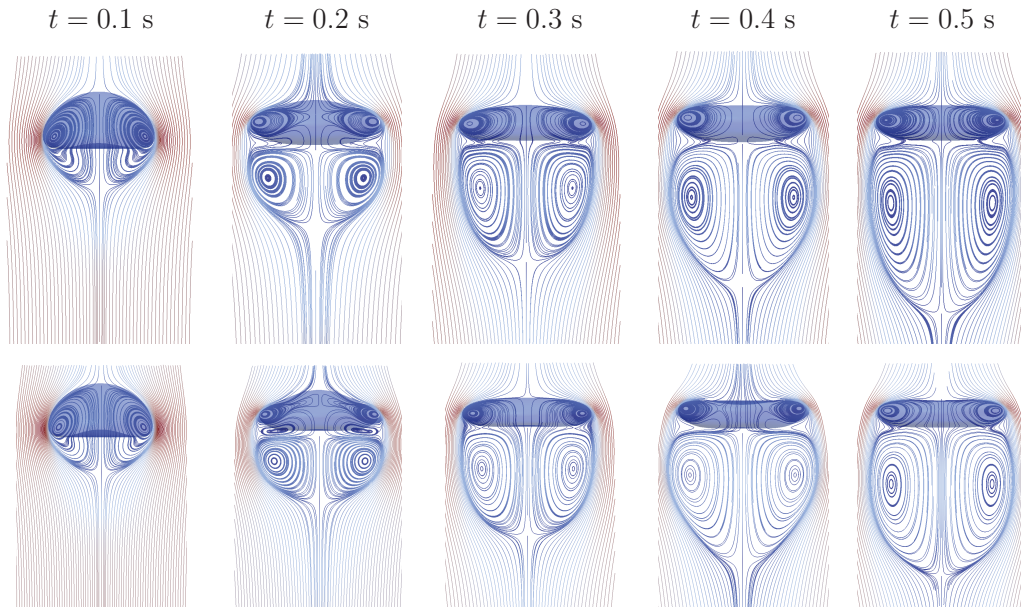


Figure 2.11: Streamlines and drop shape for $d = 3.48$ mm (upper row) and $d = 3.8$ mm (bottom row) drops at different moments

shape. The mean terminal drop velocity is equal to 66.75 mm/s, while Bertakis et al. (2010) obtained a value of 55.0 mm/s. It should be mentioned that the simulations of the 4.0 mm drop were carried out by Bertakis et al. (2010) only until $t = 0.7$ s. As can be seen in Fig. 2.10f the velocity keeps increasing until 1.75 s. The drop velocity value at $t = 0.7$ s obtained in the present study is 56.25 mm/s which is close to Bertakis et al. (2010). Also the evolution of the rise velocity in time agrees well with reference data.

To validate our numerical results of shape deformation the well known diagram by Clift et al. (1978) is used. The simulated data is plotted in the graphical correlation in Fig. 2.13. The plot shows the Reynolds number versus Eötvös for the Morton number of n -butanol/water system equal to $1.23 \cdot 10^{-6}$. The simulated data excellently matches the correlation: the 1.0 mm drop lies exactly on the curve dividing the regions of spherical and ellipsoidal drops. The correlation appears to better predict the behavior of n -butanol water system for larger drop diameters.

In addition, the numerical data was organized using Reynolds and Weber numbers. In contrast to the previous correlation, the We number contains the terminal

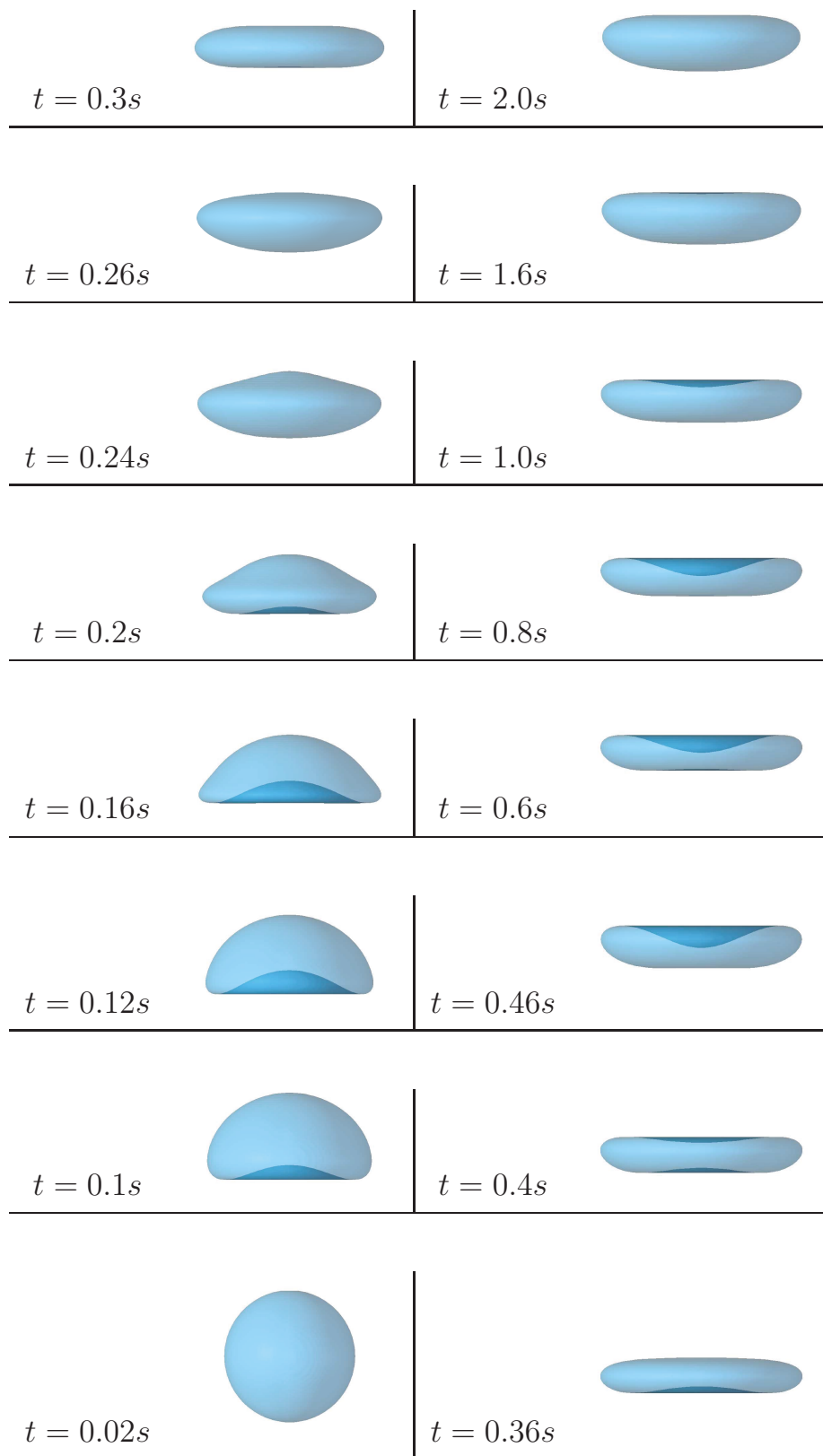


Figure 2.12: The *n*-butanol drop deformation of 4.0 mm diameter at different time steps

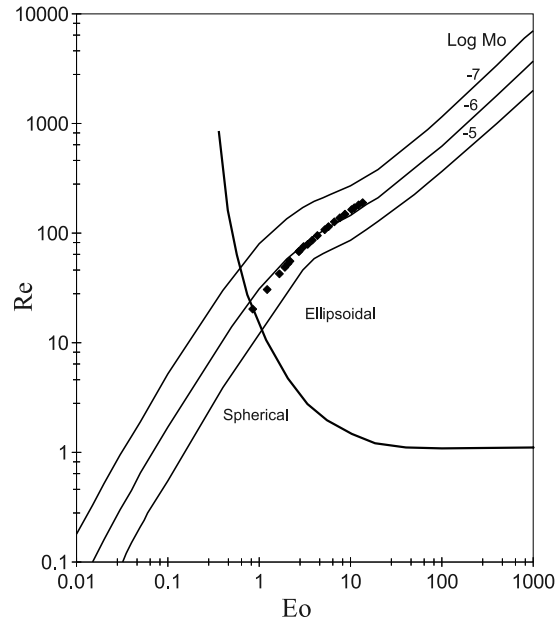


Figure 2.13: Comparison of simulated Reynolds numbers Re as a function of Eötvös number Eo for Morton number $Mo = 1.23 \cdot 10^{-6}$ to the graphical correlation by (Clift et al., 1978)

drop velocity, and shows the ratio of continuous phase internal fluid stresses (that cause the deformation of the drop) and surface tension stresses resisting the deformation. The plot is shown in Fig. 2.14, where the steady state shape of the drops are also depicted (for the shape oscillating drops the shape at the mean terminal velocity is presented). For $We \leq 1.0$ only negligibly small deviation of the drop shape from a sphere is observed. With the increase of We number, the drop is more deformed.

The ratio between Weber and Reynolds numbers gives a capillary number $Ca = u\mu_c/\sigma$. The capillary number measures the balance between two competing effects: the viscous stress of the continuous liquid that causes the drop deformation, and capillary stress that resists the deformation. In Fig. 2.15 the simulated capillary number is plotted as a function of Eötvös number. With the increase of Eo (i.e. the drop diameter since $Eo \sim d^2$) the Ca number approaches a constant value. The drop enters the shape oscillation regime when $Eo \geq 7.0$. As one can see from the graph this is the point where Ca gets to a constant value of 0.056. During the shape

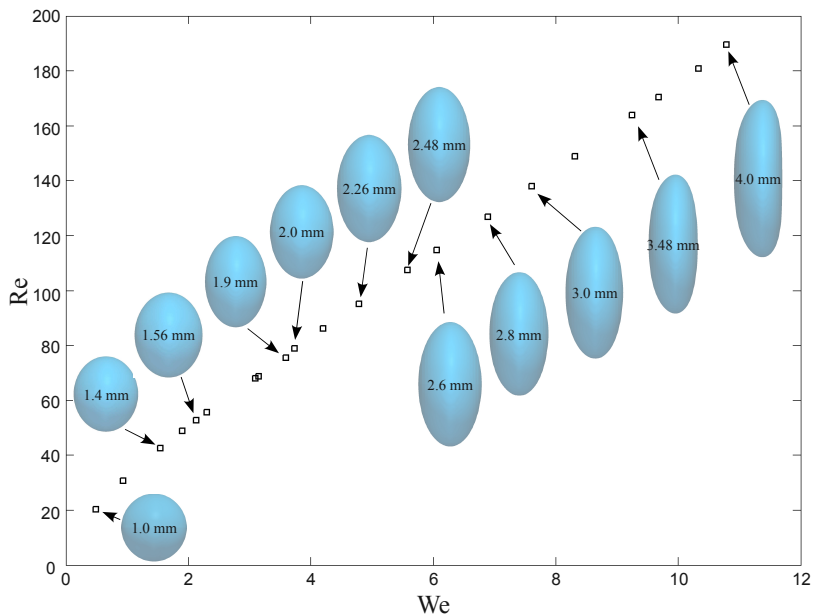


Figure 2.14: Simulated Reynolds number Re versus Weber number We plotted with drop shapes in steady-state. (Gravitational acceleration is directed from right to left)

oscillations viscous and internal forces balance not letting the drop break or return to a stable shape. With further increase of drop diameter the surrounding liquid might cause more significant drop deformations and break the drop.

2.6 Conclusion

In this paper numerical simulations of single *n*-butanol drops rising in water under the influence of gravity are presented. The free energy LBE model with TRT collision operator was used to perform three-dimensional simulations of this binary system in order to determine the drop terminal velocity and its shape. The drop diameters that were studied 1.0 – 4.0 mm spanned the regions of spherical, deformed, and oscillating droplets, allowing to test the numerical technique under different conditions relevant to liquid-liquid extraction processes. The simulations were carried out in a moving reference frame to reduce the domain size, and thus the computational cost. The computer code was developed in Fortran 90 with MPI for parallel processing.

The proposed scaling procedure allowed us to determine the parameters in lat-

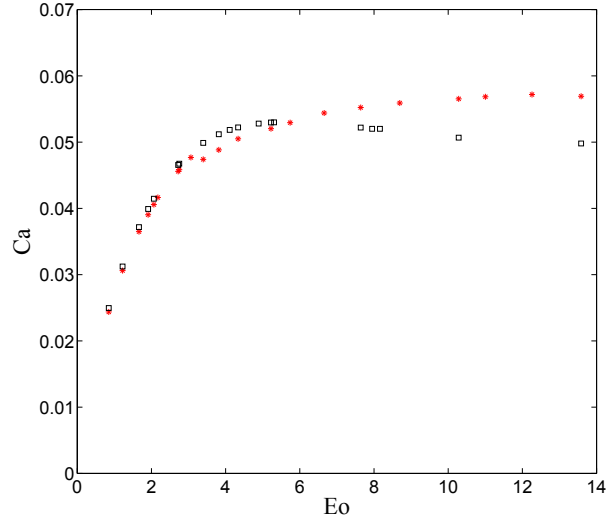


Figure 2.15: Capillary number Ca versus Eötvös number Eo ; (*) present simulations; (□) the Ca number value plotted using the terminal velocity obtained with semi-empirical correlation proposed by (Bäumler et al., 2011)

tice space, where the LBE models operate, that correspond to the real physical parameters of the given binary system. It was outlined that in order to determine the proper values of the LBE parameters it is necessary to validate the results with a benchmark solution. In our case the benchmark data were the experimental results and the results of simulations obtained using different numerical techniques. Once the numerical approach is validated, it can be applied for simulations of multiphase systems in other problem statements, e.g. consideration of *n*-butanol drop breakup or coalescence in water, or multiple drops interaction in laminar shear of fully-developed turbulent flow.

The simulation parameters as computational domain size, mesh resolution, and LBE numerical parameters were tested to verify the developed computer code. For negligible effects of boundary walls, the width of the domain should be at least three drop diameters.

The mesh resolution has a significant effect on the results. It is important to capture the essential drop deformations and oscillations, circulations inside the drop and wake development behind the drop. Mesh refinement has been performed to determine the required mesh resolution: the relative deviation between the terminal velocity obtained on the coarsest and the finest grids is 13.2% for a 1.0 mm drop.

For the same drop, the relative deviation in drop velocity obtained on the mesh resolution with which most of the simulations have been carried out and the finest mesh is 6.2%.

The simulations captured drop acceleration, shape deformation, steady motion with constant velocity of non-oscillating drop, and shape-oscillating motion of drops in the oscillatory regime. The results obtained in the study have been compared to experimental data and numerical simulations using other methods. The results show that the numerical technique can be adopted to perform multiphase simulations with moving and deforming interfaces. The results of the simulations are in good agreement with experimental and numerical data. The deviation in terminal drop velocity for small drop diameters is within 5% and up to 20 % for the largest one. The capability of the method to capture the drop shape deformation especially in the oscillating regime is also demonstrated. The results are in excellent correlation with the standard reference diagram by Clift et al. (1978) for predicting the shape of fluid particles. In addition, it was outlined that the regime of shape oscillations of the drop in the considered drop diameter range is characterized by an almost constant capillary number of $Ca = 0.056$.

The regimes of drop motion did not cover drop breakup. As future work, the *n*-butanol drops in water under simple shear flow will be considered. Such a problem will allow us to test the capability of the developed numerical technique of interface disintegration capturing. Also drop coalescence will be considered. This is one of the most challenging problems to solve since the drawback of the utilized interface capturing technique is artificial merging of the drops even in the cases where the drops should not coalesce. After the developed numerical tools have been tested using these benchmark problems, *n*-butanol drop dispersion in water will be considered with hundreds of dispersed drops subjected to turbulent flow conditions.

References

- N. K. Ahmed and M. Hecht. A boundary condition with adjustable slip length for lattice Boltzmann simulations. *J. Stat. Mech.*, P09017:1–13, 2009.
- V. E. Badalassi, H. D. Ceniceros, and S. Banerjee. Computation of multiphase systems with phase field models. *J. Comput. Phys.*, 190:371–397, 2003.
- K. Bäumlner, M. Wegener, A. R. Paschedag, and E. Bansch. Drop rise velocities and fluid dynamics behavior in standard test systems for liquid/liquid extraction - experimental and numerical investigations. *Chem. Eng. Sci.*, 66:426–439, 2011.
- E. Bertakis, S. Grob, J. Grande, O. Fortmeier, A. Reusken, and A. Pfennig. Validated simulation of droplet sedimentation with finite-element and level-set methods. *Chem. Eng. Sci.*, 65:2037–2051, 2010.
- P. L. Bhatnagar, E. P. Gross, and M. Krook. A model for collision processes in gases. I. Small amplitude processes in charged and neutral one-component systems. *Phys. Rev.*, 94:511–525, 1954.
- A. J. Bray. Theory of phase-ordering kinetics. *Adv. Phys.*, 43:357–459, 1994.
- J. W. Cahn and J. E. Hilliard. Free energy of a nonuniform system. I. Interfacial free energy. *J. Chem. Phys.*, 28:258–267, 1958.
- S. Chen and G. D. Doolen. Lattice Boltzmann method for fluid flows. *Annu. Rev. Fluid Mech.*, 30:329–364, 1998.
- R. Clift, J. R. Grace, and M. E. Weber. *Bubbles, Drops, and Particles*. Academic Press, London, 1978.

- S. R. De Groot and P. Mazur, editors. *Non-equilibrium thermodynamics*. Dover Publications, 1984.
- A. M. Dehkordi, S. Ghasemian, D. Bastani, and N. Ahmadpour. Model for excess mass–transfer resistance of contaminated liquid–liquid systems. *Ind. Eng. Chem. Res.*, 46:1563–1571, 2007.
- D. d’Humières, I. Ginzburg, M. Krafczyk, P. Lallemand, and L.-S. Luo. Multiple-relaxation-time lattice Boltzmann models in three dimensions. *Phil. Trans. R. Soc. Lond. A*, 360:437–451, 2002.
- M. Dijkhuizen, I. Roghair, M. Van Sint Annaland, and J. A. M. Kuipers. DNS of gas bubbles behaviour using an improved 3D front tracking model – Model development. *Chem. Eng. Sci.*, 65:1427–1437, 2010.
- H. Ding, P. D. M. Spelt, and C. Shu. Diffuse interface model for incompressible two-phase flows with large density ratios. *J. Comput. Phys.*, 226:2078–2095, 2007.
- I. Ginzburg. Truncation errors, exact and heuristic stability analysis of two-relaxation-times lattice Boltzmann schemes for anisotropic advection-diffusion equation. *Commun. Comput. Phys.*, 11:1439–1502, 2012.
- I. Ginzburg, F. Verhaeghe, and D. d’Humières. Two–relaxation–time lattice Boltzmann scheme: about parametrization, velocity, pressure and mixed boundary conditions. *Commun. Comput. Phys.*, 3:427–478, 2008.
- J. R. Grace, T. Wairegi, and T. H. Nguyen. Shapes and velocities of single drops and bubbles moving freely through immiscible liquids. *Trans. Instn. Chem. Engs.*, 54:167–173, 1976.
- R. M. Griffith. The effect of surfactants on the terminal velocity of drops and bubbles. *Chem. Eng. Sci.*, 17:1057–1070, 1962.
- A. K. Gunstensen, D. H. Rothman, S. Zaleski, and G. Zanetti. Lattice Boltzmann model for immiscible fluids. *Phys. Rev. A*, 43:4320–4327, 1991.

- X. He, S. Chen, and R. Zhang. A lattice Boltzmann scheme for incompressible multiphase flow and its application in simulation of Rayleigh-Taylor instability. *J. Comp. Phys.*, 152:642–663, 1999.
- M. Henschke and A. Pfennig. Mass-transfer enhancement in single-drop extraction experiments. *AIChE J.*, 45:2079–2086, 1999.
- C. W. Hirt and B. D. Nichols. Volume of fluid (VOF) method for the dynamics of free boundaries. *J. Comput. Phys.*, 39:201–225, 1981.
- S. Hu and R. C. Kintner. The fall of single liquid drops through water. *AIChE J.*, 1: 42–48, 1955.
- D. Jacqmin. Calculation of two-phase Navier–Stokes flows using phase-field modeling. *J. Comp. Phys.*, 155:96–127, 1999.
- A. I. Johnson and A. E. Hamielec. Mass transfer inside drops. *AIChE J.*, 6:145–149, 1960.
- V. M. Kendon, M. E. Cates, I. Pagonabarraga, J.-C. Desplat, and P. Bladon. Inertial effects in three-dimensional spinodal decomposition of a symmetric binary fluid mixture: a lattice Boltzmann study. *J. Fluid Mech.*, 440:147–203, 2001.
- A. J. Klee and R. E. Treybal. Rate of rise or fall of liquid drops. *AIChE J.*, 2: 444–447, 1956.
- P. M. Krishna, D. Venkateswarlu, and G. S. R. Narasimhamurthy. Fall of liquid drops in water. Drag coefficients, peak velocities, and maximum drop sizes. *J. Chem. Eng. Data*, 4:340–343, 1959a.
- P. M. Krishna, D. Venkateswarlu, and G. S. R. Narasimhamurthy. Fall of liquid drops in water. Terminal velocities. *J. Chem. Eng. Data*, 4:336–340, 1959b.
- H. Kusumaatmaja. *Lattice Boltzmann studies of wetting and spreading on patterned surfaces*. PhD thesis, University of Oxford, 2008.
- J.C. Lee. *Thermal Physics. Entropy and Free Energies*. World Scientific, 2002.

- R. Mei, L.-S. Luo, P. Lallemand, and D. d’Humières. Consistent initial conditions for lattice Boltzmann simulations. *Comput. Fluids*, 35:855–862, 2006.
- E. Michaelides. *Particles, bubbles & drops: their motion, heat and mass transfer*. World Scientific, 2006.
- A. Mussa, P. Asinari, and L.-S. Luo. Lattice Boltzmann simulations of 2D laminar flows past two tandem cylinders. *J. Com. Phys.*, 228:983–999, 2009.
- M. Ohta, S. Yamaguchi, Y. Yoshida, and M. Sussman. The sensitivity of drop motion due to the density and viscosity ratio. *Phys. Fluids*, 22:072102, 2010.
- S. Osher and J. A. Sethian. Fronts propagating with curvature dependent speed: algorithms based on Hamilton-Jacobi formulations. *J. Comp. Phys.*, 79:12–49, 1988.
- O. Penrose and P. C. Fife. Thermodynamically consistent models of phase-field type for the kinetics of phase transitions. *Physica D*, 43:44–62, 1990.
- J. Petera and L. R. Weatherley. Modelling of mass transfer from falling droplets. *Chem. Eng. Sci.*, 56:4929–4947, 2001.
- C. M. Pooley and K. Furtado. Eliminating spurious velocities in the free-energy lattice Boltzmann method. *Phys. Rev. E*, 77:046702, 2008.
- Y. Y. Renardy, M. Renardy, and V. Cristini. A new volume-of-fluid formulation for surfactants and simulations of drop deformation under shear at a low viscosity ratio. *Eur. J. Mech. B/Fluids*, 21:49–59, 2002.
- H. Rusche. *Computational fluid dynamics of dispersed two-phase Flows at high phase fractions*. PhD thesis, Imperial College of Science, Technology & Medicine, 2002.
- X. Shan and H. Chen. Lattice Boltzmann model for simulating flows with multiple phases and components. *Phys. Rev. E*, 47:1815–1819, 1993.

- R.G.M. van der Sman and S. van der Graaf. Emulsion droplet deformation and breakup with Lattice Boltzmann model. *Comput. Phys. Commun.*, 178:492–504, 2008.
- T. J. Spencer, I. Halliday, and C. M. Care. A local lattice Boltzmann method for multiple immiscible fluids and dense suspensions of drops. *Phil. Trans. R. Soc. A*, 369:2255–2263, 2011.
- J. R. Strom and R. C. Kintner. Wall effect for the fall of single drops. *AIChE J.*, 4: 153–158, 1958.
- M. Sussman, P. Smereka, and S. Osher. A level set approach for computing solutions to incompressible two-phase flow. *J. Comp. Phys.*, 114:146–159, 1994.
- M. R. Swift, E. Orlandini, W. R. Osborn, and J. M. Yeomans. Lattice Boltzmann simulations of liquid-gas and binary fluid systems. *Phys. Rev. E*, 54:5041–5052, 1996.
- G. Thorsen, R. M. Stordalen, and S. G. Terjesen. On the terminal velocity of circulating and oscillating liquid drops. *Chem. Eng. Sci.*, 23:413–426, 1968.
- M. F. Tome and S. McKee. GENSMAC: a computational marker and cell methods for free surface flows in general domains. *J. Comp. Phys.*, 110:171–186, 1994.
- R.E. Treybal. *Liquid extraction*. McGraw-Hill book company, inc., 1951.
- G. Tryggvason, B. Bunner, A. Esmaeeli, D. Juric, N. Al-Rawahi, W. Tauber, J. Han, S. Nas, and Y.-J. Jan. A front-tracking method for the computations of multi-phase flow. *J. Comp. Phys.*, 169:708–759, 2001.
- S. O. Unverdi and G. Tryggvason. A front-tracking method for viscous, incompressible, multi-fluid flows. *J. Comp. Phys.*, 100:25–37, 1992.
- R.G.M. Van der Sman. Galilean invariant lattice Boltzmann scheme for natural convection on square and rectangular lattices. *Phys. Rev. E*, 74:026705, 2006.

- T. Watanabe and K. Ebihara. Numerical simulation of coalescence and breakup of rising droplets. *Comput. Fluids*, 32:823–834, 2003.
- M. Wegener, T. Eppinger, K. Bäumlner, M. Kraume, A.R. Paschedag, and E. Bansch. Transient rise velocity and mass transfer of a single drop with interfacial instabilities – numerical investigations. *Chem. Eng. Sci.*, 64:4835–4845, 2009.
- M. Wegener, M. Kraume, and A. R. Paschedag. Terminal and transient drop rise velocity of single toluene droplets in water. *AIChE J.*, 56:2–10, 2010.
- P. Yue, J. J. Feng, C. Liu, and J. Shen. A diffuse-interface method for simulating two-phase flows of complex fluids. *J. Fluid Mech.*, 515:293–317, 2004.

Chapter 3

Lattice Boltzmann simulations of drop deformation and breakup in shear flow¹

3.1 Introduction

When drops of one liquid dispersed in another immiscible liquid are subjected to shear flow, they start to deform. If the local shear rate is sufficiently large, the drops might break up into fragments. The study of the dynamics and mechanisms of drop breakup in shear flow is of fundamental importance in dispersion science and mixing processes. Experimental and theoretical investigations in this area focus on analyzing how strong the flow should be to break the drop, what the necessary energy input is to create the required intensity of the flow, and what the resulting drop size distribution (DSD) and rheology of the mixture are (Rallison, 1984). The results obtained in such studies can be applied to the formation of dispersion and emulsions and in particular the design of efficient mixing devices (Rallison, 1984). The application of shear to a premixed emulsion of various drop sizes is a technique for the production of monodisperse droplets (Cristini and Renardy, 2006).

Stirred tank reactors are widely used to obtain liquid-liquid dispersion under turbulent flow conditions. Turbulent flows contain a spectrum of eddies of different size, intensity, and lifetime (Pope, 2000). Drops continuously interact with these

¹A version of this chapter has been published. A.E. Komrakova, Orest Shardt, D. Eskin, J.J. Derksen. *IJMF* 59(2014) 24-43

eddies. Large eddies convect small droplets with little deformation. When the droplet size is comparable to the eddy size, the drop can be significantly deformed and subsequently broken. Even though the randomness of turbulent flow implies complex drop/eddy interactions, simpler interactions can be identified. For example, a drop in a simple shear flow represents drop interaction with two co-rotating eddies in turbulent flow. The investigation of drop behavior in simple shear flow is more reproducible both experimentally and numerically than behavior in turbulent flow. The results obtained in such studies are helpful when it comes to engineering applications. To demonstrate that, consider a water-based turbulently agitated liquid-liquid system. Let the size of the drop be comparable to the Kolmogorov length scale. The kinematic viscosity of the continuous phase is of the order of $\nu = 10^{-6} \text{ m}^2/\text{s}$. The local energy dissipation rate in the impeller region (Davies, 1987) may be up to $\varepsilon = 100 \text{ W/kg}$. Based on these parameters the Kolmogorov time scale is $\tau_K = \sqrt{\nu/\varepsilon} = 10^{-4} \text{ s}$. Suppose the resulting distribution of drop radii is in the range $a = (1 - 100) \mu\text{m}$. Assume that turbulent eddies interacting with the drop create a shear rate of the order of $\dot{\gamma} = 1/\tau_K$. Then the range of drop Reynolds number defined as $\text{Re} = \dot{\gamma}a^2/\nu$ is from 0.01 to 100. This implies that even in fully-developed turbulence, drops experience interactions with eddies at low to moderate Reynolds numbers. Therefore, a study of binary systems in simple shear flow has direct relevance to complex turbulently flowing systems. One can, for example, check if the local energy dissipation rate is high enough to break drops of certain sizes and eventually obtain liquid-liquid dispersion with desired characteristics.

Starting with experiments performed by Taylor (1932, 1934), a wide range of studies has been carried out on drop deformation and breakup. These studies have been reviewed by Rallison (1984), Stone (1994), and Cristini and Renardy (2006). The “retractive end pinching” breakup mechanism was outlined by Bentley and Leal (1986). Marks (1998) investigated “elongative end pinching” by applying a strong shear to a single drop. Recent experiments have been performed by Zhao (2007) where a dilute emulsion was subjected to a simple shear flow. A map of drop breakup mechanisms in simple shear flow as a function of viscosity ratio and capillary number was presented.

A viscous drop under shear flow has also been intensively investigated by means of numerical simulations. Most of the numerical studies have been performed with the boundary integral method (Cristini et al., 2003; Janssen and Anderson, 2007; Kennedy et al., 1994; Kwak and Pozrikidis, 1998). The method has been successfully applied for drop deformation studies. However, the implementation of the boundary integral method for drop breakup and coalescence poses a major obstacle because it is very difficult to handle merging and folding interfaces: the interface points should be reconstructed, which requires significant logical programming and results in computational overhead (Li et al., 2000). The mathematical implication of the boundary integral method such as singularity of the free-space Green's kernels is discussed by Pozrikidis (1992). A way to overcome this issue is suggested by Bazhlekov et al. (2004): a higher accuracy in the vicinity of the singular point is gained, however, the performance is about an order of magnitude slower compared to a standard surface integration. An alternative numerical technique widely used to investigate drop breakup is the volume-of-fluid (VOF) method. Numerical simulation of breakup of a viscous drop in simple shear flow was carried out by Li et al. (2000). The same technique has been applied by Renardy and Cristini (2001a), Renardy et al. (2002), Khismatullin et al. (2003), Cristini and Renardy (2006). The topological changes of the interface are treated more naturally compared to the boundary integral method. The VOF method has been generalized to three-dimensional cases. However, the reconstruction of the interface requires significant computational effort that increases with the number of drops involved.

A droplet in a quiescent fluid was investigated by Van der Sman and Van der Graaf (2008) using a free energy lattice Boltzmann equation (LBE) method. The authors further analyzed the numerical criteria for a correct description of emulsions and applied the model to study drop deformation and breakup. All simulated cases were two-dimensional.

Three-dimensional numerical simulations of the classical Taylor experiment on droplet deformation in a simple shear flow have been performed by Xi and Duncan (1999). The authors applied the lattice Boltzmann method in conjunction with the interface force model of Shan and Chen (1993). Good agreement with theoretical

predictions was demonstrated for small deformations. The ability of the method to capture larger deformations and breakup events was also shown.

In the present study, the free energy lattice Boltzmann method originally proposed by Swift et al. (1996) is adopted to perform three-dimensional simulations of a single liquid drop suspended in another liquid under simple shear flow. The goal of the study is to check the capability of the method to capture the physics of drop deformation and breakup in a wide range of flow conditions: starting from near Stokes flow up to drop Reynolds numbers of 50 where inertia plays a significant role. Also the ability of the method to handle liquids with different viscosities is tested.

Diffuse interface numerical techniques require an explicit specification of the interface thickness which essentially is a numerical artifact. It is necessary to examine how this impacts the simulations, what parameters determine this additional degree of freedom, and what values of these parameters should be set for physically realistic results. In addition, it is important to outline the resolution that is sufficient to capture the physics of drop breakup while keeping a reasonable simulation time. To validate the numerical approach, its results are compared to existing experimental results and findings of numerical simulations using other methods. The present study can be considered as a development towards a numerical tool to investigate the behavior of drops in shear flow and as a verification and validation step for further applications in more complex flows. For instance, the developed code would be extended to perform Direct Numerical Simulations (DNS) of turbulent dispersion formation with hundreds of breaking and merging droplets.

The rest of the paper is organized as follows. The problem statement is outlined in Section 3.2. Section 3.3 contains the details of the numerical technique. The results of simulations are presented in Section 3.4. First, the choice of the numerical parameters that determine drop behavior in shear flow is discussed in Section 3.4.1, with additional details in A – 2. Drop deformation and breakup in Stokes flow is presented in Section 3.4.2, the influence of inertia on drop deformation is shown in Section 3.4.3, and Section 3.4.4 presents the joint influence of viscosity ratio and inertia on drop deformation and breakup scenarios. Finally, conclusions are drawn

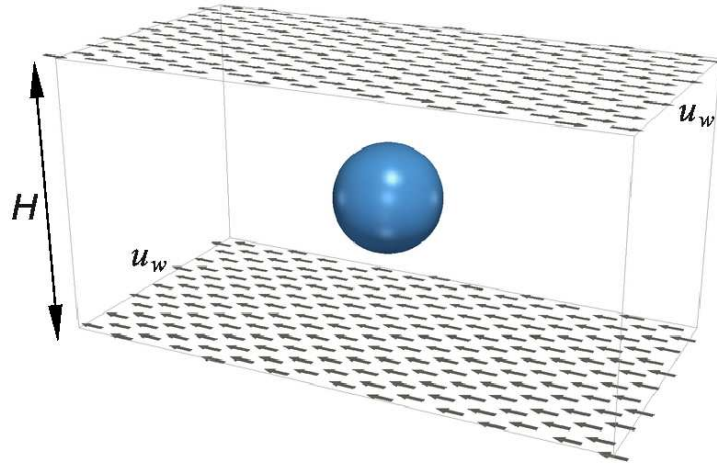


Figure 3.1: Single drop under simple shear flow

in Section 3.5.

3.2 Problem statement

A liquid drop of dynamic viscosity μ_d is suspended in another liquid of viscosity μ_c . The ratio of drop viscosity to surrounding liquid viscosity is denoted as $\lambda = \mu_d/\mu_c$. The interfacial tension between the liquids is σ . The liquids are of equal density ρ . At time $t = 0$, the drop is a sphere with radius a . The entire system undergoes simple shear flow between two parallel plates located a distance H apart (Fig. 3.1). The two plates translate in opposite directions with velocity u_w so that the shear rate is $\dot{\gamma} = 2u_w/H$.

Drop behavior in simple shear flow is determined by three dimensionless numbers which are the Reynolds number Re , the capillary number Ca , and the viscosity ratio λ :

$$Re = \frac{\dot{\gamma}a^2}{\nu} \quad Ca = \frac{a\dot{\gamma}\mu_c}{\sigma} \quad \lambda = \frac{\mu_d}{\mu_c} \quad (3.1)$$

In the case of vanishingly small Re (Stokes flow) only viscous and capillary forces determine the drop behavior. Being deformed under shear flow, the drop inclines in the direction of the flow, away from the axis of elongation which is at 45 degrees to the flow direction (Khismatullin et al., 2003). It was shown by Khismatullin et al. (2003) and is demonstrated later in this paper that the addition

of inertia changes the drop deformation and also the breakup process. The range of Reynolds numbers considered here is from 0.0625 to 50.

The ratio of viscous and capillary forces is determined by the capillary number. For each viscosity ratio λ there is a critical capillary number, Ca_c , above which the drop eventually breaks. For capillary numbers below the critical value, a steady drop shape exists. When the drop is sheared in the Stokes flow regime at $Ca \sim Ca_c$ it breaks up by the “end pinching” mechanism into daughter drops separated by smaller satellite and subsatellite droplets (Marks, 1998; Zhao, 2007). In this study, simulations close to Stokes flow conditions are performed for capillary numbers in the range of 0.1 – 0.42. This range of Ca includes drop deformation and breakup.

Finally, drop deformation and breakup depends on the viscosity ratio. When the drop is very viscous ($\lambda \gg 1$), the rate of elongation in the drop is small compared to the rate of circulation in the drop, and the drop cannot break (Cristini and Renardy, 2006). The critical viscosity ratio λ_c beyond which the drop does not break is around 3.0 for Stokes flow (Cristini and Renardy, 2006; Khismatullin et al., 2003). The critical viscosity ratio increases with increasing Reynolds number (Khismatullin et al., 2003). The viscosity ratios λ considered in this paper are 1, 2, and 3.

3.3 Numerical method

In the present study, a diffuse interface method is used to simulate the behavior of a drop in shear flow. In diffuse interface (or phase field) methods (Ding et al., 2007; Jacqmin, 1999; Magaletti et al., 2013; Yue et al., 2004) the sharp interface between fluids is represented by a thin transition region with finite thickness where fluids may mix. At any given time, the state of the system is described by the order parameter of the phase field ϕ which is the relative concentration of the two components (Badalassi et al., 2003; Cahn and Hilliard, 1958; Penrose and Fife, 1990). To simulate the fluid dynamics of a binary mixture of fluids, the continuity and momentum equations are used in conjunction with Cahn Hilliard convection-diffusion equation for the order parameter (Bray, 1994). Thus, the evolution of density, velocity

and order parameter are governed by the continuity, momentum, and convection-diffusion equations (De Groot and Mazur, 1984; Kendon et al., 2001), respectively:

$$\partial_t \rho + \partial_\alpha (\rho u_\alpha) = 0 \quad (3.2a)$$

$$\partial_t (\rho u_\alpha) + \partial_\beta (\rho u_\alpha u_\beta) = -\partial_\beta P_{\alpha\beta}^{th} + \partial_\beta v (\rho \partial_\alpha u_\beta + \rho \partial_\beta u_\alpha) \quad (3.2b)$$

$$\partial_t \varphi + \partial_\alpha (\varphi u_\alpha) = M \partial_{\beta\beta}^2 \mu \quad (3.2c)$$

where ρ and v are the density and the kinematic viscosity of the mixture, respectively. Here $P_{\alpha\beta}^{th}$ is the ‘thermodynamic’ pressure tensor. It contains two parts (Kendon et al., 2001): an isotropic contribution $P \delta_{\alpha\beta}$ that represents the ideal gas pressure and the ‘chemical’ pressure tensor $P_{\alpha\beta}^{chem}$. The chemical potential in equation (3.2c) is: $\mu(\varphi) = A\varphi - A\varphi^3 - \kappa \partial_{\alpha\alpha}^2 \varphi$. Here, $A < 0$ is a parameter of the free energy model; κ is a parameter related to the surface tension and interface thickness.

Swift et al. (1996) developed a lattice Boltzmann approach, known as the free energy model, to solve the system (3.2). Exactly this method is adopted in the present study. Two particle distribution functions are utilized: one function $f(\mathbf{r}, t)$ is used to solve the continuity (3.2a) and Navier-Stokes (3.2b) equations and the second one $g(\mathbf{r}, t)$ is used for the convection-diffusion equation (3.2c). The distribution functions evolve by a time step Δt . All simulations have been performed using a single relaxation time collision operator (Bhatnagar-Gross-Krook (BGK) model (Bhatnagar et al., 1954)). The discrete lattice Boltzmann equations have the following form:

$$\begin{aligned} f_q(r_\alpha + c_{\alpha q} \Delta t, t + \Delta t) - f_q(r_\alpha, t) &= -\frac{f_q - f_q^{eq}}{\tau_f}, \\ g_q(r_\alpha + c_{\alpha q} \Delta t, t + \Delta t) - g_q(r_\alpha, t) &= -\frac{g_q - g_q^{eq}}{\tau_g}, \end{aligned} \quad (3.3)$$

where the index q stands for the number of the discrete velocity directions; the index α stands for the Cartesian directions x , y and z ; f_q^{eq} , g_q^{eq} are discretized Maxwell-Boltzmann distributions (or equilibrium distributions); $c_{\alpha q}$ denotes the discrete velocity set and τ_f , τ_g are dimensionless relaxation parameters. The D3Q19 lattice

is adopted here where $Q = 19$ is the number of velocity directions. In this lattice arrangement, each site communicates with its six nearest and twelve diagonal neighbors. The lattice Boltzmann method operates in dimensionless lattice units (lattice space, time step, and lattice density for the length, time and density units, respectively). For the method described here, only uniform cubic lattices can be used; the mesh step Δx is taken as unity, as is the time step Δt . The discrete velocity set is defined as follows:

$$\begin{pmatrix} c_x \\ c_y \\ c_z \end{pmatrix} = \begin{bmatrix} 0 & c & -c & 0 & 0 & 0 & 0 & c & -c & c & -c & 0 & 0 & 0 & 0 & c & -c & c & -c \\ 0 & 0 & 0 & c & -c & 0 & 0 & c & c & -c & -c & c & -c & c & -c & 0 & 0 & 0 & 0 \\ 0 & 0 & 0 & 0 & 0 & c & -c & 0 & 0 & 0 & 0 & c & c & -c & -c & c & c & -c & -c \end{bmatrix}$$

where $c = \Delta x / \Delta t$ is the lattice speed.

The particle distribution functions are defined such that the following summations over all directions q at each single lattice point give the local density of the fluid, the local fluid momentum and the local order parameter, respectively:

$$\sum_q f_q = \rho \quad \sum_q c_{\alpha q} f_q = \rho u_\alpha \quad \sum_q g_q = \varphi \quad (3.4)$$

The equilibrium distributions (Kusumaatmaja, 2008) f_q^{eq} , g_q^{eq} for populations $1 \leq q \leq (Q - 1)$ are calculated using the following relations:

$$\begin{aligned} f_q^{\text{eq}} &= \frac{w_q}{c^2} \left(p_0 - \kappa \varphi (\partial_{xx}^2 \varphi + \partial_{yy}^2 \varphi + \partial_{zz}^2 \varphi) + c_{\alpha q} \rho u_\alpha + \frac{3}{2c^2} \left[c_{\alpha q} c_{\beta q} - \frac{c^2}{3} \delta_{\alpha\beta} \right] \rho u_\alpha u_\beta \right) + \\ &\quad \frac{\kappa}{c^2} \left(w_q^{xx} \partial_x \varphi \partial_x \varphi + w_q^{yy} \partial_y \varphi \partial_y \varphi + w_q^{zz} \partial_z \varphi \partial_z \varphi + w_q^{xy} \partial_x \varphi \partial_y \varphi + w_q^{xz} \partial_x \varphi \partial_z \varphi + w_q^{yz} \partial_y \varphi \partial_z \varphi \right) \\ g_q^{\text{eq}} &= \frac{w_q}{c^2} \left(\Gamma \mu + c_{\alpha q} \rho u_\alpha + \frac{3}{2c^2} \left[c_{\alpha q} c_{\beta q} - \frac{c^2}{3} \delta_{\alpha\beta} \right] \varphi u_\alpha u_\beta \right) \end{aligned} \quad (3.5)$$

while the distributions for $q = 0$ are given by:

$$f_0^{\text{eq}} = \rho - \sum_{q=1}^{Q-1} f_q^{\text{eq}} \quad g_0^{\text{eq}} = \varphi - \sum_{q=1}^{Q-1} g_q^{\text{eq}} \quad (3.6)$$

And the weights (Kusumaatmaja, 2008) are:

$$\begin{aligned}
w_{1-6} &= \frac{1}{6}, & w_{7-18} &= \frac{1}{12}, \\
w_{1-2}^{xx} &= w_{3-4}^{yy} = w_{5-6}^{zz} = \frac{5}{12}, & w_{3-6}^{xx} &= w_{1-2,5-6}^{yy} = w_{1-4}^{zz} = -\frac{1}{3}, \\
w_{7-10}^{xx} &= w_{15-18}^{xx} = w_{7-14}^{yy} = w_{11-18}^{zz} = -\frac{1}{24}, \\
w_{11-14}^{xx} &= w_{15-18}^{yy} = w_{7-10}^{zz} = \frac{1}{12}, \\
w_{1-6}^{xy} &= w_{1-6}^{yz} = w_{1-6}^{zx} = 0, & w_{7,10}^{xy} &= w_{11,14}^{yz} = w_{15,18}^{zx} = \frac{1}{4}, \\
w_{8-9}^{xy} &= w_{12-13}^{yz} = w_{16-17}^{zx} = -\frac{1}{4}, & w_{11-18}^{xy} &= w_{7-10}^{yz} = w_{7-14}^{zx} = 0.
\end{aligned} \tag{3.7}$$

The bulk pressure in equation (3.5) is defined as $p_0 = c_s^2 \rho + \frac{A}{2} \varphi^2 - \frac{3A}{4} \varphi^4$. Here $c_s^2 = 1/3$ is the speed of sound in lattice units.

The mobility M , the coefficient of mobility Γ and the relaxation parameter τ_g are connected by the following relation:

$$M = \Delta t \Gamma \left(\tau_g - \frac{1}{2} \right) \tag{3.8}$$

i.e. the parameter Γ determines the order parameter mobility M .

The liquids have different kinematic viscosity. To take this into account, the kinematic viscosity of the mixture ν is set to be a function of the order parameter φ :

$$\nu(\varphi) = \nu_c \frac{\varphi_0 - \varphi}{2\varphi_0} + \nu_d \frac{\varphi_0 + \varphi}{2\varphi_0} \tag{3.9}$$

where ν_c and ν_d are the kinematic viscosities of continuous and dispersed phases, respectively. The relaxation parameter for f_q is defined using the kinematic viscosity of the mixture:

$$\tau_f(\varphi) = \frac{\nu(\varphi)}{c_s^2 \Delta t} + \frac{1}{2} \tag{3.10}$$

For a planar interface, an analytical solution (Van der Sman and Van der Graaf, 2008) gives the φ profile $\varphi(x) = \varphi_0 \tanh(x/\xi)$. Here, $\varphi = \pm \varphi_0 = \pm 1$ is the value of order parameter in the bulk phase at either side of the interface. The thickness of the diffuse interface ξ is equal to

$$\xi = \left(\frac{2\kappa}{-A} \right)^{1/2}. \tag{3.11}$$

The surface tension σ follows from:

$$\sigma = \frac{4}{3} \kappa \frac{\varphi_0^2}{\xi}. \quad (3.12)$$

To determine the equilibrium distributions (3.5), the spatial gradients of φ have to be calculated. The stencils for gradients and Laplacian calculations adopted in this study are (Kusumaatmaja, 2008):

$$\partial_x = \frac{1}{12\Delta x} \left[\begin{pmatrix} 0 & 0 & 0 \\ -1 & 0 & 1 \\ 0 & 0 & 0 \end{pmatrix}, \begin{pmatrix} -1 & 0 & 1 \\ -2 & 0 & 2 \\ -1 & 0 & 1 \end{pmatrix}, \begin{pmatrix} 0 & 0 & 0 \\ -1 & 0 & 1 \\ 0 & 0 & 0 \end{pmatrix} \right] \quad (3.13)$$

$$\nabla^2 = \frac{1}{6\Delta x^2} \left[\begin{pmatrix} 0 & 1 & 0 \\ 1 & 2 & 1 \\ 0 & 1 & 0 \end{pmatrix}, \begin{pmatrix} 1 & 2 & 1 \\ 2 & -24 & 2 \\ 1 & 2 & 1 \end{pmatrix}, \begin{pmatrix} 0 & 1 & 0 \\ 1 & 2 & 1 \\ 0 & 1 & 0 \end{pmatrix} \right] \quad (3.14)$$

where the left, middle and right matrices show slices of the stencil when $z = \Delta x$, 0 and $-\Delta x$, respectively.

The discretized equations (3.3) are solved in two steps:

$$\begin{aligned} \text{Collision step: } f'_q(r_\alpha, t) &= f_q(r_\alpha, t) - \frac{1}{\tau_f} [f_q - f_q^{\text{eq}}] \\ g'_q(r_\alpha, t) &= g_q(r_\alpha, t) - \frac{1}{\tau_g} [g_q - g_q^{\text{eq}}] \end{aligned} \quad (3.15)$$

$$\begin{aligned} \text{Streaming step: } f_q(r_\alpha + c_{\alpha q} \Delta t, t + \Delta t) &= f'_q(r_\alpha, t) \\ g_q(r_\alpha + c_{\alpha q} \Delta t, t + \Delta t) &= g'_q(r_\alpha, t) \end{aligned} \quad (3.16)$$

To complete the mathematical description, boundary conditions have to be specified. The simulation domain with boundary conditions is depicted in Fig. 3.2. The no-slip condition is imposed on the bottom $y = 0$ and top $y = H$ plates for the f_q distribution and a Dirichlet condition of $\varphi = -\varphi_0$ for the g_q distribution. The constant velocities of the walls are applied on those planes using the procedure proposed by Mussa et al. (2009). The rest of the boundary conditions apply to both f_q and g_q . Periodic conditions are imposed on the $x = 0$ and $x = L$ planes. Because of the symmetry of the problem, only half of the drop has been considered. Such consideration requires symmetry conditions (Ahmed and Hecht, 2009) of the side planes $z = 0$ and $z = W$. The initial condition at time $t = 0$ is that the drop has a spherical shape and the velocity field is zero throughout the domain.

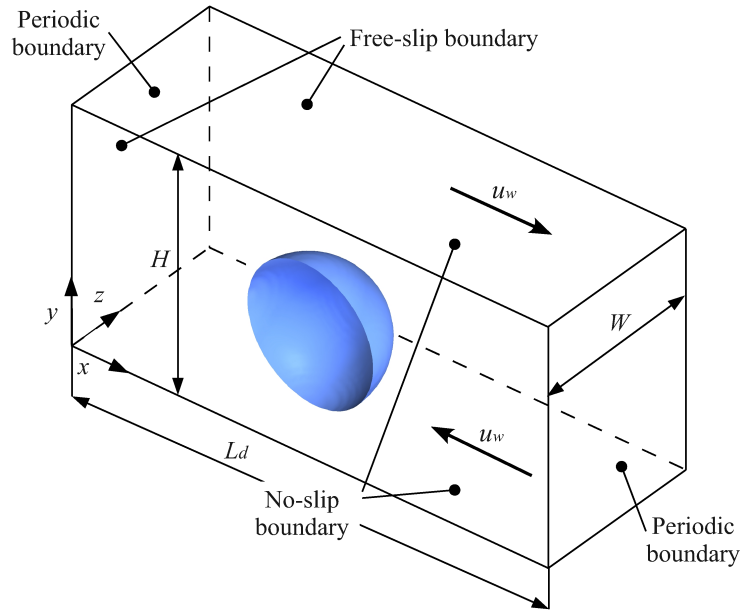


Figure 3.2: Simulation domain with boundary conditions: $x = 0$ and $x = L$ are periodic boundaries; $y = 0$ and $y = H$ are no-slip walls moving with constant velocity u_w ; $z = 0$ and $z = W$ are the symmetry planes. At $t = 0$ the drop has a spherical shape. Due to the symmetry of the problem only half of the drop has been simulated

3.4 Simulations of a single drop under simple shear flow

A computer code for three-dimensional simulations is developed using Fortran 90 in both serial and parallel versions. The parallel code uses domain decomposition and MPI (Message Passing Interface). The simulation domain is decomposed into slabs in the x direction, one for each CPU. The number of CPUs used depends on the domain size, starting from one for low resolution drops and up to eight CPUs for the highest resolution drops. Depending on the drop size, the duration of the simulations ranges from several minutes for the drops with lower resolution to 2 – 3 weeks for the drops with the highest resolution.

A simulation code for graphics processing units (GPUs) is used to facilitate convergence studies with large droplet radii (32 to 64 lattice nodes). The high memory bandwidth and parallel processing capabilities of GPUs allow fast LBE simulations due to the highly-local nature of free energy LBE calculations: only data from adjacent nodes is required to update each node in the domain. The simulations

are performed on nine NVIDIA Tesla M2070 GPUs, with three GPUs installed on each of three computational nodes. Communication between the three GPUs on one computational node occurs over system buses, while communication between computational nodes occurs over an InfiniBand interconnect and was implemented with an MPI library. The domain is split evenly among the nine GPUs along planes parallel to the sheared wall. A rotational symmetry boundary condition through the middle of the domain ($y = H/2$ in Fig. 3.2) is used to further reduce the computational expense. With this boundary condition, the domain below $y = H/2$ is not simulated. Since the GPU code was initially developed to study a different problem, binary droplet collisions and coalescence (Shardt et al., 2013), the boundary conditions in the GPU code differ subtly from those in the CPU code. The shear velocity at $y = H$ is imposed using the method of Ladd (1994). A symmetry condition is used for the phase field φ at $y = H$. The other symmetry and periodic boundary conditions are the same as in the code for CPUs. Two simulations at the same conditions, with one running on GPUs and the other on CPUs, were compared. As described in A – 3, the difference in the drop elongation L/a (see definition below) is 0.15%. The difference in boundary conditions is therefore small, and the GPU and CPU simulations may be used to study the same problem. Processing speeds for the simulations with droplet radii between 32 and 64 lattice units are 136 to 235 million lattice node updates per second (Mlups), compared to 2 Mlups on 8 CPU cores in the CPU-based simulation. The performance of both GPU- and CPU-based simulations is affected by other jobs running on the clusters, causing fluctuations in the processing speeds.

3.4.1 Choice of numerical parameters

A set of three physical dimensionless numbers (the Reynolds number Re , the capillary number Ca and the fluids viscosity ratio λ , see definitions (3.1)) fully determines drop behavior under simple shear flow. The lattice Boltzmann free energy method refers to the class of diffuse interface methods that requires an explicit specification of the interface thickness ξ and related numerical parameters (κ , A , M , Γ). Two additional dimensionless numbers need to be introduced to characterize these

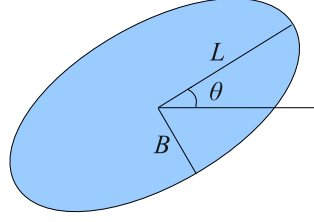


Figure 3.3: Drop elongation L , deformation $D = (L - B)/(L + B)$ and orientation angle θ measurements

degrees of freedom (Van der Sman and Van der Graaf, 2008): the interface Peclet number that relates the convection time scale to the interface diffusion time scale

$$Pe = \frac{\dot{\gamma}a\xi}{MA} \quad (3.17)$$

and the Cahn number which is the ratio between interface thickness and drop radius

$$Ch = \frac{\xi}{a} \quad (3.18)$$

Thus, the behavior of the same drop in simple shear flow in numerical space is determined by five dimensionless numbers, three of which are physical (Re , Ca , λ) and two numerical (Pe , Ch). It is necessary to investigate the choice of these numerical numbers to capture the drop behavior at given physical dimensionless numbers. The verification of the numerical technique involves an investigation of the influence of the Peclet and Cahn numbers on accuracy and stability. Subsequently the technique is validated by comparison with available literature data.

When the sheared drop evolves to a steady shape under Stokes flow conditions, two parameters are used to measure the deformation attained by the drop. The first parameter is the Taylor deformation parameter (Taylor, 1932, 1934) $D = (L - B)/(L + B)$, where L and B are the half-length and half-breadth of the drop (see Fig. 3.3), respectively. When the steady shape of the drop is not ellipsoidal any more (which is the case for shear with higher Re) then the ratio of maximum elongation to initial undeformed drop radius L/a is used to characterize the deformation. The second parameter is the orientation angle θ of the drop as defined in Fig. 3.3.

The influence of the proximity of walls was examined first. Three simulations of a drop with initial radius of $a = 20$ [lu] at $Re = 1$, $Ca = 0.27$, $\lambda = 1$, $Pe = 1$ and

Table 3.1: Wall proximity influence (H is a distance between the moving plates). Elongation L/a and orientation angle θ of a drop with undeformed radius $a = 20$ [lu] at $Ca = 0.27$, $Re = 1$, $\lambda = 1$, $Pe = 1$ and $Ch = 0.057$.

	$H = 4a$	$H = 8a$	$H = 16a$
L/a (LBE)	1.93	1.87	1.82
θ (LBE)	18.88	22.77	23.12
L/a (VOF) (Renardy and Cristini, 2001b)		1.8	
θ (VOF) (Renardy and Cristini, 2001b)		25	

$Ch = 0.057$ were carried out in domains of $8a \times 4a \times 2a$, $8a \times 8a \times 2a$ and $8a \times 12a \times 2a$. According to the VOF results presented by Renardy and Cristini (2001b) this capillary number (for given Re and λ) is right below the Ca_c which means that a steady shape of the drop is attained. The results of the present simulations together with the reference VOF results are presented in Table 3.1. The smallest distance between the plates $H = 4a$ results in higher deformation of the drop and significantly smaller inclination angle. The effect of H reduces when H is increased. The deviation between results obtained in the cases when $H = 8a$ and $16a$ is less than 3%. Simulation time increases with domain size. Further benchmark cases used domains of $8a \times 8a \times 2a$.

Three benchmark cases have been performed characterized by the following dimensionless numbers, respectively: $Re = 1$ and $Ca = 0.27$, $Re = 0.0625$ and $Ca = 0.1$, $Re = 10$ and $Ca = 0.15$. The viscosity ratio for all cases was $\lambda = 1$.

Consider the first case: $Ca = 0.27$, $Re = 1$, $\lambda = 1$. The relaxation times for both distribution functions are set to $\tau_f = \tau_g = 1$. The reference VOF results are presented in Table 3.1.

Mesh refinement was performed at different Peclet and Cahn numbers. The full set of dimensionless parameters (Re , Ca , λ , Pe and Ch) remained constant when the resolution was increased. The simulated Cahn numbers are $Ch = 0.1136$ and 0.2 , the base-line drop radius is $a = 10$ [lu]. The mesh is refined by factors of $\beta = 1.5$, 2.0 , 2.5 and 3.0 times. The resulting drop radii are 15 , 20 , 25 , and 30 [lu]. Peclet numbers of 1 , 5 and 10 are simulated.

The drop elongation and orientation angle for $Ch = 0.1136$, 0.2 and several

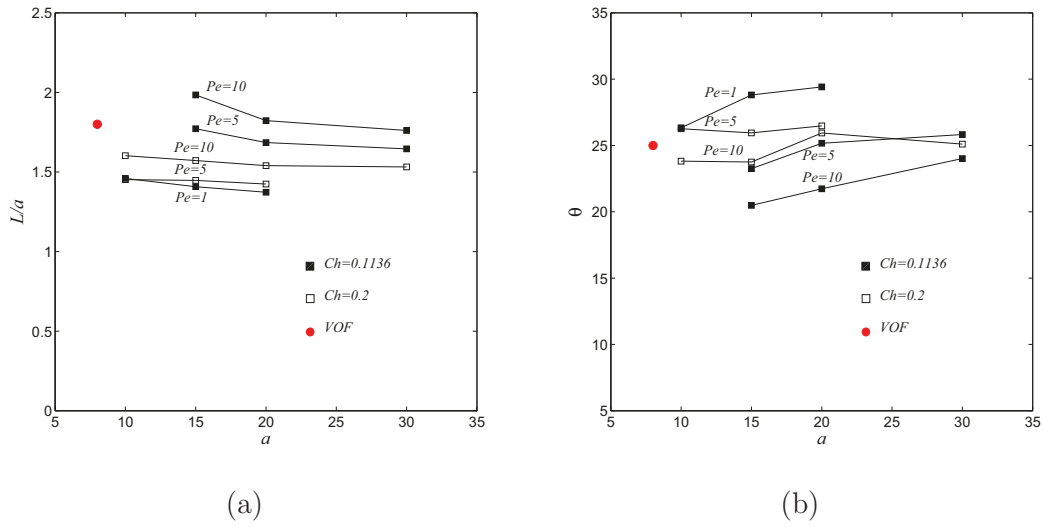


Figure 3.4: Drop deformation results at $Re = 1$, $Ca = 0.27$, $\lambda = 1$ and different Pe and Ch numbers. The L/a ratio (a) and the orientation angle θ (b) as a function of drop radius

Pe are presented in Fig. 3.4 (a) and (b), respectively. For the reference points obtained by Renardy and Cristini (2001b), the initial drop radius spanned eight dimensionless units (grid spacing). When the grid is refined, the L/a tends to reach asymptotic values. At $Ch = 0.1136$ and $Pe = 10$ the deviation of the elongation from the reference data is 2% when $a = 30$ [lu]. The orientation angle is more sensitive and grid convergence is not clear. The θ values scatter within 20% from the reference data. The minimum deviation is 0.4% at $Ch = 0.2$, $Pe = 10$ and $a = 30$ [lu]. A smaller Peclet number results in smaller deformation and larger inclination angle of the drop. At $Pe = 1$ and $Ch = 0.2$ the simulations of drops with radius in the range 10 – 30 [lu] are unstable. When the drop radius exceeds 20 [lu] the simulations are unstable at $Pe = 1$ and 5. The reason for this instability is the high mobility value M . Mobility enters the governing system of equations via the mobility coefficient Γ (see equation (3.2c)) and has an impact on stability of the simulations. For the unstable cases Γ is larger than 15. On the other hand, drops with $a < 15$ [lu] break up at $Pe = 5$ and 10. High Pe means a low mobility M . In order to maintain local equilibrium, the mobility coefficient Γ (and thus mobility M) should be large enough to allow diffusion across the interface on a time scale

faster than fluid motion (Kendon et al., 2001). Thus, when Γ is low then convection dominates over diffusion (which tends to equilibrate the interface) and the droplets break. If a too large mobility value is set (see above), the simulations may become unstable.

To check if the influence of Pe and Ch is not a result of relatively low resolution ($a \leq 30$ [lu]), an additional study with highly resolved drops was carried out using the GPU code. A base-line drop radius of $a = 32$ [lu] is specified. The results are presented in *A – 2 (Benchmark case 1)*. The same trends in the effects of Pe and Ch on the results as with lower resolution are observed. Even with higher mesh resolution Pe and Ch should be chosen with care for every simulation. For instance, the case with $Pe = 1$, $a = 64$ [lu] (the Cahn number $Ch = 0.0625$) is unstable. While the case with $Pe = 1$ and higher drop resolution $a = 75$ [lu] (the Cahn number $Ch = 0.0267$) results in $L/a = 1.79$ and $\theta = 24.92^\circ$ that matches the reference data.

For flows with $Re = 1$, the shear rate is high enough to avoid long computations and a wide range of capillary numbers can be investigated due to κ , A and Γ values that allow stable computations. The Stokes flow regime needs to have very low shear (which implies small time steps and, thus, lengthy computations). It is also more challenging because of the narrow parameter ranges for stable simulations. To obtain capillary numbers in the range of $0.1 - 0.45$, surface tension values in the range $\sigma = 10^{-4} - 10^{-3}$ [lu] are necessary. To fulfill this requirement, κ should also be small ($10^{-4} - 10^{-3}$ [lu]). To get stable simulations, special care should be taken for the choice of Γ and, consequently, the Peclet number. Simulations of drops in shear flow at near Stokes flow at $Ca = 0.1$ and $\lambda = 1$ were performed as the second benchmark case. The specified Reynolds number of $Re = 0.0625$ is the same as was taken by Li et al. (2000) in their simulations by the VOF method. The latter are used as reference data.

The results of the second benchmark case at $Re = 0.0625$, $Ca = 0.1$ and $\lambda = 1$ are presented in *A – 2 (Benchmark case 2)*. The order of magnitude of the Peclet number for the Stokes flow simulations has changed compared to the one at $Re = 1$ considered before. Pe is less than unity now. The reason is a decrease of shear

rates while the rest of the parameters have the same order of magnitude as before. The same influence of Pe on drop deformation is observed. The higher the Peclet number the higher the deformation and the smaller the inclination angle of the drop.

To check the ability of the method to handle higher Reynolds numbers, a third benchmark case was performed. The following physical parameters are specified: $Re = 10$, $Ca = 0.15$ and $\lambda = 1$. The results and analysis are presented in *A – 2 (Benchmark case 3)*. To sum up the most important findings, the influence of Pe and Ch on the result for a fixed drop radius of $a = 30$ lattice units is shown in Fig. 3.5. The data are organized in the following way: the Peclet number increases from left to right, while the Cahn number increases from top to bottom. An increase in Pe results in increased drop deformation for every case: the drop becomes more elongated. The angle of inclination towards the flow direction decreases with the increase in Pe . The increase of interface thickness apparently limits drop deformation and the development of internal circulations; the drop shortens and aligns in a vertical direction. $Re = 10$ is not high enough to clearly see the loss of symmetry over the mid-plane of the drop. Nevertheless, it can be noticed for the case with $Pe = 4$ and $Ch = 0.0379$. The tips of the drop are slightly tilted in the vertical direction. If this deformation is accurately resolved then the maximum elongation of the drop refers to the line that connects these two points. The angle of inclination will be accordingly measured between this line and the horizontal axis. On the other hand, the elongation can be measured based on the mid-plane line. That will give a smaller value of elongation and a smaller angle of inclination. In the present simulations, maximum elongation was measured based on the tips of the drop. This contributes to the deviations from the reference data.

The aim of the benchmark studies is to establish guidelines on how to specify the numerical parameters related to the interface thickness (Pe and Ch) for a given set of physical dimensionless numbers (Re , Ca and λ). The following conclusions are drawn. For every simulation one has to make a choice for drop resolution (fix the drop radius a in lattice units). With a set, the interface thickness ξ has to be specified. In other words, the Cahn number should be chosen. For the present simulations, the drop resolution can be divided into two regions based on the drop

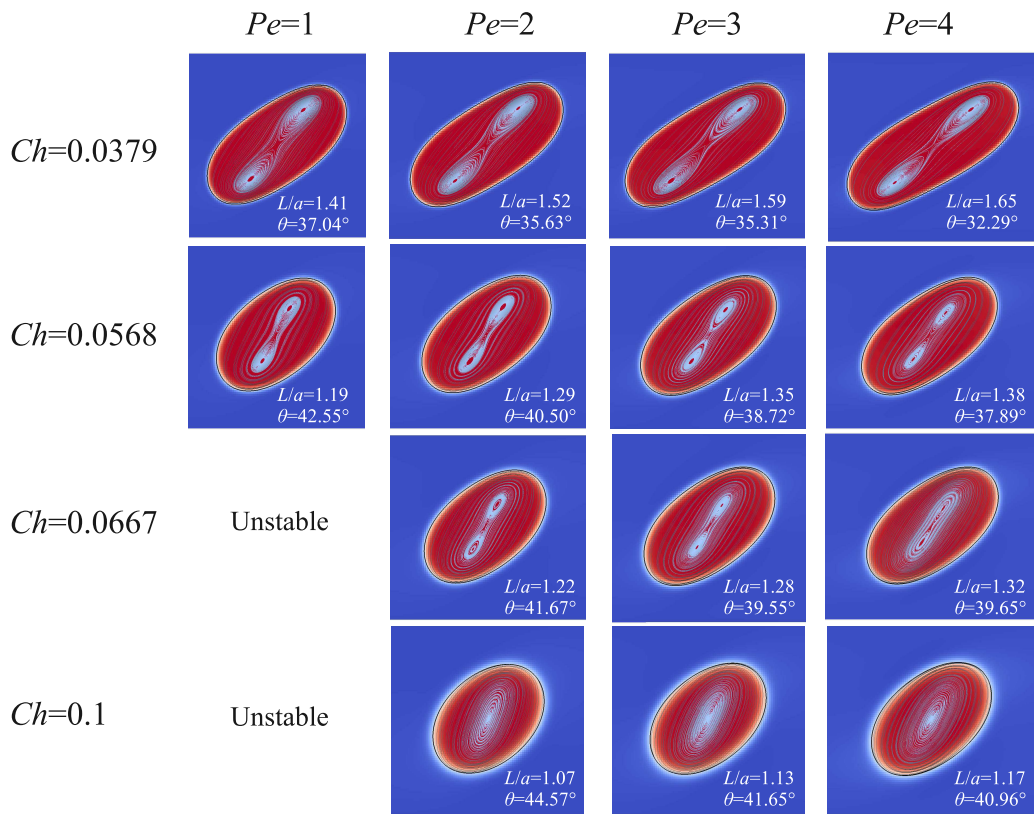


Figure 3.5: Drop shape and streamlines at steady-state for drop with radius $a = 30$ [lu] at $Re = 10$, $Ca = 0.15$, $\lambda = 1$ and different Pe and Ch numbers

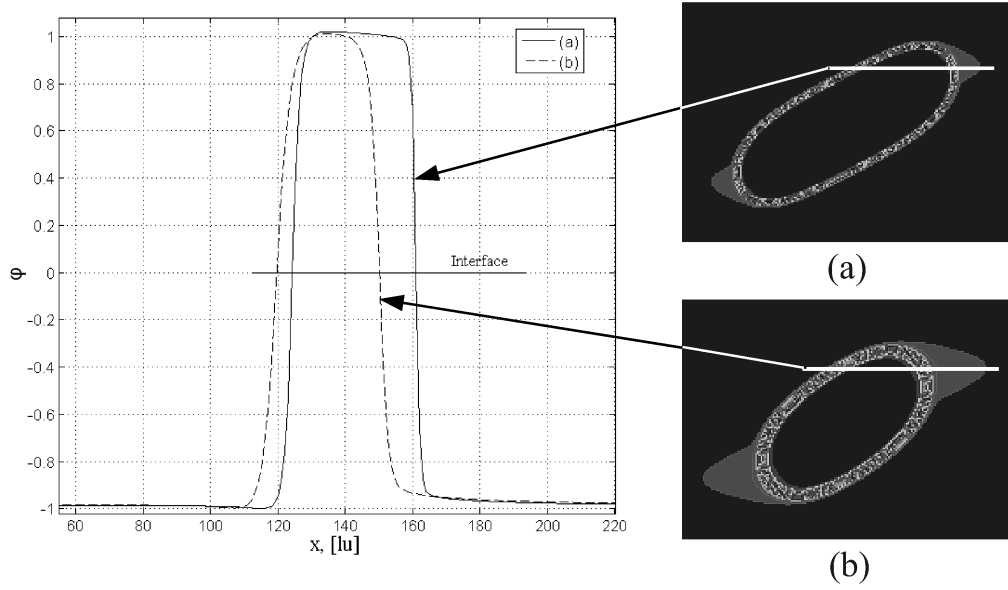


Figure 3.6: Drop shape (φ field) at steady state. The drop radius is $a = 30$ [lu] and $Pe = 3$. (a) $\xi = 1.14$ [lu], $\Gamma = 4.3$; (b) $\xi = 2$ [lu], $\Gamma = 13.3$.

radius: moderately resolved drops with $a \leq 30$ lattice units and highly resolved drops with radius $a > 30$ [lu]. The drop radius of 30 lattice units was chosen because starting from this radius the results are in the mesh independent region (see Fig. 3.4 and A – 2). For the drops of moderate resolution a thinner interface is preferable. In the present study $\xi = 1.14$ [lu] (see Kendon et al. (2001)) was adopted. For the highly resolved drops a thicker interface of two lattice units needs to be used.

Thus, the choice of Ch is related to the resolution. Now the Peclet number should be chosen. This number contains the following parameters: a , ξ , $\dot{\gamma}$, M and A . The first two (a and ξ) are already set. The shear rate $\dot{\gamma}$ is fixed by the Reynolds number. The parameter A is related to ξ and κ by equation (3.11). The interface thickness ξ is specified, while κ is fixed by the capillary number, which means A has been set as well. The only tunable parameter left is the mobility M that enters the governing equations as the mobility coefficient Γ (equation (3.8)). The diffusion over the interface should be faster than the fluid motion. According to Kendon et al. (2001) the mobility coefficient must be high to allow this. When a thicker interface

is used, the residual diffusion contaminates more of the area around the drop. The effect of contamination is shown in Fig. 3.6. The areas inside and outside of the drop near the tips are more contaminated when higher Γ with thicker interface is used (Fig. 3.6(b)): one can see the lighter gray area. To clearly show the difference between these two cases the φ distribution along the horizontal lines is plotted on the graph in Fig. 3.6. The drop edges are sharper in case (a) compared to case (b). This effect decreases when a higher drop resolution is used (because the ratio of the interface thickness and the drop size is now smaller). For this reason the smaller interface thickness is utilized for the lower resolved drops, and a thicker interface for the higher resolution simulations.

Furthermore, the choice of the mobility coefficient (and consequently Pe) has influence on stability. In most of the cases the simulations are stable for Γ in the range 1 – 15. Smaller Γ results in more deformation of the drop which can lead to breakup when a steady shape is expected. On the other hand, too high mobility can cause instability. Based on the simulation results obtained here, the smaller the surface tension value (small κ) the higher Γ is needed.

Thus, the results of the benchmark cases show that the simulations are seemingly unpredictable and dependent on Peclet and Cahn numbers. Does it mean that to obtain a trustworthy physical result one has to perform several verification simulations and figure out Pe and Ch ? To answer this question, different physical systems are further considered. In most of the simulations the Cahn number is fixed to $Ch = 0.0567$. The Peclet number varies from case to case while the mobility coefficient Γ is set equal to 8 or 10. A wide range of Reynolds and capillary numbers and viscosity ratios is examined to cover different physical phenomena. First, drop deformation and breakup in near-Stokes flow are considered at different capillary numbers. Then inertial effects are investigated at higher Reynolds numbers. Finally, the combined influence of inertia and viscosity ratio is investigated. Most of the results are compared to available literature data. Using these simulations, it is shown that even simulations at moderate resolution can be used to study drop deformation in shear.

3.4.2 Stokes flow simulations

To validate the numerical code with existing literature data, near-Stokes flow ($Re = 0.0625$) simulations of a single drop were performed for capillary numbers of $Ca = 0.2, 0.3$ and 0.4 . The initial drop radius is 20 [lu] in a simulation domain of $8a \times 8a \times 2a$. The Cahn number is fixed to $Ch = 0.0567$ and the Peclet numbers are $Pe = 0.2, 0.3$ and 0.41 for each case, respectively.

The drop deformation D and orientation angle θ in steady state as a function of the capillary number Ca along with experimental and numerical results from the literature are depicted in Fig. 3.7 (a) and (b), respectively. Our results agree well with the reference data. However, as discussed in the previous section, the results can be adjusted by variation of the Peclet number (or the diffusion coefficient Γ). Since the reference values of deformation and orientation angles are scattered, it is demonstrated that choosing Γ from the stable interval (1-15) gives the results that match reference data. Fig. 3.8 shows cross sections of the drop steady shapes and velocity fields in the $z = 0$ plane (see Fig. 3.2) for $Ca = 0.1, 0.2, 0.3$ and 0.4 . The larger the capillary number, the stronger the drop deformation and the smaller the inclination angle.

To check the ability of the method to capture the breakup event, the following situation was simulated: $Re = 0.0625$, $Ca = 0.42$ and $\lambda = 1$. Based on experiments and available numerical results the critical capillary number for liquids with equal viscosities in the Stokes regime (Li et al., 2000) is $Ca_c = 0.41$. Thus, for $Ca = 0.42$ breakup is expected. According to a reference VOF result (Li et al., 2000) (see their Fig. 11) five fragments are formed: two daughter drops, one satellite droplet and two sub-satellites. To resolve these fragments a resolution higher than $a = 20$ [lu] is required. The initial drop radius is set to 30 [lu] in a simulation domain of size $12a \times 8a \times 2a$ (the same size as in VOF reference data). The Cahn number of $Ch = 0.0379$ and the Peclet number of $Pe = 0.43$ are specified. The results are presented in Fig. 3.9 where the drop shape evolution in time is depicted. The simulated drop breaks up forming two daughter drops and one satellite droplet between them. The mesh in this simulation is not sufficiently fine to resolve sub-satellite drops.

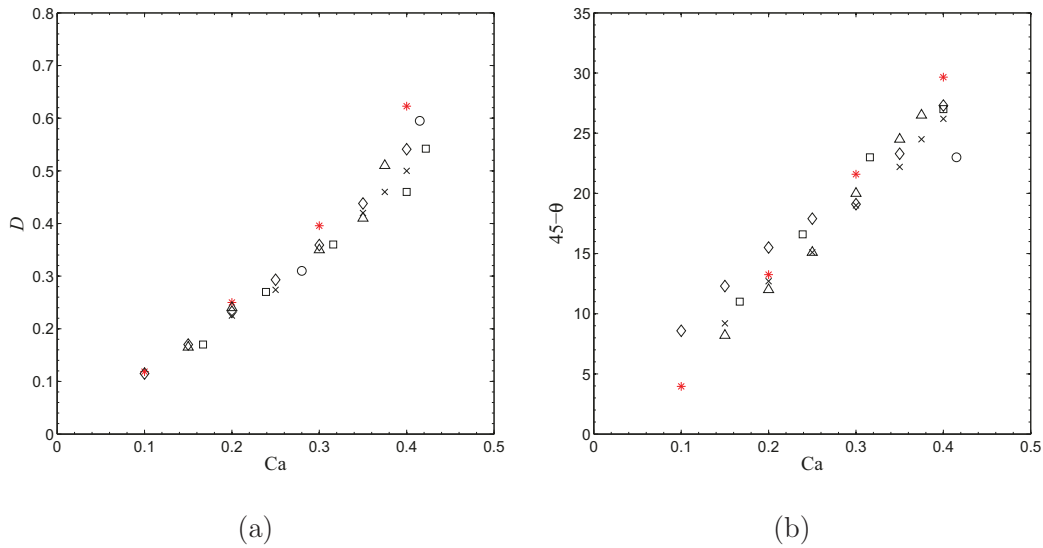


Figure 3.7: Deformation (a) and orientation (b) of a drop in simple shear flow under near Stokes conditions. Present simulation results (at $Re = 0.0625$) with free energy LBE $*$; Previous results: \diamond VOF computations of Li et al. (2000); \square boundary integral method of Rallison (1981); \times boundary integral method of Kwak and Pozrikidis (1998); \triangle boundary integral method of Kennedy et al. (1994); \circ experimental results by Rumscheidt and Mason (1961)

Further refinement (to $a = 64$ [lu] with $Pe = 0.43$ and $Ch = 0.0177$) shows the formation of sub-satellites after breakup as also reported by Li et al. (2000). The final stages of the drop shape evolution over time are presented in Fig. 3.10. The drop deforms sufficiently to reach and wrap around the ends of the periodic domain, whose size was chosen to be the same as in (Li et al., 2000). Though the domain is too small to represent the behavior of a single drop in an unbounded domain, the simulation demonstrates the ability of the method to resolve sub-satellite drops during the breakup of the thread.

3.4.3 Influence of inertia

In order to capture drop deformation and breakup at higher Reynolds numbers, three simulations were performed at a capillary number of $Ca = 0.3$ and Reynolds numbers $Re = 0.1, 0.5$ and 0.6 (the Reynolds numbers are taken the same as in the reference data by Li et al. (2000)). The initial drop radius is $a = 20$ [lu] in a simulation domain of $8a \times 8a \times 2a$. The Cahn number is $Ch = 0.0568$ and the Peclet

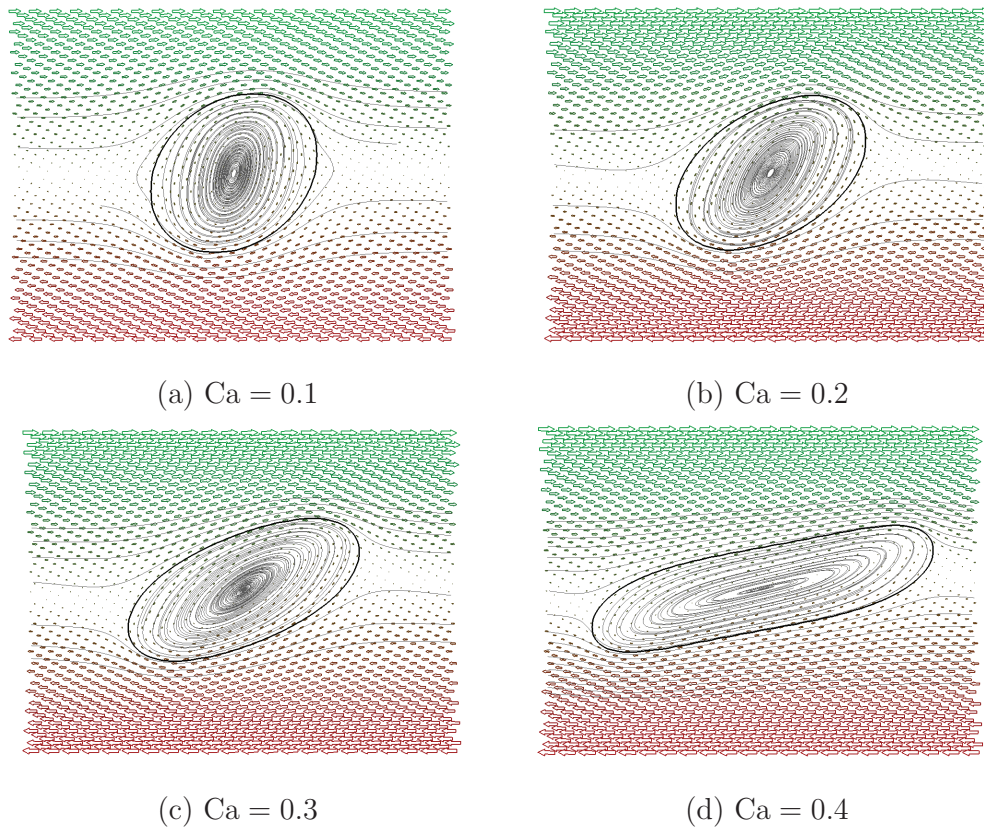


Figure 3.8: Steady state drop shape (black curve stands for the interface), streamlines and velocity fields ($x - y$ plane at $z = 0$). Stokes flow ($Re = 0.0625$), $\lambda = 1$

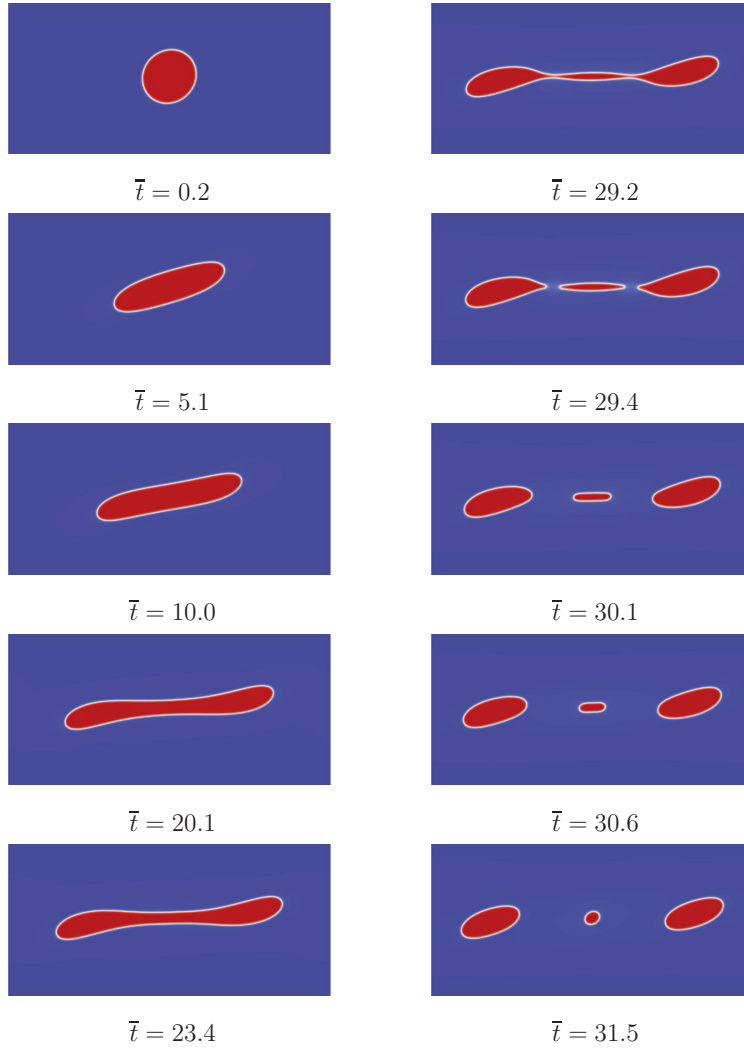
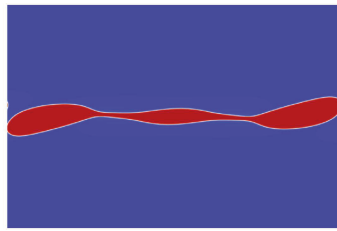
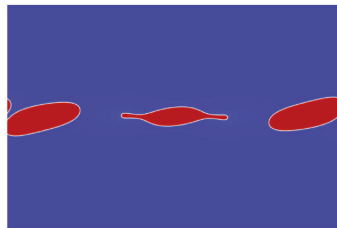


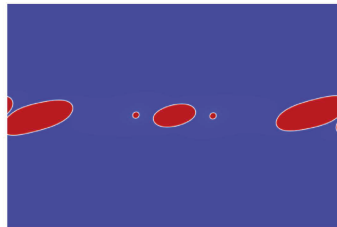
Figure 3.9: Evolution of the drop shape at $Re = 0.0625$, $Ca = 0.42$, $\lambda = 1.0$ and initial drop radius $a = 30$ [lu] ($\bar{t} = t\dot{\gamma}$). The images only show a portion of the full domain



$\bar{t} = 35.6$



$\bar{t} = 37.6$



$\bar{t} = 38.9$

Figure 3.10: Evolution of the drop shape at $Re = 0.0625$, $Ca = 0.42$, $\lambda = 1.0$ and initial drop radius $a = 64$ [lu] ($\bar{t} = t\gamma$)

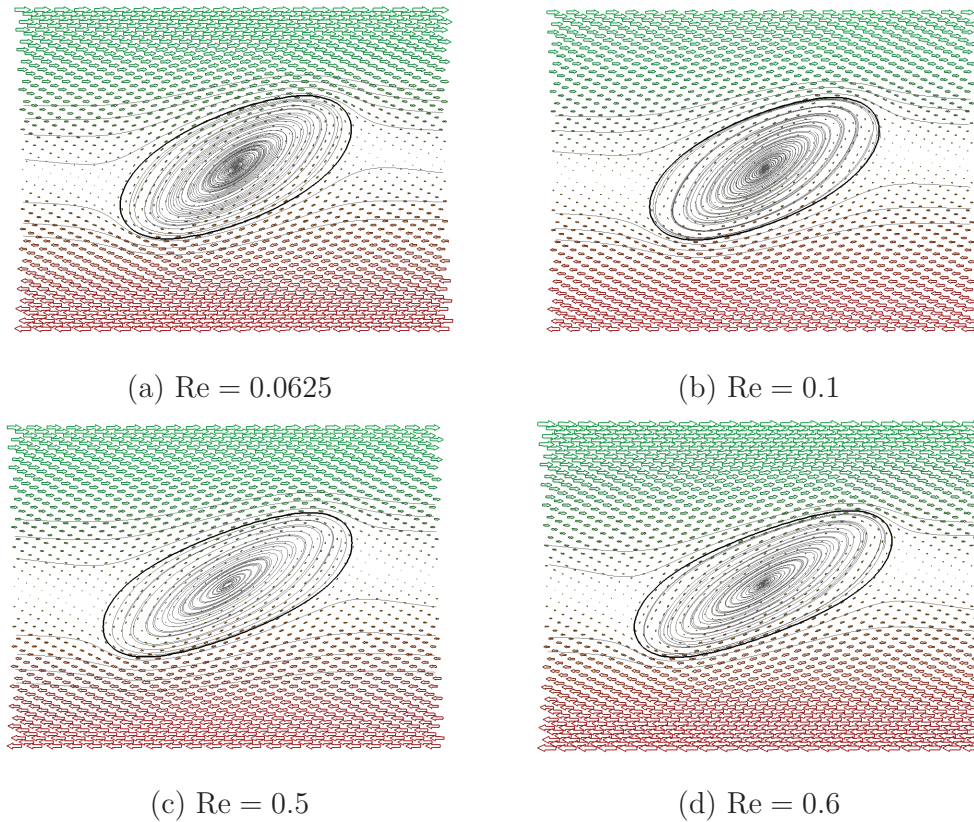


Figure 3.11: Steady-state velocity field and drop shape for $Ca = 0.3$, $\lambda = 1$ and different Re numbers

numbers are $Pe = 0.31, 0.39$ and 0.39 for each Re , respectively. The Reynolds number is increased by increasing the velocity of the wall while keeping the viscosity of both liquids equal to $\nu_d = \nu_c = 1/6$ (relaxation time $\tau_f = 1.0$).

For a fixed capillary number, an increase in the Reynolds number leads to higher drop deformation, the drop changes its shape from ellipsoidal to elongated. The drop shape at steady state together with velocity fields is illustrated in Fig. 3.11 for $Re = 0.0625, 0.1, 0.5$ and 0.6 . The results are in qualitative agreement with those presented by Li et al. (2000) (see their Fig. 18). The deformation parameter D , simulated using LBE, is listed in Table 3.2 for different Re together with the results obtained using the VOF method (Li et al., 2000). The deviation between the D values is less than 1%.

3.4.4 Joint influence of viscosity ratio and inertia

To demonstrate that different liquid viscosities can be handled, a set of simulations has been performed and the results have been compared to the VOF results reported by Khismatullin et al. (2003).

The initial drop radius of $a = 20$ [lu] (at the Cahn number $Ch = 0.0567$) in a simulation domain of $12a \times 4a \times 2a$ is considered. The Peclet number varies in the range from 1 to 5. The relaxation time of the continuous phase is $\tau_f = 0.6$, and the relaxation time for the liquid in the droplet is adjusted based on the viscosity ratio λ .

The Reynolds numbers were $Re = 1, 10$ and 50 . These are much higher Reynolds numbers than discussed so far. Khismatullin et al. (2003) reported critical capillary numbers as a function of viscosity ratio for these Re values. Since the critical capillary number was not known a priori, two capillary values were searched for every Re number: one for which the droplet attains steady state and the second one for which the drop breaks up and forms daughter droplets. In Fig. 3.12, Ca is plotted as a function of λ for the three Re numbers. The trends in Ca_c as a function of λ and Re found in the present study mimic the ones obtained using the VOF method (Khismatullin et al., 2003). However, with the increase of Re , the deviation in Ca_c values increases compared to the reference results. This can be attributed to the limited drop resolution. Grid refinement improves the results. For instance, when $Re = 50$, $\lambda = 1$ the drop with initial radius $a = 64$ [lu] ($Ch = 0.03125$) attains a steady shape at $Ca = 0.07$ and breaks at $Ca = 0.08$. This result is in a better agreement with reference data.

To highlight the influence of inertia, the shapes of the drops for different Re together with internal circulations are shown in Fig. 3.13. Only the results for

Table 3.2: Deformation parameter for different Re numbers, $Ca = 0.3$, $\lambda = 1.0$

Re	0.0625	0.1	0.5	0.6
D (LBE)	0.396	0.399	0.454	0.469
D (VOF (Li et al., 2000))	0.372	0.3968	0.45	0.4768

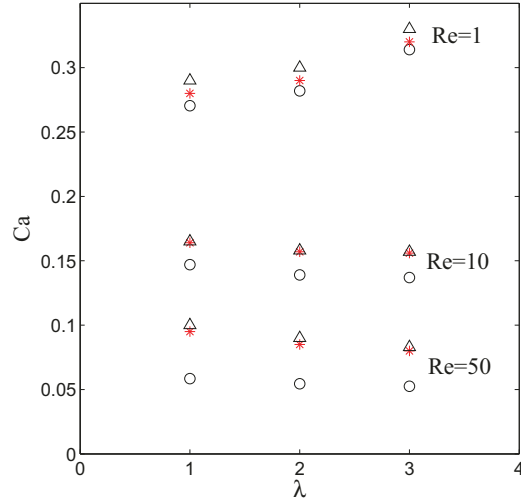


Figure 3.12: Capillary number Ca as a function of viscosity ratio λ . Present simulations with free energy LBE: * Ca for which drop attains steady shape; Δ Ca for which drop breaks up; \circ critical capillary numbers Ca_c obtained by VOF method (Khismatullin et al., 2003)

$\lambda = 1$ are presented here, but the conclusions are similar for $\lambda = 2$ and $\lambda = 3$. As one can see, with the increase of Re the steady shape of the drop is more towards the vertical direction. In Stokes flow, the drop is more symmetrical over the mid-plane with one vortex inside the drop. Inertia makes significant changes to the drop shape and velocity field: with the increase of Re the symmetry across the mid-plane vanishes and two vortices appear inside the drop (Fig. 3.13(d)). All these observations are in qualitative agreement with those reported by Renardy and Cristini (2001b).

The influence of the viscosity ratio can be analyzed using Fig. 3.14 where the shapes of the drop for $Re = 1$ and $\lambda = 1, 2$ and 3 with internal circulations at the near critical capillary number are depicted. The increase of the viscosity ratio means the drop becomes more viscous compared to the matrix liquid. Higher viscosity of the drop weakens circulation inside the drop: the vortex inside the drop in Fig. 3.14(a) is more developed compared to that shown in Fig. 3.14(c). The less viscous drop is more deformable: the symmetry over the mid-plane is lost for the drop with $\lambda = 1$ while the drop with $\lambda = 3$ is almost symmetric.

An increase of inertia also changes the breakup mechanism. To study the influ-

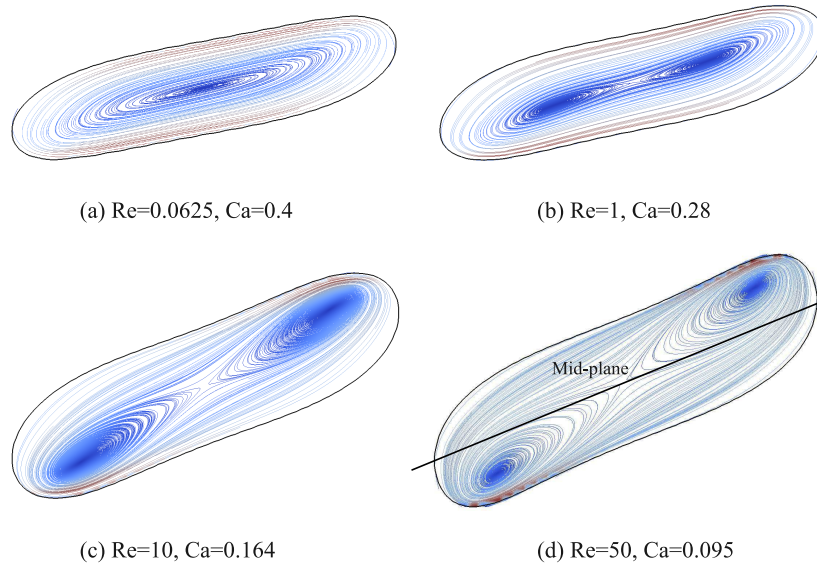
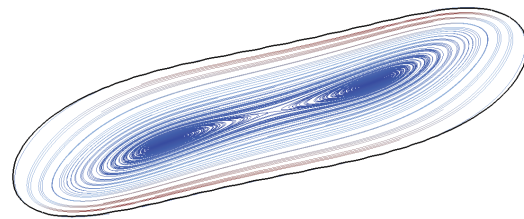


Figure 3.13: Drop shape and velocity field inside the drop for different Reynolds numbers Re and near critical capillary number Ca for each Re ($\lambda = 1$); $Ch = 0.0568$; (a) $Pe = 0.41$; (b) $Pe = 1.45$; (c) $Pe = 1$; (d) $Pe = 4.15$

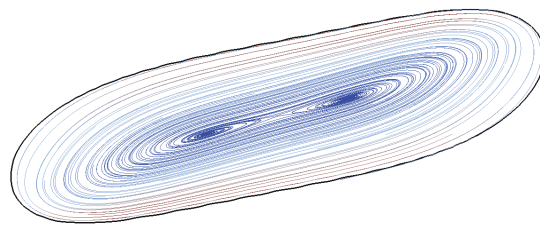
ence of the Reynolds number on breakup, simulations were performed for a system with viscosity ratio $\lambda = 2$, initial drop radius $a = 20$ [lu] for $Re = 1$ and 50 and above the critical capillary numbers for each Re . The evolution of drop shape and velocity field when $Re = 1$ is shown in Fig. 3.15. The drop stretches in the flow direction. Only one vortex is formed inside the drop up to $\bar{t} = 2.5$. When the neck in the middle of the drops begins to form, two symmetric vortices appear. The neck gradually thins and the drop breaks up forming two daughter droplets.

If inertia is increased up to $Re = 50$, significant changes in drop breakup take place (see Fig. 3.16). The tips of the drop are caught by streamlines with higher velocity that elongate the drop in the vertical direction. Two vortices are formed in the drop immediately after the start of the shear.

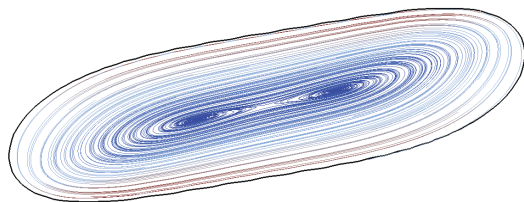
In addition, the influence of resolution was checked for $Re = 50$. The resolution is increased such that $a = 30$ [lu]. The results are presented in Fig. 3.17. This time a satellite drop forms after breakup. Moreover, the critical capillary number decreased with the increase of resolution which means the results are in better agreement with reference data if simulated with higher resolution (see Fig. 3.12).



(a) $\lambda = 1$, $Ca = 0.28$



(b) $\lambda = 2$, $Ca = 0.29$



(c) $\lambda = 3$, $Ca = 0.32$

Figure 3.14: Drop shape and internal circulations at $Re = 1$ and near critical capillary number for each λ ; $Ch = 0.0568$; (a) $Pe = 1.45$; (b) $Pe = 1.5$; (c) $Pe = 1.65$

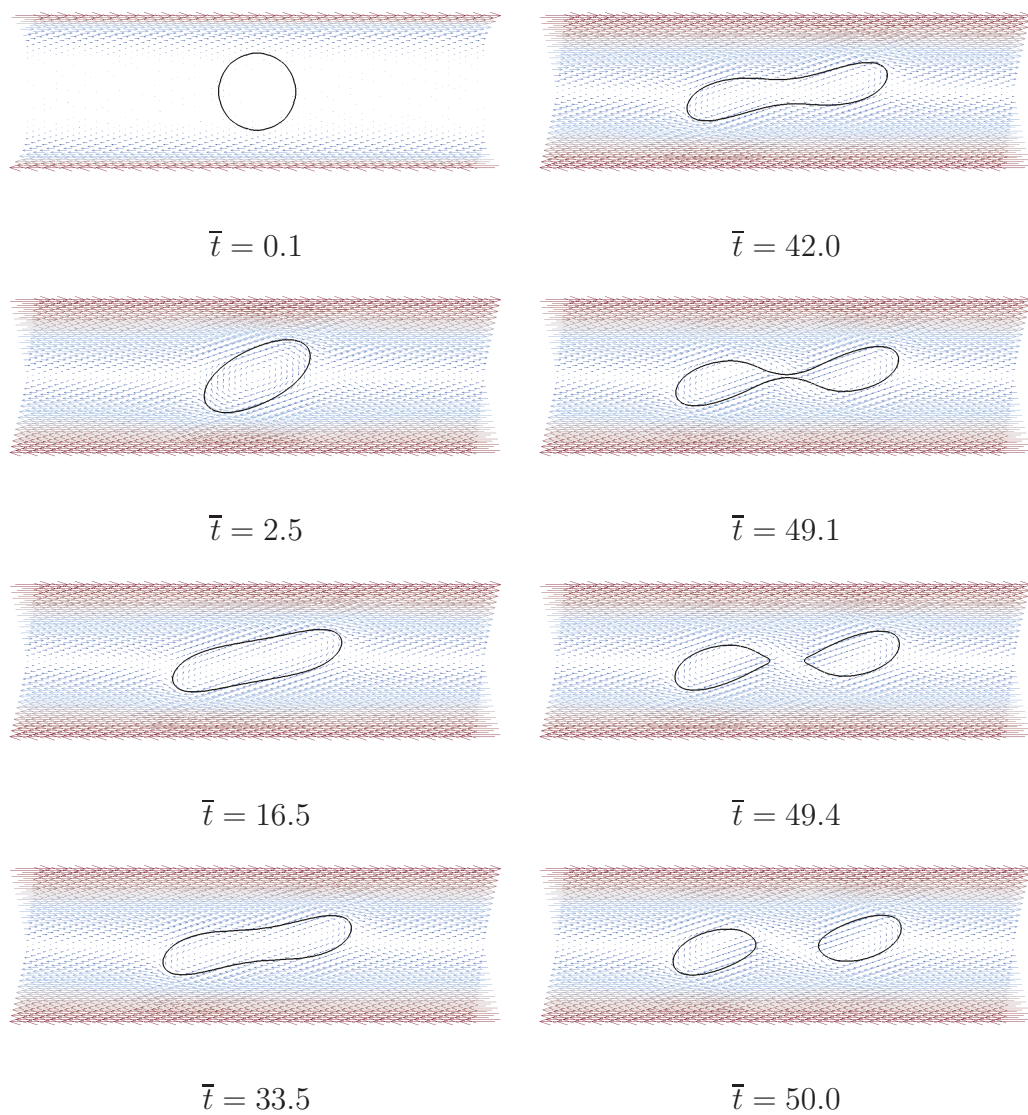


Figure 3.15: Drop shape and velocity field change in time for $Re = 1$, $Ca = 0.3$, $\lambda = 2$ ($\bar{t} = t\dot{\gamma}$). Initial drop radius $a = 20$ [lu]; the Cahn number $Ch = 0.0568$, the Peclet number $Pe = 1.55$

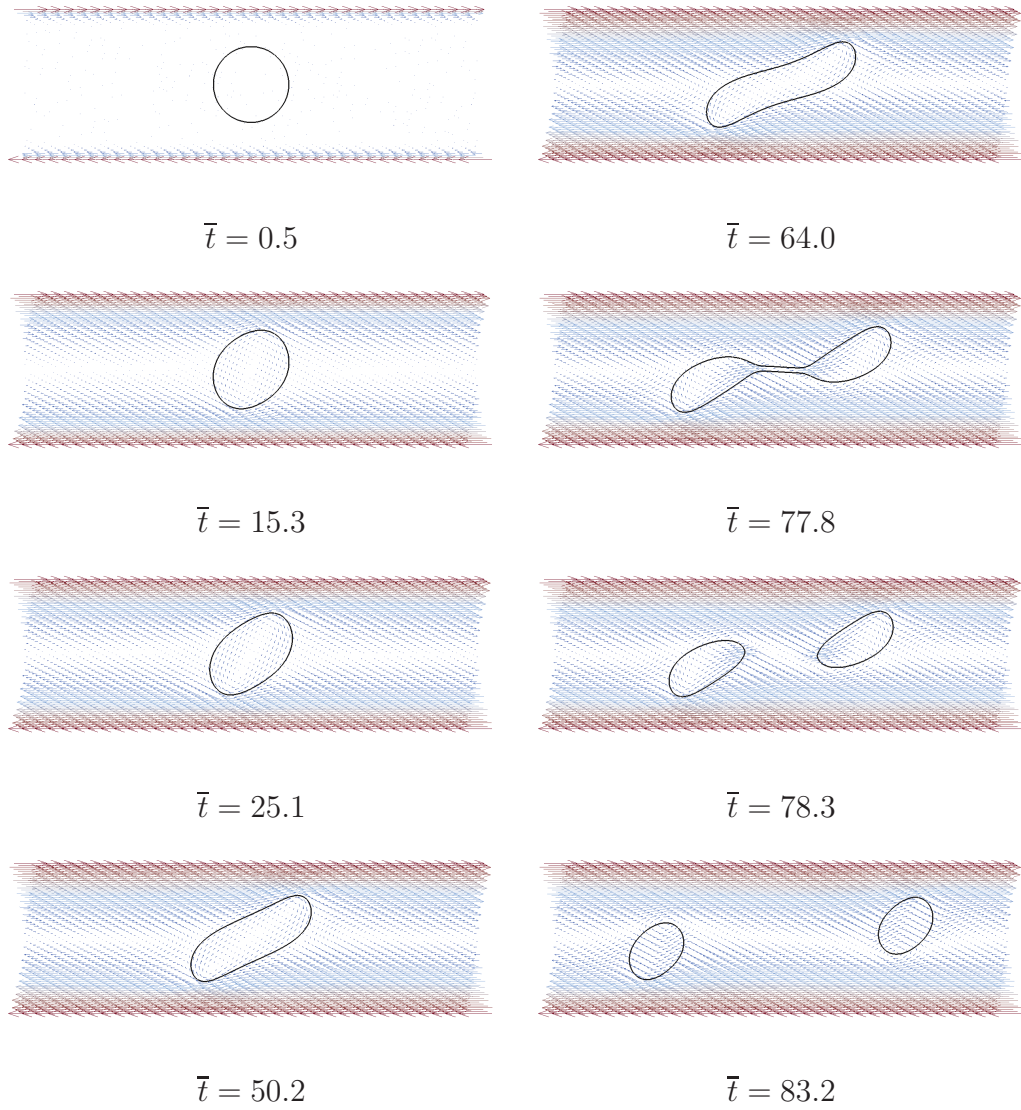


Figure 3.16: Drop shape and velocity field change in time for $Re = 50$, $Ca = 0.09$, $\lambda = 2$ ($\bar{t} = t\dot{\gamma}$). Initial drop radius $a = 20$ [lu]; the Cahn number $Ch = 0.0568$, the Peclet number $Pe = 3.93$

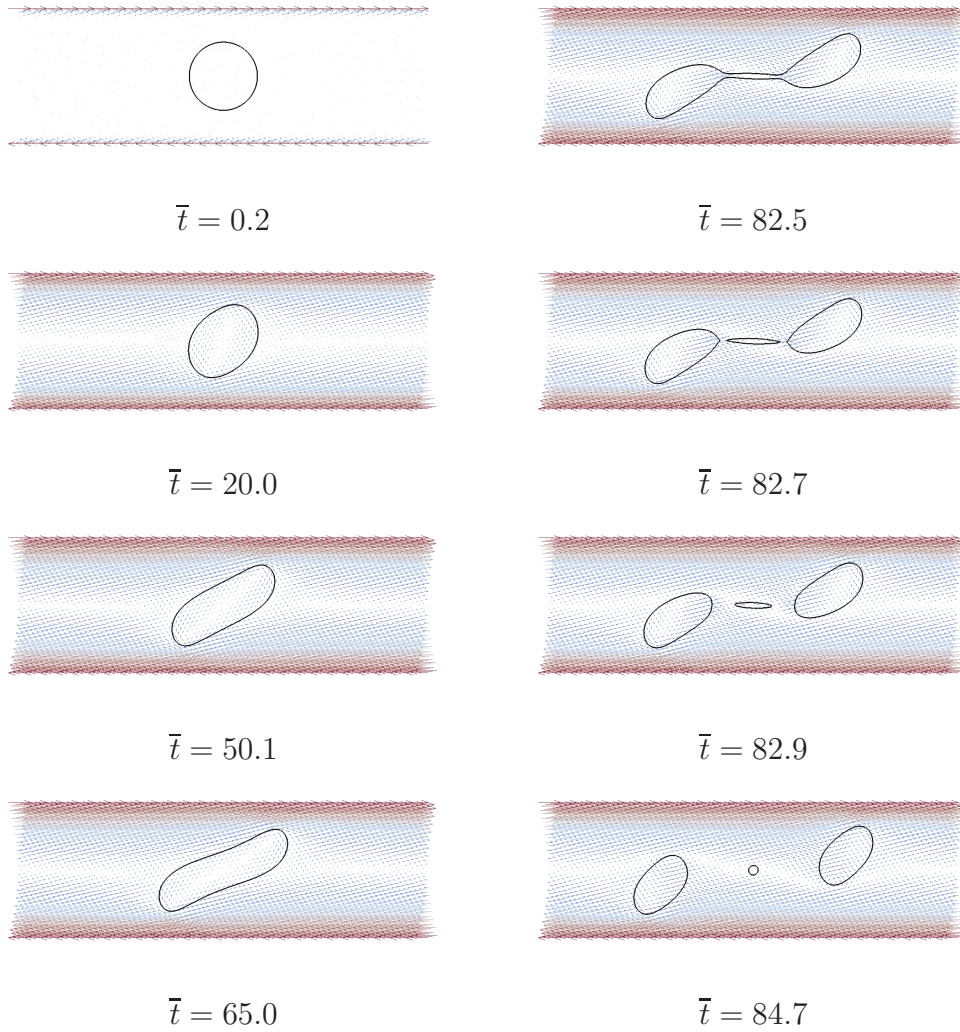


Figure 3.17: Drop shape and velocity field change in time for $Re = 50$, $Ca = 0.085$, $\lambda = 2$ ($\bar{t} = t\dot{\gamma}$). Initial drop radius $a = 30$ [lu]; the Cahn number $Ch = 0.0379$, the Peclet number $Pe = 3.71$

As one can see in Fig. 3.12, with the increase of inertia in the system even viscous drops are broken. For Stokes flow conditions, the critical capillary number significantly increases when λ approaches the value of 3. High Re numbers decrease the absolute value of critical capillary numbers and allow viscous drops to break.

3.5 Conclusions

Numerical simulations of a single liquid drops suspended in another liquid and subjected to simple shear flow have been presented. The free energy lattice Boltzmann method was used to perform three-dimensional simulations of the binary systems in order to determine the drop deformation and breakup conditions. During this study the numerical tool has been implemented, verified and validated with available reference data.

The full physical description of the problem requires three physical dimensionless numbers (the Reynolds number, the capillary number and the viscosity ratio). However, the description of the same problem in numerical space requires two additional dimensionless numbers. The adopted diffuse interface method involves the finite thickness of the interface between the two liquids and related free energy model parameters. These numerical degrees of freedom are characterized by two dimensionless numbers: the Peclet and Cahn numbers. The influence of these two numbers on accuracy and stability was investigated. A guideline on how to choose Pe and Ch in order to reveal physically realistic behavior of the drop at given Re, Ca and λ is presented below.

Three benchmark cases were performed to analyze the impact of Pe and Ch . A range of physical conditions was considered: starting from near Stokes flow and up to Reynolds of 10. The accuracy and stability are affected by the choice of Pe and Ch . A smaller Peclet number for a given Cahn number results in less deformation and smaller inclination angle of the drop. These effects hold for moderately and highly resolved drops. Correct physical behavior is captured in most of the cases.

For each benchmark case, mesh refinement studies were carried out for different

sets of Pe and Ch . Two mesh refinement principles were considered. The first principle assumes keeping all five dimensionless numbers constant when the mesh is refined, while in the second mesh refinement principle four dimensionless numbers (Re , Ca , λ , Pe) and the interface thickness remain the same. This principle follows the sharp-interface limit of Yue et al. (2010) where it is suggested to maintain the mobility value M while decreasing the Cahn number Ch . Different choices of the relationship between M and Ch might be optimal (see (Jacqmin, 2000; Magaletti et al., 2013)).

Both mesh refinement principles work: the key parameters (drop deformation and orientation angle) tend to reach asymptotic values. The results tend to mesh independency when the initial drop radius $a > 30$ lattice units. This drop size separates two regions of resolution: a region of moderate resolution when $a \leq 30$ [lu] and high resolution with $a > 30$ [lu]. However, for a given set of physical parameters (Re , Ca , λ) and different numerical parameters (Pe , Ch), the asymptotic values may differ from each other: at one Peclet number the drop may attain a steady shape, while at another Peclet number the drop may eventually break at high resolution, or the simulation might be unstable at low resolution.

The accuracy of the results is mostly determined by the mesh resolution and can only be *adjusted* by varying Ch and Pe . Drops of moderate resolution require a thinner interface. The suggested value is 1.14 [lu] (in line with the results of Kendon et al. (2001)). For highly resolved drops a thicker interface is preferable (at least two lattice units). Thus, the interface thickness is set based on the researcher's preferences on mesh resolution. Now the Cahn number is known, the Peclet number needs to be set. It was shown that a Pe specification actually is the specification of the mobility M because the rest of the parameters involved in Pe are already determined by the physical dimensionless numbers and by Ch . The mobility value is determined by the mobility coefficient Γ . The present simulations and the observations of Kendon et al. (2001) have shown that to allow diffusion over the interface to occur faster than fluid motion, the mobility coefficient should be high enough. Based on the present results, the simulations are stable when the mobility coefficient is in the range 1 – 15. The thicker the interface the higher Γ

values (i.e. smaller Pe) are required. If Pe is high then convection over the interface dominates diffusion and the interface breaks in cases where a steady state with one drop should be attained. On the other hand, too high Γ (usually $\gg 20$) might cause instability. If there is reference data then these can be used to find Pe . And then this Pe value can be used in further simulations. If the reference data is not available, it is suggested to select the mobility coefficient value from the stability range 1 – 15, then the deviation of numerical results will be within 20% for near-Stokes flow and less for Reynolds numbers of the order of one.

To demonstrate that even moderately resolved drops can be used to investigate the physics of drop deformation and breakup, further simulations were carried out. The drops of $a = 20$ and $a = 30$ [lu] were chosen with an interface thickness of 1.14 [lu]. These drops were exposed to a wide range of physical conditions ($Re = 0.0625 - 50$). The mobility coefficient was equal to 10 in most of the cases.

The results of Stokes flow simulations for deformation and breakup agree well with the results of other numerical techniques as VOF, boundary integral method and experiments. The deviation of deformation and orientation angle is within 20% for the capillary number range 0.1 – 0.4. Moderate drop resolution is not enough to capture sub-satellite drops after breakup at $Ca = 0.42$. Highly resolved drops should be used. For relatively low Reynolds numbers ($Re = 0.1, 0.5, 0.6$) and capillary numbers less than critical, the obtained drop deformation is in excellent agreement with VOF results presented by Li et al. (2000): the deviation of the drop deformation value is less than 1%. The ability of the code to handle different liquid viscosities at higher Re numbers was also tested. Even though the trend of the curves of capillary number as a function of viscosity ratio for different Reynolds numbers was captured, the deviation from VOF results (Khismatullin et al., 2003) increased for higher Re . It was demonstrated that a way to improve agreement is to increase the resolution of the LBE simulations.

The impact of the Peclet and Cahn numbers does not outweigh the valuable advantage of the utilized diffuse interface method over the interface tracking techniques: the feasibility to perform simulations of a system involving a high fraction of dispersed phase, i.e. large numbers of drops. The verified and validated numer-

ical tool will be used for industrial applications. For example, for a given binary system of two liquids under applied shear it is possible to determine the resulting drop size distribution (DSD). Or if the final product should have a certain DSD then the proper shearing conditions can be found. The advantage of numerical experiments is the possibility to visualize the entire flow. Moreover, one can modify and apply the operating conditions that are challenging to implement in a real experimental set-up. As for further steps, the developed tool will be extended for the dispersion formation simulations under turbulent flow conditions (Komrakova et al., 2013).

References

- N. K. Ahmed and M. Hecht. A boundary condition with adjustable slip length for lattice Boltzmann simulations. *J. Stat. Mech*, P09017:1–14, 2009.
- V. Badalassi, H. Cenicerros, and S. Banerjee. Computation of multiphase systems with phase field models. *J. Comp. Phys.*, 190:371–397, 2003.
- I. B. Bazhlekov, P. D. Anderson, and H. E. H. Meijer. Nonsingular boundary integral method for deformable drops in viscous flows. *Phys. Fluids*, 16:1064–1081, 2004.
- B. G. Bentley and L. G. Leal. An experimental investigation of drop deformation and breakup in steady, two-dimensional linear flows. *J. Fluid Mech.*, 167:241–283, 1986.
- P. L. Bhatnagar, E. P. Gross, and M. Krook. A model for collision processes in gases. I. Small amplitude processes in charged and neutral one-component systems. *Phys. Rev.*, 94:511–525, 1954.
- A. J. Bray. Theory of phase-ordering kinetics. *Adv. Phys.*, 43:357–459, 1994.
- J. W. Cahn and J. E. Hilliard. Free energy of a nonuniform system. I. Interfacial free energy. *J. Chem. Phys.*, 28:258–267, 1958.
- V. Cristini and Y. Renardy. Scalings for droplet sizes in shear-driven breakup: Non-microfluidic ways to monodisperse emulsions. *FDMP*, 2:77–93, 2006.
- V. Cristini, S. Guido, A. Alfani, J. B. Bławdziewicz, and M. Loewenberg. Drop breakup and fragment size distribution in shear flow. *J. Rheol.*, 47:1283–1298, 2003.

- J. Davies. A physical interpretation of drop sizes in homogenizers and agitated tanks, including the dispersion of viscous oils. *Chem. Eng. Sci.*, 42:1671–1676, 1987.
- S. De Groot and P. Mazur, editors. *Non-equilibrium thermodynamics*. Dover Publications, 1984.
- H. Ding, P. Spelt, and C. Shu. Diffuse interface model for incompressible two-phase flows with large density ratios. *J. Comp. Phys.*, 226:2078–2095, 2007.
- D. Jacqmin. Calculation of Two-Phase NavierStokes Flows Using Phase-Field Modeling. *J. Comp. Phys.*, 155:96–127, 1999.
- D. Jacqmin. Contact-line dynamics of a diffuse fluid interface. *J. Fluid Mech.*, 402: 57–88, 2000.
- P. Janssen and P. Anderson. Boundary-integral method for drop deformation between parallel plates. *Phys. Fluids*, 19:043602, 2007.
- V. Kendon, M. Cates, I. Pagonabarraga, J.-C. Desplat, and P. Bladon. Inertial effects in three-dimensional spinodal decomposition of a symmetric binary fluid mixture: a lattice boltzmann study. *J. Fluid Mech.*, 440:147–203, 2001.
- M. Kennedy, C. Pozrikidis, and R. Skalak. Motion and deformation of liquid drops, and the rheology of dilute emulsions in simple shear flow. *Comput. Fluids*, 23: 251–278, 1994.
- D. Khismatullin, Y. Renardy, and V. Cristini. Inertia-induced breakup of highly viscous drops subjected to simple shear. *Phys. Fluids*, 15:1351–1354, 2003.
- A.E. Komrakova, J.J. Derksen, D. Eskin, in press. Simulations of dispersion formation in liquid-liquid turbulent flows. In 8th International Conference on Multiphase Flow, ICMF 2013, Jeju, Korea, May 26–31.
- H. Kusumaatmaja. *Lattice Boltzmann Studies of Wetting and Spreading on Patterned Surfaces*. PhD thesis, University of Oxford, 2008.

- S. Kwak and C. Pozrikidis. Adaptive Triangulation of Evolving, Closed, or Open Surfaces by the Advancing-Front Method. *J. Comput. Phys.*, 145:61–88, 1998.
- A. J. C. Ladd. Numerical Simulations of Particulate Suspensions via a Discretized Boltzmann Equation Part I. Theoretical Foundation. *J. Fluid Mech.*, 271:285–309, 1994.
- J. Li, Y. Renardy, and M. Renardy. Numerical simulation of breakup of a viscous drop in simple shear flow through a volume-of-fluid method. *Phys. Fluids*, 12:269–282, 2000.
- F. Magaletti, F. Picano, M. Chinappi, L. Marino, and C. Casciola. The sharp-interface limit of the Cahn-Hilliard/Navier-Stokes model for binary fluids. *J. Fluid Mech.*, 714:95–126, 2013.
- C. Marks. *Drop breakup and deformation in sudden onset strong flows*. PhD thesis, University of Maryland, 1998.
- A. Mussa, P. Asinari, and L.-S. Luo. Lattice Boltzmann simulations of 2D laminar flows past two tandem cylinders. *J. Comput. Phys.*, 228:983–999, 2009.
- O. Penrose and P. Fife. Thermodynamically consistent models of phase-field type for the kinetics of phase transitions. *Physica D*, 43:44–62, 1990.
- S. Pope. *Turbulent flows*. Cambridge University Press, 2000.
- C. Pozrikidis. *Boundary integral and singularity methods for linearized viscous flow*. Cambridge University Press, 1992.
- J. Rallison. A numerical study of the deformation and burst of a viscous drop in general shear flows. *J. Fluid Mech.*, 109:465–482, 1981.
- J. Rallison. The deformation of small viscous drops and bubbles in shear flows. *Ann. Rev. Fluid Mech.*, 16:45–66, 1984.
- Y. Renardy and V. Cristini. Scalings for fragments produced from drop breakup in shear flow with inertia. *Phys. Fluids*, 13:2161–2164, 2001a.

- Y. Renardy and V. Cristini. Effect of inertia on drop breakup under shear. *Phys. Fluids*, 13:7–13, 2001b.
- Y. Renardy, V. Cristini, and J. Li. Drop fragment distributions under shear with inertia. *Int. J. Multiphase Flow*, 28:1125–1147, 2002.
- F. Rumscheidt and S. G. Mason. Particle motions in sheared suspensions. XII. deformation and burst of fluid drops in shear and hyperbolic flow. *J. Colloid Sci.*, 16:238–261, 1961.
- X. Shan and H. Chen. Lattice Boltzmann model for simulating flows with multiple phases and components. *Phys. Rev. E*, 47:1815–1819, 1993.
- O. Shardt, J. Derksen, and S. Mitra. Simulations of droplet coalescence in simple shear flow. *Langmuir*, 29:6201–6212, 2013.
- H. Stone. Dynamics of drop deformation and breakup in viscous fluids. *Annu. Rev. Fluid Mech.*, 26:65–102, 1994.
- M. Swift, E. Orlandini, W. Osborn, and J. Yeomans. Lattice Boltzmann simulations of liquid-gas and binary fluid systems. *Phys. Rev. E*, 54:5041–5052, 1996.
- G. Taylor. The viscosity of a fluid containing small drops of another fluid. *Proc. R. Soc. Lond. A*, 138:41–48, 1932.
- G. Taylor. The formation of emulsions in definable fields of flow. *Proc. R. Soc. Lond. A*, 146:501–523, 1934.
- R.G.M. van der Sman and S. van der Graaf. Emulsion droplet deformation and breakup with Lattice Boltzmann model. *Comp. Phys. Commun.*, 178:492–504, 2008.
- H. Xi and C. Duncan. Lattice boltzmann simulations of three-dimensional single droplet deformation and breakup under simple shear flow. *Phys. Rev. E*, 59: 3022–3037, 1999.

- P. Yue, J. Feng, C. Liu, and J. Shen. A diffuse-interface method for simulating two-phase flows of complex fluids. *J. Fluid Mech.*, 515:293–317, 2004.
- P. Yue, C. Zhou, and J. J. Feng. Sharp-interface limit of the Cahn-Hilliard model for moving contact lines. *J. Fluid Mech.*, 645:279–294, 2010.
- X. Zhao. Drop breakup in dilute Newtonian emulsions in simple shear flow: new drop breakup mechanisms. *J. Rheol.*, 51:367–392, 2007.

Chapter 4

Effects of dispersed phase viscosity on drop deformation and breakup in inertial shear flow¹

4.1 Introduction

Studies of drop behavior in simple flow geometries have been used to interpret data on dispersion and emulsion formation due to more complex flow structures as they occur in process equipment (Rueger and Calabrese, 2013). While most experimental and simulation research has considered creeping flow (Grace, 1982; Marks, 1998; Rallison, 1984; Rumscheidt and Mason, 1961; Stone, 1994; Zhao, 2007), drops in complex flows, such as turbulence, can experience drop Reynolds numbers anywhere in the range 0.01 – 100 (Komrakova et al., 2013). To predict whether drops will break in turbulent flow, it is necessary to understand how the conditions for breakup at moderate Reynolds numbers differ from those in creeping flow. While studies have considered the conditions for breakup in simple shear flow at Reynolds numbers up to 100 in systems with droplets that are as viscous or more viscous than the continuous phase (Khismatullin and Renardy, 2003; Renardy and Cristini, 2001), neither experiments nor simulations have been reported for the case of drops that are less viscous than their surroundings. This case is not unusual: for example, water droplets may be dispersed in a much more viscous oil (Boxall et al.,

¹A version of this chapter has been submitted. A.E. Komrakova, Orest Shardt, D. Eskin, J.J. Derksen. Phys. Fluids

2011; Rueger and Calabrese, 2013). In the oil recovery industry, well productivity can be reduced by formation damages caused by oil-based emulsions that contain brine droplets (Fjelde, 2007). If a monodisperse emulsion is formed, then damage might occur even at low dispersed phase volume fractions. An understanding of deformation and breakup behavior of low-viscosity drops in a more viscous fluid will therefore fill an important gap in current knowledge with impact on industrial applications.

In the present work, the deformation and breakup of a single drop suspended in another liquid under simple shear flow is studied with numerical simulations using a free energy lattice Boltzmann method (Swift et al., 1996). The details of the method, its verification and validation can be found in (Komrakova et al., 2013). The physical problem is determined by three dimensionless numbers: the drop Reynolds number $Re = \dot{\gamma}a^2/\nu_c$, the capillary number $Ca = a\dot{\gamma}\mu_c/\sigma$, and the viscosity ratio $\lambda = \mu_d/\mu_c$. Here, a is the undeformed drop radius; $\dot{\gamma}$ is the shear rate; ν_c is the kinematic viscosity of the continuous phase; μ_c, μ_d are the dynamic viscosities of continuous and dispersed phases, respectively; and σ is the interfacial tension between the liquids.

The goal of this study is to investigate the behavior of a drop at a fixed Reynolds number $Re = 10$ over a range of viscosity ratios $\lambda = 0.1 - 2$, with a focus on $\lambda < 1$. For each λ it is necessary to determine the critical capillary number Ca_c that must be exceeded to break a drop. At subcritical capillary numbers, the drop achieves a steady final shape. The internal circulation patterns and the deformation parameters (elongation and orientation angle; see definitions below) are used to characterize the steady shape. When a supercritical capillary number is simulated, the drop breaks, and the breakup mechanism depends on the values of Ca and λ . Changes in the drop breakup process are examined as the capillary number increases from 20% above critical, to 50 and 100%.

The distinct characteristic of numerical simulations is that the entire deformation and breakup processes can be visualized revealing peculiarities of the events. However, in order to study physical processes numerically, it is necessary to select numerical parameters that produce trustworthy physical results. It was shown by

Komrakova et al. (2013) that in addition to the three physical dimensionless numbers mentioned above (the Reynolds number, the capillary number and the viscosity ratio), two numerical dimensionless numbers have to be specified. In the diffuse interface method, which is used in this work, the finite thickness of the interface between the two liquids and related free energy model parameters are involved. These numerical degrees of freedom are characterized by two dimensionless numbers (Van der Sman and Van der Graaf, 2008): the interface Peclet Pe number and the Cahn Ch number. The interface Peclet number $Pe = \dot{\gamma}a\xi/(MA)$ relates the convection time scale to the interface diffusion time scale. The Cahn number $Ch = \xi/a$ is the ratio of the interface thickness and drop radius. Here, ξ is the interface thickness, M is the mobility, and A is a free energy model parameter. In the present study, the guidelines as developed by Komrakova et al. (2013) have been applied to specify Pe and Ch .

The rest of the paper is organized as follows. In Section 4.2 a brief description of the numerical method and its implementation are presented. In Section 4.3 the ability of the method to compute flows over the required range of viscosity ratios is demonstrated. The results of drop deformation and breakup are presented in Section 4.4. Conclusions are drawn in Section 4.5.

4.2 Numerical method and its implementation

The behavior of a drop in shear flow is studied numerically with the diffuse interface free energy lattice Boltzmann equation (LBE) method developed by Swift et al. (1996). The details of diffuse interface (or phase field) methods can be found in (Ding et al., 2007; Jacqmin, 1999; Yue et al., 2004); our implementation of the method is presented in (Komrakova et al., 2013). In particular, the interface between the two components is represented by a thin transition region with a finite thickness in which the composition varies smoothly. The composition of the system is described by the order parameter φ which is the relative concentration of the two components (Badalassi et al., 2003; Cahn and Hilliard, 1958; Penrose and Fife, 1990). To simulate the fluid dynamics of the binary mixture of fluids, the continuity

and momentum equations are solved in conjunction with Cahn Hilliard convection-diffusion equation for the order parameter (Bray, 1994). Thus, the evolution of density, velocity and order parameter are governed by the continuity, momentum, and convection-diffusion equations (Kendon et al., 2001):

$$\partial_t \rho + \partial_\alpha (\rho u_\alpha) = 0 \quad (4.1a)$$

$$\partial_t (\rho u_\alpha) + \partial_\beta (\rho u_\alpha u_\beta) = -\partial_\beta P_{\alpha\beta}^{th} + \partial_\beta \nu (\rho \partial_\alpha u_\beta + \rho \partial_\beta u_\alpha) \quad (4.1b)$$

$$\partial_t \varphi + \partial_\alpha (\varphi u_\alpha) = M \partial_{\beta\beta}^2 \mu \quad (4.1c)$$

where u_α is the velocity; the index α stands for the Cartesian directions x , y and z ; ρ and ν are the density and the kinematic viscosity of the mixture, respectively. Here $P_{\alpha\beta}^{th}$ is the ‘thermodynamic’ pressure tensor. It contains two parts (Kendon et al., 2001): an isotropic contribution $P \delta_{\alpha\beta}$ that represents the ideal gas pressure and the ‘chemical’ pressure tensor $P_{\alpha\beta}^{chem}$. The chemical potential in equation (4.1c) is: $\mu(\varphi) = A\varphi - A\varphi^3 - \kappa \partial_{\alpha\alpha}^2 \varphi$. Here, $A < 0$ and κ are parameters of the free energy model that are related to the surface tension and interface thickness; M is the mobility.

In LBE two particle distribution functions are utilized to solve system (4.1): one function $f(\mathbf{r}, t)$ is used to solve the continuity (4.1a) and Navier-Stokes (4.1b) equations and the second one $g(\mathbf{r}, t)$ is used for the convection-diffusion equation (4.1c). The distribution functions evolve by a time step Δt . All simulations have been performed using a single relaxation time collision operator (Bhatnagar-Gross-Krook (BGK) model (Bhatnagar et al., 1954)). The discrete lattice Boltzmann equations for the evolution of f and g have the following form:

$$\begin{aligned} f_q(r_\alpha + c_{\alpha q} \Delta t, t + \Delta t) - f_q(r_\alpha, t) &= -\frac{f_q - f_q^{eq}}{\tau_f}, \\ g_q(r_\alpha + c_{\alpha q} \Delta t, t + \Delta t) - g_q(r_\alpha, t) &= -\frac{g_q - g_q^{eq}}{\tau_g}, \end{aligned} \quad (4.2)$$

where the index q counts over the number of the discrete velocity directions; f_q^{eq} , g_q^{eq} are the discretized Maxwell-Boltzmann distributions (or equilibrium distributions); $c_{\alpha q}$ denotes the discrete velocity set and τ_f , τ_g are dimensionless relaxation parameters. The equilibrium distributions f_q^{eq} , g_q^{eq} are given in (Kusumaatmaja,

2008). The D3Q19 lattice is adopted here where $D = 3$ denotes three-dimensional flow and $Q = 19$ is the number of velocities. In this lattice arrangement, each site communicates with its six nearest and twelve diagonal neighbors. The lattice Boltzmann method operates in dimensionless lattice units (lattice space, time step, and lattice density for the length, time and density units, respectively). For the method described here, only uniform cubic lattices can be used; the mesh step Δx is taken as unity, as is the time step Δt .

The distribution functions are defined such that the following summations over all directions q at each lattice point give the local density of the fluid ρ , the local fluid momentum ρu_α and the local order parameter φ , respectively:

$$\sum_q f_q = \rho \quad \sum_q c_{\alpha q} f_q = \rho u_\alpha \quad \sum_q g_q = \varphi \quad (4.3)$$

The two liquids have different kinematic viscosities. To implement this, the kinematic viscosity of the mixture ν is set to be a function of the order parameter φ :

$$\nu(\varphi) = \nu_c \frac{\varphi_0 - \varphi}{2\varphi_0} + \nu_d \frac{\varphi_0 + \varphi}{2\varphi_0} \quad (4.4)$$

where ν_c and ν_d are the kinematic viscosities of continuous and dispersed phases, respectively; and $\varphi = \pm\varphi_0 = \pm 1$ is the value of the order parameter in the bulk phase on either side of the interface. The relaxation parameter for f_q varies with the composition according to:

$$\tau_f(\varphi) = \frac{\nu(\varphi)}{c_s^2} + \frac{1}{2} \quad (4.5)$$

Here $c_s^2 = 1/3$ is the speed of sound in lattice units.

The mobility M (see eq. (4.1c)) is determined by the coefficient of mobility Γ and the relaxation parameter τ_g according to:

$$M = \Gamma \left(\tau_g - \frac{1}{2} \right) \quad (4.6)$$

For a planar interface, an analytical solution (Van der Sman and Van der Graaf, 2008) gives the φ profile $\varphi(x) = \varphi_0 \tanh(x/\xi)$ (x is the coordinated normal to interface). The thickness of the diffuse interface is characterized by a characteristic

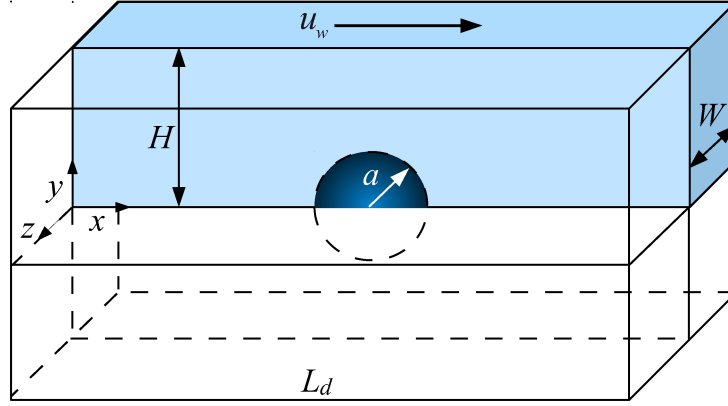


Figure 4.1: Simulation domain with the following boundary conditions: $x = 0$ and $x = L_d$ are periodic boundaries; $y = 0$ has a rotational symmetry boundary condition; $y = H$ is a no-slip wall moving with constant velocity u_w ; $z = 0$ and $z = -W$ are symmetry planes. At $t = 0$ the drop has a spherical shape with initial radius a . Due to the symmetry of the problem only one quarter of the domain needed to be simulated

length ξ :

$$\xi = \left(\frac{2\kappa}{-A} \right)^{1/2}. \quad (4.7)$$

The interfacial tension σ follows from:

$$\sigma = \frac{4}{3} \kappa \frac{\phi_0^2}{\xi}. \quad (4.8)$$

A simulation code for multiple graphics processing units (GPUs) (Shardt et al., 2013) was used to perform all simulations. The simulation domain is shown in Fig. 4.1. A symmetry boundary condition through the middle of the domain ($z = 0$) and a rotational symmetry boundary condition ($y = 0$) were used to avoid unnecessary computations. With these boundary conditions, only a quarter of the full domain was simulated (the highlighted volume in Fig. 4.1). The shear velocity at $y = H$ was imposed using the method of Ladd (1994). A symmetry condition was used for the phase field ϕ at $y = H$. Periodic boundary conditions were imposed on the $x = 0$ and $x = L$ planes. Typical processing speeds for the simulations were 200 – 480 million lattice node updates per second (Mlups) for the smaller and larger domains, respectively.

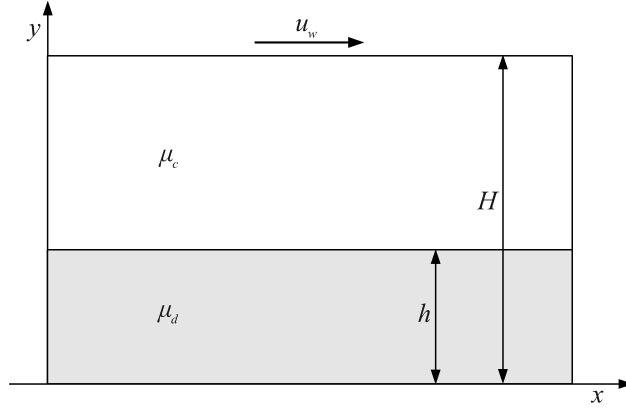


Figure 4.2: A slice of the simulation domain at $z = 0$ for validation simulations of stratified shear flow; $h = 64$ [lu], $H = 4h$, $\lambda = \mu_d/\mu_c = 0.1 - 2$.

4.3 Stratified flow benchmark

Validation simulations were performed to assess the numerical method over the range of viscosity ratios from $\lambda = 0.1$ to 2. A stratified sheared flow for which an analytical solution exists was considered. A slice at $z = 0$ of a $0.5h \times 4h \times 0.5h$ (x, y, z) simulation domain (where $h = 64$ [lu]) is shown in Fig. 4.2. Only a quarter of the full domain was simulated (rotational symmetry at $y = 0$). The full domain therefore represents three sheared liquid layers. The full height of the inner fluid layer is 128 lattice units [lu]. The boundary conditions are the same as described above.

The stratified flow simulations require specification of the following parameters: the interface thickness ξ , the parameters A and κ , the mobility M , and the coefficient of mobility Γ . These parameters were chosen the same as for a sheared drop (that will be considered later), and then used in the benchmark simulations to assess the accuracy of simulations with these parameters.

The procedure for selecting the numerical parameters according to the guidelines of Komrakova et al. (2013) is as follows. First, the drop resolution is specified: the drop radius is chosen to be 64 lattice units to perform high-resolution simulations that can resolve the satellite and sub-satellite drops formed after breakup. This drop size requires an interface thickness of at least two lattice units (Komrakova et al., 2013), and therefore $\xi = 2$ [lu] is chosen. Consequently, the Cahn

number is $Ch = 0.03$. The second step is to determine the Peclet number, which requires specifying several parameters. The relaxation time of the continuous fluid phase is kept constant at $\tau_f = 0.7$ which specifies a continuous phase viscosity of $\nu_c = 1/15$ [lu]. The shear rate $\dot{\gamma}$ follows from the Reynolds number, which is 10 in the present study: $\dot{\gamma} = \text{Re} \cdot \nu_c / a^2$. The interfacial tension σ is determined by the capillary number: $\sigma = a\dot{\gamma}\mu_c / \text{Ca}$ (where $\mu_c = \rho\nu_c$ and the density $\rho = 1$ in lattice units). To determine Pe , an estimate of the typical Ca is needed, which is not known yet, as the critical capillary number is an output of the simulation. For an initial estimate, $\text{Ca} = 0.15$ is used, which is the near-critical value for $\lambda = 1$ reported by Khismatullin and Renardy (2003). The interfacial tension σ and interface thickness ξ give the value of κ (see (4.8)): $\kappa = 3\sigma\xi / (4\phi_0^2)$. Finally, with κ and ξ specified, the value of the parameter A is (see (4.7)): $A = 2\kappa/\xi^2$. Thus only one parameter remains to be specified in the Peclet number – the mobility M which is determined by the mobility coefficient Γ . Every simulation in the present study was performed with the relaxation time for the phase field $\tau_g = 1$ which implies $M = \Gamma/2$ (see (4.6)). Consequently, $Pe = 12.0/\Gamma$. As shown in (Komrakova et al., 2013), to perform stable simulations the mobility coefficient should be chosen in the range 1 – 15. Furthermore, it was outlined that for the case at $\text{Re} = 10$, $\text{Ca} = 0.15$ and $\lambda = 1$, $Pe > 4$ yields results that agree well with reference data. For that reason it was decided to set the Peclet number to $Pe = 6$. Therefore, $\Gamma = 2$ was used in the benchmark simulations.

The x -velocity component in the fluid as a function of y (see Fig. 4.2) for different viscosity ratios λ is presented in Fig. 4.3. The relative deviation of velocity values from the analytical solution ($\delta = |u_{\text{analytical}} - u_{\text{numerical}}| / u_{\text{analytical}} \cdot 100\%$) is shown in Fig. 4.4. Calculation of δ with $u_{\text{analytical}} = 0$ was not performed because the first node in the y -direction is located half a lattice space from the boundary. As one can see, the overall largest deviation occurs with $\lambda = 2$ which is 2.5% and happens on the interface. For the rest of the λ values, the relative deviation from the analytical solution is within $\pm 1\%$. It is concluded that the method can deal with viscosity ratios $0.1 \leq \lambda \leq 2$ in a consistent manner.

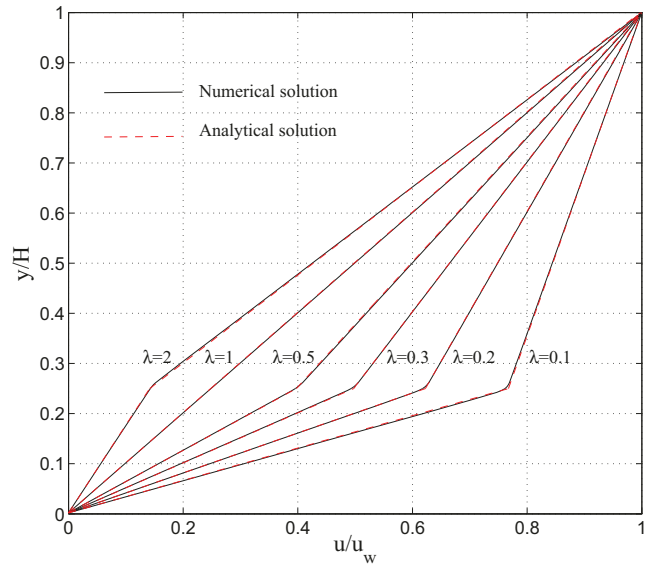


Figure 4.3: The x -velocity component as a function of position between the domain center and the sheared plate for different λ in stratified flow; $y/H = 0.25$ is the location of the interface

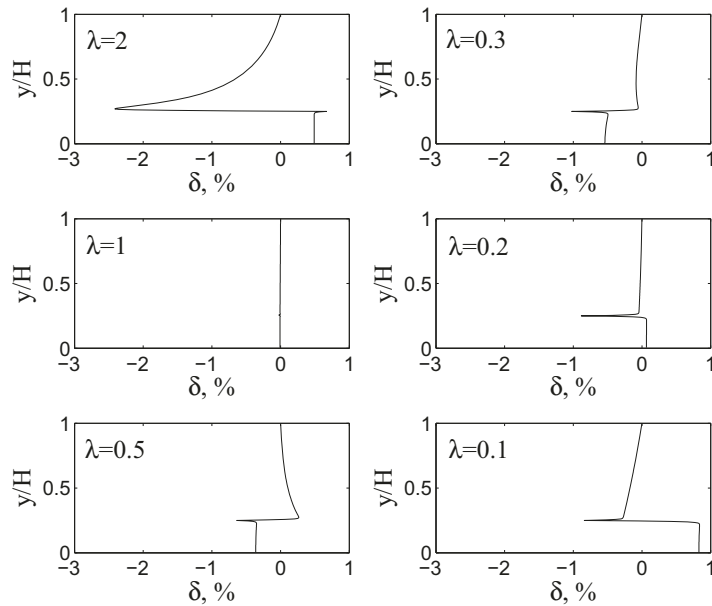


Figure 4.4: Relative deviation of x -velocity component in the fluid between numerical and analytical solutions as a function of position between the domain center and the sheared plate for different λ in stratified flow; $y/H = 0.25$ is the location of the interface

Table 4.1: Capillary number Ca as a function of viscosity ratio λ at $Re = 10$

λ	2.0	1.0	0.5	0.3	0.2	0.15	0.1
Highest subcritical Ca	0.148	0.154	0.163	0.169	0.177	0.183	0.192
Lowest supercritical Ca	0.149	0.155	0.164	0.170	0.178	0.184	0.193
Ca_c (Khismatullin and Renardy, 2003)	0.139	0.147					

4.4 Results

The simulations to determine critical capillary numbers were performed with an initial drop radius $a = 64$ lattice units in a $16a \times 4a \times 2a$ (x, y, z) domain size (a quarter of the full domain). The height of the domain is the same as used in the reference simulations of Khismatullin and Renardy (2003). Additionally, the influence of the proximity of walls was considered in (Komrakova et al., 2013) and it was shown that $H = 4a$ is sufficient to avoid confinement effects. The thickness of the interface was two lattice units so that $Ch = 0.03$. The diffusion coefficient Γ was set to 2 (as in the benchmark). This gives Peclet numbers in the range 5 – 8 depending on the capillary number specified for each simulation. The reference data presented by Khismatullin and Renardy (2003) for $\lambda = 1$ and 2 were used for validation.

Two capillary numbers were searched for every λ : one for which the droplet does not break and attains a steady state (highest subcritical Ca) and the second one for which the drop breaks into fragments (lowest supercritical). The critical capillary number is determined as the arithmetic average of these two values. The results are presented in Fig. 4.5 and in Table 4.1. The relative deviation of Ca_c from the reference data is 5 and 7% for $\lambda = 1$ and 2, respectively. For λ in the range 0.1 to 2, the critical capillary number increases as the viscosity ratio decreases.

In the literature, two parameters are used to measure the deformation of the drop when a steady shape exists: the Taylor deformation parameter and the orientation angle (Taylor, 1932, 1934). Inertia (which is relevant for shear with $Re = 10$) changes the steady shape of drops from ellipsoidal (at Stokes flow) to elongated. Moreover, the symmetry over the mid-plane of the drop (see Fig. 4.6) might be lost. For that reason in this work the ratio of maximum elongation to initial un-

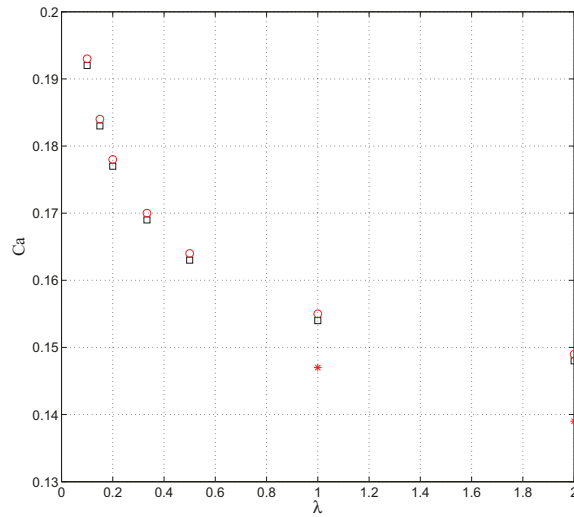


Figure 4.5: Capillary number Ca as a function of viscosity ratio λ for the Reynolds number $Re = 10$. Present simulations with free energy LBE: \square Ca for which drop attains steady shape; \circ Ca for which drop breaks; $*$ critical capillary numbers Ca_c obtained by VOF method (Khismatullin and Renardy, 2003)

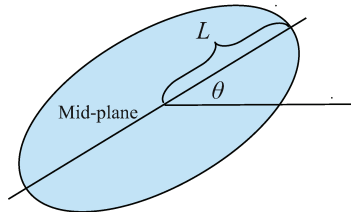


Figure 4.6: Drop elongation L and orientation angle θ measurements

deformed drop radius L/a is used to characterize the deformation instead of the Taylor deformation parameter. The second parameter is the orientation angle θ of the drop. The maximum elongation of the drop is the length of the line that connects two points at the tips of the drop located at the maximum distance apart. The angle of inclination (or orientation angle) is accordingly measured between this line and the horizontal axis.

The drop deformation at the highest subcritical capillary numbers for different viscosity ratios is presented in Fig. 4.7. As the viscosity ratio decreases the drop becomes more elongated (Fig. 4.7 (a)). The inclination angle decreases as λ decreases (Fig. 4.7 (b)).

The steady shape of the drop and internal circulations at the highest subcritical

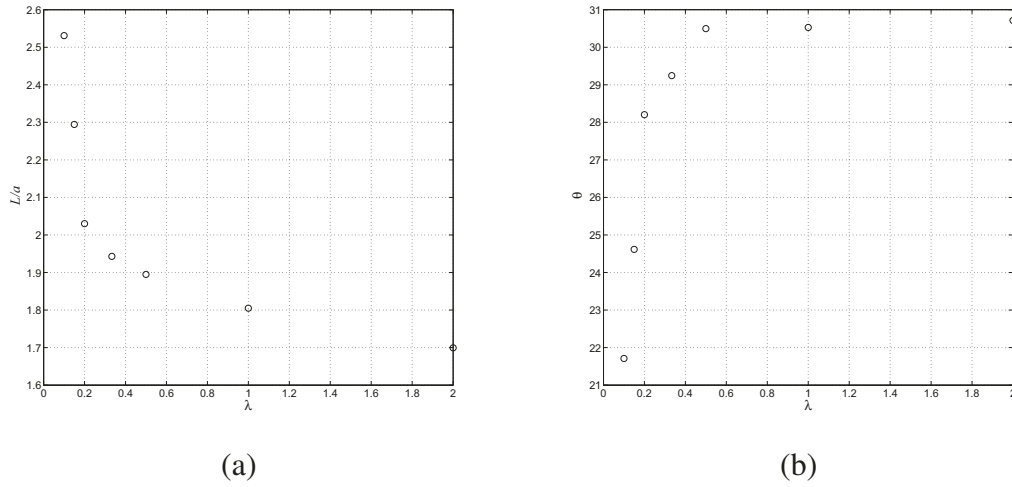


Figure 4.7: Drop deformation results at $Re = 10$. The L/a ratio (a) and the orientation angle θ (b) as a function of viscosity ratio λ at the highest subcritical Ca (the square symbols in Fig. 4.5)

capillary numbers for each viscosity ratio are depicted in Fig. 4.8. At $\lambda = 2$ the shape of the drop is almost symmetrical over the mid-plane; but the tips of the drop are slightly tilted away from the mid-plane. The drop has a ‘capsule’ shape. At $Re = 10$ (unlike Stokes flow) two vortices develop inside the drop over the entire range of λ . As λ decreases, the drop becomes more elongated and less symmetrical over the mid-plane. In addition, the drop becomes more deformable, and the internal circulations follow the pattern of the drop shape. At a viscosity ratio of 0.1, the tips of the drop are clearly tilted away from the mid-plane. The symmetry across the mid-plane is lost.

The viscosity ratio λ also significantly affects the breakup process. Consider the differences in breakup process between $\lambda = 2$ (Fig. 4.9) and 0.1 (Fig. 4.11) at the lowest supercritical capillary numbers. The evolution of drop shape and velocity field for $\lambda = 2$ at $Ca = 0.149$ is depicted in Fig. 4.9. By the time instant $\bar{t} = 19.9$, the shape of the drop is almost ellipsoidal, and only one vortex has formed inside the drop. By $\bar{t} = 39.4$, the drop becomes elongated. Starting from this time, two vortices form and they become fully-developed by $\bar{t} = 85.0$. The drop starts necking in the middle at about $\bar{t} = 104.5$. The shape of the drop changes from elongated to dumbbell. The drop continues to stretch while thinning its center portion. Eventu-

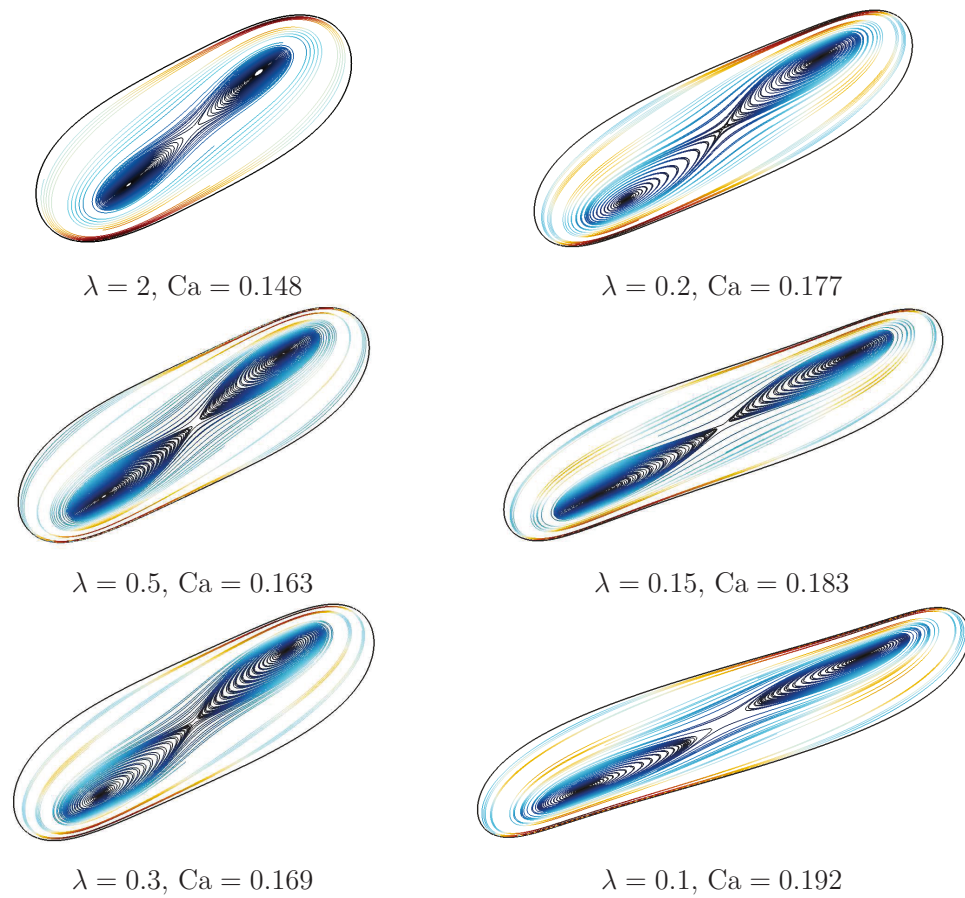


Figure 4.8: Drop shape and internal circulations at $Re = 10$ and the highest sub-critical capillary number for each viscosity ratio λ . The colour of the streamlines shows the speed based on x - and y -velocity components in the $(x - y)$ section (see Fig. 4.1) and varies from minimum (dark blue) to maximum (dark red) values

ally a thin bridge develops that connects two ‘bulbs’ formed at the ends of the drop (see time instant $\bar{t} = 132.8$). Further shearing of the drop leads to the ‘bulbs’ pinching off, forming two daughter droplets and one satellite between them ($\bar{t} = 134.1$). When the satellite drop retracts at $\bar{t} = 135.1$ a tendency to form two sub-satellite droplets can be seen (see the enlarged image in Fig. 4.10). However, the satellite drop retracts faster than the two bridges thin. Finally only one satellite drop appears ($\bar{t} = 135.7$). After breakage, the satellite drop stays stationary, while the daughter droplets move away ($\bar{t} = 137.0$). This drop breakup mechanism has been called end-pinching (Marks, 1998; Stone et al., 1986; Zhao, 2007).

The evolution of drop shape and velocity field when the viscosity ratio is $\lambda = 0.1$ at $Ca = 0.193$ is shown in Fig. 4.11. Two vortices form inside the drop right from the beginning ($\bar{t} = 18.2$). By the time instant $\bar{t} = 65.4$, the drop elongates and loses symmetry over the mid-plane. The direction of the vortices inside the drop slows down the drop elongation starting at $\bar{t} = 98.0$ (see the L/a change in time for $\lambda = 0.1$ in Fig. 4.13). At $\bar{t} = 114.3$ the drop starts rotating clockwise away from the axis of elongation. The central part of the drop is completely aligned with the flow at $\bar{t} = 125.0$. After that it continues rotation and thins. By the time instant $\bar{t} = 128.8$ a bridge that connects the ‘bulbs’ of the drop is formed. During the thinning of the bridge, the ‘bulbs’ of the drop move slowly away from each other. Finally, the bridge breaks. Three fragments are formed: two daughter droplets and one satellite drop between them ($\bar{t} = 130.2$).

For every viscosity ratio $\lambda = 2, 1, 0.5, 0.3, 0.2, 0.15$, and 0.1 only three fragments form after breakup at $Ca \sim Ca_c$ by the end-pinching mechanism: two daughter droplets and one satellite between them. In general, at higher λ the drop is more elongated before breakup. However, drop elongation before breakup strongly depends on how close the specified capillary number is to the critical value. Bławdziewicz et al. (2002) showed analytically for creeping flow conditions it is difficult to obtain accurate critical capillary numbers due to the divergence of the time required to reach stationary state. In experimental studies, there is uncertainty of determining whether a drop is gradually breaking or gradually attaining a stationary shape at shear rates very close to the critical value (Cristini et al., 2003). The same difficulty

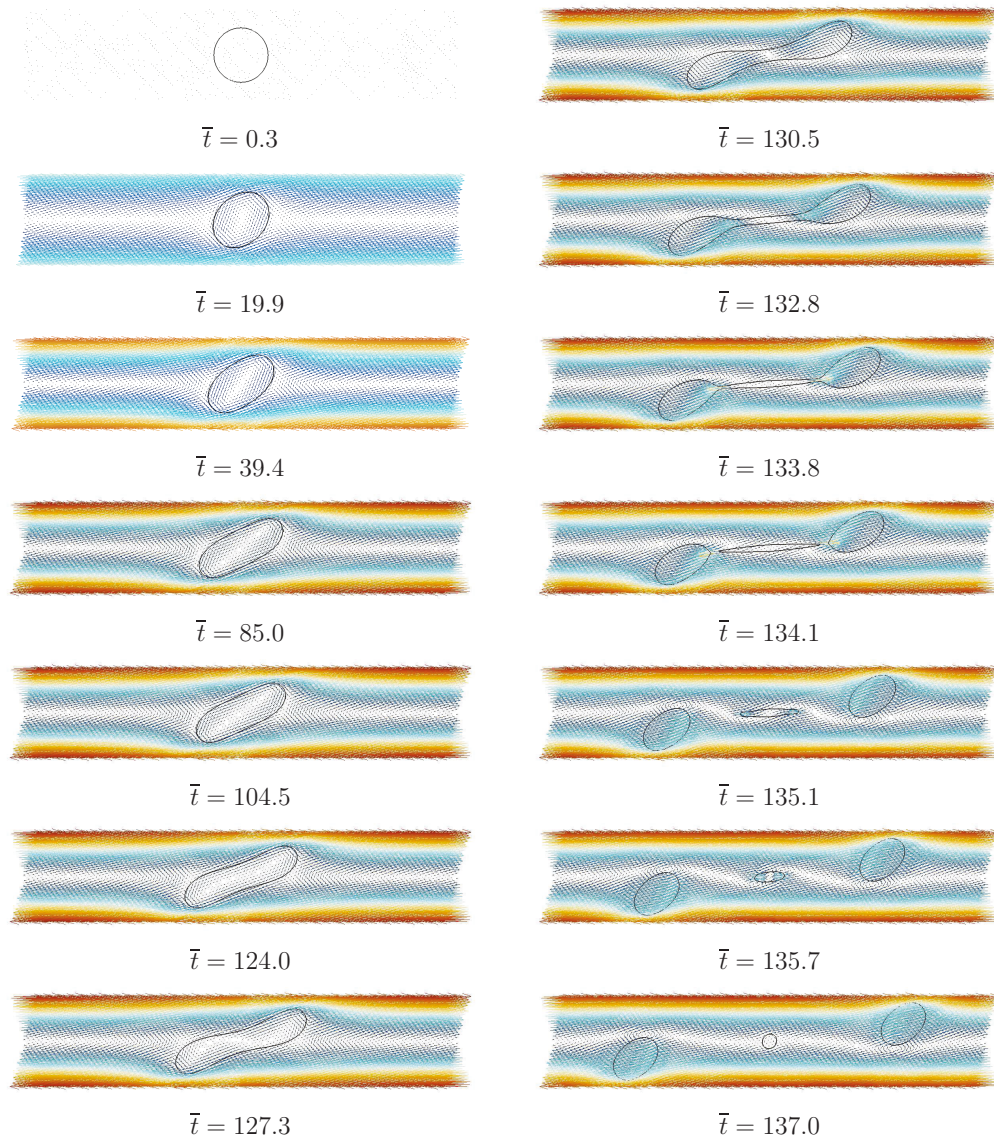


Figure 4.9: Drop shape and velocity field over time at the lowest supercritical capillary number $Ca = 0.149$, $Re = 10$, $\lambda = 2$ ($\bar{t} = t\dot{\gamma}$). The images show $\sim 40\%$ of the full domain height. Colour indicates velocity magnitude from lowest (dark blue) to highest (dark red)

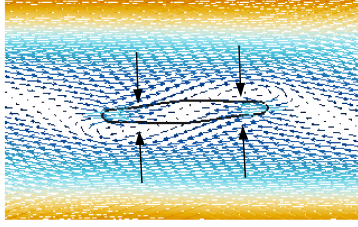


Figure 4.10: Enlarged image of satellite drop shape and velocity field at $Ca = 0.149$, $Re = 10$, $\lambda = 2$ and $\bar{t} = 135.1$ showing a tendency to form two sub-satellite drops due to formation of bridges at the locations indicated by the arrows

applies to numerical computations (Cristini and Renardy, 2006). The L/a ratio at the moment of breakage as a function of λ is plotted in Fig. 4.12. As one can see, L/a when $\lambda = 0.15$ is larger than L/a when $\lambda = 0.2$. This non-monotonic behavior is related to the time to break the drop which behaves in a complex manner as a function of λ (see Fig. 4.13 where the L/a ratio is plotted as a function of time for different λ). In each case the time needed to break the drop can be related to the orientation of the bridge under the influence of inertia. Figure 4.14 shows the drop shape and velocity field for different λ at the time just before breakup. When $\lambda = 2$ the angle between the bridge and x -direction is sharp (see Fig. 4.14). When $\lambda = 0.5$ the bridge is horizontal. For smaller viscosity ratios the bridge forms an obtuse angle with x -direction. The volume of the bridge decreases as the viscosity ratio decreases, making smaller satellite drops after breakup. In addition, the proximity of Ca to the critical value Ca_c also affects the time needed to break the drop. The rate of drop elongation at early stages of deformation steadily increases as λ decreases (see Fig. 4.13).

In addition, for every viscosity ratio the initial elongation process (from the beginning of deformation up to the moment of neck formation) is slow. Once the neck in the middle of the drop starts to form, the elongation rate increases. The same observations were reported by Stone et al. (1986) who investigated drop behavior in a linear two-dimensional flow under creeping flow conditions.

As demonstrated, for instance, by Zhao (2007) for creeping flow, the breakup process depends on the viscosity ratio and capillary number. Thus it is of interest to see these dependencies for $Re = 10$. Therefore the cases with $\lambda = 2$ and 0.1

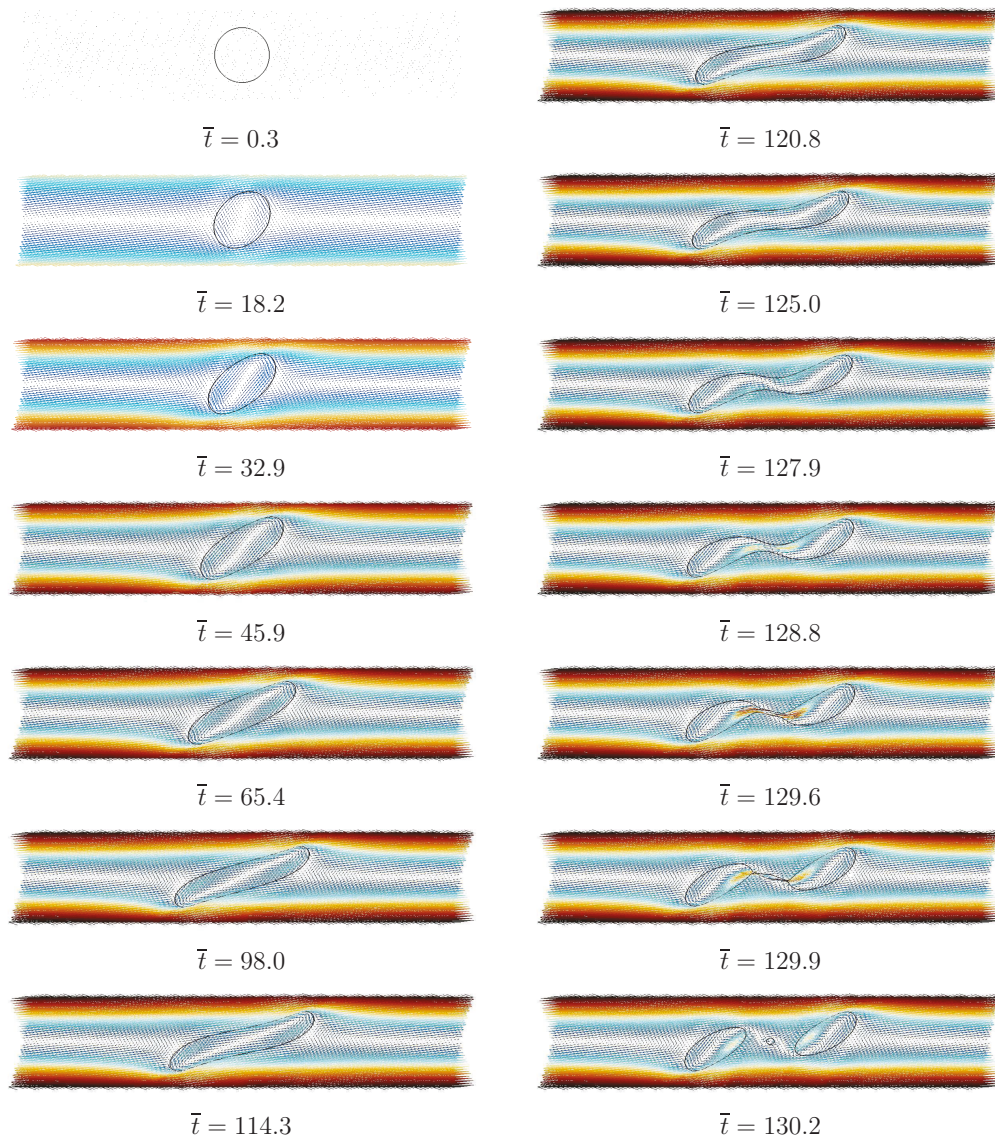


Figure 4.11: Drop shape and velocity field over time at the lowest supercritical capillary number $Ca = 0.193$, $Re = 10$, $\lambda = 0.1$. The images show $\sim 40\%$ of the full domain height. Colour indicates velocity magnitude from lowest (dark blue) to highest (dark red) values

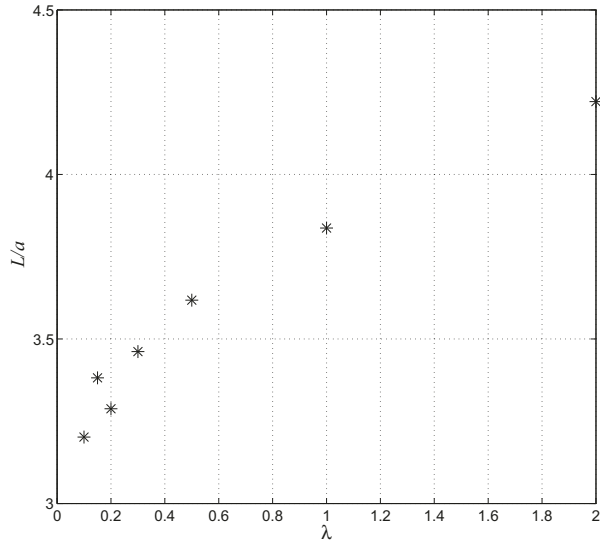


Figure 4.12: The L/a ratio at the moment of breakage as a function of viscosity ratio λ at the lowest supercritical capillary number

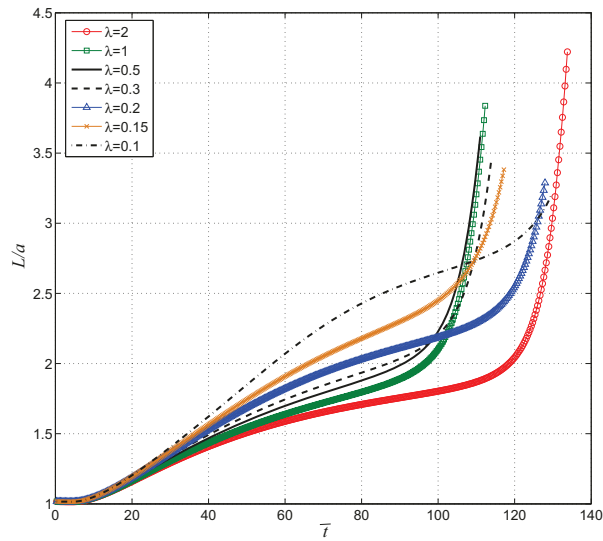


Figure 4.13: The L/a ratio as a function of time for different viscosity ratios at the corresponding lowest supercritical capillary numbers. The time series are stopped at the time instant just before the breakup event

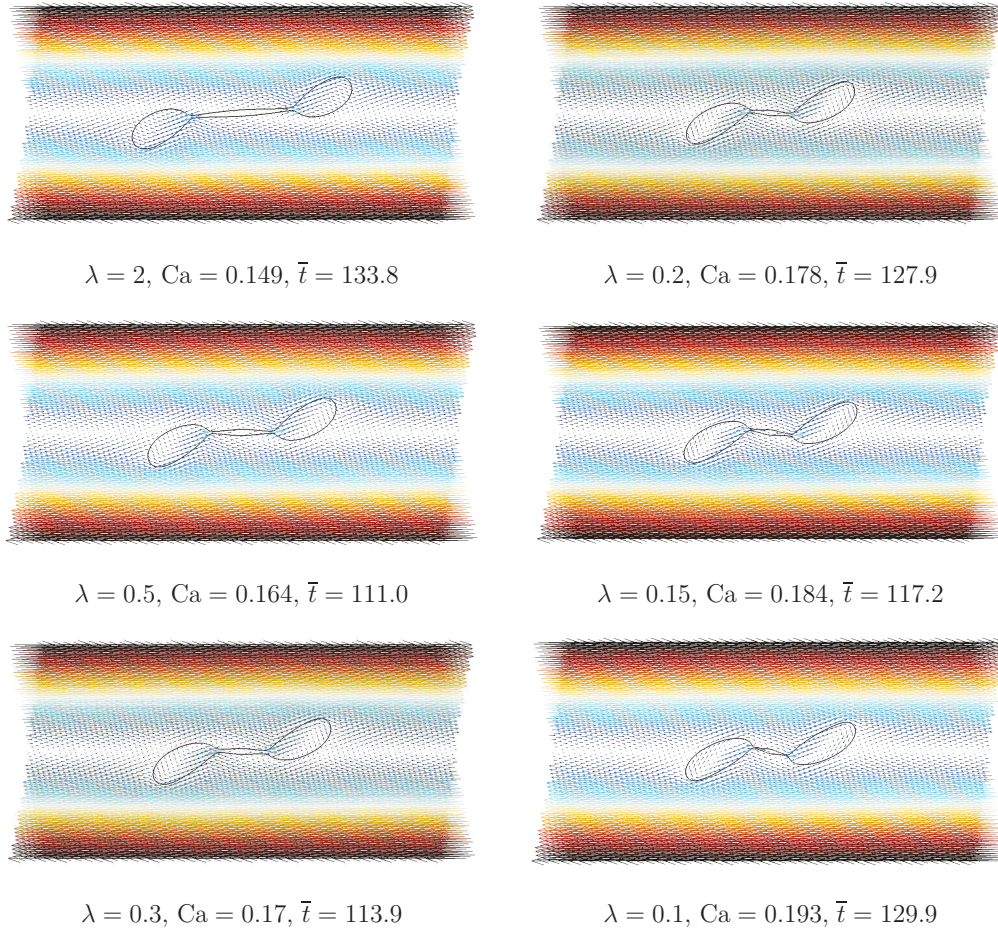


Figure 4.14: Drop shape and velocity field for different viscosity ratios at $Ca \sim Ca_c$ (the lowest supercritical value) just before breakup. Colour indicates velocity magnitude from lowest (dark blue) to highest (dark red) values

Table 4.2: Effect of mesh resolution

Drop radius a , [lu]	$\lambda = 0.1$		$\lambda = 2$	
	48	64	48	64
Highest subcritical Ca	0.191	0.192	0.151	0.148
Lowest supercritical Ca	0.192	0.193	0.152	0.149

have been studied at $Ca = 1.2Ca_c$, $Ca = 1.5Ca_c$, and $Ca = 2Ca_c$ (and as before $Re = 10$). Based on experimental observations of Zhao (2007) and our results with $Ca \sim Ca_c$ at $\lambda = 2$, at higher supercritical capillary numbers the drop will elongate more before breakup. Due to the larger elongation, longer simulation domains are required. Unless otherwise stated, the simulations were performed in $40a \times 4a \times 2a$ domains (a quarter of the full domain) with an initial undeformed drop radius $a = 48$ [lu] and interface thickness $\xi = 2$ [lu] (the Cahn number $Ch = 0.04$). The mobility coefficient Γ varied from 2 to 6 to keep the Peclet number in the range 5 to 7.

To assess the accuracy of the method at the lower mesh resolution (drop radius $a = 48$ [lu]; previously it was 64) the critical Ca for $\lambda = 0.1$ and 2 were determined and compared to the higher resolution results. The comparison is presented in Table 4.2. The deviation of Ca_c obtained at $a = 48$ and 64 is 0.5% and 2% for $\lambda = 0.1$ and 2, respectively. Good agreement is therefore demonstrated, and the lower resolution was used for further studies. Since the critical capillary numbers determined at higher mesh resolution are more accurate, their values were used in setting Ca in the simulations at the higher supercritical capillary numbers.

Drop breakup at $Ca = 1.2Ca_c$ for $\lambda = 2$ and 0.1 is shown in Fig. 4.15 (a) and (b), respectively. The deformation happens in the same manner as it does at the lowest supercritical capillary number. The drop breaks by the end-pinching mechanism. In both cases five fragments are formed after breakup. Two sub-satellites appear upon retraction of the satellite drop after the bridge breaks. Additionally, the drops are broken at different angles: compare the location of the sub-satellites for $\lambda = 2$ and 0.1 at the last frames in Fig. 4.15.

Zhao (2007) experimentally investigated drop breakup in dilute Newtonian emulsions in simple shear creeping flow over a wide range of viscosity ratios ($0.0017 < \lambda < 3.5$). It was demonstrated that a drop at $Ca \sim Ca_c$ is broken under steady shear

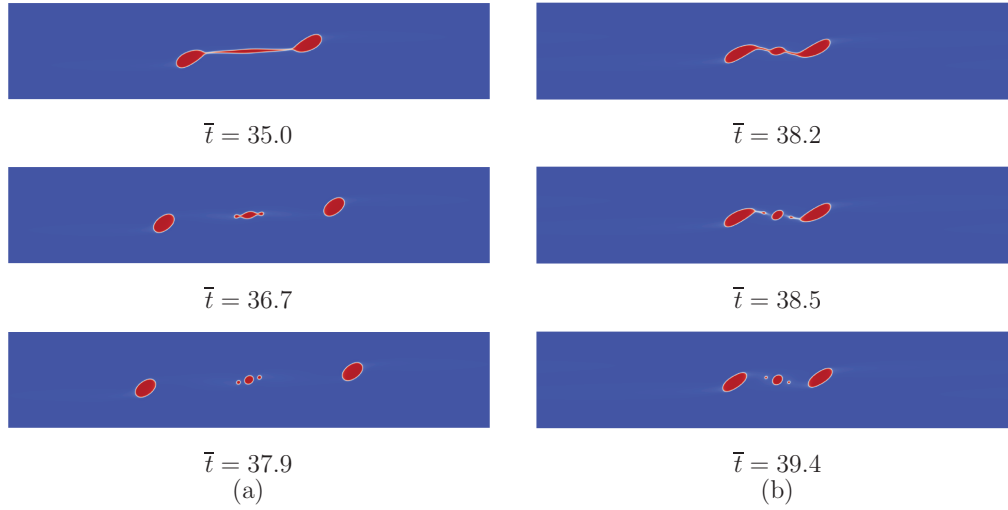


Figure 4.15: Drop breakup process at $Ca = 1.2Ca_c$: (a) $\lambda = 2$; $Ca = 0.178$ (b) $\lambda = 0.1$; $Ca = 0.231$

by the end-pinching mechanism into two equal sized daughter drops (and possible satellite and sub-satellites) for the entire range of viscosity ratio studied. Our results of drop deformation and breakup at the higher Reynolds number of $Re = 10$ at $Ca \sim Ca_c$ and $Ca = 1.2Ca_c$ are in line with these observations at lower Re . However, inertia changes the initial stages of drop deformation: it induces two vortices inside the drop and the drop loses its symmetry across the mid-plane. In contrast to this, under creeping flow conditions the initially spherical drop is deformed into an ellipsoid. The rest of the breakup process occurs in the same manner in both cases: the drop stretches forming a neck in the middle. Eventually the neck breaks after thinning and the drop disintegrates into two daughter drops separated by smaller satellite and sub-satellite drops. In addition it was outlined by Zhao (2007) that as λ decreases, the ends of the deformed drop become more slender and increasingly pointed. Similar behavior is seen at our higher Reynolds number (compare the drop ends in Fig. 4.14 for $\lambda = 2$ and $\lambda = 0.1$).

The drop breakup processes at $Ca = 1.5Ca_c$ when $\lambda = 2$ and 0.1 are presented in Fig. 4.16 (a) and (b), respectively. The initial drop deformation happens in the same manner as it does for lower capillary numbers for each viscosity ratio. At $\bar{t} = 22.6$ the drop with $\lambda = 2$ starts necking while the drop when $\lambda = 0.1$ is still

elongating. Because of the high viscosity of the dispersed phase ($\lambda = 2$), the drop is significantly stretched. As a result the bridge thins forming two necks ($\bar{t} = 31.5$), and then the drop ends pinch off ($\bar{t} = 33.6$). The daughter droplets move away from each other. The central thread retracts after breakup, forming satellite drops at both ends ($\bar{t} = 35.9$). At later time, the thread is broken by the end-pinching mechanism. In the end, eight fragments are produced after breakup ($\bar{t} = 39.1$). When $\lambda = 0.1$, the drop is less elongated compared to the case with $\lambda = 2$. After the first breakup event ($\bar{t} = 32.7$) the fragments move slowly away from each other while the central portion of the drop retracts. The neck formed in the middle ($\bar{t} = 34.7$) is not thin enough to break. Eventually only five fragments are formed. Thus shear of a more viscous drop at $Ca = 1.5Ca_c$ produces more drops than shear of a less viscous drop. In addition, daughter droplets move away faster from each other when $\lambda = 2$ compared to $\lambda = 0.1$.

It is necessary to note that small satellite and especially sub-satellite drops disappear almost immediately after formation (e.g. see Fig. 4.16 (a) frames at $\bar{t} = 37.9$ and $\bar{t} = 39.1$). That means higher mesh resolution, i.e. larger initial drop radius in lattice units, is required to resolve drops of this size (see (Komrakova et al., 2013) for details, where it was shown that increasing resolution allows smaller drops relative to the initial drop size to remain). Additionally, the domain length for the case with $\lambda = 2$ is not enough (the drop wraps around the ends of the periodic domain, see last frame in Fig. 4.16 (a)). Nevertheless, the drop breakup in the domain center is not affected by this event.

The drop breakup process at $Ca = 2Ca_c$ and $\lambda = 0.1$ is shown in Fig. 4.17. The drop is broken into nine fragments by repetition of the end-pinching mechanism. As noted by Zhao (2007) in Stokes flow, the drops deform into longer threads with increasing capillary number. The same conclusion holds at $Re = 10$ for viscosity ratios of 0.1 and 2.

If a drop with $\lambda = 2$ is sheared at $Ca = 2Ca_c$, significant elongation is expected before breakup. Moreover, a thin cylindrical thread is expected to appear. In order to resolve small fragments and avoid influence of horizontal periodicity, it is necessary to run this simulation in a longer domain and with a higher mesh resolution.

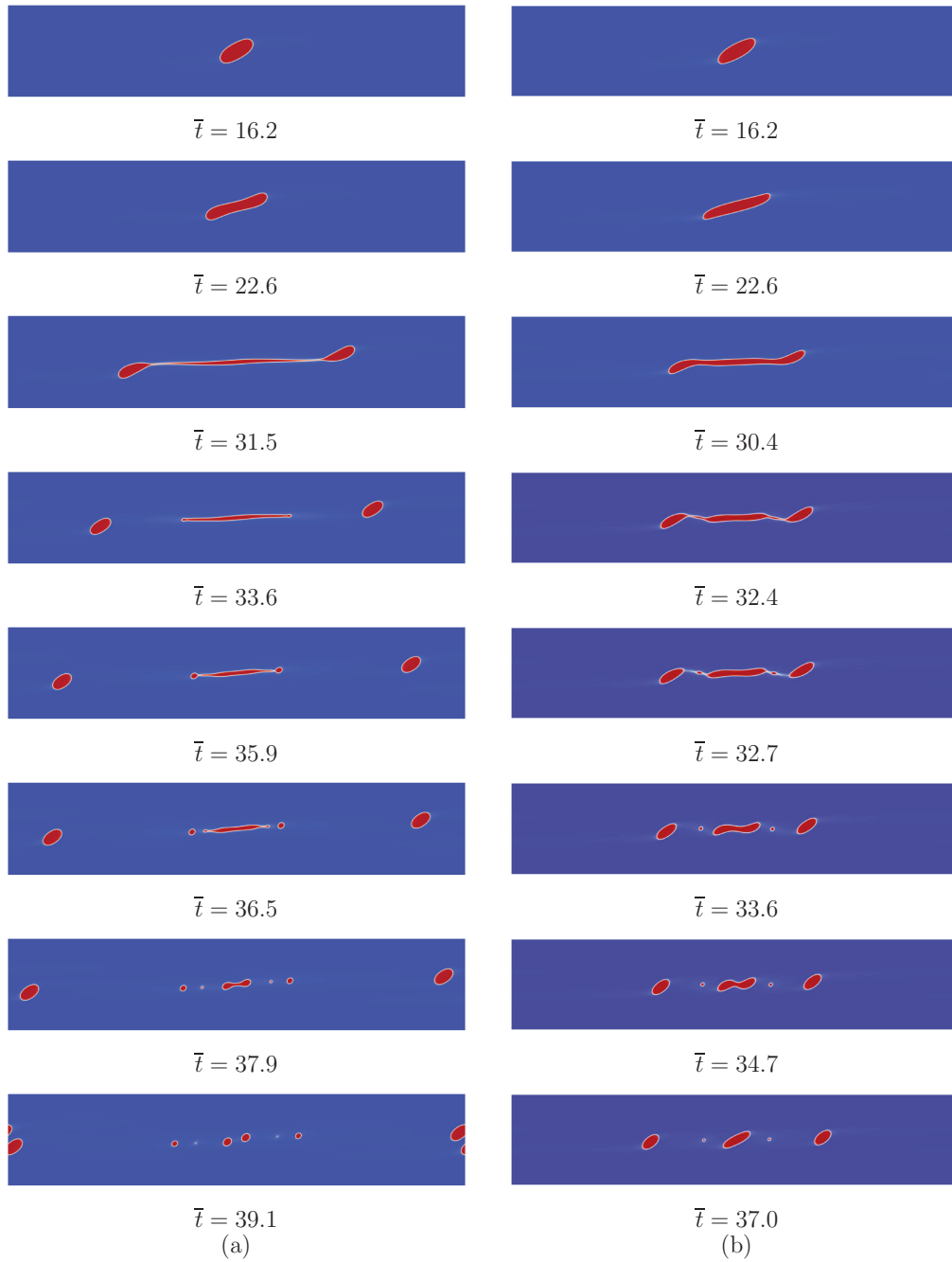


Figure 4.16: Drop breakup process at $Ca = 1.5Ca_c$: (a) $\lambda = 2$; $Ca = 0.223$ (b) $\lambda = 0.1$; $Ca = 0.289$

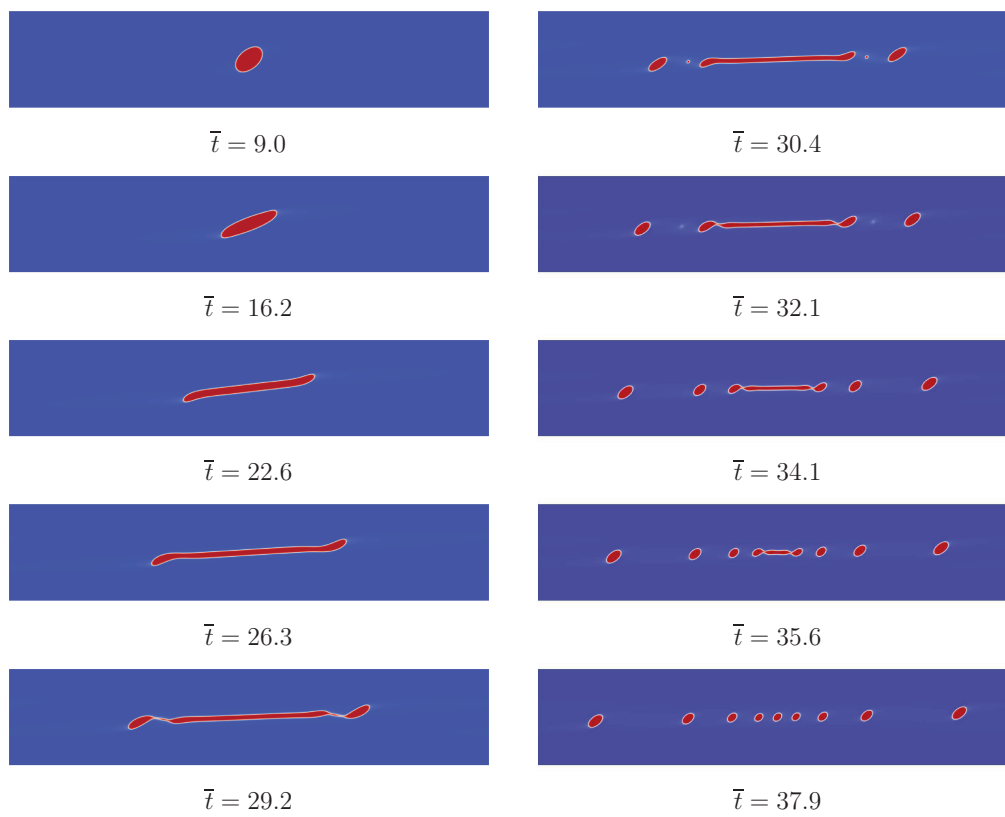


Figure 4.17: Drop breakup process at $Ca = 2Ca_c = 0.385$ and $\lambda = 0.1$

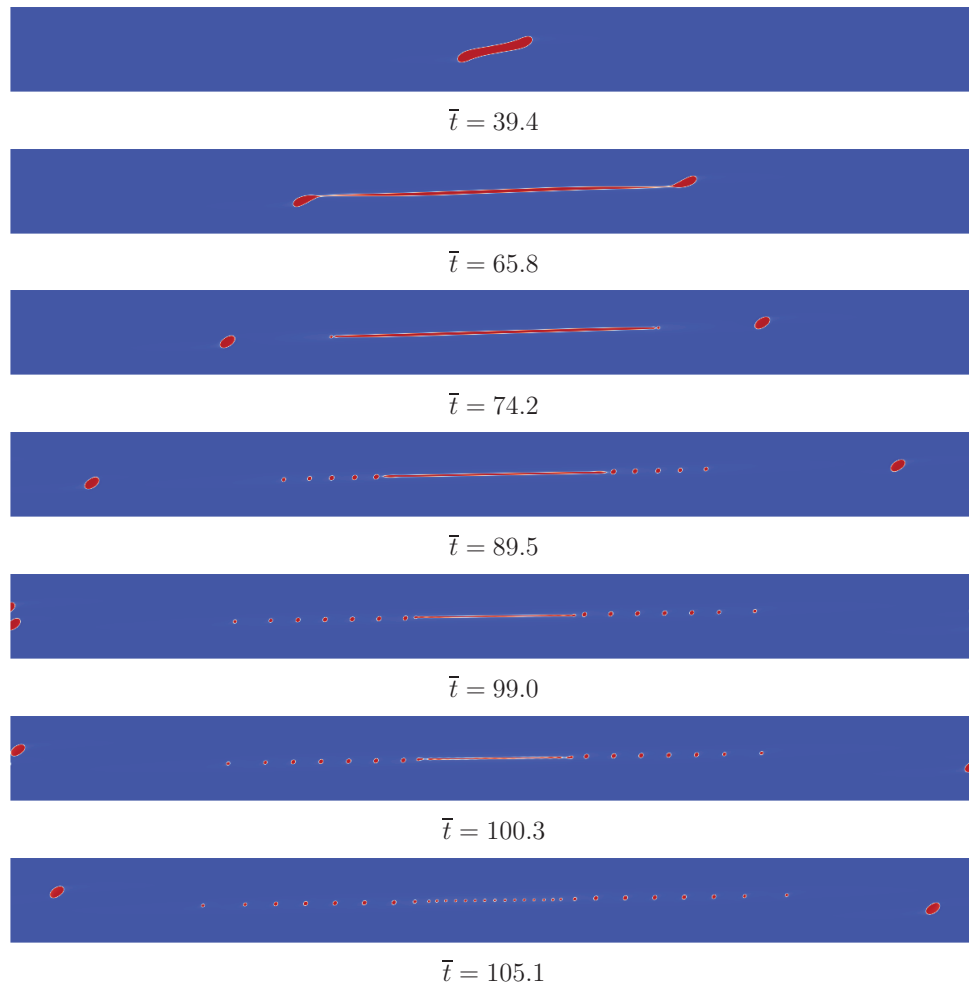


Figure 4.18: Drop breakup process at $Ca = 2Ca_c = 0.297$ and $\lambda = 2$

Therefore an undeformed drop radius of $a = 64$ [lu] and a $91.5a \times 4a \times 2a$ simulation domain were chosen. The results are presented in Fig. 4.18. As expected, the high λ and Ca values cause the formation of a long thin thread that connects the drop ends ($\bar{t} = 65.8$). After the first breakup by end-pinching, two daughter droplets appear. Next, the thread breaks by the end-pinching mechanism again, producing drops of almost equal size but slightly smaller compared to the first drops. Eventually, the cylindrical thread stretches sufficiently that capillary wave breakup occurs ($\bar{t} = 100.3$) due to the growth of axial fluctuations in the thread diameter (Marks, 1998). Moreover, this event produces drops of equal size ($\bar{t} = 105.1$). Enlarged images of the capillary wave breakup event are presented in Fig. 4.19.

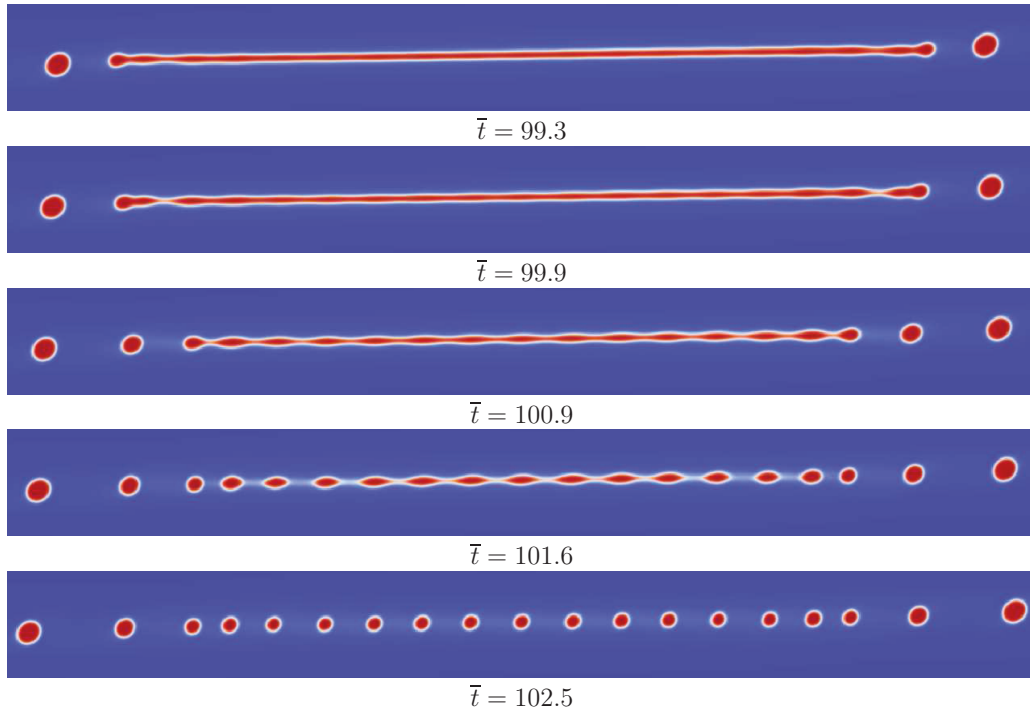


Figure 4.19: Capillary wave breakup at $Ca = 2Ca_c$ and $\lambda = 2$ (The images show a portion of the full domain)

4.5 Conclusions

A free energy lattice Boltzmann method was used to perform three-dimensional simulations of single liquid drops suspended in another liquid and subjected to simple shear flow. The guidelines presented by Komrakova et al. (2013) were used to choose the parameters of the numerical method. In this paper, the influence of dispersed phase viscosity on the behavior of sheared drops with inertia ($Re = 10$) was investigated.

A validation simulation of stratified shear flow was conducted to show that the numerical method can handle viscosity ratios (dispersed phase viscosity over continuous phase viscosity) in a range $\lambda = 0.1 - 2$. The results at worst deviated 2.5% from the analytical solution at $\lambda = 2$, and were within 1% for the rest of the λ values.

High resolution simulations were performed over the range of viscosity ratios $\lambda = 0.1 - 2$ at different capillary numbers. The critical capillary number Ca_c for

every λ was determined. The Ca_c value decreases as λ increases. At the highest subcritical capillary number, the drop becomes less elongated and more oriented towards the vertical axis with increasing viscosity ratio. Unlike creeping flow, at $Re = 10$ two vortices form inside the drop and loss of symmetry across the mid-plane of the drop is observed.

The results show how the breakup process depends on the viscosity ratio and the capillary number. High λ values result in significant drop elongation before breakup. However, the elongation depends on the specified capillary number. Drop breakup due to end-pinching was observed in every simulation performed: ‘bulbs’ form at the ends of the stretched drop and eventually pinch off. The first breakup event produces the largest daughter droplets for every viscosity ratio considered. Depending on the volume of the center portion of the drop, further breakups might occur. The number of fragments is a function of the viscosity ratio and capillary number. As Ca increases the number of produced fragments increases. More fragments are formed for higher λ at a given ratio between specified capillary number and the critical capillary number corresponding to each λ . For $\lambda = 0.1$ drops only break by the end-pinching mechanism at $Ca_c \leq Ca \leq 2Ca_c$. When $\lambda = 2$ at $Ca = 2Ca_c$ the tread becomes sufficiently elongated that capillary wave breakup occurs. Thus the necessary condition for the capillary wave breakup is a sufficiently high capillary number (for given λ) to stretch the drop to a sufficient thinness. For the low viscosity ratio $\lambda = 0.1$, $Ca = 2Ca_c$ is insufficient to break the drop by the capillary wave breakup mechanism.

At the lowest supercritical capillary number, the rate of drop elongation during the initial stage of deformation increases as λ decreases. The time needed to break the drop is related to the orientation of the bridge that connects the ends of the drop. The bridge volume decreases as λ decreases.

The results of the present study can find industrial applications, such as in production and processing of emulsions and liquid-liquid dispersion. In these processes, the drop size distribution of the final product is of great importance. The proposed numerical method could be used to determine the drop size distribution (DSD) of given liquids and shearing conditions. Alternatively, the shearing condi-

tions required for a desired DSD can be estimated. For instance, capillary wave breakup produces drops of equal size. Knowledge of the conditions when this breakup mechanism occurs may improve the efficiency of monodisperse emulsion production. Moreover, the sizes of the daughter droplets formed as a result of the breakage event for $\lambda = 0.1$ at $Ca = 2Ca_c$ are also nearly monodisperse. This phenomenon can be used for production of monodisperse emulsions in a device as simple as a colloid mill, representing a narrow gap Taylor-Couette device.

References

- V. Badalassi, H. Cenicerros, and S. Banerjee. Computation of multiphase systems with phase field models. *J. Comp. Phys.*, 190:371–397, 2003.
- P. L. Bhatnagar, E. P. Gross, and M. Krook. A model for collision processes in gases. I. Small amplitude processes in charged and neutral one-component systems. *Phys. Rev.*, 94:511–525, 1954.
- J. Bławdziewicz, V. Cristini, and M. Loewenberg. Critical behavior of drops in linear flows: I. Phenomenological theory for drop dynamics near critical stationary states. *Phys. Fluids*, 14:2709–2718, 2002.
- J. Boxall, C. Koh, E. Sloan, A. Sum, and D. Wu. Droplet size scaling of water-in-oil emulsions under turbulent flow. *Langmuir*, 28:104–110, 2011.
- A. J. Bray. Theory of phase-ordering kinetics. *Adv. Phys.*, 43:357–459, 1994.
- J. W. Cahn and J. E. Hilliard. Free energy of a nonuniform system. I. Interfacial free energy. *J. Chem. Phys.*, 28:258–267, 1958.
- V. Cristini and Y. Renardy. Scalings for droplet sizes in shear-driven breakup: non-microfluidic ways to monodisperse emulsions. *FDMP*, 2:77–93, 2006.
- V. Cristini, S. Guido, A. Alfani, J. Bławdziewicz, and M. Loewenberg. Drop breakup and fragment size distribution in shear flow. *J. Rheol.*, 47:1283–1298, 2003.
- H. Ding, P. Spelt, and C. Shu. Diffuse interface model for incompressible two-phase flows with large density ratios. *J. Comp. Phys.*, 226:2078–2095, 2007.

- I. Fjelde. Formation damages caused by emulsions during drilling with emulsified drilling fluids. *SPE*, 105858:1–8, 2007.
- H. Grace. Dispersion phenomena in high viscosity immiscible fluid systems and application of static mixers as dispersion devices in such systems. *Chem. Eng. Commun.*, 14:225–277, 1982.
- D. Jacqmin. Calculation of two-phase NavierStokes flows using phase-field modeling. *J. Comp. Phys.*, 155:96–127, 1999.
- V. Kendon, M. Cates, I. Pagonabarraga, J.-C. Desplat, and P. Bladon. Inertial effects in three-dimensional spinodal decomposition of a symmetric binary fluid mixture: a lattice boltzmann study. *J. Fluid Mech.*, 440:147–203, 2001.
- D. Khismatullin and Y. Renardy. Inertia-induced breakup of highly viscous drops subjected to simple shear. *Phys. Fluids*, 15:1351–1354, 2003.
- A. Komrakova, O. Shardt, D. Eskin, and J. Derksen. Lattice Boltzmann simulations of drop deformation and breakup in shear flow. *IJMF*, accepted, 2013.
- H. Kusumaatmaja. *Lattice Boltzmann Studies of Wetting and Spreading on Patterned Surfaces*. PhD thesis, University of Oxford, 2008.
- A. J. C. Ladd. Numerical simulations of particulate suspensions via a discretized Boltzmann equation Part I. Theoretical foundation. *J. Fluid Mech.*, 271:285–309, 1994.
- C. Marks. *Drop breakup and deformation in sudden onset strong flows*. PhD thesis, University of Maryland, 1998.
- O. Penrose and P. Fife. Thermodynamically consistent models of phase-field type for the kinetics of phase transitions. *Physica D*, 43:44–62, 1990.
- J. Rallison. The deformation of small viscous drops and bubbles in shear flow. *Ann. Rev. Fluid Mech.*, 16:45–66, 1984.

- Y. Renardy and V. Cristini. Effect of inertia on drop breakup under shear. *Phys. Fluids*, 13:7–13, 2001.
- P. Rueger and R. Calabrese. Dispersion of water into oil in a rotor-stator mixer. Part 1: drop breakup in dilute systems. *Chem. Eng. Res. Des.*, 91:2134–2141, 2013.
- F. Rumscheidt and S. G. Mason. Particle motions in sheared suspensions. XII. deformation and burst of fluid drops in shear and hyperbolic flow. *J. Colloid Sci.*, 16:238–261, 1961.
- O. Shardt, J. Derksen, and S. Mitra. Simulations of droplet coalescence in simple shear flow. *Langmuir*, 29:6201–6212, 2013.
- H. Stone. Dynamics of drop deformation and breakup in viscous fluids. *Annu. Rev. Fluid Mech.*, 26:65–102, 1994.
- H. Stone, B. Bentley, and G. Leal. An experimental study of transient effects in the breakup of viscous drops. *J. Fluid Mech.*, 173:131–158, 1986.
- M. Swift, E. Orlandini, W. Osborn, and J. Yeomans. Lattice Boltzmann simulations of liquid-gas and binary fluid systems. *Phys. Rev. E*, 54:5041–5052, 1996.
- G. Taylor. The viscosity of a fluid containing small drops of another fluid. *Proc. R. Soc. Lond. A*, 138:41–48, 1932.
- G. Taylor. The formation of emulsions in definable fields of flow. *Proc. R. Soc. Lond. A*, 146:501–523, 1934.
- R.G.M. van der Sman and S. van der Graaf. Emulsion droplet deformation and breakup with Lattice Boltzmann model. *Comp. Phys. Commun.*, 178:492–504, 2008.
- P. Yue, J. Feng, C. Liu, and J. Shen. A diffuse-interface method for simulating two-phase flows of complex fluids. *J. Fluid Mech.*, 515:293–317, 2004.
- X. Zhao. Drop breakup in dilute Newtonian emulsions in simple shear flow: new drop breakup mechanisms. *J. Rheol.*, 51:367–392, 2007.

Chapter 5

Numerical study of turbulent liquid-liquid dispersions¹

5.1 Introduction

Turbulently-induced mixing of two immiscible liquids is a common operation in chemical, petroleum, pharmaceutical, mining, and food industries. Even though liquid-liquid mixing has been extensively studied experimentally and theoretically in terms of hydrodynamic and interface science aspects, the process remains as one of the most difficult and least understood mixing problems (Paul et al., 2004). A broad range of experimental research has resulted in practical correlations to characterize liquid-liquid dispersions (Berkman and R.V., 1988; Boxall et al., 2011; Brown and Pitt, 1972; Calabrese et al., 1986; Collins and Knudsen, 1970; Davies, 1987; Ravelet et al., 2007; Rueger and Calabrese, 2013; Sleicher, 1962; Weinstein and Treybal, 1973). With the rapid development of computational facilities, modelling and numerical simulation became valuable additions to the experiments in order to study dispersed systems.

Detailed characterization of two liquids mixing and interactions of dispersed and carrying phases requires a two-phase flow method that resolves the interface. Interface-tracking (e.g. boundary-integral, finite-element, and immersed boundary) and interface-capturing (lattice Boltzmann, level-set, volume-of-fluid (VOF), and phase-field) methods have been used to perform multi-phase simulations (Cristini

¹A version of this chapter will be submitted to a journal.

and Tan, 2004). In interface-tracking methods the interface between the fluids is sharp and fluid properties vary discontinuously over the interface. These methods are very accurate for simulating the onset of breakup and coalescence, but do not work through the transitions: in order to break or merge drops, complex somewhat arbitrary ‘cut-and-connect’ algorithms have to be employed to change the topology of the meshes (Cristini and Tan, 2004). In interface-capturing methods, the interface is implicitly captured by volume functions that use the data from the same fixed grid on which the flow is calculated. Fluid properties change smoothly over the diffuse interface between two fluids. These methods do not require any ‘cut-and-connect’ operations, no interface treatments or reconstructions are needed which makes them suitable for simulating breakup and coalescence in immiscible two-fluid systems (Cristini and Tan, 2004). In the present study, a diffuse interface free energy lattice Boltzmann equation (LBE) method (Swift et al., 1996) is adopted for turbulent liquid-liquid dispersion simulations. In addition, the physics of drop interaction on the microscopic level can be naturally incorporated. Moreover, the important advantages of LBE are simplicity of programming and parallelization of the algorithm which allows for very detailed simulations.

The first attempt to perform direct numerical simulations (DNSs) of turbulent dispersed liquid-liquid flows using LBE has been done by Derksen and Van den Akker (2007). An isothermal model based on kinetic theory proposed by He et al. (1999) was used for two-phase flow modeling. The authors presented a novel multi-scale approach to model the dynamics of liquid-liquid dispersion in a fully periodic three-dimensional domain in which homogeneous isotropic turbulence was generated by means of random forcing. The promising results showed that the proposed numerical approach can contribute to understanding of immiscible liquids mixing.

Droplet breakup in homogeneous and isotropic turbulence was numerically simulated by Toschi et al. (2010) using LBE. The authors utilized the multi-component Shan-Chen model (Shan and Chen, 1993) for two-phase flow modeling, supplemented with a large scale force to stir turbulence. The method was validated and applied for the study of turbulent emulsion flow (Biferale et al., 2011); the proba-

bility distribution function of droplets' accelerations was presented.

The droplet size distribution of water-in-oil type emulsions of a moderate viscosity ratio of 0.3 and with oil-soluble amphiphilic surfactant in forced, steady, homogeneous turbulence was studied using lattice Boltzmann simulations by Skartlien et al. (2013). The details of the numerical method can be found in (Nekovee et al., 2000). The authors studied the effect of surfactant on the DSD defined under different levels of turbulent kinetic energy.

In the present study, DNSs are performed to study a turbulently agitated liquid-liquid dispersion. Large-scale parallel computations are carried out in three-dimensional, fully-periodic cubic domains. In such domains, a stationary homogeneous isotropic turbulence is generated by means of linear forcing (Lundgren, 2003). The resolved Kolmogorov scales range from $\eta_K = 1$ to 10 dimensionless lattice units [lu]. Two considered sizes of the domain edge L_d are 500 and 1000 [lu]. To check that the simulation domain size is sufficiently large to avoid self-correlation, the single-phase turbulence is examined before introduction of the second phase.

The physical size of a simulation domain is 1.76^3 mm^3 (with $L_d = 500$ [lu]) and 3.52^3 mm^3 (with $L_d = 1000$ [lu]) which is much smaller than the volume of any standard mixing device. The results obtained even in such a domain can be useful for industrial applications. A wide variety of mixing devices are used to produce liquid-liquid dispersions. Among them are stirred tanks, static mixers, and rotor-stator mixers. Each device has different geometry and capacity, creates various flow structures, and provides a range of agitation rates. The properties of the produced dispersion, such as stability, apparent viscosity, rheology, and interfacial area available for transfer processes, are determined by the size of the drops in the system. The resulting drop size distribution (DSD) and the specified energy input (that is defined by capabilities of a mixing device) are closely related (Rueger and Calabrese, 2013). It was experimentally demonstrated by Cutter (1966) that in stirred tanks which are widely used for dispersion formation, the dissipation of power is inhomogeneous, which causes spatial variations of the DSD. Thus the drop sizes can be related not to an average power input but to a local value of energy dissipation. Davies (1987) showed that the relationship between the local power dissipation per

unit mass of the liquid and the DSD (represented by the maximum stable drop diameter, d_{\max}) is independent of the specifics of the mixer geometry, and can be applied for different mixing devices. Later Zhou and Kresta (1998) experimentally proved an idea of Hinze (1955) that the maximum local energy dissipation rate creates the stresses that eventually break the drops. Therefore, in order to break a drop to a desired size a certain intensity of the maximum local shear stress is needed which requires a specified local energy dissipation rate (Rueger and Calabrese, 2013). Thus energy input per unit mass (or energy dissipation rate) in a domain considered in the present study can be considered as a local value compared to the size of industrial equipment. It is possible to relate the local energy dissipation rate and parameters of the dispersion. In addition, homogeneous isotropic turbulence generated throughout the domain minimizes the effects of non-homogeneity, allowing to obtain more fundamental results.

The free energy LBE method for two-phase flow modeling is a diffuse interface method. The interface evolves naturally due to the thermodynamic mechanism employed. However, diffuse interface methods suffer from numerical dissolution of small droplets (Van der Sman and Van der Graaf, 2008). Our previous studies (Komrakova et al., Jeju, Korea, May 26-31) outlined that in order to mitigate the drop dissolution effect, it is necessary to increase the resolution of the Kolmogorov scales which are the smallest dynamic scales in the turbulent field, and have the smallest size of drops in the range 20 – 30 [μ]. One of the goals of this study is to show that the dissolution effect can be mitigated if this condition is satisfied. In addition, a drawback of the method is that it exhibits unphysically easy coalescence when drops are in close proximity (Jia et al., 2008). This issue will also be addressed in this study.

The numerical method was verified and validated using simulations of drop deformation and breakup in simple shear flow (Komrakova et al., 2014a,b). The effects of interface-related numerical parameters on accuracy and stability were demonstrated by Komrakova et al. (2014a). The authors established guidelines on how to specify these parameters to reveal physically realistic drop behavior. These guidelines were successfully applied to investigate the effect of dispersed phase vis-

cosity on the behavior of a sheared drop at a drop Reynolds number $Re = 10$ over a range of viscosity ratios $\lambda = 0.12$ (dispersed phase viscosity over continuous phase viscosity). The guidelines and results obtained in the sheared drop simulations of (Komrakova et al., 2014a,b) are used in the present study to determine the numerical parameters for turbulently flowing two-phase system. Effects of Kolmogorov scale resolution and dispersed phase volume fraction (ranging from 0.001 to 0.2) on dispersion formation are examined. The process of dispersion formation is visualized, capturing drop breakup and coalescence on the microscopic scale. In each case the drop size distribution and mean diameters are determined and related to turbulent properties.

The rest of the paper is organized as follows. Section 5.2 contains the details of the numerical method. The simulation parameters are presented in Section 5.3. The results of one- and two-phase flow simulations are presented in Sections 5.4 and 5.5, respectively. Finally, conclusions are drawn in Section 5.6.

5.2 Mathematical formulation

A diffuse interface free energy lattice Boltzmann equation method proposed by Swift et al. (1996) is adopted here to perform the simulations. The details of diffuse interface (or phase field) methods can be found in (Jacqmin, 1999; Magaletti et al., 2013; Yue et al., 2004). The interface between the two components is represented by a thin transition region with a finite thickness in which the composition varies smoothly. The order parameter ϕ which is the relative concentration of the two components (Badalassi et al., 2003; Cahn and Hilliard, 1958; Penrose and Fife, 1990) describes the composition of the system. To simulate the fluid dynamics of the binary mixture of fluids, the continuity and momentum equations are solved in conjunction with Cahn Hilliard convection-diffusion equation for the order parameter (Bray, 1994). The evolution of density, velocity and order parameter are governed by the continuity, momentum, and convection-diffusion equations, re-

spectively (Kendon et al., 2001):

$$\partial_t \rho + \partial_\alpha (\rho u_\alpha) = 0 \quad (5.1a)$$

$$\partial_t (\rho u_\alpha) + \partial_\beta (\rho u_\alpha u_\beta) = -\partial_\beta P_{\alpha\beta}^{th} + \partial_\beta \nu (\rho \partial_\alpha u_\beta + \rho \partial_\beta u_\alpha) + \rho F_{t\alpha} \quad (5.1b)$$

$$\partial_t \varphi + \partial_\alpha (\varphi u_\alpha) = M \partial_{\beta\beta}^2 \mu \quad (5.1c)$$

where u_α is the velocity; the index α stands for the Cartesian directions x , y and z ; ρ and ν are the density and the kinematic viscosity of the mixture, respectively. Here $P_{\alpha\beta}^{th}$ is the ‘thermodynamic’ pressure tensor. It contains two parts (Kendon et al., 2001): an isotropic contribution $P\delta_{\alpha\beta}$ that represents the ideal gas pressure and the ‘chemical’ pressure tensor $P_{\alpha\beta}^{chem}$. The chemical potential in equation (5.1c) is: $\mu(\varphi) = A\varphi - A\varphi^3 - \kappa \partial_{\alpha\alpha}^2 \varphi$. Here, $A < 0$ and κ are parameters of the free energy model that are related to the surface tension and interface thickness; M is the mobility; $F_{t\alpha}$ is the forcing term to generate turbulence (discussed below).

Two distribution functions are utilized to solve system (5.1): one function $f(\mathbf{r}, t)$ is used to solve the continuity (5.1a) and Navier-Stokes (5.1b) equations and the second one $g(\mathbf{r}, t)$ is used for the convection-diffusion equation (5.1c). The distribution functions evolve by a time step Δt . All simulations have been performed using a single relaxation time collision operator (Bhatnagar-Gross-Krook (BGK) model (Bhatnagar et al., 1954)). The discrete lattice Boltzmann equations for the evolution of f and g have the following form:

$$\begin{aligned} f_q(r_\alpha + c_{\alpha q}\Delta t, t + \Delta t) - f_q(r_\alpha, t) &= -\frac{f_q - f_q^{eq}}{\tau_f} + F_q, \\ g_q(r_\alpha + c_{\alpha q}\Delta t, t + \Delta t) - g_q(r_\alpha, t) &= -\frac{g_q - g_q^{eq}}{\tau_g}, \end{aligned} \quad (5.2)$$

where the index q counts over the number of the discrete velocity directions; f_q^{eq} , g_q^{eq} are the discretized Maxwell-Boltzmann distributions (or equilibrium distributions); F_q is the forcing term; $c_{\alpha q}$ denotes the discrete velocity set and τ_f and τ_g are dimensionless relaxation parameters. The equilibrium distributions f_q^{eq} , g_q^{eq} are given in Kusumaatmaja (2008). The D3Q19 lattice is adopted here where $D = 3$ denotes three-dimensional flow and $Q = 19$ is the number of velocities. In this lattice arrangement, each site communicates with its six nearest and twelve diagonal

neighbors. The lattice Boltzmann method operates in dimensionless lattice units [lu] (lattice space, time step, and lattice density for the length, time and density units, respectively). For the method described here, only uniform cubic lattices can be used; the mesh step Δx is taken as unity, as is the time step Δt .

The distribution functions are defined such that the following summations over all directions q at each lattice point give the local density of the fluid ρ , the local fluid momentum ρu_α and the local order parameter φ , respectively:

$$\sum_q f_q = \rho \quad \sum_q c_{\alpha q} f_q = \rho u_\alpha + \frac{F_{t\alpha}}{2} \quad \sum_q g_q = \varphi \quad (5.3)$$

The forcing term is incorporated as follows:

$$F_q = w_q (c_{\alpha q} F_{t\alpha}) \quad (5.4)$$

where $F_{t\alpha}$ is the macroscopic force embedded in momentum equation (5.1b) and w_q are the weight coefficients (Kusumaatmaja, 2008).

In order to consider two liquids with different kinematic viscosities, the kinematic viscosity of the mixture ν is set to be a linear function of the order parameter φ :

$$\nu(\varphi) = \nu_c \frac{\varphi_0 - \varphi}{2\varphi_0} + \nu_d \frac{\varphi_0 + \varphi}{2\varphi_0} \quad (5.5)$$

where ν_c and ν_d are the kinematic viscosities of continuous and dispersed phases, respectively; and $\varphi = \pm\varphi_0 = \pm 1$ is the value of the order parameter in the bulk phase on either side of the interface. The relaxation parameter for f_q varies with the composition according to:

$$\tau_f(\varphi) = \frac{\nu(\varphi)}{c_s^2} + \frac{1}{2} \quad (5.6)$$

Here $c_s^2 = 1/3$ is the speed of sound in lattice units.

The mobility M (see eq. (5.1c)) is determined by the coefficient of mobility Γ and the relaxation parameter τ_g according to:

$$M = \Gamma \left(\tau_g - \frac{1}{2} \right) \quad (5.7)$$

For a planar interface, an analytical solution (Van der Sman and Van der Graaf, 2008) gives the φ profile $\varphi(x) = \varphi_0 \tanh(x/\xi)$ (x is the coordinated normal to the

interface). The thickness of the diffuse interface is characterized by the characteristic length ξ :

$$\xi = \left(\frac{2\kappa}{-A} \right)^{1/2}. \quad (5.8)$$

The interfacial tension σ follows from:

$$\sigma = \frac{4}{3} \kappa \frac{\varphi_0^2}{\xi}. \quad (5.9)$$

Statistically stationary homogeneous isotropic turbulence is generated throughout the simulation domain. The viscous dissipation extracts energy from the system. To sustain a constant turbulence during the simulation, the energy input is organized on the integral scale by means of forcing. The linear forcing proposed by (Lundgren, 2003) is adopted here. A local force proportional to the local velocity is imposed in the liquid. In this case, the momentum equation (5.1b) gets a forcing term $F_{t\alpha} = A_f u_\alpha$ and the parameter A_f is determined as

$$A_f = \frac{\varepsilon}{3u_{\text{rms}}^2} \quad (5.10)$$

where ε is the volume-averaged energy dissipation rate per unit mass which is an input parameter, u_{rms} is the volume-averaged root-mean-square fluid velocity which is an output parameter calculated every time step.

The detailed exploration of linear forcing has been carried out by (Rosales and Meneveau, 2005). The authors confirmed that the linear force implementation in physical space gives the same results as when applied in spectral space. In addition, this type of forcing was successfully implemented in the context of the LBE method by several authors (Derksen, 2008; Valino et al., 2010).

The turbulence generation method requires a non-zero velocity field to start with. Thus, at $t = 0$ the velocity field was initialized using the following relations (Derksen, 2008):

$$u_x = u_{\text{init}} \sin\left(\frac{2\pi j}{\lambda_0}\right) \quad u_y = u_{\text{init}} \sin\left(\frac{2\pi k}{\lambda_0}\right) \quad u_z = u_{\text{init}} \sin\left(\frac{2\pi i}{\lambda_0}\right) \quad (5.11)$$

where $\lambda_0 = 1.01L/4$, $i = j = k = (1 : L)$; $u_{\text{init}} = 5u_K$ is the maximum velocity in the initial distribution; L_d is the domain edge size; and u_K is the Kolmogorov velocity scale.

The code was implemented in Fortran 90 with message passing interface (MPI) for parallel processing. The fully-periodic three-dimensional domain was divided into equal cubic sub-domains in every direction, one for each CPU. With 125 CPUs, the processing time varied from two days for the simulation with the lowest resolution of the Kolmogorov scales in a 500^3 domain and up to 3 months for simulations in a 1000^3 domain.

5.3 Simulation parameters

Lattice Boltzmann methods operate in lattice space, therefore, all parameters should be defined in lattice units. For the adopted LBE method, the density value in the incompressible limit should be equal to unity. Thus, the density of continuous ρ_c and dispersed ρ_d phases in lattice space is set to $\rho_c = \rho_d = 1$ in lattice units [lu]. The kinematic viscosity of the continuous liquid is related to the relaxation time for the f_q distribution function as follows: $\nu_c = c_s^2(\tau_f - 0.5)$. The relaxation time corresponding to the continuous phase is set to 0.51 for simulation with the highest energy input, and 0.53 for the rest of the simulations. These values are specified to satisfy the incompressibility limit, i.e., the velocity fluctuations in lattice units should not be greater than $0.1c_s$. The kinematic viscosity of the dispersed phase (and the related relaxation time) is determined based on the ratio of dispersed to continuous phase viscosities $\lambda = \mu_d/\mu_c$. The relaxation time for the second distribution function g_q is set to unity in each simulation $\tau_g = 1$.

Special care should be taken when setting up the numerical parameters related to the interface, which are: the interface thickness ξ , the free energy model parameters A and κ , the mobility M , and the coefficient of mobility Γ . The values of these parameters are related to the drop size which varies during dispersion formation. Being exposed to continuously changing turbulent flow, drops undergo a variety of simultaneously occurring events caused by interactions with turbulent eddies that convect, deform, merge and break them. However, a connection with the flow in a simpler geometry, such as simple shear flow, can help to determine the interface-related numerical parameters. For example, a drop in a simple shear flow is akin to

a drop interacting with two co-rotating eddies in turbulent flow. It was outlined by Komrakova et al. (2014a) that for a drop in simple shear flows numerical parameters related to the interface are determined by two dimensionless numbers: the interface Peclet number $Pe = \dot{\gamma}a\xi/(MA)$ which relates the convection time scale to the interface diffusion time scale, and the Cahn number $Ch = \xi/a$ which is the ratio of the interface thickness and drop radius. Here, $\dot{\gamma}$ is the shear rate, and a is the drop radius. It was shown that the accuracy of drop deformation and breakup simulations is determined by mesh resolution and can be adjusted by Pe and Ch . High-resolution drops with radii larger than 30 [lu] require a thicker interface thickness $\xi \geq 2$ [lu], while drops with $a < 30$ [lu] need thinner interfaces (Komrakova et al., 2014a). The goal of the present simulations is to resolve small drops after multiple breakup processes. Therefore, the interface thickness is set to $\xi = 1.14$ [lu]. The values of A and κ are related to the interfacial tension (see equations (5.8) and (5.9)). The latter one is set to $\sigma = 0.01$ [lu]. According to a guideline of Komrakova et al. (2014a) higher interfacial tension (bigger κ) requires a smaller diffusion coefficient Γ . Based on their range of κ and Γ values, the diffusion coefficient in the present simulations is set to $\Gamma = 4$.

Simulation parameters are listed in Table 5.1. Each simulation is performed in a fully-periodic cubic domain with an edge size L_d . Cases with $L_d = 500$ and 1000 [lu] are examined. Simulation cases cover a wide range of energy dissipation. The characteristic velocity of turbulent flow u^* is used to determine the energy dissipation using the scaling law (Tennekes and Lumley, 1973) $\varepsilon = (u^*)^3/L$. It is necessary to note that increase of the resolution of Kolmogorov length scale η_K requires decrease of energy dissipation ε in lattice units. These parameters are related as follows (Pope, 2000):

$$\eta_K = \left(\frac{v_c^3}{\varepsilon} \right)^{1/4} \quad (5.12)$$

Since viscosity of the continuous phase v_c is constant, η_K can be changed by variation of ε .

Turbulent flow at high Reynolds numbers is characterized by the energy cascade (Pope, 2000). In the energy cascade there are two main processes: the transfer

Table 5.1: Simulation parameters: L_d is the cubic simulation domain edge length; u^* is the characteristic velocity; ν_c is the kinematic viscosity of continuous phase; η_K is the Kolmogorov length scale

	u^* , [lu]	ν_c , [lu]	η_K , [lu]
$L_d = 500$ [lu]	0.03	0.003	1
	0.02	0.01	2.5
	0.01	0.01	5
	0.004	0.01	10
$L_d = 1000$ [lu]	0.03	0.01	2.5

of energy from larger to successively smaller scales determined by the energy dissipation rate ε , and the viscous dissipation determined by the kinematic viscosity ν_c . The Kolmogorov length scale η_K separates two sub-ranges of this cascade: the inertial (length scale is significantly larger than Kolmogorov length scale $l \gg \eta_K$) and viscous (length scale is of the order of or less than Kolmogorov length scale $l < \eta_K$). Inertial stresses determine the flow in the inertial sub-range while viscous stresses are negligible. Viscous effects are dominant in the viscous sub-range and responsible for the energy dissipation. Depending on whether it is the inertial or the viscous stresses that are dominant when balanced against restoring forces, the maximum stable droplet size falls in either the inertial sub-range or the viscous sub-range (Boxall et al., 2011). The restoring forces that counteract external deformation of droplets are due to interfacial tension, and the force associated with the viscosity of the drop.

The simulations are performed in the following way. Homogeneous isotropic turbulence with known energy dissipation rate is generated throughout the domain. Then the second phase is injected. The drop size distribution of the steady state dispersion is characterized by two representative drop sizes: the Sauter mean diameter d_{32} , and the maximum stable drop diameter, d_{\max} , that can resist breakup. The d_{\max} is determined as the maximum volume-equivalent drop diameter. The Sauter mean diameter is the ratio of the third and the second moment of the drop size distribution:

$$d_{32} = \frac{\sum_{i=1}^k d_i^3}{\sum_{i=1}^k d_i^2} \quad (5.13)$$

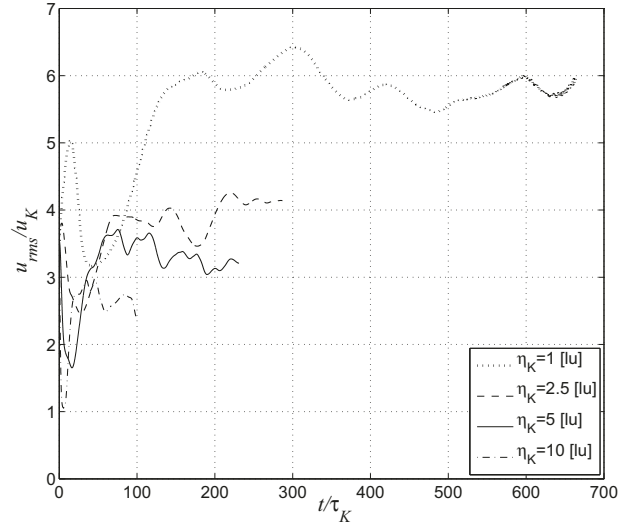


Figure 5.1: Volume-averaged root-mean-square fluid velocity u_{rms} as a function of time in one-phase systems for varying resolution of Kolmogorov scales (η_K is the Kolmogorov length scale). The simulation domain size is 500^3 . The parameters are related to the corresponding Kolmogorov scales

where d_i is the diameter of drop i and k is the number of drops in the system. Drop sizes are expressed in terms of their volume-equivalent diameter $d_i = (6V/\pi)^{1/3}$. The d_{32} is directly related to the interfacial area per unit volume a_V in the dispersion which is an important industrial parameter: $d_{32} = 6\phi/a_V$ (where ϕ is the holdup of the dispersed phase).

5.4 Single-phase turbulence

Fully-developed turbulence was generated in the simulation domain before injection of the second phase. In each case, the initial velocity field was specified according to equations (5.11). The evolution in time of the volume-averaged root-mean-square fluid velocity of one-phase systems for different cases of Kolmogorov length scale resolution η_K is shown in Fig. 5.1. Both velocity and time are scaled with the corresponding Kolmogorov velocity $u_K = (v_c \varepsilon)^{1/4}$ and time $\tau_K = (v_c / \varepsilon)^{1/2}$ scales. It takes at least $100\tau_K$ to generate the turbulence.

The velocity magnitude fields in the cross-sections of the 500^3 domain when

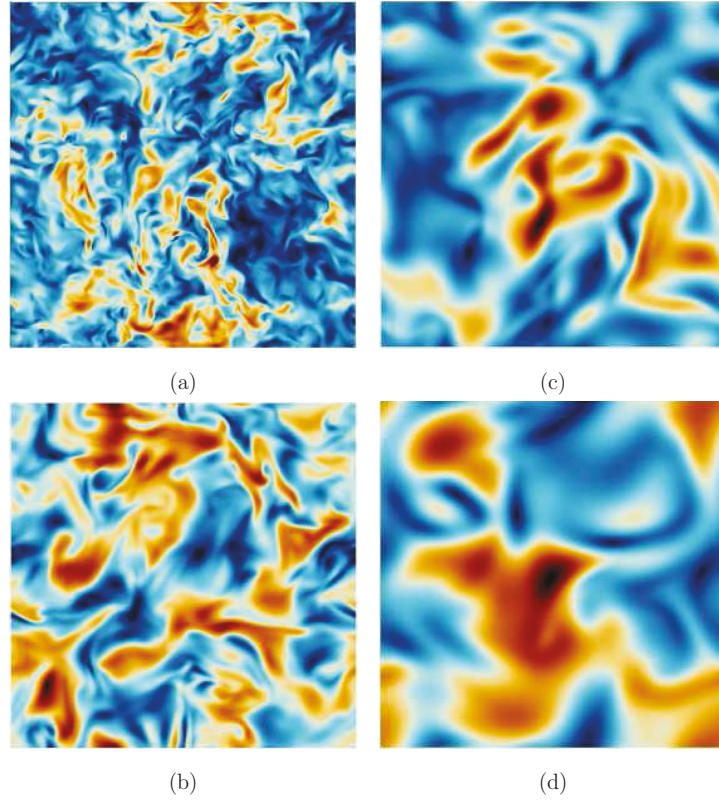


Figure 5.2: Velocity magnitude fields of fully-developed turbulent flows in the cross-sections of 500×500 [lu] for different resolution of Kolmogorov scales. (a) $\eta_K = 1$ [lu]; (b) $\eta_K = 2.5$ [lu]; (c) $\eta_K = 5$ [lu]; (d) $\eta_K = 10$ [lu]

turbulence is fully-developed are presented in Fig. 5.2. Even with $\eta_K = 1$ [lu] the turbulence is resolved. To see the structures of the turbulent flow, the vector plots are shown in the cross-sections of the 1000^3 domain in Fig. 5.3.

For the case with the Kolmogorov length scale $\eta_K = 5$ [lu] at time instant $t = 199.2\tau_K$ the longitudinal $f(r)$ and lateral $g(r)$ two-point velocity correlation functions are determined. These functions give a measure for the velocity correlation for two points at distance r apart in any direction (Batchelor, 1953), and can be calculated as follows:

$$f(r) = \frac{\overline{u_p(\mathbf{x})u_p(\mathbf{x}+\mathbf{r})}}{u_{\text{rms}}^2} \quad g(r) = \frac{\overline{u_n(\mathbf{x})u_n(\mathbf{x}+\mathbf{r})}}{u_{\text{rms}}^2} \quad (5.14)$$

where u_p and u_n denote velocity components at a point \mathbf{x} parallel and normal, respectively, to the separation vector \mathbf{r} .

The calculation of the correlation function has been performed via sampling of

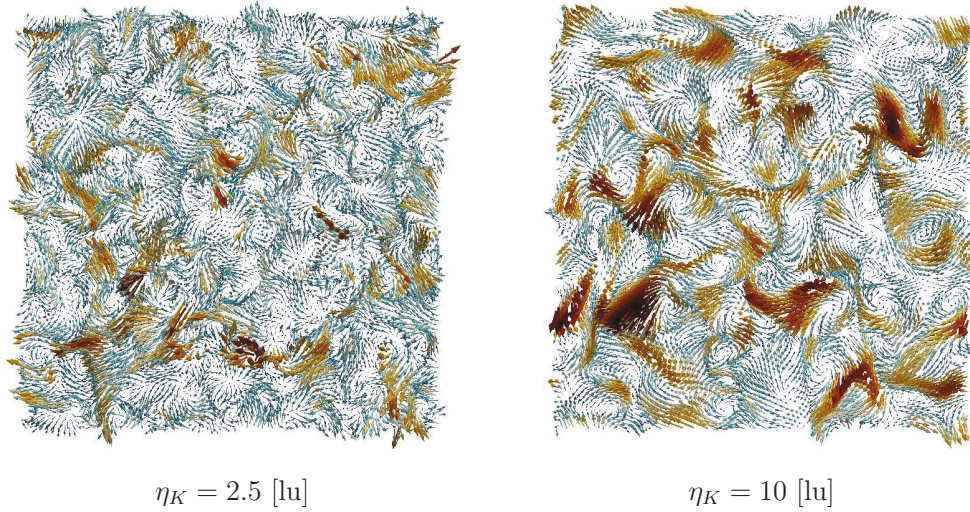


Figure 5.3: Velocity fields of fully-developed single-phase turbulent flow in the cross-sections of a 1000^3 domain for different resolution of Kolmogorov length scale η_K

the flow field with a large number ($\sim 10^6$) of randomly placed points (the description of the procedure can be found in ten Cate et al. (2006)). The results are presented in Fig. 5.4 . As one can see both curves exhibit the well-known behavior of the correlation functions for turbulent flow (e.g. shown in Batchelor (1953)). Since both functions become zero at large separations, the domain size is sufficiently large to avoid self-correlations.

5.5 Two-phase flow

5.5.1 Effect of Kolmogorov scale resolution

A simulation with the lowest resolution of Kolmogorov scales ($\eta_K = 1$ [lu]) was performed in a 500^3 domain with a dispersed phase volume fraction $\phi = 0.005$ and viscosity ratio $\lambda = 1$. A single droplet with initial undeformed diameter of $106\eta_K$ was injected into the fully-developed turbulent flow.

The dispersion formation process is visualized by plotting the iso-surfaces of the order parameter $\phi = 0$ (which represent the liquid-liquid interface) at different time instances (Fig. 5.5). At the moment $t = 3.3\tau_K$ starting from the drop injection, the drop is already significantly deformed. By the time $t = 19.9\tau_K$, small droplets have

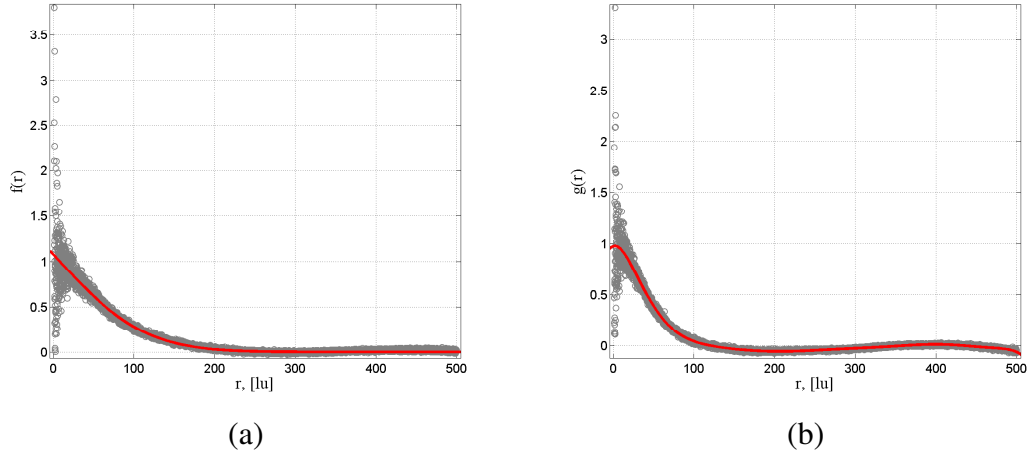


Figure 5.4: Longitudinal (a) and lateral (b) velocity correlation functions for the case with Kolmogorov length scale resolution $\eta_K = 5$ [lu] at the time instant $t = 199.2\tau_K$. Symbols refer to the value of the functions at a given distance between two points; curves represent the data fit

been formed. The large dispersed phase structure is, however, not yet disintegrated. Finally, the drop is broken into small fragments (see $t = 59.7\tau_K$).

By the time $t = 59.7\tau_K$, most of the drops have diameters less than $10\eta_K$ ($d < 10$ [lu]) approaching the viscous sub-range of the energy spectrum. When the drop size becomes comparable to the Kolmogorov length scale, the drops interact with the eddies that create shear of the order of $\dot{\gamma} = 1/\tau_K$. In order to compare this drops interaction to a drop behavior in simple shear flow, the dimensionless numbers based on drop radius a are used. The drop Reynolds number for a drop with radius $a = 5$ [lu] is $Re = \dot{\gamma}a^2/\nu_c = 25$. The relevant capillary number for the viscous sub-range is $Ca = a\dot{\gamma}\mu_c/\sigma = 0.05$. In order to break the drop, the critical capillary number Ca_c should be exceeded. According to the results presented by (Khismatullin et al., 2003) who studied drop breakup in simple shear flow, the critical capillary number at $Re = 10$ is $Ca_c = 0.147$ and at $Re = 50$ is $Ca_c = 0.058$ for $\lambda = 1$. This means that at $Re = 25$ the critical capillary number is in between these two values. Consequently, the drops of radii ~ 5 [lu] and smaller might not be broken under the present agitation conditions. However, complex interactions with multiple eddies might lead to drop breakup. Droplets of diameter $\sim \eta_K$ could be satellites and sub-satellites formed after breakup of larger droplets.

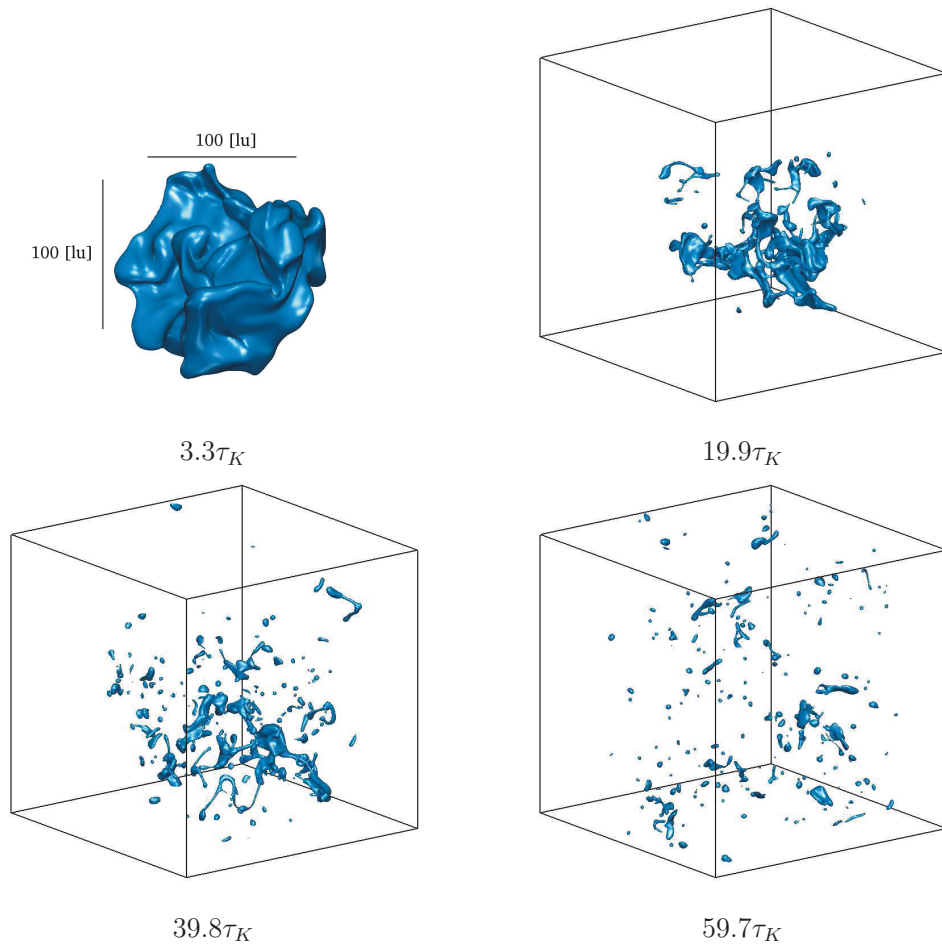


Figure 5.5: Iso-surfaces of order parameter $\varphi = 0$ at different time instants relative to the Kolmogorov time scale τ_K for the case with $\eta_K = 1$ [lu] and viscosity ratio $\lambda = 1$. The dispersed phase volume fraction is $\phi = 0.005$. The moment of drop injection refers to $t = 0$

In addition, the numerical method is plagued by numerical dissolution of small drops. These drops disappear almost immediately after generation. The change in time of the number of drops in the system is shown in Fig. 5.6 (a). The number of drops increases with time reaching maximum and then decreases to zero. A decrease in the number of drops to zero is a numerical effect. The ratio of the dispersed phase volume V to the initial drop volume V_{init} is plotted versus time in Fig. 5.6 (b). The maximum drop diameter and the Sauter mean diameter as functions of time are presented in Fig. 5.7. Because of dissolution, both of them eventually go down to zero. To reduce the dispersed phase dissolution, it is suggested to improve the resolution of Kolmogorov scales so that the minimum size of the drops after breakup is in the range 20 – 30 lattice units. The numerical dissolution of the drop can be considered as a numerical mass transfer process between the liquids. The Peclet number which relates the convection time scale to the diffusion time scale can be used to characterize this process. Smaller Pe results in lower mass transfer rate since diffusion process has larger time scale than convection. It can be shown that an increase of η_K resolution leads to smaller Peclet number. For simplicity, consider a single drop of radius equal to the Kolmogorov length scale $a = \eta_K$. The drop is deformed in a shear flow characterized by a shear rate $\dot{\gamma} = 1/\tau_K$, where $\tau_K = (v_c/\varepsilon)^{0.5}$. Using relation (5.12), the shear rate is $\dot{\gamma} = v_c/\eta_K^2$. Then the Peclet number $Pe = a\dot{\gamma}\xi/(MA) = \xi v_c/(MA\eta_K)$. Consequently, the ratio of Peclet numbers for the cases with higher η_{K2} and lower η_{K1} resolution is $Pe_2/Pe_1 = \eta_{K1}/\eta_{K2}$. That means the numerical dissolution rate in the case characterized by Pe_2 is reduced.

It was shown experimentally, for instance, by Lovick et al. (2005); Pacek et al. (1998) that the DSD of a liquid-liquid dispersion formed under turbulent flow conditions is close to a log-normal distribution. The drop size distribution for the case with the highest energy input is shown in Fig. 5.8 (a) at time instant $t = 59.7\tau_K$. Probability plots are used to assess whether data comes from a certain distribution. In Fig. 5.8 (b) the numerically obtained distribution is compared to a log-normal distribution (for the same time instant as the DSD shown in Fig. 5.8 (a)). The strongest deviation from the log-normal distributions are for the smallest and largest

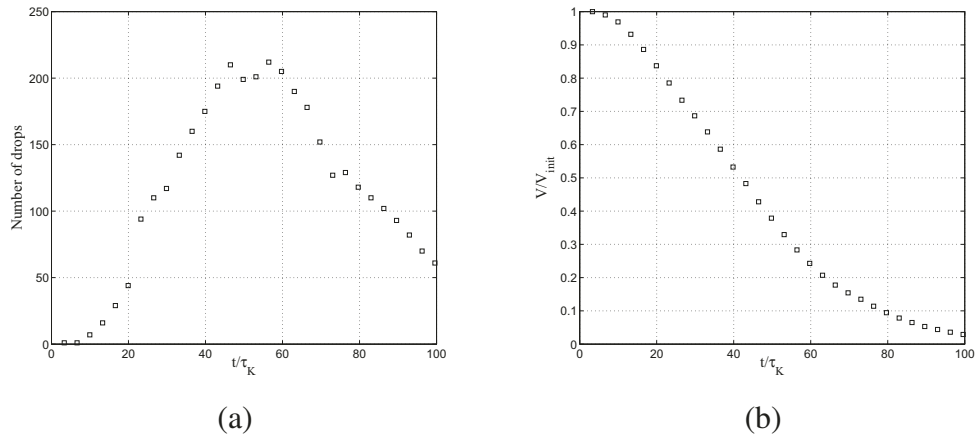


Figure 5.6: Number of drops (a) and dispersed volume V in the system relative to the initial value V_{init} (b) as functions of time for the case with Kolmogorov length scale resolution $\eta_K = 1$ [lu] and viscosity ratio $\lambda = 1$. The dispersed phase volume fraction is $\phi = 0.005$

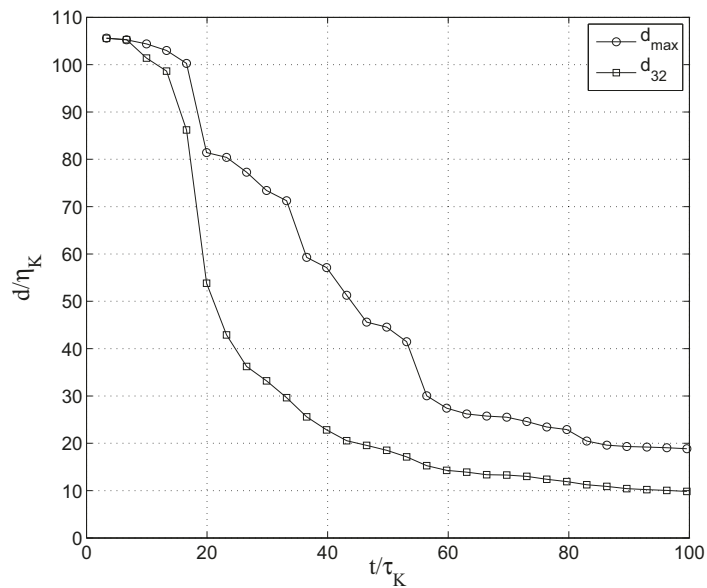


Figure 5.7: Dimensionless maximum d_{max} and Sauter mean d_{32} diameters as a function of time for the case with Kolmogorov length scale resolution $\eta_K = 1$ [lu] and viscosity ratio $\lambda = 1$. The dispersed phase volume fraction is $\phi = 0.005$

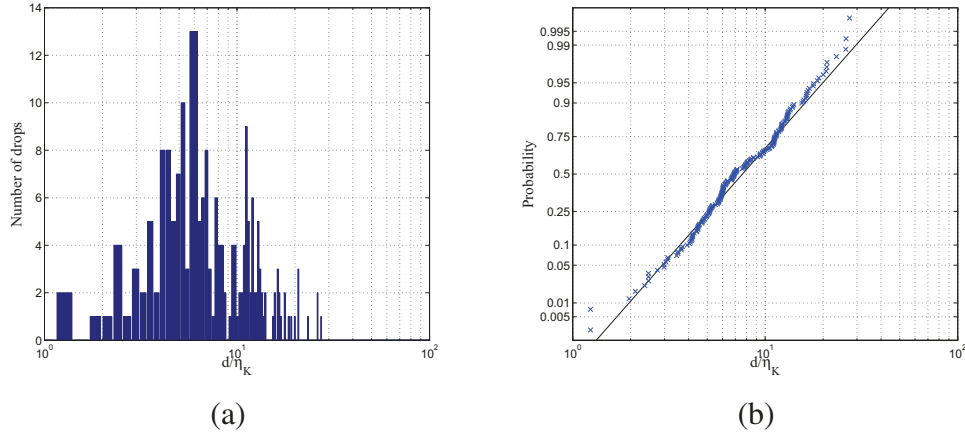


Figure 5.8: Drop size distribution (a) and cumulative log-normal probability plot (b) for the case with the Kolmogorov length scale resolution $\eta_K = 1$ [lu], viscosity ratio $\lambda = 1$, dispersed phase volume fraction $\phi = 0.005$ at the time instant $t = 59.7\tau_K$

droplets. The reason is an underestimation of small droplet size due to numerical dissolution. The largest droplets might break if the simulation is continued.

Now consider the results of the simulations with the higher resolution of the Kolmogorov length scale $\eta_K = 2.5$ [lu]. The simulations were performed in a 500^3 domain with one initial drop of diameter $d = 42.4\eta_K$ [lu] that results in a dispersed phase volume fraction $\phi = 0.005$. Two viscosity ratios were examined $\lambda = 1$ and $1/3$.

With the increase of the Kolmogorov scale resolution the dispersed phase dissolution is reduced (compare Fig. 5.9(b) with Fig. 5.6(b)). The number of drops as a function of time for $\lambda = 1$ and $1/3$ is shown in Fig. 5.9(a). Significantly less drops are produced compared to the case with $\eta_K = 1$ [lu] because the domain size gets smaller by $(2.5)^3$.

The factor of three difference in viscosity between the liquids is not sufficient to see a prominent difference in the number of drops generated. Nevertheless, more drops form when $\lambda = 1/3$ which is physically correct, since the counteracting internal viscous forces become weaker. Generation of more drops results in larger interfacial area which leads to faster drop dissolution (see Fig. 5.9(b)). The liquid-liquid interface at different time instance when $\lambda = 1$ and $1/3$ is demonstrated in Fig. 5.10. As one can see, the system with less viscous dispersed phase has

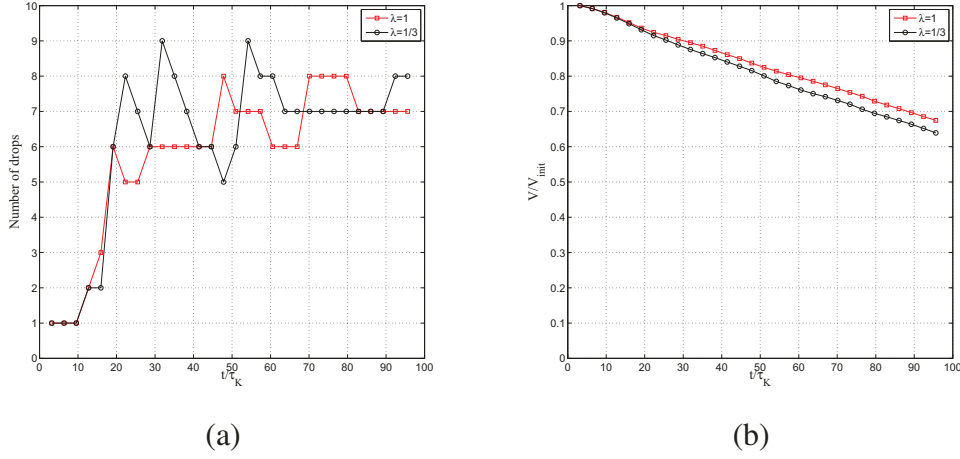


Figure 5.9: Number of drops (a) and dispersed volume V in the system relative to the initial value V_{init} (b) as functions of time for the cases with Kolmogorov length scale resolution $\eta_K = 2.5$ [lu] and viscosity ratio $\lambda = 1$ and $1/3$. The dispersed phase volume fraction is $\phi = 0.005$

more droplets (compare Fig. 5.10 (b) and (e)). The maximum drop diameter and the Sauter mean diameter for the case with Kolmogorov length scale resolution in $\eta_K = 2.5$ [lu] are presented in Fig. 5.11.

In turbulent flow, the drop is broken due to interactions with turbulent eddies. To isolate drop breakup events and minimize the probability of drop coalescence, a dilute dispersion formation was considered characterized by a dispersed phase volume fraction $\phi = 0.001$ and a Kolmogorov length scale resolution of $\eta_K = 2.5$ [lu]. The initial drop radius is $a = 32$ [lu] ($d = 25.5\eta_K$). Assume that co-rotating turbulent eddies interacting with the drop create a shear rate of the order of $\dot{\gamma} = 1/\tau_K$. Then the drop Reynolds number $\text{Re} = 155$. The entire process of dispersion formation is demonstrated in Fig. 5.12. The diameters of the four drops at $t = 26.3\tau_K$ are: $19.5\eta_K$, $18.1\eta_K$, and two drops with diameter of $8.6\eta_K$. The captured drop deformation and breakup process in turbulent flow mimics drop behavior in simple shear flow: elongation, necking, and breakage with formation of larger daughter drops and two satellite droplets.

With further increase of the Kolmogorov scale resolution up to $\eta_K = 10$ [lu], the injected $10.6\eta_K$ diameter drop stays almost spherical (Fig. 5.13).

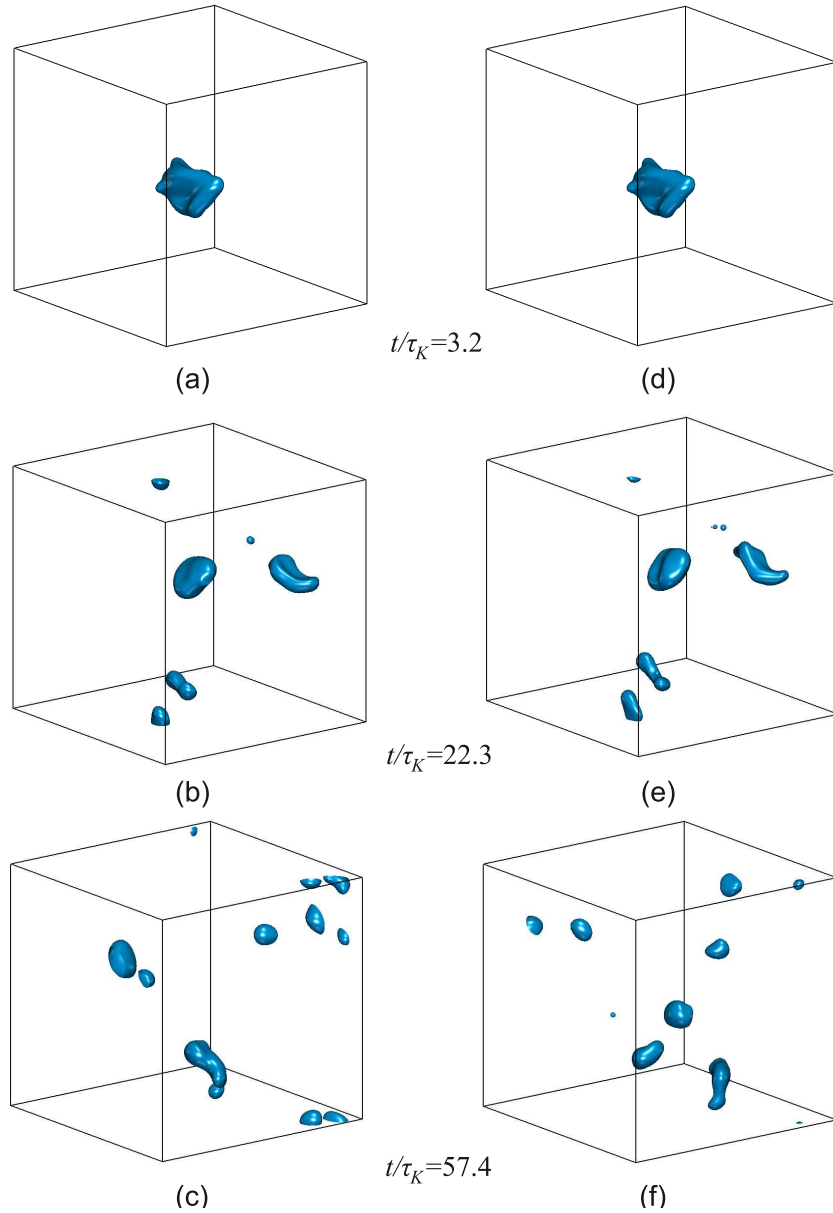


Figure 5.10: Iso-surfaces of order parameter $\phi = 0$ at different time instants relative to the Kolmogorov time scale τ_K for the case with $\eta_K = 2.5$ [lu]; (a)-(c) viscosity ratio is $\lambda = 1$; (d)-(f) viscosity ratio is $\lambda = 0.3$. The dispersed phase volume fraction is $\phi = 0.005$. Drop injection time refers to $t = 0$

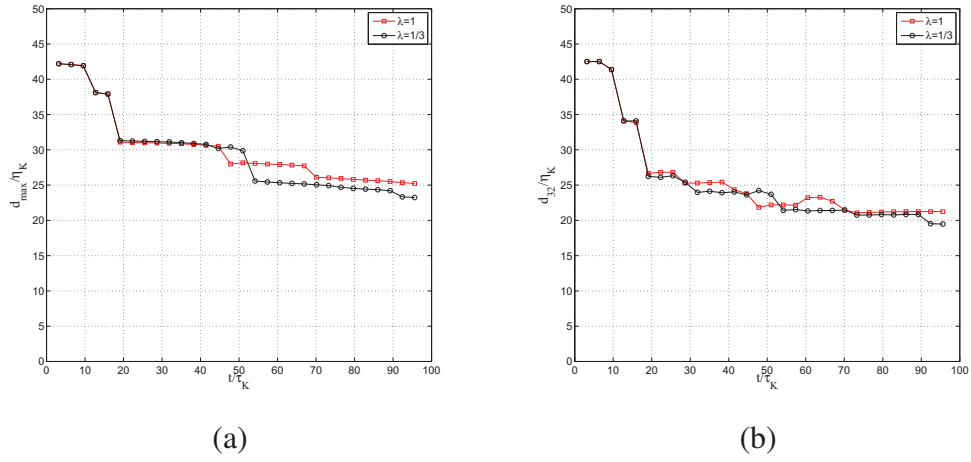


Figure 5.11: Dimensionless maximum d_{\max} (a) and Sauter mean d_{32} (b) diameters as functions of time for the cases with Kolmogorov length scale resolution $\eta_K = 2.5$ [lu] and viscosity ratios $\lambda = 1$ and 0.3 . The dispersed phase volume fraction is $\phi = 0.005$

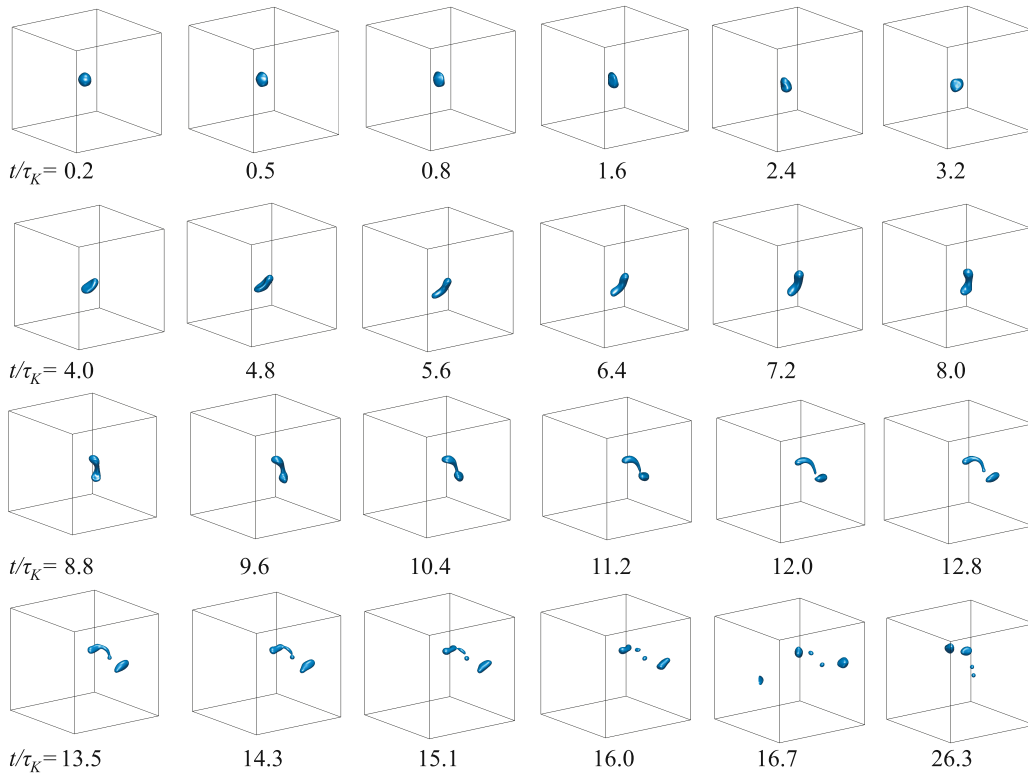


Figure 5.12: Iso-surfaces of order parameter $\varphi = 0$ at different time instants relative to the Kolmogorov time scale τ_K for the case with $\eta_K = 2.5$ [lu] and viscosity ratio $\lambda = 1$. The dispersed phase volume fraction is $\phi = 0.001$. Drop injection time refers to $t = 0$

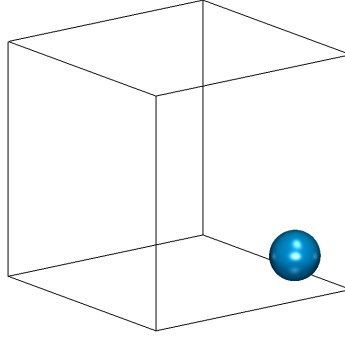


Figure 5.13: Dispersed phase at $t = 14.7\tau_K$ for the case with $\eta_K = 10$ [lu] and viscosity ratio $\lambda = 1$. The dispersed phase volume fraction is $\phi = 0.005$. The moment of drop injection refers to $t = 0$

5.5.2 Effect of dispersed phase volume fraction

Liquid-liquid dispersion formation at high loadings of dispersed phase was examined for the cases with the Kolmogorov length scale resolution $\eta_K = 2.5$ [lu], equal phase viscosities, and at dispersed phase volume fractions $\phi = 0.05$ and 0.2 . The simulations were carried out in a 500^3 domain. The initial size of the injected drop was $91.0\eta_K$ and $144.5\eta_K$ for $\phi = 0.05$ and 0.2 , respectively.

A higher dispersed phase volume fraction significantly reduces the dissolution. The specific surface (ratio between interfacial area and dispersed phase volume) gets smaller, thus, the numerical mass transfer over the interface is less efficient. The number of drops as a function of time is shown in Fig. 5.14 (a). The change in time of dispersed phase volume relative to the initial value is depicted in Fig. 5.14 (b). When $\phi = 0.2$ the V/V_{init} levels off to the value of 0.96 . For this case when breakup and coalescence reach equilibrium the number of drops in the system obtains an average value of ~ 45 (Fig. 5.14 (a)).

The iso-surfaces of $\phi = 0$ at different time instants for the cases of $\phi = 0.05$ and 0.2 are shown in Fig. 5.15. The maximum drop diameter and the Sauter mean diameter are presented in Fig. 5.16 (a) and (b), respectively. When $\phi = 0.2$ the d_{max} and d_{32} fluctuate around their average values.

For both values of dispersed phase holdup it is not possible to obtain a dispersion: droplets continuously break and coalesce, and a large volume of dispersed

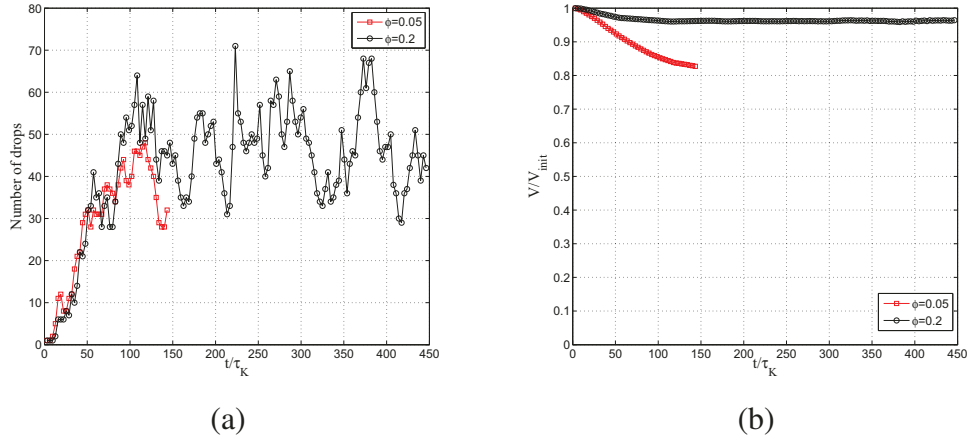


Figure 5.14: Number of drops (a) and dispersed volume V in the system relative to the initial value V_{init} (b) as functions of time for the cases with Kolmogorov length scale resolution $\eta_K = 2.5$ [lu] and viscosity ratio $\lambda = 1$. The dispersed phase volume fraction is $\phi = 0.05$ and 0.2

phase remains connected (especially at $\phi = 0.2$). An example of simultaneous breakage and coalescence events is shown in Fig. 5.17 for the case when $\phi = 0.2$. Even though the drops are broken efficiently into smaller drops, easy coalescence which is an issue of the numerical method, prevents dispersion formation. In diffuse interface methods, the drop interfaces have a finite thickness. If they overlap for sufficient time during the collision, the drops coalesce (Jia et al., 2008). A possible way to suppress easy coalescence is a significant increase of resolution (Shardt et al., 2013). In this case, the simulations of turbulent flow with multiple droplets involved will be computationally unaffordable. However, the overestimated coalescence rate is not the only reason that prevents dispersion formation. Experimentally, it is not always possible to mix pure immiscible liquids. For instance, Rueger and Calabrese (2013) pointed that it was not possible to achieve complete dispersion experimentally for pure systems above dispersed phase volume fraction 0.05. Only the addition of a sufficient amount of surfactant allowed to acquire data for stable dispersions up to $\phi = 0.5$.

The DSD at $\phi = 0.2$ is plotted at different time instants in Fig. 5.18 (upper row). A drop with volume-equivalent diameter close to the initial value remains in the system while smaller droplets form, and then merge with others (coalescence).

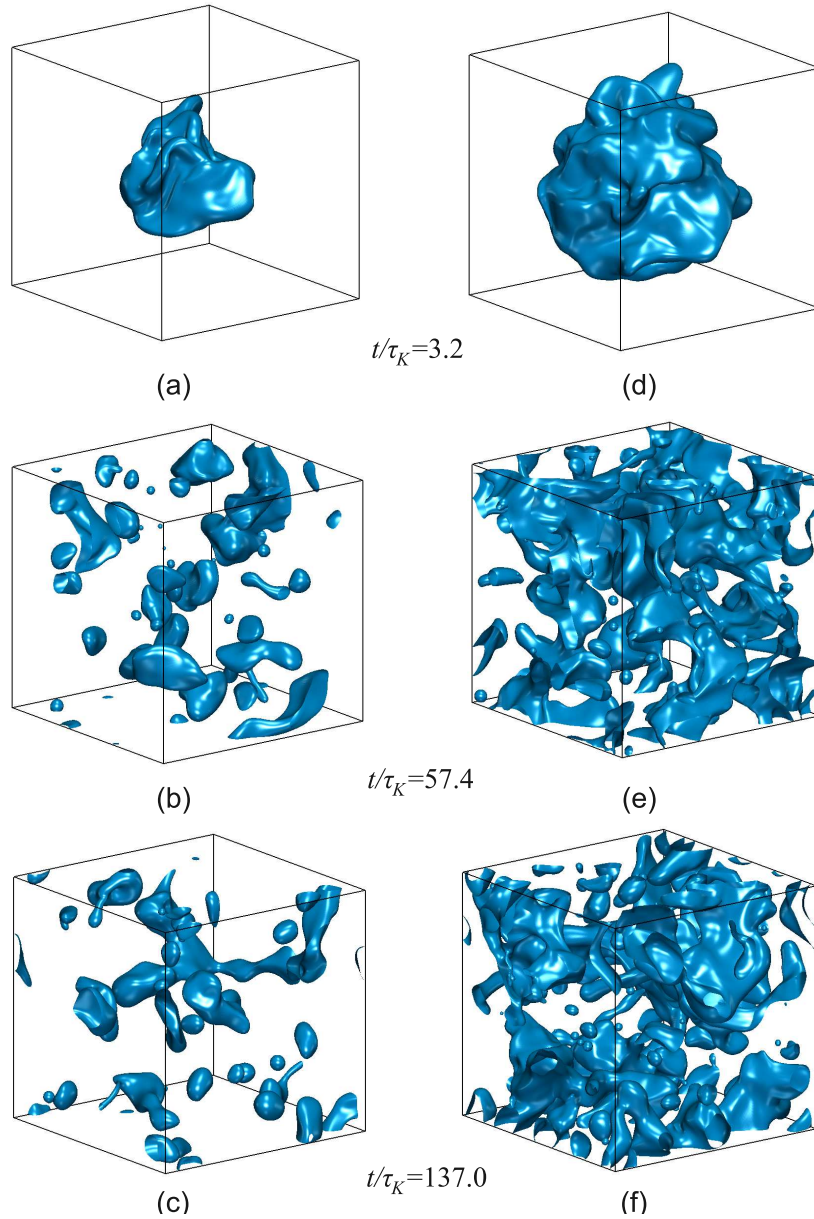


Figure 5.15: Iso-surfaces of order parameter $\phi = 0$ at different time instants relative to the Kolmogorov time scale τ_K for the case with $\eta_K = 2.5$ [lu]; (a)-(c) dispersed phase volume fraction is $\phi = 0.05$; (d)-(f) dispersed phase volume fraction is $\phi = 0.2$. Viscosity ratio is $\lambda = 1$. The moment of drop injection refers to $t = 0$

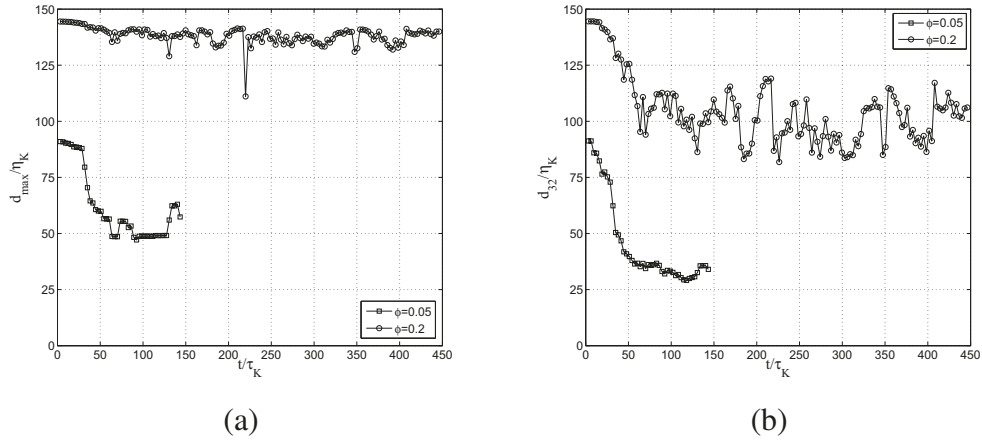


Figure 5.16: Dimensionless maximum d_{\max} (a) and Sauter mean d_{32} (b) diameters as functions of time for the case with Kolmogorov length scale resolution $\eta_K = 2.5$ [lu] and viscosity ratio $\lambda = 1$. The dispersed phase volume fraction is $\phi = 0.05$ and 0.2

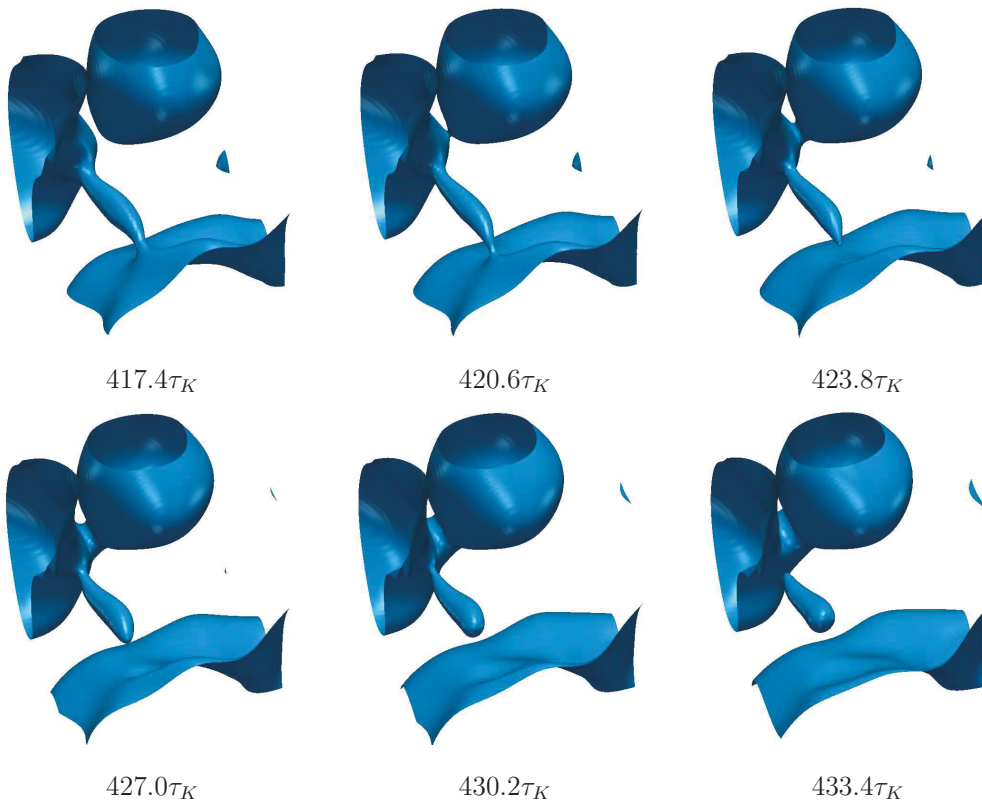


Figure 5.17: Simultaneous breakage and coalescence events happening in the system with $\eta_K = 2.5$ [lu] and the dispersed phase volume fraction $\phi = 0.2$. Viscosity ratio is $\lambda = 1$

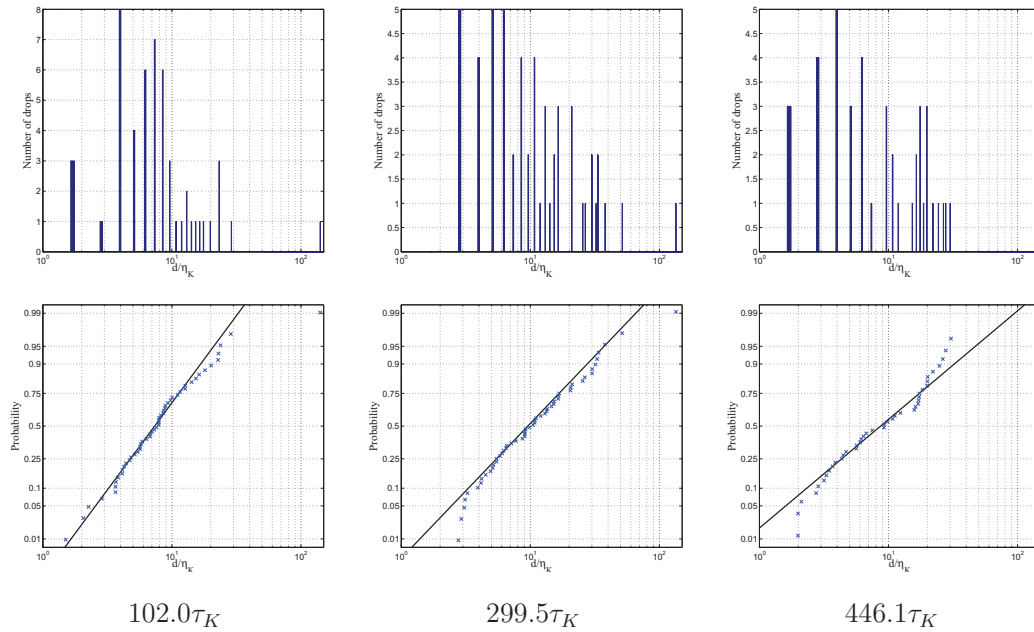


Figure 5.18: Drop size distribution (a) and probability plots (b) at different time instants for system with $\eta_K = 2.5$ [lu]. The viscosity ratio $\lambda = 1$, the dispersed phase volume fraction $\phi = 0.2$

Moreover, small drops that are formed have higher chances to coalesce rather than dissolve. It can be seen from Fig. 5.18 that a significant amount of small drops are produced but they do not reach the size of the order of the Kolmogorov length scale. This means that they coalesce with the bulk of the dispersed phase liquid. Even though one large volume-equivalent drop remains, the rest of the drops tend to follow a log-normal distribution as shown in the cumulative distributions in Fig. 5.18 (bottom row).

Simulations with the Kolmogorov length scale resolution $\eta_K = 2.5$ [lu] were also performed on a larger scale with domain edge size $L_d = 1000$ [lu]. As the initial condition 125 drops of diameter $46.3\eta_K$ were injected into a fully-developed turbulent flow. The dispersed phase volume fraction is $\phi = 0.14$. The evolution of the dispersed phase in time is shown in Fig. 5.19. As one can see, the dominant mechanism of drop breakup is by end-pinching. At time $t = 35\tau_K$ (with 99 drops in the system) a lot of thin elongated structures have been formed (bridges that connect drops). By the time $t = 38.2$, most of these bridges are broken producing

many satellite and sub-satellite droplets, such that the number of drops in the system increases up to 140. The number of drops in the system and relative dispersed phase volume as functions of time are shown in Fig. 5.20.

5.5.3 Effect of dispersed phase volume fraction and resolution of Kolmogorov scales

Simulation with $\eta_K = 5$ [lu] were carried out in a 500^3 domain. As the initial condition 125 drops of diameter $12.8\eta_K$ were injected into fully-developed turbulent flow. The dispersed phase volume fraction is $\phi = 0.14$.

The evolution of the liquid-liquid interface is presented in Fig. 5.21. As one can see, only one drop is eventually formed, mostly due to easy coalescence. In addition, the high volume of dispersed phase results in frequent collision of drops, while small energy input makes collisions efficient and drops merge (low droplet-droplet relative velocity). However, breakup events also take place in this system: when smaller drops collide with larger ones, the collisions result in temporary drop merges and then breakup. An example of such an event is shown in Fig. 5.22.

The number of drops in the system as a function of time is presented in Fig. 5.23 (a) and the volume of the dispersed phase evolution in time is plotted in Fig. 5.23 (b). The drop dissolution effect is negligibly small in this case. The maximum drop diameter and Sauter mean diameter as functions of time are shown in Fig. 5.24.

5.5.4 Energy spectra in one- and two-phase turbulent flow

The scale separation calculated as ratio between the simulation domain edge length and the Kolmogorov length scale L_d/η_K defines the reproduction of inertial energy sub-range. Fig. 5.25 shows the kinetic energy spectra of one-phase fully-developed turbulent flow (black curves) for different cases of Kolmogorov scales resolution. The viscous sub-range of the turbulent energy spectrum is always reproduced. The reproduction of the inertial sub-range improves with the increase of L_d/η_K , and follows the slope of Kolmogorov universal scaling law ($E(k) \sim k^{-5/3}$) at small wave numbers (or large length scales). The energy spectrum curve becomes horizontal at high wavenumbers k for $\eta_K = 5$ and 10 [lu] because at these values of k the machine

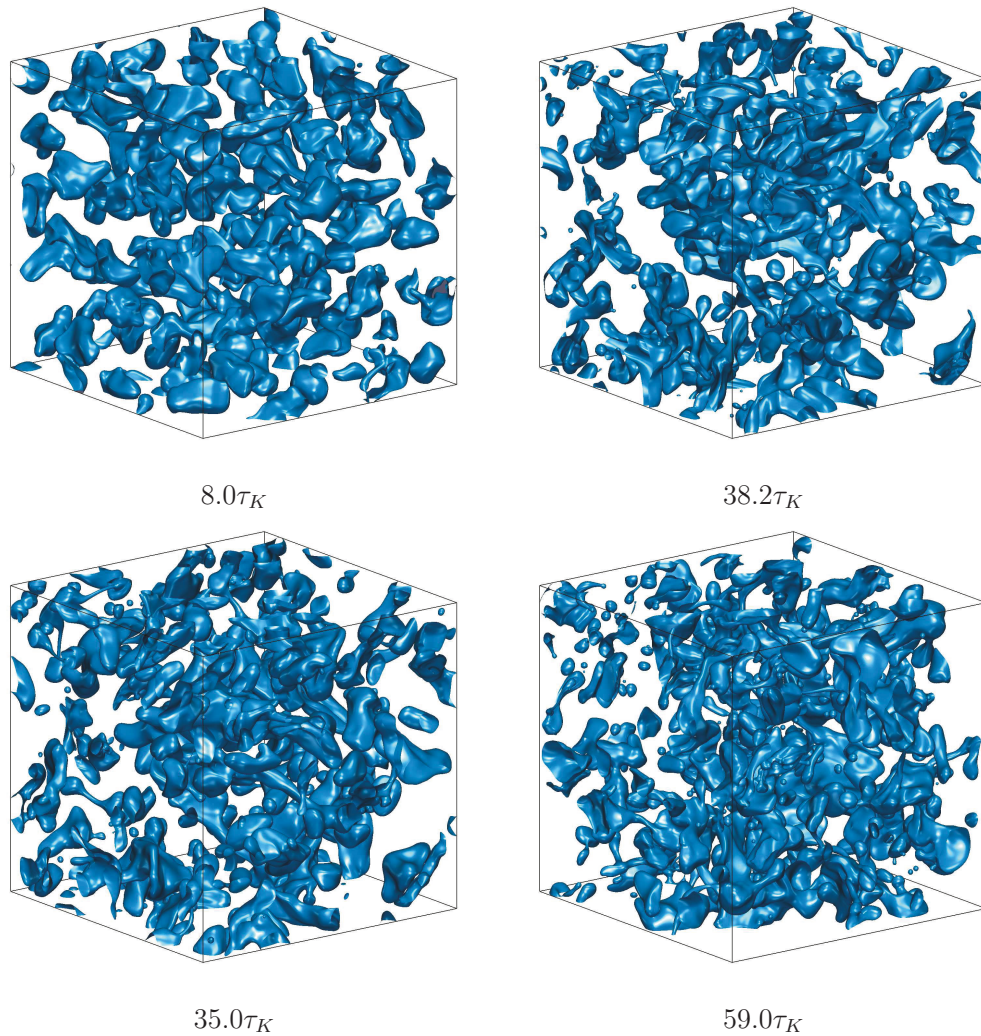


Figure 5.19: Iso-surfaces of order parameter $\phi = 0$ at different time instants relative to the Kolmogorov time scale τ_K for the case with $\eta_K = 2.5$ [lu] in a 1000^3 simulation domain; dispersed phase volume fraction is $\phi = 0.14$. Viscosity ratio is $\lambda = 1$. The moment of drop injection refers to $t = 0$

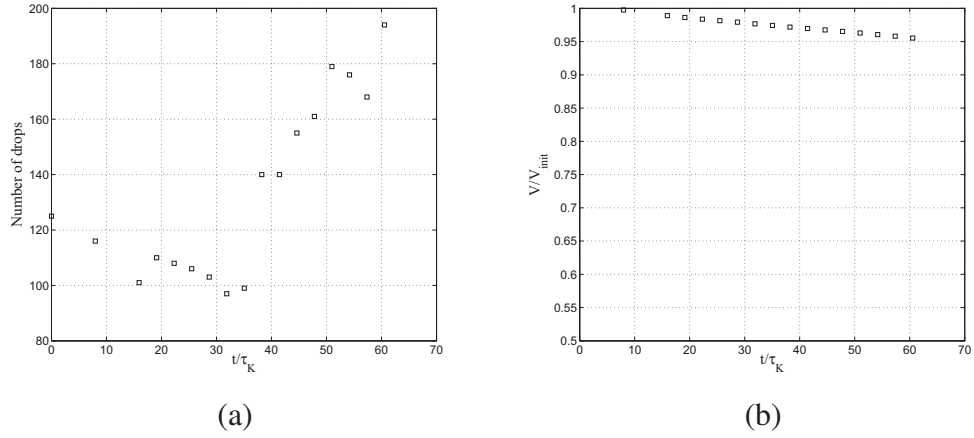


Figure 5.20: Number of drops (a) and dispersed volume V in the system relative to the initial value V_{init} (b) as functions of time for the cases with Kolmogorov length scale resolution $\eta_K = 2.5$ [lu] and viscosity ratio $\lambda = 1$. The dispersed phase volume fraction is $\phi = 0.14$, the simulation domain edge $L_d = 1000$ [lu]

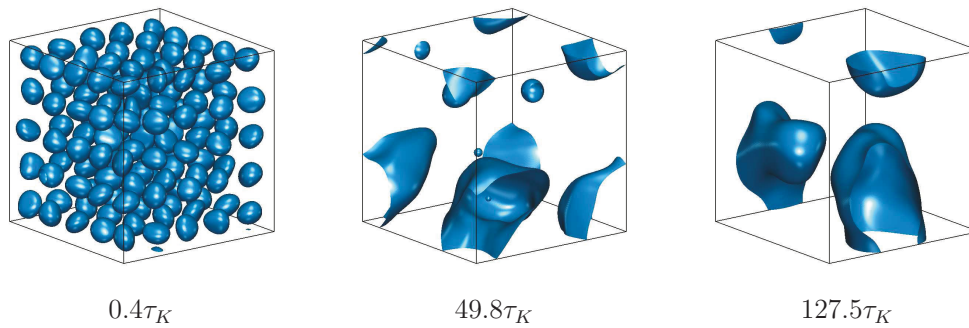


Figure 5.21: Iso-surfaces of order parameter $\phi = 0$ at different time instants relative to the Kolmogorov time scale τ_K for the case with $\eta_K = 5$ [lu] and viscosity ratio $\lambda = 1$. The dispersed phase volume fraction is $\phi = 0.14$. Drop injection time refers to $t = 0$

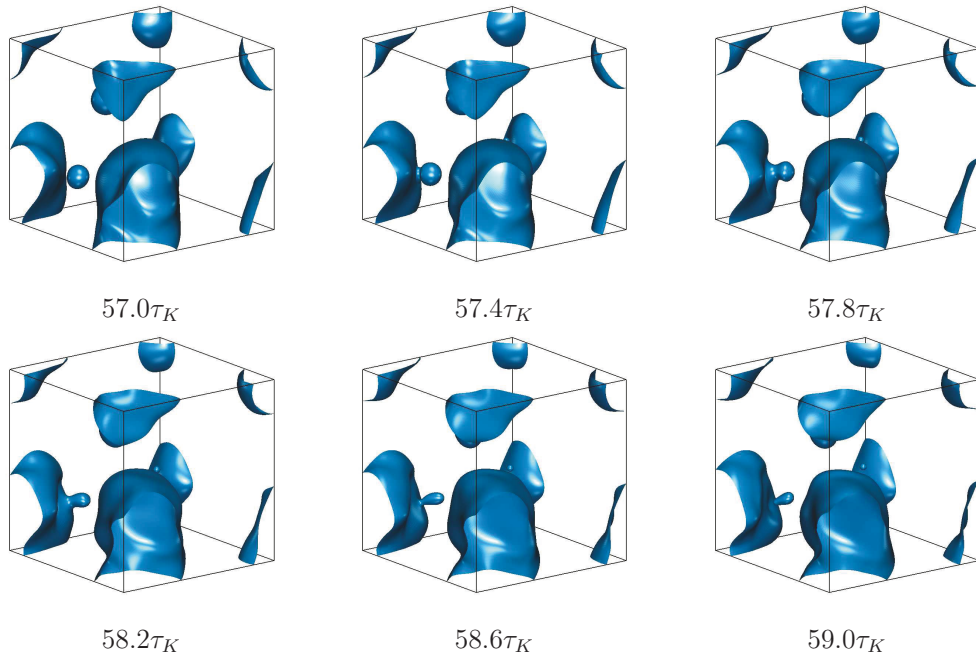


Figure 5.22: Iso-surfaces of order parameter $\varphi = 0$ at different time instants relative to the Kolmogorov time scale τ_K for the case with $\eta_K = 5$ [lu] and viscosity ratio $\lambda = 1$. The dispersed phase volume fraction is $\phi = 0.14$. The drop temporary coalescence, followed by breakup is shown in the left bottom corner of the domain

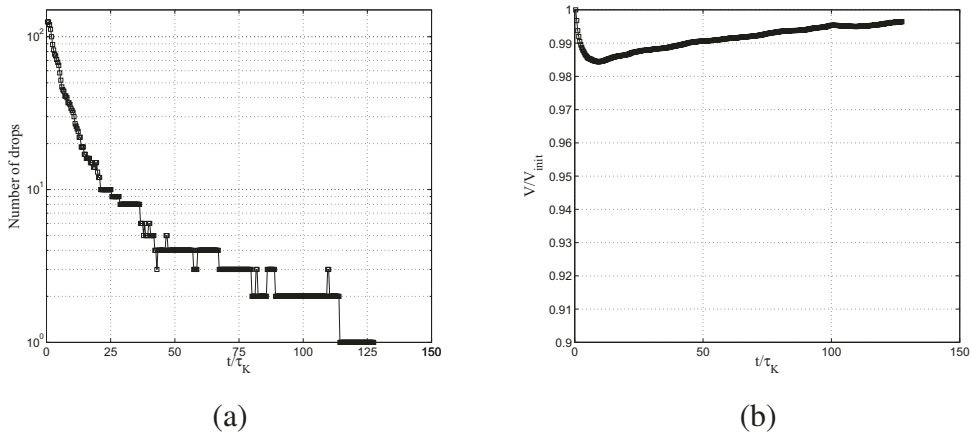


Figure 5.23: Number of drops (a) and dispersed volume V in the system relative to the initial value V_{init} (b) as functions of time for the case with Kolmogorov length scale resolution $\eta_K = 5$ [lu] and viscosity ratio $\lambda = 1$. The dispersed phase volume fraction is $\phi = 0.14$

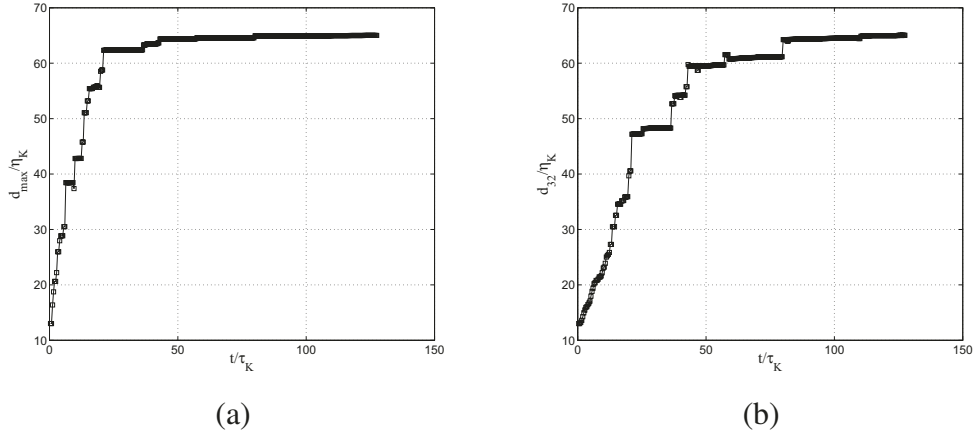


Figure 5.24: Dimensionless maximum d_{\max} (a) and Sauter mean d_{32} (b) diameters as functions of time for the case with Kolmogorov length scale resolution $\eta_K = 5$ [lu] and viscosity ratio $\lambda = 1$. The dispersed phase volume fraction is $\phi = 0.14$

accuracy is reached for corresponding energy values E .

The kinetic energy spectrum changes dramatically when the second phase is injected. Energy spectra of one- and two-phase turbulent flows that correspond to different resolution of Kolmogorov scales are presented in Fig. 5.25. As one can see, there is a significant energy gain at high wave numbers or length scales which are of the order of and smaller than Kolmogorov length scale η_K . Furthermore, the energy gain is more notable for higher η_K resolution. This issue has a numerical background. An increase of η_K assumes a decrease of the energy dissipation rate. As a result, the velocities in lattice units get smaller. Artificial numerical issues arise when velocities approach the magnitudes of spurious currents representing a numerical peculiarity of diffuse interface methods including LBE (Van der Sman and Van der Graaf, 2008). In two-phase turbulent flow the velocity magnitude becomes comparable to the magnitude of spurious currents over the liquid-liquid interface. It is demonstrated in Fig. 5.26 for the case of $\eta_K = 2.5$ and $\phi = 0.2$ that small amplitude velocity spikes appear on the interfaces over the length scales in the range 1 – 10 lattice units which is smaller than and of the order of the Kolmogorov length scale. These spikes provide significant energy input in the viscous sub-range where energy gain is observed. For the case with the highest energy input, the velocities over the interface are higher than the spurious currents, which is why the

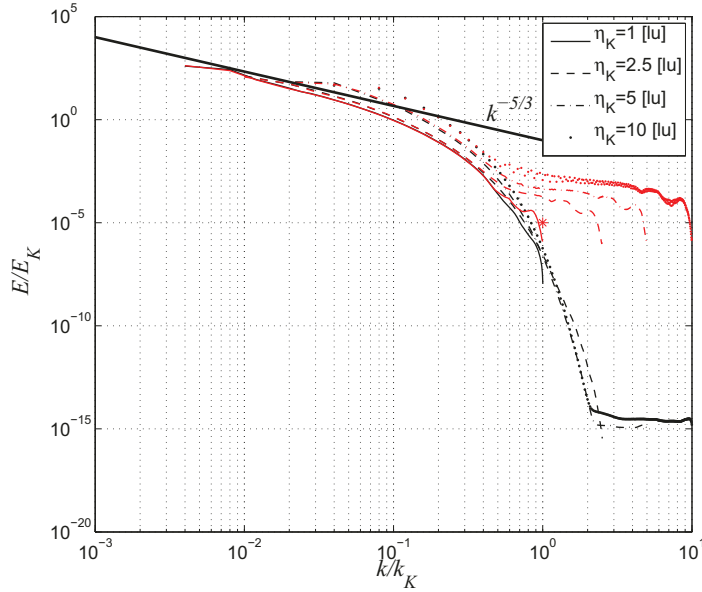


Figure 5.25: Kinetic energy spectrum in one- (black curves) and two-phase (red curves) systems for different resolution of Kolmogorov scales. Energy is scaled with $E_K = \varepsilon^{2/3} \eta_K^{5/3}$; wave number is scaled with $k_K = 2\pi/\eta_K$. Marker * stands for the wavenumber corresponding to the Kolmogorov length scale η_K

energy gain is smaller.

In every simulation performed, the maximum and the Sauter mean diameters are larger than the corresponding η_K . This means that drop sizes mainly fall in the inertial sub-range of the energy cascade, and, therefore, we expect that the breakup and coalescence dynamics is not strongly affected by the energy spikes appearing on scales that are smaller than η_K .

5.6 Conclusions

Numerical simulations of liquid-liquid dispersion formation in turbulent flow have been presented. A free energy lattice Boltzmann method was used to perform large-scale, three-dimensional simulations of the binary system. Simulations were carried out in cubic fully-periodic domains of 500^3 and 1000^3 lattice units. Homogeneous isotropic turbulence was generated throughout the domain by means of linear forcing. Liquids of equal density were considered. The viscosity ratio (dispersed phase

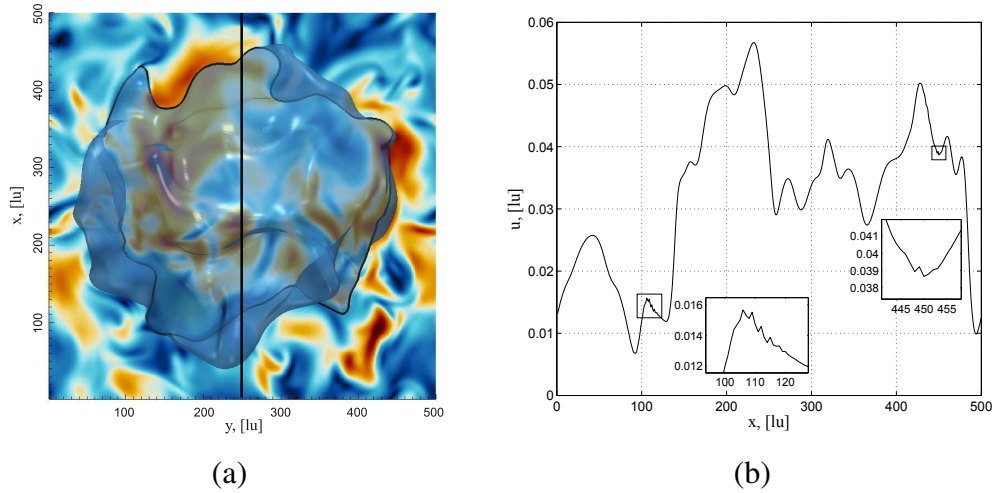


Figure 5.26: Deformed drop and velocity magnitude field (a); velocity magnitude along the black vertical line shown on the left (b). The figure demonstrates the appearance of small velocity spikes over the liquid/liquid interface

over continuous phase viscosity) varied between $\lambda = 1$ and 0.3.

In each simulation, the process of dispersion formation is visualized. The number of drops in the system, the maximum drop diameter, and the Sauter mean diameter are all tracked as functions of time. Several numerical issues of the method are encountered. The method is plagued by numerical dissolution of small drops. It is demonstrated that in order to mitigate the drop dissolution effect, it is necessary to increase the resolution of the Kolmogorov scales. The numerical dissolution of drops can be considered as a numerical mass transfer process between the liquids. The process is characterized by the Peclet number which relates the convection and diffusion time scales. Since time scale of a diffusive process is much larger than of convective, smaller Peclet results in slower dissolution. It is shown that the Peclet number decreases as the resolution of the Kolmogorov scales increases. Moreover, increase of the concentration of the dispersed phase also reduces the dissolution effect. In this case, the specific area gets smaller, thus slowing the numerical mass transfer through the interface. If experimentally it is more challenging to investigate dense systems, in the context of LBE, highly-concentrated systems are advantageous: the dissolution is reduced allowing to better study the physics of the system.

However, with the dispersed phase volume fraction higher than 0.05 it is not possible to form a dispersion, a large portion of dispersed phase remains connected. With the increase of the dispersed phase fraction, drop collisions become more frequent and most of them results in coalescence. Small droplets are likely to coalesce rather than dissolve. In physical system, drops collide, form a thin film of continuous phase between them, the film drains, and eventually ruptures. Drops should be in contact sufficiently long for the film to drain and rupture. Otherwise, the collision is not efficient, and the drops do not merge. In numerical simulations of turbulent dispersion, the drop collision results in merging, except for several cases when the collision process is changed due to interactions with turbulent eddies. Easy coalescence occurs because multiple drop interfaces can occupy the same computational cell. Thus, in order to suppress unphysical coalescence, it is necessary to resolve the film between the drops which requires enormous mesh resolution (see e.g. (Shardt et al., 2013)).

With the present implementation of the free energy LBE method, it is not possible to obtain a representative energy spectrum of two-phase turbulent flow. It is known that LBE methods are prone to spurious currents over the interface due to discretization of the velocity space. The order of magnitude of the velocity field is comparable to the magnitude of the spurious currents. In addition, the spurious currents appear on the diffuse interface. They interfere with the Kolmogorov length scales which leads to significant unphysical energy gain at high wave numbers. The size of the resolved drops, the maximum drop diameter and the Sauter mean diameter, are larger than the corresponding η_K . Thus, they fall into the inertial sub-range of energy cascade, and, therefore, the breakup and coalescence dynamics is not affected by the energy spikes appearing on the scales, which are smaller and of order of η_K .

When the drawbacks of the method are resolved, the developed numerical approach could be used to broaden the understanding of liquid-liquid mixing. The relation between energy input and the resultant DSD can be determined. The size of each drop in dense dispersions can be measured in-line with no disturbance of the flow. Since the dispersed and continuous phase interactions in well-controlled

homogeneous isotropic turbulent flow are resolved on microscopic level, it is possible to derive more fundamental breakup and coalescence kernels even in dense systems, that can be later used in population balance equations.

References

- V.E. Badalassi, H.D. Cenicerros, and S. Banerjee. Computation of multiphase systems with phase field models. *J. Comp. Phys.*, 190:371–397, 2003.
- G.K. Batchelor. *The theory of homogeneous turbulence*. Cambridge university press, 1953.
- P.D. Berkman and R.V. Calabrese. Dispersion of viscous liquids by turbulent flow in a static mixer. *AIChE J.*:602–609, 1988.
- P. L. Bhatnagar, E. P. Gross, and M. Krook. A model for collision processes in gases. I. Small amplitude processes in charged and neutral one-component systems. *Phys. Rev.*, 94:511–525, 1954.
- L. Biferale, P. Perlekar, M. Sbragaglia, S. Srivastava, and F. Toschi. A lattice boltzmann method for turbulent emulsions. *J. Phys.: Conference Series*, 318:052017, 2011.
- J.A. Boxall, C.A. Koh, E.D. Sloan, A.K. Sum, and D.T. Wu. Droplet size scaling of water-in-oil emulsions under turbulent flow. *Langmuir*, 28:104–110, 2011.
- D.E. Brown and K. Pitt. Drop size distribution of stirred non-coalescing liquid-liquid system. *Chem. Eng. Sci.*, 27:577–583, 1972.
- A. J. Bray. Theory of phase-ordering kinetics. *Adv. Phys.*, 43:357–459, 1994.
- R.V. Calabrese, T.P.K. Chang, and P.T. Dang. Drop breakup in turbulent stirred-tank contactors. Part I: Effect of dispersed-phase viscosity. *AIChE J.*, 32:657–666, 1986.

- A. ten Cate, E. van Vliet, J.J. Derksen, and H.E.A. Van den Akker. Application of spectral forcing in lattice–Boltzmann simulations of homogeneous turbulence. *Computers and Fluids*, 35:1239–1251, 2006.
- J. W. Cahn and J. E. Hilliard. Free energy of a nonuniform system. I. Interfacial free energy. *J. Chem. Phys.*, 28:258–267, 1958.
- S.B. Collins and J.G. Knudsen. Drop-size distributions produced by turbulent pipe flow of immiscible liquids. *AIChE J.*, 16:1072–1080, 1970.
- V. Cristini and Y.-C. Tan. Theory and numerical simulation of droplet dynamics in complex flows—a review. *Lab Chip*, 4:257–264, 2004.
- L. A. Cutter. Flow and turbulence in a stirred tank. *AIChE J.*, 12:35–45, 1966.
- J.T. Davies. A physical interpretation of drop sizes in homogenizers and agitated tanks, including the dispersion of viscous oils. *Chem. Eng. Sci.*, 42:1671–1676, 1987.
- J.J. Derksen and H.E.A. Van den Akker. Multi-scale simulations of stirred liquid-liquid dispersions. *ICHEME*, 85:697–702, 2007.
- J.J. Derksen. Flow-induced forces in sphere doublets. *J. Fluid Mech.*, 608:337–356, 2008.
- X. He, S. Chen, and R. Zhang. A lattice Boltzmann scheme for incompressible multiphase flow and its application in simulation of Rayleigh-Taylor instability. *J. Comp. Phys.*, 152:642–663, 1999.
- J.O. Hinze. Fundamentals of the hydrodynamic mechanism of splitting in dispersion processes. *AIChE J.*, 1:289–295, 1955.
- D. Jacqmin. Calculation of two-phase Navier–Stokes flows using phase–field modeling. *J. Comp. Phys.*, 155:96–127, 1999.
- X. Jia, J.B. McLaughlin, and K. Kontomaris. Lattice Boltzmann simulations of flows with fluidfluid interfaces. *Asia-Pac. J. Chem. Eng.*, 3:124–143, 2008.

- V.M. Kendon, M.E. Cates, I. Pagonabarraga, J.-C. Desplat, and P. Bladon. Inertial effects in three-dimensional spinodal decomposition of a symmetric binary fluid mixture: a lattice boltzmann study. *J. Fluid Mech.*, 440:147–203, 2001.
- D. B. Khismatullin, Y. Renardy, and V. Cristini. Inertia-induced breakup of highly viscous drops subjected to simple shear. *Phys. Fluids*, 15:1351–1354, 2003.
- A. E. Komrakova, J.J. Derksen, and D. Eskin. Simulations of dispersion formation in liquid-liquid turbulent flows. In *8th International Conference on Multiphase Flow, ICMF 2013*, Jeju, Korea, May 2631.
- A. E. Komrakova, O. Shardt, D. Eskin, and J. J. Derksen. Lattice Boltzmann simulations of drop deformation and breakup in shear flow. *IJMF*, 59:24–43, 2014a.
- A. E. Komrakova, O. Shardt, D. Eskin, and J.J. Derksen. Effects of dispersed phase viscosity on drop deformation and breakup in inertial shear flow. *Phys. Fluids*, submitted, 2014b.
- H. Kusumaatmaja. *Lattice Boltzmann Studies of Wetting and Spreading on Patterned Surfaces*. PhD thesis, University of Oxford, 2008.
- J. Lovick, A.A. Mouza, S.V. Paras, G.J. Lye, and P. Angeli. Drop size distribution in highly concentrated liquidliquid dispersions using a light back scattering method. *J. Chem. Technol. Biotechnol.*, 80:545–552, 2005.
- T.S. Lundgren. Linearly forced isotropic turbulence. *Annual Research Briefs*, 461–473, 2003.
- F. Magaletti, F. Picano, M. Chinappi, L. Marino, and C.M. Casciola. The sharp-interface limit of the Cahn-Hilliard/Navier-Stokes model for binary fluids. *J. Fluid Mech.*, 714:95–126, 2013.
- M. Nekovee, P. V. Coveney, H. Chen, and B. M. Boghosian. Lattice-Boltzmann model for interacting amphiphilic fluids. *Phys. Rev. E*, 62:8282–8294, 2000.

- A.W. Pacek, C.C. Man, and A.W. Nienow. On the sauter mean diameter and size distributions in turbulent liquid/liquid dispersions in a stirred vessel. *Chem. Eng. Sci.*, 53:2005–2011, 1998.
- E.L. Paul, V.A. Atiemo-Obeng, and S.M. Kresta, editors. *Handbook of Industrial Mixing: Science and Practice*. John Wiley & Sons, Inc., 2004.
- O. Penrose and P. Fife. Thermodynamically consistent models of phase-field type for the kinetics of phase transitions. *Physica D*, 43:44–62, 1990.
- S.B. Pope. *Turbulent flows*. Cambridge University Press, 2000.
- F. Ravelet, R. Delfos, and J. Westerweel. Experimental studies of liquid-liquid dispersion in a turbulent shear flow. *arXiv:0707.1398v2 [physics.flu-dyn]*, pages 1–6, 2007.
- C. Rosales and C. Meneveau. Linear forcing in numerical simulations of isotropic turbulence: Physical space implementations and convergence properties. *Phys. Fluids*, 17:095106, 2005.
- P.E. Rueger and R.V. Calabrese. Dispersion of water into oil in a rotor-stator mixer. Part 1: dropbreakup in dilute systems. *Chem. Eng. Res. Des.*, 91:2122–2133, 2013.
- R. Skartlien, E. Sollum, and H. Schumann. Droplet size distributions in turbulent emulsions: Breakup criteria and surfactant effects from direct numerical simulations. *J. Chem. Phys.*, 139:174901, 2013.
- X. Shan and H. Chen. Lattice Boltzmann model for simulating flows with multiple phases and components. *Phys. Rev. E*, 47:1815–1819, 1993.
- O. Shardt, J.J. Derksen, and S. K. Mitra. Simulations of droplet coalescence in simple shear flow. *Langmuir*, 29:6201–6212, 2013.
- C.A. Sleicher. Maximum stable drop size in turbulent flow. *AIChE Journal*, 8: 471–477, 1962.

- R.G.M. van der Sman and S. van der Graaf. Emulsion droplet deformation and breakup with Lattice Boltzmann model. *Comp. Phys. Commun.*, 178:492–504, 2008.
- M.R. Swift, E. Orlandini, W.R. Osborn, and J.M. Yeomans. Lattice Boltzmann simulations of liquid-gas and binary fluid systems. *Phys. Rev. E*, 54:5041–5052, 1996.
- H. Tennekes and J.L. Lumley. *A first course in turbulence*. The MIT Press, 1973.
- F. Toschi, P. Perlekar, L. Biferale, and M. Sbragaglia. Droplet breakup in homogeneous and isotropic turbulence. *arXiv:1010.1795*, pages 1–4, 2010.
- L. Valino, J. Martin, and G. Hazi. Dynamics of Isotropic Homogeneous Turbulence with Linear Forcing Using a Lattice Boltzmann Method. *Flow Turbulence Combust*, 84:219–237, 2010.
- B. Weinstein and Treybal. Liquid-liquid contacting in unbaffled, agitated vessels. *AIChE J.*, 19:304–312, 1973.
- P. Yue, J.J. Feng, C. Liu, and J. Shen. A diffuse-interface method for simulating two-phase flows of complex fluids. *J. Fluid Mech.*, 515:293–317, 2004.
- G. Zhou and S.M. Kresta. Correlation of mean drop size and minimum drop size with the turbulence energy dissipation and the flow in an agitated tank. *Chem. Eng. Sci.*, 53:2063–2079, 1998.

Chapter 6

Conclusions and outlook

6.1 Conclusions

In the present project, a numerical approach to study liquid-liquid dispersions has been developed. The free energy LBE model was used to perform three-dimensional direct numerical simulations of binary liquid systems. A computer code was created using FORTRAN 90 in serial and parallel versions. The parallel code used domain decomposition and the MPI (Message Passing Interface) platform. The number of processors to perform simulation varied depending on the considered problem from 1 to 125 with a memory usage of 8 GB per processor. In addition, the capability of the code to run simulations on 1000 processors with 3D domain decomposition of a fully-periodic domain was successfully tested. The vast majority of jobs was performed on WestGrid clusters. The data were visualized in ParaView.

The developed approach has been verified, validated and applied to study several research problems: a single *n*-butanol drop rising in water under the influence of gravity, the behavior of a single liquid drop suspended in another liquid and subjected to simple shear flow, and formation of turbulent liquid-liquid dispersions. The results of these studies show that the numerical approach can be adopted to perform simulations with moving, deforming, rupturing and merging liquid-liquid interfaces.

The accuracy of the results is primarily determined by the mesh resolution. Based on the simulations of sheared drops, two regions of resolution are outlined: a region of moderate resolution with drop radii $a \leq 30$ lattice units and high resolu-

tion with $a > 30$ [lu]. It has been demonstrated that even moderately resolved drops can be used to investigate the physics of drop deformation and breakup. Shape-oscillating motion of drops in the oscillatory regime is captured for a drop of radius $a = 30$ [lu], while the process of drop deformation followed by breakup is revealed for the drops with initial undeformed drop radius of $a = 20$ [lu]. The fact that the behavior of lower-resolved drops can be captured is very valuable for simulations of dispersion formation in turbulent flow: satellite and sub-satellite drop formed after breakup are resolved, and it is feasible to simulate systems with hundreds of drops. Even though mesh resolution plays a key role in accuracy, numerical parameters should also be chosen with special care.

The diffuse interface free energy LBE method is characterized by a finite thickness of the interface between the two liquids which is much larger than the actual physical thickness estimated as tens of Angströms (Yang and Li, 1996). The interface thickness and related free energy model parameters introduce numerical degrees of freedom. It is relatively easy to set the interface-related parameters if there is benchmark data such as experimental results or results of simulations obtained using other reliable numerical techniques. If so, it is necessary to validate the developed numerical approach with a reference solution, and determine the interface-related numerical parameters. Once the numerical approach is validated, it can be applied to study problem under different conditions or problems with no reference solution. This approach to determine the numerical parameters was successfully applied in the study of a rising *n*-butanol drop (Chapter 2).

However, benchmark solutions are not always available, while the parameters still have to be specified. In the study of a single sheared drop (Chapter 3) it is demonstrated that the numerical degrees of freedom of the diffuse interface method are characterized by two dimensionless numbers: the Peclet Pe and Cahn Ch numbers. A guideline on how to choose Pe and Ch in order to obtain physically realistic behavior of the drop at given Reynolds number Re , capillary number Ca and viscosity ratio λ is presented. To develop this guideline, several benchmark simulations were performed. The impact of Pe and Ch on accuracy and stability of the method was analyzed in a range of physical conditions from near-creeping flow to Reynolds

of 10. As a conclusion, accuracy and stability are affected by the choice of Pe and Ch . Even though for a given set of physical parameters (Re , Ca , λ) correct physical behavior is captured in most of the cases, different numerical parameters (Pe , Ch) may give different simulation results: at one Peclet number the drop may attain a steady shape, while at another Peclet number the drop may eventually break at high resolution, or the simulation might be unstable at low resolution. It is shown that for a drop with radius a , specification of Ch and Pe is actually the specification of the interface thickness ξ and the mobility coefficient Γ , respectively, because the rest of the parameters involved in the dimensionless numbers are already determined by the chosen drop resolution and the physical dimensionless numbers. If no reference data exist, it is recommended to set these parameters as follows. Drops of moderate resolution require a thinner interface. The suggested value is 1.14 [lu] (in line with the results of Kendon et al. (2001)). For highly resolved drops a thicker interface is preferable (at least two lattice units). And it is suggested to select the mobility coefficient value from the stability range 1 – 15.

This guideline was followed when setting up the parameters for a study of a low viscosity drop in highly viscous liquid under inertial shear flow (Chapter 4). This system is relevant to many industrial processes, but has hardly been studied at a fundamental level. High resolution simulations were performed over the range of viscosity ratios $\lambda = 0.1 - 2$ at $Re = 10$ and different capillary numbers allowing to determine the critical capillary number, the drop breakup mechanism and the visualization of the drop deformation and breakage processes.

The issues in choosing the Peclet and Cahn numbers does not outweigh the advantage of the diffuse interface method over other numerical techniques: the feasibility to perform simulations of a system involving a high fraction of dispersed phase, i.e. large numbers of drops, such as a turbulent liquid-liquid dispersion. Based on the guidelines and the results of studies of sheared drop, the parameters to simulate the formation of liquid-liquid dispersion have been specified (Chapter 5). Three-dimensional simulations were carried out in fully-periodic cubic domains with grids of size 500^3 and 1000^3 . The simulations were executed as follows: first, one-phase homogeneous isotropic turbulence with a well-controlled energy dissi-

pation rate was generated throughout the domain by means of linear forcing. Four levels of Kolmogorov length scale resolution have been considered $\eta_K = 1, 2.5, 5$ and 10 [lu]. Even with $\eta_K = 1$ [lu] the turbulence was resolved. The second phase was instantaneously injected into fully-developed turbulent flow. The process of dispersion formation was then followed and visualized, revealing the details of breakup and coalescence. The volume-equivalent diameter of every drop was measured providing information on DSD of the dispersion. Based on these measurements, the maximum and the Sauter mean diameters were calculated. However, several numerical issues have been encountered.

It is known that LBE methods are prone to spurious currents over the interface due to discretization of the velocity space. In order to estimate the magnitude of these parasitic velocities, the equilibration of a single stationary drop was simulated. Spurious velocities over the interface are of the order of $10^{-4} - 10^{-5}$ in lattice units, while the order of the velocity field in the rising and sheared drop simulations is of 10^{-2} [lu]. Thus, the velocities related to the spurious currents are several orders of magnitude smaller than the physical velocities. In simulations of turbulent dispersion, the order of velocity field is of $10^{-4} - 10^{-3}$ [lu] which is comparable to spurious currents. In addition, the spurious currents appear on the diffuse interface which makes it difficult to obtain a representative energy spectrum of two-phase turbulent flow. The spurious velocities that appear at the scales comparable to the Kolmogorov length scales η_K lead to significant unphysical energy gain at high wavenumbers. Nevertheless, in every simulation performed the maximum and the Sauter mean diameters are larger than the corresponding η_K . This means that they fall into inertial sub-range of energy cascade, and, therefore, the breakup and coalescence dynamics is not affected by the velocity spikes appearing at the high wavenumbers.

Another peculiarity of the diffuse interface methods is the numerical dissolution of small drops. The dissolution of drops rising under gravity and deforming under shear is negligible since the initial undeformed diameter of the drops of $20 - 30$ [lu] is large enough so that the evolution of the system occurs faster than the drops dissolve. However, numerical dissolution has an impact on the simulation results

when drop breakage occurs and small daughter, satellite and sub-satellite droplets are formed. The volume-equivalent diameter of the fragments can be 10 [lu] and smaller. These droplets dissolve almost immediately after formation which makes it difficult to measure the DSD of the dispersion. A straightforward thing to do to overcome this issue is to increase the resolution of the simulation, i.e. increase the diameter of the initial undeformed drop. In this case, the size of the drops produced after breakup increases as well, therefore, they can be captured and measured. For instance, high-resolution simulations allowed to reveal capillary wave breakup demonstrated in Chapter 4.

In turbulent two-phase flow simulations, however, increase of mesh resolution is computationally very expensive. In addition, turbulent dispersion formation is characterized by multiple breakup processes, and small satellite and sub-satellite are very likely to appear after consecutive breakages. In order to mitigate drop dissolution in such system, it is suggested to increase the resolution of the Kolmogorov scales. The numerical dissolution of drops can be considered as a numerical mass transfer process between the liquids. The process is characterized by the Peclet number which relates the convection time scale to the interface diffusion time scale. Smaller Peclet means that diffusion dominates over convection. Since the time scale of a diffusive process is much larger than of convective, smaller Peclet results in lower dissolution rate. It is shown that the Peclet number decreases as the resolution of the Kolmogorov scales increases. An additional way to mitigate the drop dissolution is to increase the concentration of the dispersed phase. In this case, the specific area gets smaller, thus, lowering the numerical mass transfer through the interface. If experimentally it is more challenging to investigate dense systems, in the context of LBE, highly-concentrated systems are advantageous: the dissolution is reduced allowing to better study the physics of the system.

With the increase of the dispersed phase fraction, drop collisions become more frequent and may result in coalescence. In physical system, drops collide, form a thin film of continuous phase between them, the film drains, and eventually ruptures. Drops should be in contact sufficiently long for the film to drain and rupture. Otherwise, the collision is not efficient, and the drops do not merge. In numerical

simulations of turbulent dispersion, the drop collision results in merging, except for several cases when the collision process is changed due to interactions with turbulent eddies. Easy coalescence occurs because multiple drop interfaces can occupy the same computational cell. Thus, in order to suppress unphysical coalescence, it is necessary to resolve the film between the drops which requires enormous mesh resolution (see e.g. (Shardt et al., 2013)). Another option is to introduce surfactants as it has been done by Skartlien et al. (2013).

Nevertheless, even with the outlined numerical drawbacks, the developed numerical approach can contribute to a deeper understanding of liquid-liquid systems in a wide range of operating conditions from creeping shear to fully-developed turbulent flows. One of the most valuable capabilities of the approach is visualization of the flow: whether it is evolution of initially spherical drop rising under the influence of gravity, deformation of a drop during sudden onset of shear or the bursting of a drop in a turbulent flow field. The approach can be used to gain fundamental knowledge on liquid-liquid systems: determination of terminal drop rise velocities and the conditions for the shape-oscillating regime for single rising droplets. Drop breakup mechanism for drop in shear can be determined. And it also useful for industrial application: for a given binary system of two liquids under applied shear it is possible to determine the DSD, or if the final product should have a certain DSD then the proper shearing conditions can be found. For a given binary liquid system, the critical capillary number can be found. The binary liquid systems subjected to inertial shear flow at capillary numbers much higher than the critical have not been extensively studied on fundamental level. This gap can be filled with the use of the present approach. Also it is possible to consider sheared drops in confined channels, and assess the drop deformation and breakup mechanisms with wall effects.

When turbulently-induced dispersion are considered, it is possible to relate the local energy dissipation and the DSD of the system. Moreover, the volume-equivalent diameter of every drop is measured in-line without any disturbance of the flow. Based on these data, the maximum, mean, and minimum drop diameters are easily calculated. The rates of drop breakup and coalescence can be determined and used to construct sub-models for CFD methods and kernels for PBEs.

6.2 Outlook

The promising results of the simulations motivate further development of the approach so as to serve as a valuable addition to experimental studies. As for the future work, it is necessary to test the sensitivity of the results of turbulent dispersion formation with respect to the interface-related numerical parameters and spatial resolution. An influence of the length of the cubic domain edge L_d should also be considered especially in cases with high resolution of Kolmogorov length scale. Simulation domain sizes larger than 1000^3 require further optimization of the developed computer code.

It is also of interest to study in detail the relation between turbulence and the DSD of liquid-liquid dispersion. How do the turbulent flow patterns change with an introduction of the second phase especially at high dispersed phase concentrations? Most importantly, it is necessary to estimate an effect of spurious currents on the interface dynamics and, eventually, on the DSD. In the present study, it was assumed that the breakup and coalescence events are not affected by parasitic velocities, since the latter ones appear at the scales much smaller than the drop size. However, this assumption should be quantitatively justified. Furthermore, representative energy spectrum of two-phase turbulent flow should be revealed that requires elimination or at least reduction of the spurious currents. This task is a subject of ongoing research (see e.g. (Lee, 2009; Lee and Fischer, 2006; Pooley and Furtado, 2008; Wagner, 2002)). Connington and Lee (2012) reviewed spurious currents and their elimination in multiphase LBE methods including the free energy model. It is noted by authors that none of the discussed methods can eliminate spurious currents during the transient part of a simulation. The reduction or elimination of spurious velocity typically occurs long after equilibrium has been reached. In case of liquid-liquid dispersions, energy spectrum can be obtained only during dynamic equilibrium in the system. A way to minimize the influence of the spurious currents is to determine the numerical LBE parameters (e.g. the relaxation time) such that the velocity values throughout the domain would have magnitudes larger than the magnitudes of the spurious currents.

In the present study, the size of the resolved drops fell into the inertial sub-range of energy spectrum. It is interesting to see what happens in the system when the drop size reduces to the scales less than Kolmogorov.

Additionally, it is necessary to validate the dispersion formation process which requires knowledge of the numerical LBE parameters that refer to the real physical binary liquid system. The numerical parameters of *n*-butanol/water system have already been determined in Chapter 2. Thus, these values can be used to simulate turbulent dispersion formation of *n*-butanol drops in water. Moreover, the two-relaxation-time (TRT) collision operator (Ginzburg et al., 2008) was incorporated in that studies. So the existing code based on the single-relaxation-time collision operator (Bhatnagar et al., 1954) should be extended to utilize the TRT. This study will show an influence of collision operator choice on accuracy and stability. Also this binary liquid system can be considered under shear flow conditions. It will be possible to compare the deformation and breakup of a single *n*-butanol drop suspended in water and subjected to simple shear and the behavior of the same drop in turbulent flow.

Once the numerical issues are resolved, the approach can be applied to study different physical systems and influence of physical properties and agitation conditions on DSD.

References

- P. L. Bhatnagar, E. P. Gross, and M. Krook. A model for collision processes in gases. I. Small amplitude processes in charged and neutral one-component systems. *Phys. Rev.*, 94:511–525, 1954.
- K. Connington and T. Lee. A review of spurious currents in the lattice Boltzmann method for multiphase flows. *J. Mech. Sci. Technol.*, 26:3857–3863, 2012.
- I. Ginzburg, F. Verhaeghe, and D. d’Humières. Two-relaxation-time lattice Boltzmann scheme: about parametrization, velocity, pressure and mixed boundary conditions. *Commun. Comput. Phys.*, 3:427–478, 2008.
- V.M. Kendon, M.E. Cates, I. Pagonabarraga, J.-C. Desplat, and P. Bladon. Inertial effects in three-dimensional spinodal decomposition of a symmetric binary fluid mixture: a lattice boltzmann study. *J. Fluid Mech.*, 440:147–203, 2001.
- T. Lee. Effects of incompressibility on the elimination of parasitic currents in the lattice Boltzmann equation method for binary fluids. *Computers and Mathematics with Applications*, 58:987–994, 2009.
- T. Lee and P.F. Fischer. Eliminating parasitic currents in the lattice Boltzmann equation method for nonideal gases. *Phys. Rev. E*, 74:046709, 2006.
- C.M. Pooley and K. Furtado. Eliminating spurious velocities in the free-energy lattice Boltzmann method. *Phys. Rev. E*, 77:046702–1–9, 2008.
- O. Shardt, J.J. Derksen, and S. K. Mitra. Simulations of droplet coalescence in simple shear flow. *Langmuir*, 29:6201–6212, 2013.

- R. Skartlien, E. Sollum, and H. Schumann. Droplet size distributions in turbulent emulsions: Breakup criteria and surfactant effects from direct numerical simulations. *J. Chem. Phys.*, 139:174901, 2013.
- A. J. Wagner. The origin of spurious velocities in lattice Boltzmann *Int. J. Mod. Phys. B*, 17:193, 2002.
- C. Yang and D. Li A method of determining the thickness of liquid-liquid interfaces. *Colloids and Surfaces A: Physicochemical and Engineering Aspects*, 113:51–59, 1996.

Appendix

A-1 The D3Q19 model parameters

The D3Q19 model is used to discretize the velocity space (D. d’Humières et al., 2002). The lattice vectors are separated into two groups. Velocities \mathbf{c}_{1-6} point in the nearest neighbor directions:

$$\begin{pmatrix} c_{x1-6} \\ c_{y1-6} \\ c_{z1-6} \end{pmatrix} = \begin{bmatrix} c & -c & 0 & 0 & 0 & 0 \\ 0 & 0 & c & -c & 0 & 0 \\ 0 & 0 & 0 & 0 & c & -c \end{bmatrix}$$

and \mathbf{c}_{7-18} point in the 12 square diagonal directions

$$\begin{pmatrix} c_{x7-18} \\ c_{y7-18} \\ c_{z7-18} \end{pmatrix} = \begin{bmatrix} c & -c & c & -c & 0 & 0 & 0 & 0 & c & -c & c & -c \\ c & c & -c & -c & c & -c & c & -c & 0 & 0 & 0 & 0 \\ 0 & 0 & 0 & 0 & c & c & -c & -c & c & c & -c & -c \end{bmatrix} \quad (\text{A-1})$$

The equilibrium distributions (H. Kusumaatmaja, 2008) $f_q^{\text{eq}}, g_q^{\text{eq}}$ for population $q = (1 - 18)$ are calculated as follows

$$f_q^{\text{eq}} = \frac{w_q}{c^2} \left(p_0 - \kappa (\partial_{xx}^2 \varphi + \partial_{yy}^2 \varphi + \partial_{zz}^2 \varphi) + c_{\alpha q} \rho u_\alpha + \frac{3}{2c^2} \left[c_{\alpha q} c_{\beta q} - \frac{c^2}{3} \delta_{\alpha\beta} \right] \rho u_\alpha u_\beta \right) + \frac{\kappa}{c^2} \left(w_q^{xx} \partial_x \varphi \partial_x \varphi + w_q^{yy} \partial_y \varphi \partial_y \varphi + w_q^{zz} \partial_z \varphi \partial_z \varphi + w_q^{xy} \partial_x \varphi \partial_y \varphi + w_q^{xz} \partial_x \varphi \partial_z \varphi + w_q^{yz} \partial_y \varphi \partial_z \varphi \right) \quad (\text{A-2})$$

$$g_q^{\text{eq}} = \frac{w_q}{c^2} \left(\Gamma \mu + c_{\alpha q} \rho u_\alpha + \frac{3}{2c^2} \left[c_{\alpha q} c_{\beta q} - \frac{c^2}{3} \delta_{\alpha\beta} \right] \rho u_\alpha u_\beta \right) \quad (\text{A-3})$$

while the distributions for $q = 0$ are given by

$$f_0^{\text{eq}} = \rho - \sum_{q=1}^{18} f_q^{\text{eq}} \quad (\text{A-4})$$

$$g_0^{\text{eq}} = \varphi - \sum_{q=1}^{18} g_q^{\text{eq}}$$

and the bulk pressure is $p_0 = c_s^2 \rho + \frac{A}{2} \varphi^2 + \frac{3B}{4} \varphi^4$

And the weights (H. Kusumaatmaja, 2008) read:

$$\begin{aligned}
w_{1-6} &= \frac{1}{6}, \quad w_{7-18} = \frac{1}{12}, \\
w_{1-2}^{xx} &= w_{3-4}^{yy} = w_{5-6}^{zz} = \frac{5}{12}, \quad w_{3-6}^{xx} = w_{1-2,5-6}^{yy} = w_{1-4}^{zz} = -\frac{1}{3}, \\
w_{7-10}^{xx} &= w_{15-18}^{xx} = w_{7-14}^{yy} = w_{11-18}^{zz} = -\frac{1}{24}, \\
w_{11-14}^{xx} &= w_{15-18}^{yy} = w_{7-10}^{zz} = \frac{1}{12}, \\
w_{1-6}^{xy} &= w_{1-6}^{yz} = w_{1-6}^{zx} = 0, \quad w_{7,10}^{xy} = w_{11,14}^{yz} = w_{15,18}^{zx} = \frac{1}{4}, \\
w_{8,9}^{xy} &= w_{12,13}^{yz} = w_{16,17}^{zx} = -\frac{1}{4}, \quad w_{11-18}^{xy} = w_{7-10}^{yz} = w_{7-14}^{zx} = 0.
\end{aligned} \tag{A-5}$$

The stencils for the gradients and Laplacian calculations in the pressure tensor and chemical potential are

$$\partial_x = \frac{1}{12\Delta x} \left[\begin{pmatrix} 0 & 0 & 0 \\ -1 & 0 & 1 \\ 0 & 0 & 0 \end{pmatrix}, \begin{pmatrix} -1 & 0 & 1 \\ -2 & 0 & 2 \\ -1 & 0 & 1 \end{pmatrix} \begin{pmatrix} 0 & 0 & 0 \\ -1 & 0 & 1 \\ 0 & 0 & 0 \end{pmatrix} \right] \tag{A-6}$$

$$\nabla^2 = \frac{1}{6\Delta x^2} \left[\begin{pmatrix} 0 & 1 & 0 \\ 1 & 2 & 1 \\ 0 & 1 & 0 \end{pmatrix}, \begin{pmatrix} 1 & 2 & 1 \\ 2 & -24 & 2 \\ 1 & 2 & 1 \end{pmatrix} \begin{pmatrix} 0 & 1 & 0 \\ 1 & 2 & 1 \\ 0 & 1 & 0 \end{pmatrix} \right] \tag{A-7}$$

where the left, middle and right matrices show slices of the stencil when $c_{zq} = c$, 0 and $-c$, respectively.

References

- D. d’Humières, I. Ginzburg, M. Krafczyk, P. Lallemand, and L.-S. Luo Multiple-relaxation-time lattice Boltzmann models in three dimensions. *Phil. Trans. R. Soc. Lond. A*, 360:437, 2002.
- H. Kusumaatmaja. Lattice Boltzmann studies of wetting and spreading on patterned surfaces. *University of Oxford*, Ph.D. thesis, 2008.

A-2 Benchmark cases

Benchmark case 1. Simulation parameters are $Re = 1$, $Ca = 0.27$, $\lambda = 1$. To verify that at higher mesh resolution the same influence of Pe and Ch holds, mesh refinement cases were considered with the base-line drop radius of $a = 32$ [lu]. The refinement factors of 1.5 and 2.0 gave drop radii of 48 and 64 [lu]. The Cahn numbers of $Ch = 0.0355$ and 0.0625 at Peclet numbers of 1, 3 and 10 were examined.

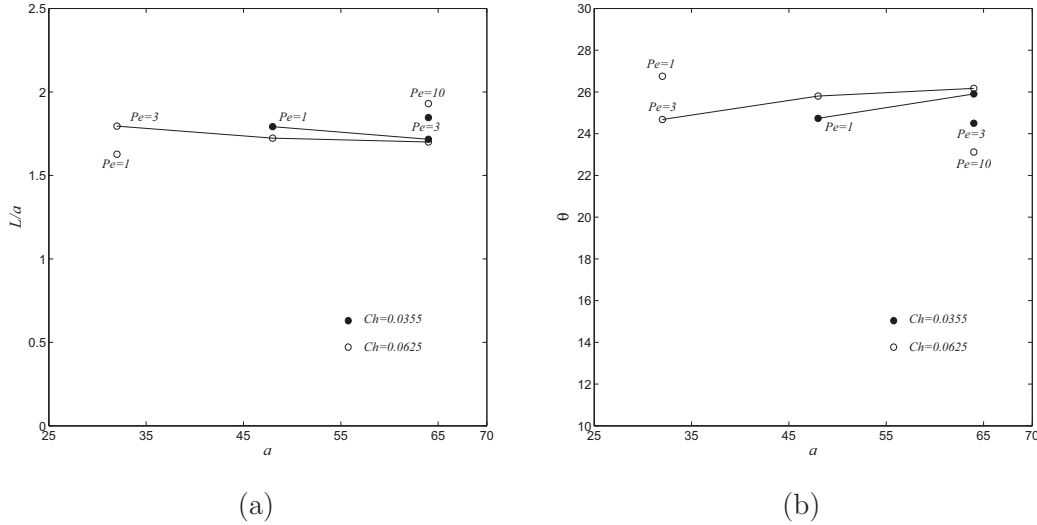


Figure A-1: Drop deformation results at $Re = 1$, $Ca = 0.27$, $\lambda = 1$ and different Pe and Ch numbers. The L/a ratio (a) and the orientation angle θ (b) as a function of drop radius (Benchmark 1)

The drop elongation and orientation angle are presented in Fig. A – 1 (a) and (b), respectively. When $Ch = 0.0625$ and $Pe = 1$ the simulations are unstable for $a = 48$ [lu] ($\Gamma = 34.56$ for this case). Breakup of the droplet takes place in the following cases: $Pe = 1$, $Ch = 0.0355$ and $a = 32$ [lu]; $Pe = 3$, $Ch = 0.0355$ and $a \leq 48$ [lu]; $Pe = 10$, $Ch = 0.0625$ and $a \leq 48$ [lu]. Thus, the same trends with Pe on the results as at lower mesh resolution are observed: higher Peclet numbers lead to more deformation and smaller inclination angle of the drop.

Benchmark case 2. Simulation parameters are $Re = 0.0625$, $Ca = 0.1$, $\lambda = 1$. The relaxation times for both distribution functions were set to $\tau_f = \tau_g = 1$.

In what follows two mesh refinement principles are considered. In the first mesh refinement principle all dimensionless parameters are kept constant (physical Re , Ca and λ and numerical Pe and Ch). The second mesh refinement principle assumes keeping Re , Ca , λ , Pe and ξ the same when the mesh is refined. The thickness of

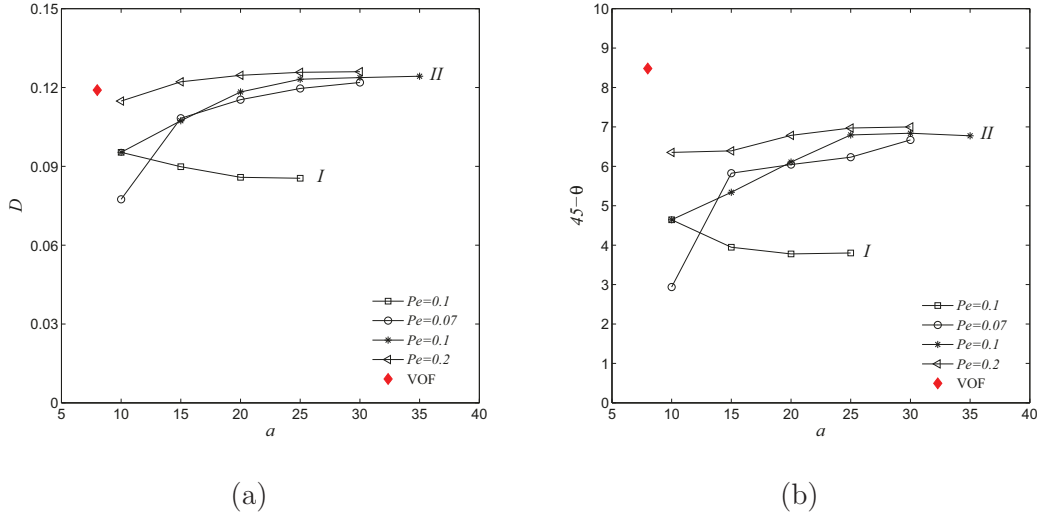


Figure A-2: Drop deformation D (a) and orientation angle of a drop θ (b) for different drop radius a at $Re = 0.0625$, $Ca = 0.1$ and $\lambda = 1$; I first principle of mesh refinement at $Ch = 0.1136 = const$; II second principle of mesh refinement with $\xi = 1.14 = const$. Reference VOF computations of Li et al. (2000) are $D = 0.119$ and $(45 - \theta) = 8.48^\circ$ (Benchmark 2)

the interface is a numerical artifact and the reasoning is that Ch should approach zero when the grid is refined thereby approaching the real (physical) situation. This mesh refinement principle can be considered as approaching the sharp-interface limit (Yue et al., 2010). Both principles are tested further. A base-line drop radius of 10 [lu] was chosen. The refinement factors β were 1.5, 2.0, 2.5 and 3.0. The first principle was tested at $Pe = 0.1$ and $Ch = 0.1136$. The second one was performed with fixed interface thickness of $\xi = 1.14$ [lu] and different Pe numbers of 0.07, 0.1 and 0.2.

The results of drop deformation and orientation angle for the Stokes flow simulations are presented in Fig. A-2 (a) and (b), respectively. Convergence for increased resolution towards an asymptotic value is observed in each case. This means that both mesh refinement principles work: upon refinement the solution tends to become mesh independent. However, at $Pe = 0.1$, $Ch = 0.1136$ and $a = 30$ [lu] the simulations are unstable.

When $a \geq 20$ [lu] and constant interface thickness $\xi = 1.14$ [lu] the deformation results D agree well between different Pe . In addition, the deformation D is in a good agreement with the reference VOF result (the deviation is less than 1% for the finest drops). However, the deviation of the orientation angle θ from the reference data is around 20%.

Benchmark case 3. Physical simulation parameters are $Re = 10$, $Ca = 0.15$, $\lambda = 1$. This capillary number is right below the critical value for the given Re as discussed by Renardy and Cristini (2001). The reference VOF results (Renardy and Cristini, 2001) have $L/a = 1.9$ and $\theta = 23^\circ$. To obtain the required Re , the viscosity of the liquids was lowered by setting the relaxation time to $\tau_f = 0.56$. A mesh refinement procedure was performed with a base-line drop radius of $a = 20$ [lu]. The refinement factors were $\beta = 1.5$ and 2.0 (drop radii of 30 and 40 lattice units). The Cahn numbers were 0.0568 and 0.1. Also the second mesh refinement principle was tested with two constant interface thickness $\xi = 1.14$ and 2.0 lattice units.

The simulation results are organized in Fig. A – 3 and A – 4 where the L/a ratio and the orientation angle θ are plotted versus drop radius a , respectively. In Fig. A – 3(a) and A – 4(a) the results of the first principle at $Ch = 0.0568$ and the second one with fixed $\xi = 1.14$ [lu] at different Pe numbers are shown. The plot in Fig. A – 3(b) and A – 4(b) shows similar results but for constant $Ch = 0.1$ and the fixed interface thickness in 2 [lu]. A significant difference from the reference data is observed for both deformation parameters. However, the reference results of Renardy and Cristini (2001) show unexpected non-monotonic trends. Renardy and Cristini (2001) present L/a and θ as functions of the Reynolds number ranging from 0.0625 to 100. The results at $Re = 10$ and $Ca = 0.15$ deviate from the general trend: by interpolation of nearby results a smaller value of L/a and a higher θ would be expected. For example, Renardy and Cristini (2001) show $L/a = 1.8$ and $\theta = 25^\circ$ at $Re = 1$ and $Ca = 0.27$. At $Re = 60$ and $Ca = 0.053$ the result is $L/a = 1.52$ and $\theta = 53^\circ$. In both cases the capillary number is sub-critical. Thus, for the case at $Re = 10$ and $Ca = 0.15$ an elongation between 1.52 and 1.8 is expected since the drop shortens as Re increases. Similarly, an orientation angle between 25° and 53° is expected because the drops tend to align more vertically for higher Re . In addition, the deviation between the present and reference data can be minimized if the Peclet number is increased.

The results based on the first mesh refinement principle (constant Ch) converge marginally better than the results based on the second one (constant ξ). The simulations of the drops with $a = 40$ [lu] and fixed $\xi = 1.14$ [lu] at $Pe = 3$ and 4 resulted in breakup. The reason is a low mobility coefficient Γ . When $a = 40$ [lu] and $Ch = 0.1 = const$ at $Pe = 1.5$ and 2 the simulations are unstable because of a too high Γ value ($\Gamma = 107$ and 80, respectively). Drops are more deformed if they have a thinner interface. In addition an increase in Pe leads to an increase of deformation.

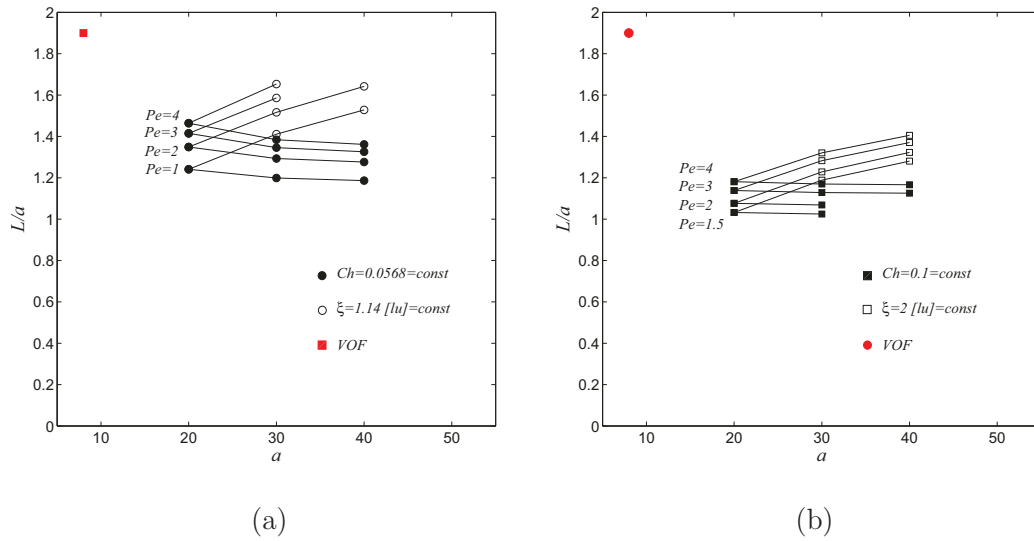


Figure A-3: Elongation of a drop L related to initial drop radius a for different drop radii. $Re = 10$, $Ca = 0.15$, $\lambda = 1$. Cases denoted by \bullet , \blacksquare refer to the first principle of mesh refinement; cases denoted by \circ , \square refer to the second principle of mesh refinement (Benchmark 3)

The droplets incline more when Pe is smaller.

In the Stokes flow limit, only one vortex forms inside the drop (see Fig. 3.8). The drop inclines towards the flow direction and has an ellipsoidal shape. With increasing Reynolds number, three major events take place (Renardy and Cristini, 2001). First, the drop becomes more aligned with the vertical axis and shortens in the horizontal direction. Second, two vortices appear in the drop. And the third change is that the symmetry over the mid-plane at steady state is lost (see Fig. 3.13). These effects can also be observed in Fig. 5(c) presented by Renardy and Cristini (2001). To validate the present numerical technique, the velocity field inside the drop was compared to the reference data.

In Fig. A-5 the drop shapes together with streamlines inside the drop are plotted for the cases with $Pe = 1$ for two types of mesh refinement: (a)-(c) fixed $Ch = 0.0568$ (the first principle); (a), (d), (e) fixed interface thickness $\xi = 1.14 [lu]$. $Pe = 1$ has been chosen because the drop does not break in the entire range of drop radii. The black curves in Fig. A-5 show the interface ($\varphi = 0$). In every case two vortices can be seen. However, the drop is deformed differently. Consider the first type of mesh refinement (figures (a)-(c)). With increasing resolution, the interface widens, and the drop deforms less and shortens in the flow direction. On the other hand, finer drops with thinner interface (figures (d) and (e)) are more

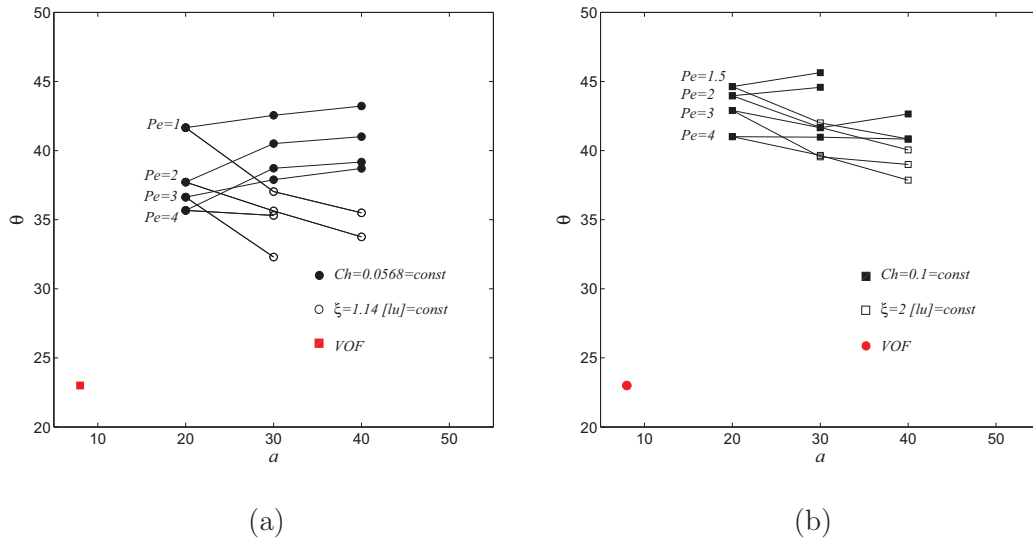
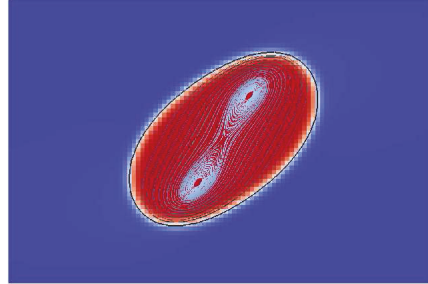


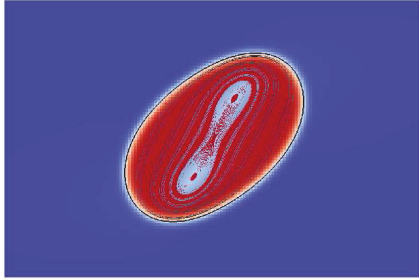
Figure A-4: Orientation angle of a drop θ for different drop radii. $Re = 10$, $Ca = 0.15$, $\lambda = 1$. Cases denoted by \bullet , \blacksquare refer to the first principle of mesh refinement; cases denoted by \circ , \square refer to the second principle of mesh refinement

deformed compared to the base-case. The internal circulations migrate almost to the tips of the drop (compare figure (c) and (d)). The same remarks refer to other cases at different Pe .

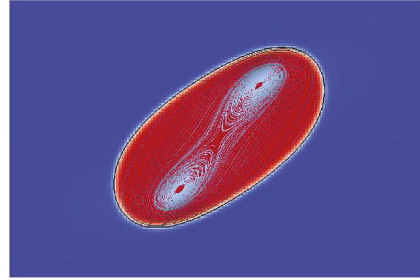
Now consider a higher Ch (with the interface thickness of 2 [lu]). The drop shape and internal circulations are shown in Fig. A – 6 at $Pe = 4$ for different mesh refinement types: (a)-(c) constant $Ch = 0.1$ (the first principle); (a), (d), (e) fixed interface width of two lattice units. $Pe = 4$ was chosen because simulations are stable in the entire range of drop radii. As one can see, none of the mesh refinement simulations with the first principle were able to capture two vortices inside the drop. The interface is so thick relative to the drop diameter that the circulations cannot develop. When the size of the drop was increased while keeping the interface thickness constant, two vortices were captured (figures (d) and (e)). However the intensity of these circulations is different. The finest drop has more developed flow inside.



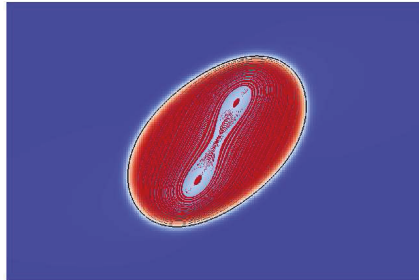
(a) $a = 20$ [lu], $\xi = 1.14$ [lu], $Ch = 0.0568$



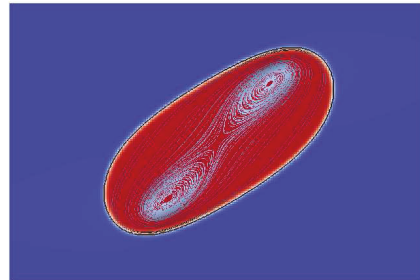
(b) $a = 30$ [lu], $\xi = 1.7$ [lu], $Ch = 0.0568$



(d) $a = 30$ [lu], $\xi = 1.14$ [lu], $Ch = 0.0379$

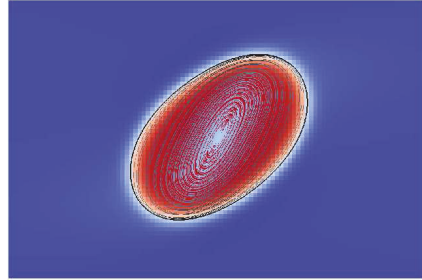


(c) $a = 40$ [lu], $\xi = 2.28$ [lu], $Ch = 0.0568$

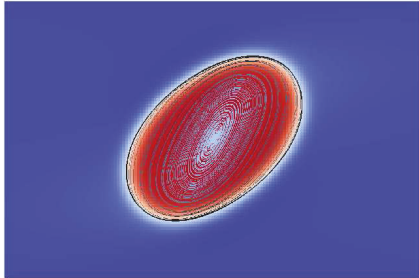


(e) $a = 40$ [lu], $\xi = 1.14$ [lu], $Ch = 0.0284$

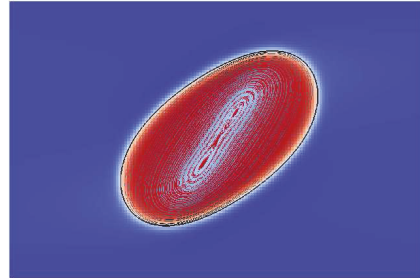
Figure A-5: Drop shape (φ field) and streamlines at steady-state at $Re = 10$, $Ca = 0.15$, $\lambda = 1$, $Pe = 1$ and different Ch numbers: (a)-(c) the first principle of mesh refinement; (a), (d), (e) the second principle of mesh refinement (Benchmark 3)



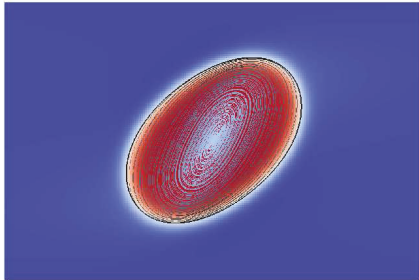
(a) $a = 20$ [lu], $\xi = 2$ [lu], $Ch = 0.1$



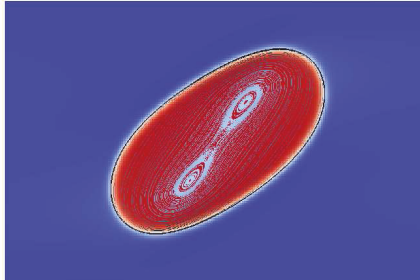
(b) $a = 30$ [lu], $\xi = 3$ [lu], $Ch = 0.1$



(d) $a = 30$ [lu], $\xi = 2$ [lu], $Ch = 0.067$



(c) $a = 40$ [lu], $\xi = 4$ [lu], $Ch = 0.1$



(e) $a = 40$ [lu], $\xi = 2$ [lu], $Ch = 0.05$

Figure A-6: Drop shape (φ field) and streamlines at steady-state at $Re = 10$, $Ca = 0.15$, $\lambda = 1$, $Pe = 4$ and different Ch numbers: (a)-(c) the first principle of mesh refinement; (a), (d), (e) the second principle of mesh refinement (Benchmark 3)

References

- J. Li, Y.Y. Renardy and M. Renardy. Numerical simulation of breakup of a viscous drop in simple shear flow through a volume-of-fluid method. *Phys. Fluids.*, 12: 269–282, 2000.
- Y.Y. Renardy and V. Cristini. Effect of inertia on drop breakup under shear. *Phys. Fluids.*, 13:7–13, 2001.
- P. Yue, C. Zhou and J. J. Feng. Sharp-interface limit of the Cahn-Hilliard model for moving contact lines. *J. Fluid Mech.*, 645:279–294, 2010.

A-3 Comparison of CPU and GPU codes

To compare the results of the CPU and GPU codes, the following simulation was performed: a drop with radius $a = 20$ [lu] in a simulation domain of $6.4a \times 6.4a \times 6.4a$ (full size before symmetry-type boundary conditions) at $Re = 0.375$, $Ca = 0.1$, $\lambda = 1$, $Pe = 3.2$, and $Ch = 0.1$. The evolution of drop elongation L/a in time is shown in Fig. A – 7. The relative deviation between steady state values is 0.15%. This deviation is attributed to the difference in the velocity fields caused by the use of two different types of velocity boundary conditions. The velocity of the moving wall in the CPU code was set using a procedure proposed by Mussa et al. (2009), and in GPU code the boundary condition of Ladd (1994) was utilized. In the method of Mussa et al. (2009), the wall is located exactly on the last node, while in the method of Ladd (1994) the wall is located one-half grid spacing beyond the last fluid node. This difference is shown in Fig. A – 8 where the horizontal velocity component obtained with the two codes is plotted along a line starting from the centre of the drop and up to the sheared wall. Since the difference between the elongation of the drop in simulations with the two codes is negligibly small, it is concluded that the CPU and GPU codes produce effectively identical results.

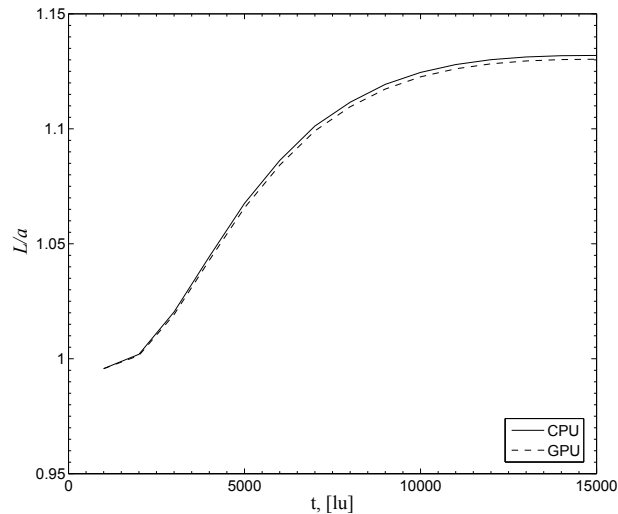
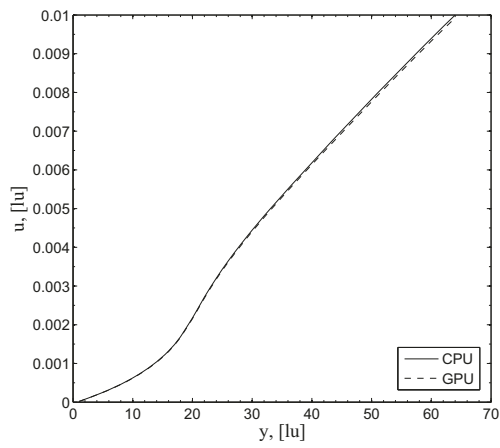
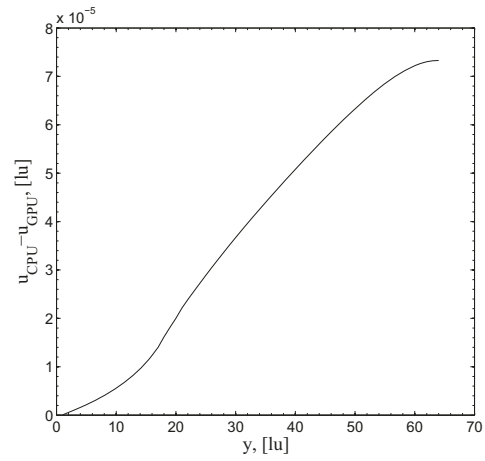


Figure A-7: Drop elongation L/a change in time obtained using CPU and GPU codes



(a)



(b)

Figure A-8: The horizontal velocity component u obtained using CPU and GPU codes as a function of vertical coordinate y starting from the drop centre and up to the wall (a) and the difference between these two values (b)

References

- A. J. C. Ladd. Numerical Simulations of Particulate Suspensions via a Discretized Boltzmann Equation Part I. Theoretical Foundation. *J. Fluid Mech.*, 271:285–309, 1994.
- A. Mussa, P. Asinari and L.-S. Luo. Lattice Boltzmann simulations of 2D laminar flows past two tandem cylinders. *J. Comput. Phys.*, 228:983–999, 2009.